The Measurements on the Branching Fractions and Asymmetries of $B \to K\ell^+\ell^-$ and $B \to K^*\ell^+\ell^-$ Decays

Liang Sun

Department of Physics and Technology
University of Bergen

August 2008

Thesis submitted in partial fulfilment of the requirements for the

degree of Philosophiae Doctor (PhD)

Acknowledgments

Three years have passed since I started working on the field of particle physics in a completely strange land. I could not make it to this day without warm-hearted assistance and support from people in Norway, USA, and my beloved homeland, China.

First of all, I want to express my special thanks to my supervisor, Professor Gerald Eigen for all the help through the years. I am extremely grateful for his patient guidance so that I could start my career in the field of particle physics. His dedication and enthusiasm in the research have deeply impressed me.

I want to thank my colleagues at SLAC. In the past years, Kevin Flood has helped me in nearly every stage of my research on the rare B decays. The completion of my work would not have been possible without his insightful advice. I also owe my thanks to other members of our analysis working group. They have also played important roles in the analyses and offered me a lot of help. Among them Chris Schilling has made predominant contribution in the angular measurements of $B \to K^* \ell^+ \ell^-$ decays. I would like to thank the members of two review committees who have been always very critical to our analyses and provided many thoughtful comments.

Life in a foreign land is always not easy at the beginning. Fortunately I've met quite a few very nice people in Bergen. I want to thank Professor Dieter Röhrich, Ingrid Ofte, Hongyan Yang, Trygve Buanes, Xuemin Gao and many others, who have helped me out of a lot of difficulties.

I want to thank with all my heart to my parents for their support and encouragement all along. They have suffered great pains in raising and educating me for the past over twenty years. I also want to thank my elder brother for his continuous support. He has been always proud of me.

Finally, I would like to thank my wife, Fang Wang. I do owe her a lot for not being able to be together with her for the past three years. The love, encouragement, support, and all kinds of help I have got from her are beyond any words of description.

Preface

Particle physics has emerged as a result of the development of both quantum physics and nuclear physics since the 1950's and 1960's. During that time, a large number of sub-atomic particles were discovered and analyzed in the experiments, the quantum mechanics and quantum field theory were applied to explain their structures and interactions. For the classification of then known particles and understanding of their fundamental interactions, the Standard Model [1, 2, 3] of particle physics came into shape in the early 1970's by integrating a group of proposed theories, such as the unification of electromagnetic and weak interactions, the spontaneous symmetry breaking for explaining the origin of particle masses. With perfect agreement with the experiments, the Standard Model has prevailed ever since and is generally considered as a rather successful theory.

However, the Standard Model is not a complete theory, as it still faces some puzzles and gravity as a fundamental interaction is not included in the theory. A more fundamental theory beyond the Standard Model is expected for explaining physical phenomena at very high energy scale.

Also known as high-energy physics, particle physics requires to analyze particles at high energy scale for probing for new physics. Modern high energy experiments normally utilize gigantic accelerators to accelerate charged particles (electrons, protons, ions) to high energy ranging from a few GeV up to TeV scale. These high energy particles are then guided through beam pipes and collide to trigger reactions at very high energy.

B physics has become an important field of study since the 1980's, as a number of important inputs for particle physics can be measured at high precision. Among these inputs the most interesting are for the probe of matter-antimatter symmetry, which may be the key for solving the puzzle of the excess of matter over antimatter in the early universe. Through colliding high energy electrons and positions, the *BABAR* experiment has accumulated a large data sample of ~ 400 million $B\bar{B}$ pairs since its starting in late 1999.

This thesis describes an overview of a variety of measurements on the rare decays $B \rightarrow K\ell^+\ell^-$ and $B \rightarrow K^*\ell^+\ell^-$ based on a sample of about 384 million $B\bar{B}$ pairs collected in the *BABAR* experiment from 1999 to 2006. The $\ell^+\ell^-$ pair is either e^+e^- or $\mu^+\mu^-$. These decays are highly suppressed in the Standard Model, and could be very sensitive to new physics beyond the Standard Model. In the first chapter of this thesis, the theoretical motivation for the measurements is presented. Chapter 2 briefly describes the SLAC/PEP-II accelerator complex and the *BABAR* detector is given. Chapter 3 describes the selection of $B \rightarrow K^{(*)}\ell^+\ell^-$ events.

Chapter 4 describes measurements of the total and partial branching ratios in two different regions of dilepton invariant mass squared (q^2) separated by J/ψ resonance for different final states of $B \to K^{(*)}\ell^+\ell^-$. The central values with statistical and systematic errors, the statistical significances and the upper limits at 90% and 95% confidence level are also computed using appropriate experimental techniques. Assuming isospin and lepton flavor symmetry, the total branching fractions we have observed are:

$$\mathcal{B}(B_d \to K\ell^+\ell^-) = (0.394^{+0.073}_{-0.069} \pm 0.020) \times 10^{-6},$$

$$\mathcal{B}(B_d \to K^*\ell^+\ell^-) = (1.11^{+0.19}_{-0.18} \pm 0.07) \times 10^{-6}.$$

For each result, the first uncertainty is statistical, and the second is systematic.

In Chapter 4, we also search for direct CP violation ($\mathcal{A}_{CP}$), lepton-flavor ratios, and isospin asymmetries ($\mathcal{A}_I$) in the two q^2 regions. Most of our results are in reasonable agreement with previous measurements and the Standard Model predictions. However the isospin asymmetries we have measured in the q^2 region below the J/ψ resonance are $\mathcal{A}_I(B \to K\ell^+\ell^-) = -1.43^{+0.56}_{-0.85} \pm 0.05$ and $\mathcal{A}_I(B \to K^*\ell^+\ell^-) = -0.56^{+0.17}_{-0.15} \pm 0.03$, which differ respectively by 3.2σ and 2.7σ, including systematic uncertainties, from null results as expected in the Standard Model. By combining these two results, we obtain the isospin asymmetry $\mathcal{A}_I(B \to K^{(*)}\ell^+\ell^-) = -0.64^{+0.15}_{-0.14} \pm 0.03$, with a difference of 3.9σ (including systematic uncertainties) from zero.

Chapter 5 describes measurements of longitudinal K^* polarization (F_L) and lepton forward-backward asymmetry ($\mathcal{A}_{FB}$) for the $B \to K^*\ell^+\ell^-$ decays in two q^2 regions separated by the J/ψ resonance. For the $B \to K^*\ell^+\ell^-$ decays and in the q^2 region below the J/ψ resonance we observe $F_L = 0.35 \pm 0.16 \pm 0.04$ and $\mathcal{A}_{FB} = 0.24^{+0.18}_{-0.23} \pm 0.05$. While in the q^2 region above the J/ψ resonance, we have $F_L = 0.71^{+0.20}_{-0.22} \pm 0.04$ and $\mathcal{A}_{FB} = 0.76^{+0.52}_{-0.32} \pm 0.07$. These results are compared to the predictions from the Standard Model, as well as several new physics models. The observed values of F_L and $\mathcal{A}_{FB}$ are in reasonable agreement with the Standard Model.

Finally, Chapter 6 concludes with a brief discussion on all the results we have measured, and an outlook for future experiments on B physics is also presented.

In addition to the study of rare B decays, I also have performed studies of crystal non-uniformity in the *BABAR* electromagnetic calorimeter. Different non-uniformity models for the crystals have been evaluated and better agreement with data has been achieved using a non-linear non-uniformity model. This study is presented in Appendix I.

Contents

List of Figures

List of Tables

Chapter 1

Introduction

The rare decay $B \to X_s \ell^+ \ell^-$ for a B meson proceeds through a $b \to s \ell^+ \ell^-$ transition, which is a Flavor-Changing Neutral Current (FCNC) process and forbidden at tree level in the framework of the Standard Model [1, 2, 3]. This chapter will show a series of observable physical properties related to the $b \to s \ell^+ \ell^-$ transition, and required techniques, such as the Operator Product Expansion, to make theoretical predictions for these properties. The predictions based on the Standard Model and a few new physics models are presented and compared with each other, to show the potential of these observations for probing for new physics.

1.1 The Standard Model

The Standard Model is essential for classifying the elementary particles. Those elementary particles constituting matter, in the Standard Model, are fermions, which have an intrinsic spin of 1/2. The fermions are grouped into either quarks with color charge or colorless leptons. Both quarks and leptons are organized into three families, with each family consisting of one pair of up-type quark ($u_i = u, c, t$) and down-type quark ($d_i = d, s, b$) or one down-type lepton ($\ell_i = e^-, \mu^-, \tau^-$) and its corresponding chargeless neutrino ($\nu_i = \nu_e, \nu_\mu, \nu_\tau$). The corresponding particles from each family are almost identical, except for their different masses.

The three fundamental interactions (electromagnetic, weak, and strong) among these fermions are mediated by a group of spin-1 gauge bosons. The color-charged quarks interact with each other by exchanging gluons. There are 8 different gluons, corresponding to 8 generators of the SU(3) gauge group in quantum chromodynamics (QCD). The massless photons mediate the electromagnetic interaction between all electrically charged particles, which are well described by quantum electrodynamics (QED) with U(1) gauge group. All 12 fermions carry weak charges and thus couple with $W^\pm$ and neutral Z bosons, as described in the next sub-section.

1.1.1 Weak Interaction and Higgs Mechanism

Governed by a chiral gauge theory of gauge group $SU(2)_L$, the weak interaction only involves left-handed fermions as doublets [4]:

$$\begin{pmatrix} \nu_e \\ e^- \end{pmatrix}_L, \quad \begin{pmatrix} \nu_\mu \\ \mu^- \end{pmatrix}_L, \quad \begin{pmatrix} \nu_\tau \\ \tau^- \end{pmatrix}_L, \tag{1.1}$$

$$\begin{pmatrix} u \\ d' \end{pmatrix}_L, \quad \begin{pmatrix} c \\ s' \end{pmatrix}_L, \quad \begin{pmatrix} t \\ b' \end{pmatrix}_L. \tag{1.2}$$

Three types of vector bosons $(W^\pm, W^0)$ will enter the $\mathrm{SU}(2)_L$ symmetry corresponding to 3 generators in the group. These bosons do not couple with right-handed fermions.

As first proposed by Steven Weinberg in 1967 [2], the weak interaction is further unified with the electromagnetic interaction under a $\mathrm{SU}(2)_L \times \mathrm{U}(1)_Y$ gauge group. W^0 mixes with the electromagnetic gauge boson B in linear combinations to form the observed neutral Z boson and photon field (denoted as A): $Z \equiv -B \sin\theta_W + W^0$, $A \equiv B \cos\theta_W + W^0$, where θ_W is the weak mixing angle (also known as the Weinberg Angle).

So far, the massive behavior of W and Z bosons cannot be explained due to the lack of mass terms in the electroweak Lagrangian. To solve this problem, a scalar field named Higgs field, and with a non-zero vacuum expectation value (VEV) was introduced. The simplest form of the field is expressed by a single complex doublet $\phi \equiv \begin{pmatrix} \phi^+ \\ \phi^0 \end{pmatrix}$. This scalar field interacts with the electroweak field through Yukawa coupling to initiate the *spontaneous symmetry breaking* for the $\mathrm{SU}(2)_L \times \mathrm{U}(1)_Y$ gauge symmetry. Therefore, W and Z bosons obtain a mass proportional to the VEV. This phenomenon is known as the Higgs mechanism [5, 6, 7].

1.1.2 The CKM Matrix and CP Violation

Through the Higgs mechanism, leptons and quarks can also obtain a mass proportional to the VEV from the Yukawa interaction terms. However, as indicated by the primes in Equation 1.2, the flavor eigenstates of down-type quarks (d', s', b') are not the same as their mass eigenstates (d, s, b). The relationship between the flavor and mass eigenstates of down-type quarks is described by the Cabibbo-Kobayashi-Maskawa (CKM) matrix [8, 9], which is a 3×3 unitary matrix defined by:

$$\begin{pmatrix} V_{ud} & V_{us} & V_{ub} \\ V_{cd} & V_{cs} & V_{cb} \\ V_{td} & V_{ts} & V_{tb} \end{pmatrix} \begin{pmatrix} d \\ s \\ b \end{pmatrix} = \begin{pmatrix} d' \\ s' \\ b' \end{pmatrix}, \tag{1.3}$$

where a CKM matrix element $V_{qq'}$ describes the coupling strength between the quark flavors q and q'. The CKM matrix only has four free parameters: three mixing angles and one complex phase. In the Standard Model, this phase alone is responsible for CP violation in hadronic transitions involving the weak interaction, where CP is a combined transformation of charge conjugation (C) and parity reversal (P).

1.2 Physics Beyond the Standard Model

Despite the successes of the Standard Model on its excellent agreement with current experimental observations, there still exist speculations that new physics beyond the

Standard Model could arise at a higher energy (TeV) scale, while the Standard Model only works as a low energy effective form of a more fundamental theory.

Set at a symmetry which relates each Standard Model elementary particle with a new type of particle, supersymmetry (SUSY) is generally considered as the most popular candidate for new physics. It is aimed at solving two outstanding issues [10] in the Standard Model. One is the divergence of the Higgs mass from the self-energy corrections, also known as the hierarchy problem. In the SUSY model, each fermion is assigned a corresponding type of boson as its superpartner, and vice-versa. The corrections can thus be reduced by pairing all the fermionic and bosonic Higgs loop for cancellation.

The other issue is the unification of the strong, weak, and electromagnetic interactions. Distinct from the Standard Model, the inverse gauge couplings of these three interactions can be unified at the Grand Unification Theory (GUT) energy scale of $\mathcal{O}\left(10^{16}\right)$ GeV according to some SUSY models [10].

Among the SUSY models which can fulfill the unification requirement and compatible with the Standard Model, the simplest one is the Minimal Supersymmetric Standard Model (MSSM) as the minimal extension to the Standard Model. This model predicts superpartners of the Standard Model particles with masses as low as a few hundred GeV [10], which offers us possibilities for searching for new physics at the electroweak scale.

In the MSSM, quarks (q) and leptons (ℓ) are associated respectively with spin-0 squarks $(\tilde{q})$ and sleptons $(\tilde{\ell})$ as their superpartners, while the superpartners for gluons (g), W and B gauge bosons are spin-1/2 gluninos $(\tilde{g})$, winos $(\tilde{W})$ and binos $(\tilde{B})$. For the Higgs sector, two additional Higgs doublets with vacuum expectation values ν_1 and ν_2 are required to express additional degrees of freedom. The ratio $\tan \beta = \nu_2/\nu_1$ is a free parameter. Therefore, the Higgs sector is expanded to consist of two (light/heavy) CP-even Higgs bosons (h/H), one CP-odd Higgs boson (A), and two charged Higgs bosons $(H^{\pm})$, instead of only one in the Standard Model. The superpartners of these Higgs bosons (Higgsinos) mix with the superpartners of electroweak gauge bosons $(\tilde{W}, \tilde{B})$ to form mass eigenstates as neutralinos $(\tilde{\chi}^0)$ or charginos $(\tilde{\chi}^{\pm})$ [10].

1.3 The $B \to X_s \ell^+ \ell^-$ Rare Decays

Due to color confinement, quarks are confined with each other by the strong interaction to form quark-antiquark bound states as mesons or three-quark bound states as baryons. Therefore, quarks can only be indirectly observed through mesons and baryons. In order to study the $b \to s \ell^+ \ell^-$ process, we turn to the $B \to X_s \ell^+ \ell^-$ decays, where the B mesons are either charged $(B^+ = u\bar{b}, B^- = \bar{u}b)$ or neutral $(B^0 = d\bar{b}, \bar{B}^0 = \bar{d}b)$.

1.3.1 The Flavor-Changing Neutral Current (FCNC) Processes

In the Standard Model, the FCNC processes are forbidden at tree level. Therefore the $b \to s \ell^+ \ell^-$ FCNC transition can only occur at high orders through loop or box
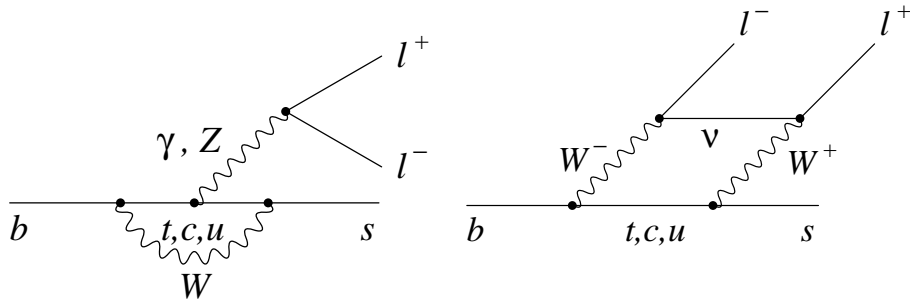
Figure 1.1: The Standard Model Feynman diagrams for the $b \to s\ell^+\ell^-$ transition at leading order. Left: Photon or Z penguin diagram; Right: W box diagram. In the penguin diagram, the Z or photon is emitted from either W boson or an intermediate quark (t, c, u). [11]

diagrams. Figure 1.1 shows the leading order (LO) penguin and box diagrams for the $b \to s\ell^+\ell^-$ transition. Due to the unitarity requirement of the CKM matrix:

$$V_{us}^* V_{ub} + V_{cs}^* V_{cb} + V_{ts}^* V_{tb} = 0,$$

the $b \to s$ FCNC transition involving the mediation of three families of up-type quarks will be canceled out in sum completely if all the quarks have equal masses. However, this is not the case and the transition is allowed to occur at suppressed rates. This suppression on the neutral currents is known as the Glashow-Iliopoulos-Maiani (GIM) mechanism [12], which was proposed by Glashow, Iliopoulos, and Maiani in 1970 to explain the highly suppressed $K^0 \to \mu^+\mu^-$ decay rate and led to the discovery of c quark (before that only three quarks u, d and s were known to exist).

In the FCNC transition, various intermediate particles with a wide energy range are involved. The energy scale μ varies from a normalization scale much higher than W boson mass $m_W (\sim 80\,\mathrm{GeV})$, and falls between m_W and b quark mass $m_b (\sim 5\,\mathrm{GeV})$, then goes down to the QCD scale Λ_{QCD} at a few hundred MeV [13]. Therefore, it will be rather cumbersome to make accurate quantitative calculation of QCD effects by counting on all different scales concurrently, specifically the following two energy regions separated by the mass of heavy quark b m_b:

- The high energy scales larger than m_b, which correspond to short-distance contributions and can be dealt with by using perturbative QCD [14];

- The low energy scales down to Λ_{QCD}, which correspond to long-distance contributions. The running QCD coupling constant will be very large, and different non-perturbative techniques, such as lattice QCD [15] and QCD sum rules [16], will apply here.

1.3.2 The Operator Product Expansion

The complexity of dealing with different energy scales could be partly relieved by considering the short-distance and long-distance contributions separately with corre-

sponding proper techniques. The Operator Product Expansion (OPE), as proposed by Wilson in 1969 [17], then works as an interface to incorporate them. The low-energy effective Hamiltonian for the $b \to s\ell^+\ell^-$ transition ($|\Delta B| = 1$) is expressed in terms of 10 local operators [4, 18, 19, 20]:

$$\mathcal{H}_{eff} = -\frac{4G_F}{\sqrt{2}} V_{ts}^* V_{tb} \sum_{k=1}^{10} C_k(\mu) \mathcal{O}_k(\mu) \ . \tag{1.4}$$

Here G_F is the Fermi coupling constant, $V_{ts}^* V_{tb}$ is the product of the CKM matrix elements related to the $b \to t \to s$ quark transition (the contributions from other lighter up-type quarks are negligible), $\{C_k(\mu)\}$ are scale-dependent Wilson coefficients parametrized from perturbative calculation with μ denoting the appropriate renormalization scale. The local operators $\{\mathcal{O}_k(\mu)\}$ are functions of scale μ defined in [19].

With the OPE, the long-distance contributions enter the local operators $\{\mathcal{O}_k(\mu)\}$, while the short-distance contributions are represented by the Wilson coefficients. They are separated by μ. Typically μ will be chosen around m_b for the convenience of B decay studies.

By keeping only the most relevant operator indices involving top quark for the $b \to s\ell^+\ell^-$ FCNC transition, and neglecting the mass of s quark, the matrix element for $b \to s\ell^+\ell^-$ is written as [19, 21, 22]:

$$
\begin{aligned}
\mathcal{M}\left(b \to s\ell^+\ell^-\right) &= \left\langle s\ell^+\ell^- \right| \mathcal{H}_{eff} \left| b \right\rangle \\
&= \frac{4G_F \alpha}{\sqrt{2}\pi} V_{ts}^* V_{tb} \left[C_9^{eff} \overbrace{\bar{s}_L \gamma_\mu b_L \bar{\ell}\gamma^\mu \ell}^{\mathcal{O}_{9V}} \right. \\
&\left. + C_{10}^{eff} \overbrace{\bar{s}_L \gamma^\mu b_L \bar{\ell}\gamma_\mu \gamma_5 \ell}^{\mathcal{O}_{10A}} - 2C_7^{eff} \overbrace{m_b \bar{s}_L i\sigma_{\mu\nu}\frac{q^\nu}{q^2} b_R \bar{\ell}\gamma^\mu \ell}^{\mathcal{O}_7} \right] \ . \tag{1.5}
\end{aligned}
$$

Here γ_μ are the gamma matrices, and γ^5 is the fifth gamma matrix defined as a product of the gamma matrices $\gamma^5 \equiv i\gamma^0\gamma^1\gamma^2\gamma^3$, $\sigma_{\mu\nu} = \frac{i}{2}[\gamma_\mu, \gamma_\nu]$. s, b, ℓ are fields of corresponding quarks or leptons, the quark fields are assigned with subscripts L or R to indicate their handedness (L/R for the left-/right- handed). q^2 is the di-lepton invariant mass squared ($q^2 \equiv m_{\ell\ell}^2$). $\mathcal{O}_7$ is the electromagnetic dipole operator which dominates the $b \to s\gamma$ photon penguin processes. $\mathcal{O}_{9V}$ and $\mathcal{O}_{10A}$ are two semileptonic operators resulting from the linear combination of the Z penguin diagram and W box diagram shown in Figure 1.1. C_7^{eff} and C_9^{eff} are effective Wilson coefficients incorporating contributions from the neglected four-quark operators $\mathcal{O}_{1-6}$, while C_{10}^{eff} is a function only of q^2 and μ [22, 23, 24].

1.3.3 The $B \to X_s\ell^+\ell^-$ decays in SUSY models

In the theories beyond the Standard Model, the $B \to X_s\ell^+\ell^-$ decays can also be mediated by heavier SUSY particles, such as charged Higgs bosons, charginos, or
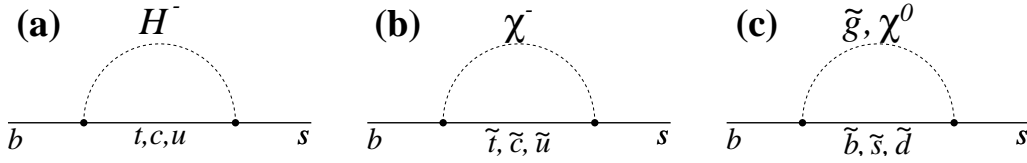
Figure 1.2: Examples of diagrams containing new physics contributions for the $b \rightarrow s\ell^+\ell^-$ transition. They represent contributions from: (a) charged Higgs (H^-); (b) squark ($\tilde{t}, \tilde{c}, \tilde{u}$) and chargino ($\chi^-$); (c) squark ($\tilde{b}, \tilde{s}, \tilde{d}$) and gluino ($\tilde{g}$) /neutralino ($\chi^0$).

gluninos [25, 26, 27, 28]. These processes are represented by the new loop diagrams shown in Figure 1.2.

It is a conventional tactic to make an assumption that most of the new physics effects can be represented in the expansion form Equation 1.5 by modifying the effective Wilson coefficients C_7^{eff}, C_9^{eff} and C_{10}^{eff} while the Standard Model operator bases are kept intact [20]. So if new physics arises, one or more of these Wilson coefficients may be significantly varied from their predicted Standard Model values, typically with a flip of the sign.

1.3.4 Differential Decay Rates

The $B \rightarrow X_s\ell^+\ell^-$ inclusive decay processes are dominated by the $b \rightarrow s\ell^+\ell^-$ transition. Neglecting terms of order $\mathcal{O}\left(m_\ell^2/m_b^2\right)$ and lepton mass terms for the cases $\ell = e, \mu$, we can get the following form for the differential decay rate as a function of q^2 in the next-to-next-to-leading order (NNLO) approximation [19, 20]:

$$
\frac{d\Gamma\left(B \rightarrow X_s\ell^+\ell^-\right)}{dq^2} = \left(\frac{\alpha}{4\pi}\right)^2 \frac{G_F^2 m_{b,pole}^5 \left|V_{ts}^* V_{tb}\right|^2}{48\pi^3} \left(1 - q^2/m_{b,pole}^2\right)^2 \times
$$
$$
\left[\left(1 + 2q^2/m_{b,pole}^2\right)\left(\left|C_9^{eff}\right|^2 + \left|C_{10}^{eff}\right|^2\right) + \right.
$$
$$
\left. 4\left(1 + 2m_{b,pole}^2/q^2\right)\left|C_7^{eff}\right|^2 + 12\mathrm{Re}\left(C_7^{eff} C_9^{eff*}\right)\right]. \quad (1.6)
$$

Here the Standard Model values of C_7^{eff}, C_9^{eff} and C_{10}^{eff} at the b mass scale $\mu_b = 4.6$ GeV are expected to be around -0.3, 4.2 and -4.2, respectively in the next-to-leading order (NLO) calculation [29]. At low q^2, the partial branching fraction is dominated by C_7^{eff}. With the increase of q^2, C_9^{eff} and C_{10}^{eff} will gradually take over the domination, but the $C_7^{eff} - C_9^{eff}$ interference term will still be influenced by the relative phase of these two amplitudes.

In the actual branching fraction calculation for $B \rightarrow X_s\ell^+\ell^-$, the large uncertainty brought in by the factor $m_{b,pole}^5$ in Equation 1.6 is eliminated by adopting the following customary form for $\mathcal{B}^{B \rightarrow X_s\ell^+\ell^-}$ [20]:

$$
\mathcal{B}^{B \rightarrow X_s\ell^+\ell^-}\left(q^2\right) = \frac{\mathcal{B}_{\exp}^{B \rightarrow X_c e \bar{\nu}_e}}{\Gamma\left(B \rightarrow X_c e \bar{\nu}_e\right)} \frac{d\Gamma\left(B \rightarrow X_s\ell^+\ell^-\right)}{dq^2}. \quad (1.7)
$$

The explicit expression for the semileptonic decay width $\Gamma (B \to X_c e \overline{\nu}_e)$ can be found in *e.g.* [22]. The total theoretical uncertainty in the prediction of $\mathcal{B}^{B \to X_s \ell^+ \ell^-}$ is $\sim$ 15% [20].

For exclusive B decays, $B \to K^{(*)}$ form factors will be included in the calculation, which introduces complexities and uncertainties to the theoretical prediction. But these decay channels are much easier to measure in experiments than the inclusive modes. By neglecting second-order mass terms m_K^2/m_B^2 and m_ℓ^2/m_B^2, the q^2 distribution form for the exclusive $B \to K \ell^+ \ell^-$ decay is expressed as [30]:

$$\frac{d\Gamma (B \to K\ell^+\ell^-)}{dq^2} \propto \left(1 - q^2/m_B^2\right)^3 \times$$
$$\left[\left(\left|C_9^{eff}\right|^2 + \left|C_{10}^{eff}\right|^2\right) f_+^2 \left(q^2\right) + \left|C_7^{eff}\right|^2 f_T^2 \left(q^2\right) + \right.$$
$$\left. \frac{4m_b}{m_B + m_K}\text{Re}\left(C_7^{eff} C_9^{eff*}\right) f_+ \left(q^2\right) f_T \left(q^2\right)\right], \tag{1.8}$$

where f_+ and f_T are two $B \to K$ form factors that typically decrease with the increase of q^2. In the pole region ($q^2 \sim 0$), the contribution from $B \to K\gamma^*$ photon penguin processes is null due to angular momentum conservation.

For calculating the hadronic matrix elements in the exclusive $B \to K^* \ell^+ \ell^-$ decays, an approach called QCD factorization is recently adopted, which is superior to previous calculations due to the inclusion of the corrections from "non-factorizable" strong-interaction contributions [31]. In this approach, a longitudinal universal function $\xi_\parallel(q^2)$ and a transverse universal function $\xi_\perp(q^2)$ are introduced to parameterize the heavy-to-light form factors appearing in the hadronic matrix elements [32]. In the lowest order, these two universal functions are related to seven distinct $B \to K^*$ form factors (denoted by $A_{0,1,2}$ for axial vector form factors, $T_{1,2,3}$ for tensor form factors, and V for the standard vector form factor, all are q^2-dependent) [32]:

$$\frac{M_B}{M_B + m_{K^*}}V(q^2) \equiv \frac{M_B + m_{K^*}}{2E(q^2)}A_1(q^2) \equiv T_1(q^2) \equiv \frac{M_B}{2E(q^2)}T_2(q^2) \equiv \xi_\perp(q^2),$$
$$\frac{m_{K^*}}{E(q^2)}A_0(q^2) \equiv \frac{M_B + m_{K^*}}{2E(q^2)}A_1(q^2) - \frac{M_B - m_{K^*}}{M_B}A_2(q^2) \equiv \frac{M_B}{2E(q^2)}T_2(q^2) - T_3(q^2) \equiv \xi_\parallel(q^2) \tag{1.9}$$

Here M_B and m_{K^*} are the masses of B and K^* mesons, respectively. E is the energy of K^* and has the relationship $E \simeq (M_B^2 - q^2)/2M_B$.

Expressed by $\xi_\perp$ and $\xi_\parallel$ and with lepton masses neglected, the q^2 distribution function for $B \to K^* \ell^+ \ell^-$ decays is in a rather complicated form as [28, 33]:

$$\frac{d\Gamma (B \to K^*\ell^+\ell^-)}{dq^2} \propto \lambda(q^2, m_{K^*}^2)^3 \left[\frac{8}{3}\frac{2q^2}{M_B^2}\xi_\perp(q^2)^2(\mid C_9^\perp(q^2) \mid^2 + C_{10}^2) \right.$$
$$\left. + \frac{4}{3}\left(\frac{E\xi_\parallel(q^2)}{m_{K^*}}\right)^2(\mid C_9^\parallel(q^2) \mid^2 + C_{10}^2\Delta_\parallel(q^2)^2)\right], \tag{1.10}$$

where $\lambda(q^2, m_{K^*}^2)$ is a kinematic function defined as:

$$\lambda(q^2, m_{K^*}^2) = \left[\left(1 - \frac{q^2}{M_B^2} \right)^2 - \frac{2m_{K^*}^2}{M_B^2} \left(1 + \frac{q^2}{M_B^2} \right) + \frac{m_{K^*}^4}{M_B^4} \right]^{1/2},$$

and $\Delta_\parallel(q^2)$ arises from the corrections to the form factor $A_2(q^2)$. The functions $\mathcal{C}_9^\perp(q^2)$ and $\mathcal{C}_9^\parallel(q^2)$ are generalized forms for the effective Wilson coefficients C_7^{eff} and C_9^{eff}. In the lowest order, they are given by:

$$
\begin{aligned}
\mathcal{C}_9^{(0)\perp}(q^2) &= C_9^{eff}(q^2) + \frac{2m_b M_B}{q^2} C_7^{eff}, \\
\mathcal{C}_9^{(0)\parallel}(q^2) &= C_9^{eff}(q^2) + \frac{2m_b}{M_B} C_7^{eff}.
\end{aligned}
\tag{1.11}
$$

The predicted $B \to K^* \ell^+ \ell^-$ q^2 distribution is generally similar to that for the inclusive decays. In the photon pole region ($q^2 \sim 0$), which is associated with C_7^{eff} and received cut-off at $q_{min}^2 = (2m_\ell)^2$, the contribution from the photon penguin amplitude is now allowed to be almost on-shell by the angular momentum conservation, which also enhances the $B \to K^* e^+ e^-$ decay rates relative to the $B \to K^* \mu^+ \mu^-$ rates due to much lower mass requirement for producing an $e^+ e^-$ pair [20].

Besides QCD factorization, another factorization approach called soft-collinear effective theory (SCET) [34, 35] is also widely used to deal with the perturbative strong interaction effects in B decays. However, both approaches are only capable of providing reliable predictions for the decay rates with $q^2 \leq 7\,\mathrm{GeV}^2/c^4$ below charmonium threshold [29, 35].

There are several models based on the Standard Model on the market for the calculation of $B \to K^{(*)}$ form factors, such as light-cone QCD sum rules (LCSR) [20, 30, 36], the lattice-constrained dispersion quark model (DQM) [37], and three-point QCD sum rules (PQCD) [38], while the LCSR is the most widely used. These form factor models are used in the predictions on the total branching fractions of $B \to K^{(*)} \ell^+ \ell^-$ decays, which contain large uncertainties and differ significantly from each other. These predictions with different form factor models are summarized in Table 1.1 and Figure 1.3.

Table 1.1 and Figure 1.3 also provide recently measured branching fractions from three independent experiments, which show discrepancies at the level of a few standard deviations. However the theoretical predictions on the total branching fractions are even less precise than the experimental uncertainties due to the large uncertainties brought in by the form factor models. The capability of testing the Standard Model through measuring the total branching fractions alone is thus largely constrained.

The partial branching fraction predictions also suffer from the hadronic uncertainties, though to a slighter extent. Figure 1.4 shows the partial branching fraction predictions for both $B \to K \ell^+ \ell^-$ and $B \to K^* \ell^+ \ell^-$ decays in the Standard Model. The theoretical uncertainties are about 35% [30], which are dominated by the hadronic uncertainties from the form factors.

The q^2 distributions for both $B \to K \ell^+ \ell^-$ and $B \to K^* \ell^+ \ell^-$ decays can be altered significantly according to the predictions based on some of the SUSY models. These predictions are also depicted in Figure 1.4.

Form Factor Model		Branching Fractions ($/10^{-6}$)	
		$B \to K \ell^+ \ell^-$	$B \to K^* \mu^+ \mu^-$
Ali *et al.* '02 [20]	LCSR	0.35 ± 0.12	1.19 ± 0.39
Zhong *et al.* '02 [36]	LCSR	0.84 ± 0.24	1.78 ± 0.70
Ali *et al.* '99 [30]	LCSR	0.57 ± 0.16	1.90 ± 0.52
Chen and Geng '02 [39]	PQCD	0.53 ± 0.10	1.34 ± 0.17
Melikhov *et al.* '98 [38]	DQM	0.44	1.15
Experiment		$B \to K \ell^+ \ell^-$	$B \to K^* \ell^+ \ell^-$
BABAR '03 [40]		$0.65^{+0.14}_{-0.13} \pm 0.04$	$0.88^{+0.33}_{-0.29} \pm 0.10$
Belle '04 [41]		$0.550^{+0.075}_{-0.070} \pm 0.027$	$1.65^{+0.23}_{-0.22} \pm 0.10$
BABAR '06 [11]		$0.34 \pm 0.07 \pm 0.02$	$0.78^{+0.19}_{-0.17} \pm 0.11$
CDF '08 ($\mu^+ \mu^-$ only) [42]		$0.59 \pm 0.15 \pm 0.04$	$0.81 \pm 0.30 \pm 0.10$

Table 1.1: Recent $B \to K^{(*)} \ell^+ \ell^-$ branching fraction predictions and measurements. For each of the measured results, the first uncertainty is statistical, the second is systematic.
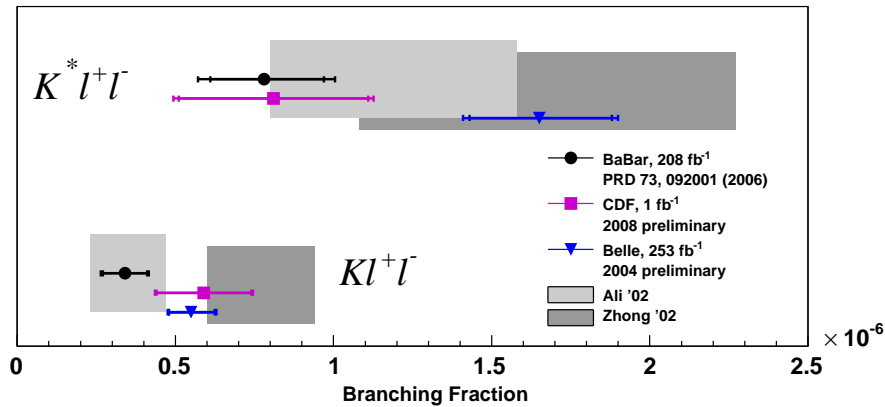
Figure 1.3: Recent predictions and measurements of the total branching fractions of $B \to K^{(*)}\ell^+\ell^-$.
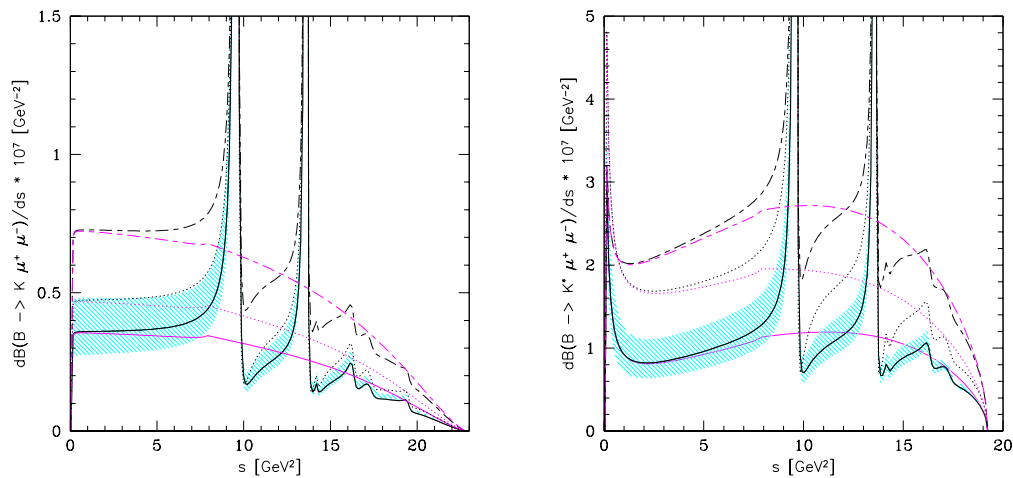
Figure 1.4: Predictions of partial branching fractions of $B \to K\ell^+\ell^-$ (left) and $B \to K^*\ell^+\ell^-$ (right) decays, as functions of $s \equiv q^2$. The red lines show the pure short-distance contributions, and lower than the black lines with long-distance contributions included. The solid lines correspond to the Standard Model predictions, and the shaded areas are the form factor-related uncertainties. The dotted and dashed lines show the predictions based on two different SUSY models. [30]

1.3.5   Direct CP Asymmetry

Besides the branching fractions, the direct CP asymmetries $\mathcal{A}_{CP}$ of the decay modes $B^\pm \to K^\pm\ell^+\ell^-$ and $B \to K^*\ell^+\ell^-$ are also of interest. In these decay modes, the flavor of b quark in a B meson is directly tagged from its decay products.

The direct $\mathcal{A}_{CP}$ is defined as:

$$\mathcal{A}_{CP} \equiv \frac{\Gamma\left(\overline{B} \to \overline{K}^{(*)}\ell^+\ell^-\right) - \Gamma\left(B \to K^{(*)}\ell^+\ell^-\right)}{\Gamma\left(\overline{B} \to \overline{K}^{(*)}\ell^+\ell^-\right) + \Gamma\left(B \to K^{(*)}\ell^+\ell^-\right)}. \tag{1.12}$$

In the Standard Model, $\mathcal{A}_{CP}$ for $B \to K^*\ell^+\ell^-$ decays is predicted to be rather small and of order $\mathcal{O}\left(10^{-4}\right)$ [43]. However new physics at the electroweak scale could provide a considerable large enhancement of order one [44, 45].

1.3.6   Lepton Flavor Asymmetry

Furthermore, the lepton flavor asymmetry ratios

$$R_K = \mathcal{B}\left(B \to K\mu^+\mu^-\right)/\mathcal{B}\left(B \to Ke^+e^-\right) \tag{1.13}$$

and

$$R_{K^*} = \mathcal{B}\left(B \to K^*\mu^+\mu^-\right)/\mathcal{B}\left(B \to K^*e^+e^-\right) \tag{1.14}$$

are predicted with much smaller theoretical uncertainties than the branching fractions, since the hadronic uncertainties are largely canceled in the ratios. In the Standard Model, R_K has a prediction ($R_K^{SM} = 1.0000 \pm 0.0001$) very close to unity, and the e^+e^- and $\mu^+\mu^-$ rates differ only due to a small difference in the phase space of order (m_μ^2/m_b^2) [46]. For the $B \to K^*\ell^+\ell^-$ decays, above the pole region ($q^2 > 4m_\mu^2$), R_{K^*} is also expected to be close to unity ($R_{K^*}^{SM} = 0.991 \pm 0.002$) [46]. Taking the pole region into account will bring a large enhancement to the e^+e^- rates due to the contribution of the photon penguin. The expected Standard Model value for R_{K^*} in the entire q^2 region is 0.73 ± 0.01 [46].

The ratios are sensitive to the presence of a supersymmetric neutral Higgs with large $\tan\beta$, which indicates a Higgs mass possibly below the mass of B meson [48, 49]. This SUSY Higgs could give $\sim 10\%$ corrections to both R_K and R_{K^*} due to an enhanced rate in the muon modes [46, 50]. The enhancement results from a "Higgs
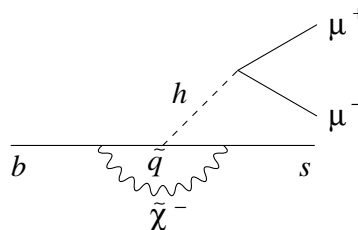
Figure 1.5: The example Feynman diagram of a light SUSY Higgs process which may enhance $R_{K^{(*)}}$.
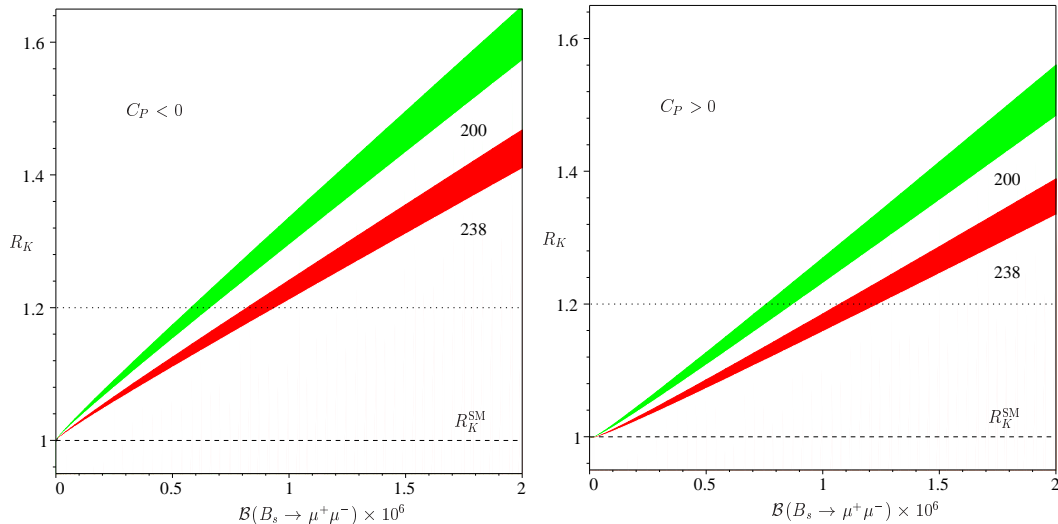
Figure 1.6: Correlation between R_K and $\mathcal{B}\left(B_s \to \mu^+\mu^-\right)$ for the cases of $C_P > 0$ (left) and $C_P < 0$ (right) [46]. The colored bands are for different B_s decay constant values: $f_{B_s} = 200$ MeV (green) and $f_{B_s} = 238$ MeV (red). C_7^{eff} is assumed to have the same sign as in the Standard Model, while both C_9^{eff} and C_{10}^{eff} keep their Standard Model values. In the Standard Model prediction, we have $\mathcal{B}^{SM}\left(B_s \to \mu^+\mu^-\right) \sim 4 \times 10^{-9}$ [47].

penguin" diagram involving a sizable squark-gaugino loop, as shown in Figure 1.5. The coupling between the Higgs and the lepton pair is described by including two additional terms $C_S \mathcal{O}_S$ and $C_P \mathcal{O}_P$ in the OPE formalism (Equation 1.4) as [46]:

$$\mathcal{H}_{eff} = -\frac{4G_F}{\sqrt{2}} V_{ts}^* V_{tb} \left\{ \sum_{k=1}^{10} C_k\left(\mu\right) \mathcal{O}_k\left(\mu\right) + C_S\left(\mu\right) \mathcal{O}_S\left(\mu\right) + C_P\left(\mu\right) \mathcal{O}_P\left(\mu\right) \right\} . \quad (1.15)$$

Here the notations S and P for the Wilson coefficients $C_{S,P}$ and local operators $\mathcal{O}_{S,P}$ represent scalar and pseudoscalar contributions, respectively [46]. For the Standard Model Higgs, these contributions are highly suppressed since C_S and C_P have the Standard Model values $C_{S,P}^{SM} \sim \frac{m_\ell m_b}{m_W^2}$ [46]. In the models beyond the Standard Model, C_S and C_P can be considerably enhanced. With the assumption of no right-handed currents, R_K is highly correlated with the branching fraction $\mathcal{B}\left(B_s \to \mu^+\mu^-\right)$, as shown in Figure 1.6 for the case that C_7^{eff} has the same sign as predicted in the Standard Model, and $C_{9,10}^{eff}$ hold their Standard Model values [46]. Through combining the measurements on R_K and $\mathcal{B}\left(B_s \to \mu^+\mu^-\right)$, the scalar and pseudoscalar contributions will thus be tightly constrained.

1.3.7 Isospin Asymmetry

The isospin asymmetry $\mathcal{A}_I$ can be induced via "non-factorizable" contributions, in which the spectator quark is involved in the $B \to K^{(*)}\ell^+\ell^-$ processes by radiating a virtual photon [28]. As the spectator quarks are different, the charged and neutral B
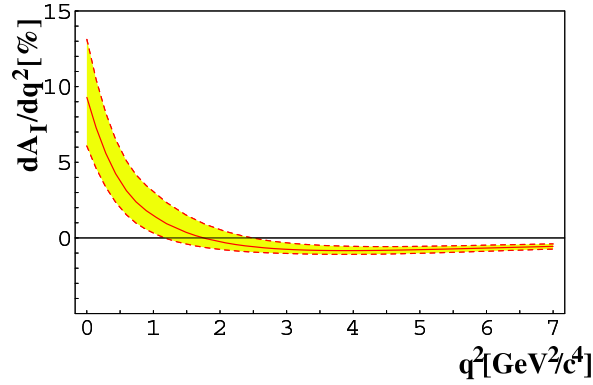
Figure 1.7: The Standard Model prediction of $\mathcal{A}_I$ as a function of q^2 in the low q^2 region for $B \to K^* \ell^+ \ell^-$ [28]. The shaded band shows the uncertainties in the prediction, and the solid line is the central value of the Standard Model prediction.
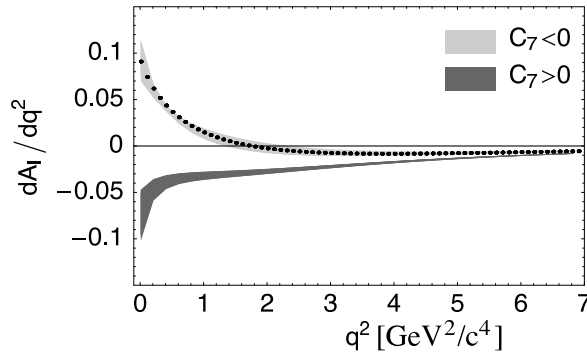
Figure 1.8: The expected $\mathcal{A}_I$ as a function of q^2 in the low q^2 region for $B \to K^* \ell^+ \ell^-$ with different C_7^{eff} signs [28]. The light band corresponds to the Standard Model prediction, while the band in black shows the prediction from a new physics model with flipped-sign C_7^{eff}.

mesons can have different partial decay widths. $\mathcal{A}_I$ provides another observable to test the Standard Model. The CP-averaged isospin asymmetry for exclusive $B \to K^{(*)} \ell^+ \ell^-$ decays is defined as [28]:

$$\frac{d\mathcal{A}_I(q^2)}{dq^2} \equiv \frac{d\Gamma\left(B^0 \to (K/K^*)^0 \ell^+ \ell^-\right)/dq^2 - d\Gamma\left(B^\pm \to (K/K^*)^\pm \ell^+ \ell^-\right)/dq^2}{d\Gamma\left(B^0 \to (K/K^*)^0 \ell^+ \ell^-\right)/dq^2 + d\Gamma\left(B^\pm \to (K/K^*)^\pm \ell^+ \ell^-\right)/dq^2}.$$

(1.16)

Figure 1.7 shows the Standard Model prediction for $\mathcal{A}_I$ as a function of q^2 in the low q^2 region for $B \to K^* \ell^+ \ell^-$. $\mathcal{A}_I$ is predicted to be positive at very small q^2. With the increase of q^2, $\mathcal{A}_I$ decreases and crosses zero at $q^2 \sim 2$ GeV^2/c^4. It will then reach asymptotically a value of $\sim -1\%$. Integrating over the entire low q^2 region also yields a very small value of order $\mathcal{O}(10^{-2})$.

At the presence of a new physics model which results in the C_7^{eff} sign opposite of that in the Standard Model, a distinct pattern of $\mathcal{A}_I$ in the low q^2 is predicted to be

completely below zero, as shown in Figure 1.8. In this case, the integrated $\mathcal{A}_I$ value is expected to be well below zero and could have a magnitude of order $\mathcal{O}(10^{-1})$.

1.3.8 Angular Asymmetries in $B \to K^* \ell^+ \ell^-$ Decays

In the $B \to K^* \ell^+ \ell^-$ decays, the angular asymmetries are well predicted in the Standard Model with a relatively high precision, since the form factor related uncertainties are considerably reduced. Among these asymmetries, the most interesting ones are the di-lepton forward-backward asymmetry $\mathcal{A}_{FB}$ and the longitudinal polarization of K^* F_L. The measurements of these two observables rely on the knowledge of the angular variables $\cos\theta_\ell$ and $\cos\theta_K$ in the decays, which are shown in Figure 1.9. Following the sign conventions used in [28, 43], the angle θ_ℓ is defined as the flight direction of $\ell^+(\ell^-)$ with respect to the direction of $B(\bar{B})$ meson in the di-lepton rest frame, while the angle θ_K is defined as the angle between the kaon and the B meson in the K^* rest frame. The angle ϕ between the decay planes of the di-lepton system and K^* in the B rest frame is also defined in Figure 1.9. Assuming an on-shell K^*, the three angles θ_ℓ, θ_K and ϕ and the di-lepton invariant mass q^2 are able to make a complete description of the $B \to K^* \ell^+ \ell^-$ decay with the following form of the differential decay rate [43, 51]:

$$\frac{d^4\Gamma(B \to K^* \ell^+ \ell^-)}{dq^2 d\cos\theta_\ell d\cos\theta_K d\phi} = \frac{9}{32\pi} I(q^2, \theta_K, \theta_\ell, \phi). \tag{1.17}$$

where

$$\begin{aligned} I = \ & I_1 + I_2 \cos 2\theta_\ell + I_3 \sin^2\theta_\ell \cos 2\phi + I_4 \sin 2\theta_\ell \cos\phi + I_5 \sin\theta_\ell \cos\phi \\ & I_6 \cos\theta_\ell + I_7 \sin\theta_\ell \sin\phi + I_8 \sin 2\theta_\ell \sin\phi + I_9 \sin^2\theta_\ell \sin 2\phi, \end{aligned} \tag{1.18}$$

and the functions I_{1-9} [51] in Equation 1.18 can be written in terms of three transversity amplitudes contributing to the decay: $A_0(q^2)$, $A_\perp(q^2)$, and $A_\parallel(q^2)$, which represent the longitudinal amplitude (S-wave), the transverse amplitude (P-wave), and the parallel amplitude (D-wave), respectively. The K^* polarizations correspond to the
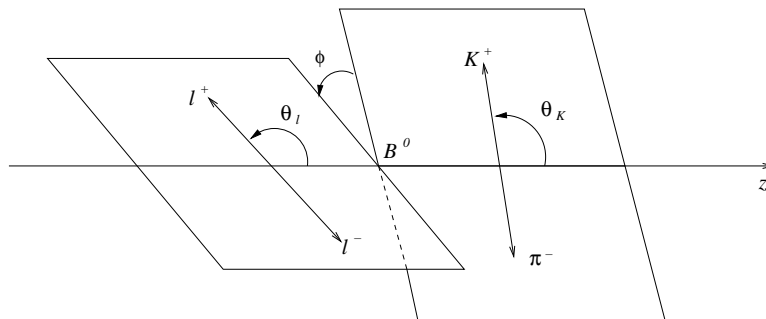
Figure 1.9: The definition of angular variables in the $B^0 \to K^*(\to K^+\pi^-)\ell^+\ell^-$ decay. [51]

fractions of longitudinal and transverse polarization F_L and F_T, which are expressed via the ratios of transversity amplitudes of K^* [51]:

$$F_L\left(q^2\right) = \frac{\left|A_0\left(q^2\right)\right|^2}{\left|A_0\left(q^2\right)\right|^2 + \left|A_\perp\left(q^2\right)\right|^2 + \left|A_\parallel\left(q^2\right)\right|^2}, \tag{1.19}$$

$$F_T\left(q^2\right) \equiv 1 - F_L\left(q^2\right) = \frac{\left|A_\perp\left(q^2\right)\right|^2 + \left|A_\parallel\left(q^2\right)\right|^2}{\left|A_0\left(q^2\right)\right|^2 + \left|A_\perp\left(q^2\right)\right|^2 + \left|A_\parallel\left(q^2\right)\right|^2}. \tag{1.20}$$

The F_L value over a certain range of q^2 can be determined through fitting to the distribution of $\cos\theta_K$. Neglecting lepton mass terms of order m_ℓ^2/q^2 and integrating out q^2, ϕ and θ_ℓ in Equation 1.17, the resulting $\cos\theta_K$ distribution is written as:

$$\frac{1}{\Gamma}\frac{d\Gamma\left(B \to K^* \ell^+ \ell^-\right)}{d\cos\theta_K} = \frac{3}{2}F_L\cos^2\theta_K + \frac{3}{4}\left(1 - F_L\right)\left(1 - \cos^2\theta_K\right). \tag{1.21}$$

The forward-backward asymmetry $\mathcal{A}_{FB}$ in $B \to K^* \ell^+ \ell^-$ decays is defined by the cosine of the angle θ_ℓ [28, 52]:

$$\frac{d\mathcal{A}_{FB}}{dq^2} \equiv \frac{1}{d\Gamma/dq^2}\left(\int_0^1 d\cos\theta_\ell\frac{d^2\Gamma\left(B \to K^* \ell^+ \ell^-\right)}{dq^2 d\cos\theta_\ell} - \int_{-1}^0 d\cos\theta_\ell\frac{d^2\Gamma\left(B \to K^* \ell^+ \ell^-\right)}{dq^2 d\cos\theta_\ell}\right). \tag{1.22}$$

The $\mathcal{A}_{FB}$ for $B \to K^* \ell^+ \ell^-$ arises from the $V - A$ nature of weak processes, in which a pseudoscalar decays into vector-vector final states and all three helicities of vector states are allowed by angular momentum conservation. The $\mathcal{A}_{FB}$ shows a q^2-dependence [30]:

$$\frac{d\mathcal{A}_{FB}}{dq^2} \propto -\left\{\mathrm{Re}\left(C_9^{eff}C_{10}^{eff}\right)V\left(q^2\right)A_1\left(q^2\right) + \frac{m_b}{q^2}\mathrm{Re}\left(C_7^{eff}C_{10}^{eff}\right) \times \right.$$
$$\left.\left[V\left(q^2\right)T_2\left(q^2\right)\left(1 - \frac{m_{K^*}}{m_B}\right) + A_1\left(q^2\right)T_1\left(q^2\right)\left(1 + \frac{m_{K^*}}{m_B}\right)\right]\right\}. \tag{1.23}$$

Similar to Equation 1.20, $\mathcal{A}_{FB}$ can also be expressed in terms of left-handed and right-handed transversity amplitudes (marked by notations L and R):

$$\mathcal{A}_{FB}\left(q^2\right) = \frac{3}{2}\frac{\mathrm{Re}\left(A_{\parallel L}\left(q^2\right)A_{\perp L}^*\left(q^2\right)\right) - \mathrm{Re}\left(A_{\parallel R}\left(q^2\right)A_{\perp R}^*\left(q^2\right)\right)}{\left|A_0\left(q^2\right)\right|^2 + \left|A_\perp\left(q^2\right)\right|^2 + \left|A_\parallel\left(q^2\right)\right|^2}. \tag{1.24}$$

Based on the above form for $\mathcal{A}_{FB}$, neglecting terms of order m_ℓ^2/q^2, and integrating out q^2, ϕ and θ_K in Equation 1.17, the $\cos\theta_\ell$ distribution can be written in terms of F_L and $\mathcal{A}_{FB}$ as:

$$\frac{1}{\Gamma}\frac{d\Gamma\left(B \to K^* \ell^+ \ell^-\right)}{d\cos\theta_\ell} = \frac{3}{4}F_L\left(1 - \cos^2\theta_\ell\right) + \frac{3}{8}\left(1 - F_L\right)\left(1 + \cos^2\theta_\ell\right) + \mathcal{A}_{FB}\cos\theta_\ell. \tag{1.25}$$
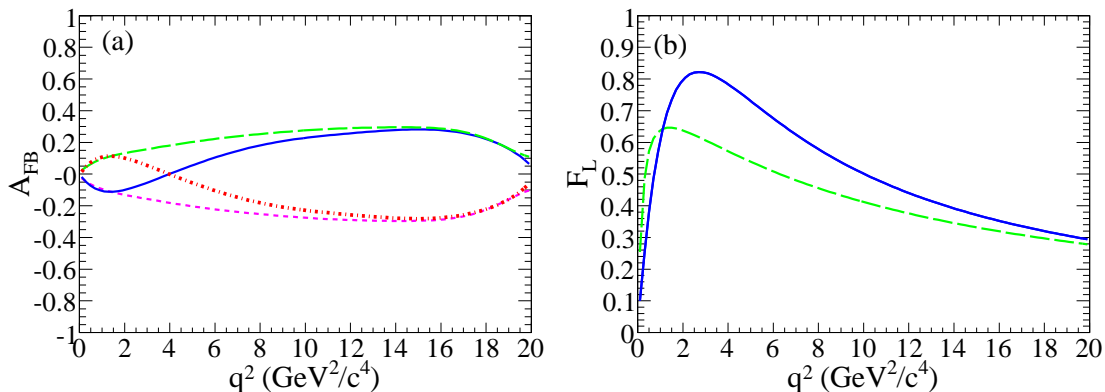
Figure 1.10: The predicted (a) $\mathcal{A}_{FB}$ and (b) F_L values as functions of q^2 for $B \rightarrow K^*\ell^+\ell^-$ decays. The predictions are from the Standard Model (solid) and several new physics scenarios: flipped-sign C_7^{eff} (long dash), flipped-sign $C_9^{eff}C_{10}^{eff}$ (short dash), and both C_7^{eff} and $C_9^{eff}C_{10}^{eff}$ with flipped signs (dash-dot). For the F_L plot, the curves with flipped-sign $C_9^{eff}C_{10}^{eff}$ are not shown since this kind of sign flipping will not bring any noticeable change to the curve shapes.

Together with Equation 1.21, we now have F_L in both $\cos\theta_K$ and $\cos\theta_\ell$ distributions, and $\mathcal{A}_{FB}$ as a linear coefficient in the $\cos\theta_\ell$ distribution. Based on these two distribution functions, we can fit to an ensemble of the observations of $\cos\theta_K$ and $\cos\theta_\ell$ to extract F_L and $\mathcal{A}_{FB}$. Detailed experimental techniques are introduced in Chapter 5.

Figure 1.10 shows the predicted $\mathcal{A}_{FB}$ and F_L values as functions of q^2 for the decays $B \rightarrow K^*\ell^+\ell^-$ in the Standard Model, as well as for a few new physics scenarios with different signs on the Wilson coefficients. In the Standard Model, C_7^{eff} and C_{10}^{eff} are predicted to be negative, while C_9^{eff} is positive. Therefore it is apparent that $\mathcal{A}_{FB}$ is expected to be negative in the Standard Model at low q^2 due to the dominance of negative C_7^{eff}. With the increase of q^2 over a certain value q_0^2, $\mathcal{A}_{FB}$ will be constantly positive. The zero-crossing point has been well predicted in the Standard Model to be $q_0^2 = 4.2\pm0.6\,\mathrm{GeV^2/c^4}$ at NLO [28]. The uncertainty in the q_0^2 prediction is mainly from the form factor calculation. Figure 1.11 depicts the predicted $\mathcal{A}_{FB}$ in the Standard Model as a function of q^2 in the low q^2 below the J/ψ resonance.

Due to possible new physics contributions at the electroweak scale, the Wilson coefficient C_7^{eff} and/or the product of Wilson coefficients $C_9^{eff}C_{10}^{eff}$ may differ considerably from their Standard Model values. We only consider three simple cases with sign flips, which result in three different $\mathcal{A}_{FB}$ variation patterns, as shown in Figure 1.10. The measurement of $\mathcal{A}_{FB}$ in the low q^2 region below the J/ψ resonance will place a strong constraint on C_7^{eff}, as the flipped-sign C_7^{eff} model will yield an $\mathcal{A}_{FB}$ value significantly larger than the Standard Model prediction. The zero-crossing point q_0^2 is also not present in the flipped-sign C_7^{eff} model, thus q_0^2 will be highly sensitive to the sign of C_7^{eff}. However, currently we do not have sufficient experimental data to perform a reasonable measurement on q_0^2, since a large amount of events are required to be within a narrow q^2 region surrounding q_0^2. For q^2 above the J/ψ resonance, $C_9^{eff}C_{10}^{eff}$ will be tightly constrained, as a highly negative $\mathcal{A}_{FB}$ is expected in the models with $C_9^{eff}C_{10}^{eff}$ sign different from that in the Standard Model.
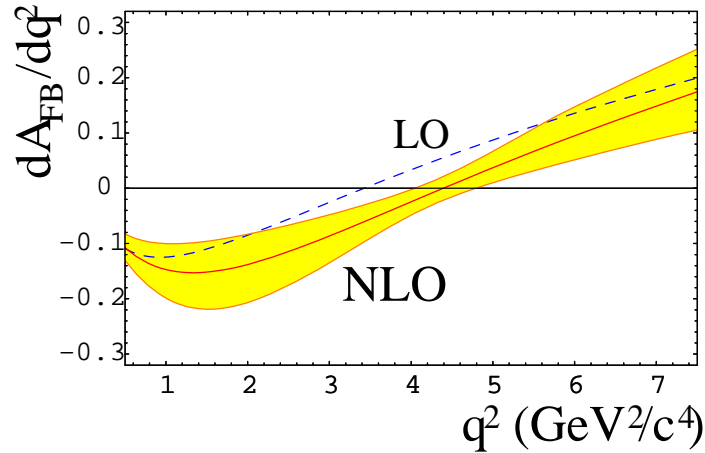
Figure 1.11: The Standard Model predictions of $\mathcal{A}_{FB}$ as a function of q^2 at LO (dashed line) and NLO (solid central line) below the J/ψ resonance for $B \rightarrow K^* \ell^+ \ell^-$ [33]. The band shows the theoretical uncertainties in the NLO calculation.

The kaon longitudinal polarization F_L, however, is only sensitive to the sign of C_7^{eff}. At low q^2, the measured F_L value from experiments will also be a strong indication of the sign of C_7^{eff}, as the case with flipped-sign C_7^{eff} yields a significantly lower F_L value than the Standard Model prediction.

In the $B \rightarrow K \ell^+ \ell^-$ decays, due to angular momentum conservation, the terms contributing to the angular asymmetry are suppressed. The $\cos \theta_\ell$ distribution is a symmetric function in the form of $(1 - \cos^2 \theta_\ell)$ [30]. However, if the scalar (C_P) or pseudoscalar (C_P) terms are introduced in the effective Hamiltonian $\mathcal{H}_{eff}$ for $B \rightarrow K \ell^+ \ell^-$ as described in §1.3.6, the angular distribution $\frac{1}{\Gamma} \frac{d^2 \Gamma (B \rightarrow K \ell^+ \ell^-)}{dq^2 d \cos \theta_\ell}$ will then deviate from $(1 - \cos^2 \theta_\ell)$ by including a linear term for $\cos \theta_\ell$ [53]. By integrating over q^2 and collecting terms including $\cos \theta_\ell$, the angular distribution is simplified to:

$$\frac{1}{\Gamma} \frac{d\Gamma (B \rightarrow K \ell^+ \ell^-)}{d \cos \theta_\ell} = \frac{3}{4} (1 - F_S) (1 - \cos^2 \theta_\ell) + \frac{1}{2} F_S + \mathcal{A}_{FB} \cos \theta_\ell, \qquad (1.26)$$

where $F_S \in [0, 1]$ indicates the new physics contribution. In the limit of without new scalar or pseudoscalar terms $(F_S = 0)$, we obtain $\mathcal{A}_{FB} = 0$. Since even in the presence of this new physics contribution, the $\mathcal{A}_{FB}$ is still expected to be small (of order $\mathcal{O}(10^{-2})$ or less) [54], we will mainly perform the $\mathcal{A}_{FB}$ measurements in the $B \rightarrow K \ell^+ \ell^-$ decays for the purpose of validating our experimental techniques.

Chapter 2

The *BABAR* Experiment

The studies on the $B \rightarrow K^{(*)}\ell^+\ell^-$ decays rely on the data collected in the *BABAR* experiment, which is located at the Stanford Linear Accelerator Center and started data-taking in 1999. The facilities of the experiment consist of an asymmetric electron-positron collider, PEP-II, for producing B mesons, whose decay products are detected in the *BABAR* detector. While the primary design goal for the *BABAR* detector is to search for *CP* asymmetries in neutral B decays, it still fits well into the studies on other B meson related topics. In this chapter, following a brief description on the PEP-II collider, the different components of the *BABAR* detector are introduced. A detailed and dedicated description on the *BABAR* detector can be found elsewhere [55].

2.1 The e^+e^- B Factory and PEP-II Collider

The PEP-II collider consists of two independent storage rings, one for 9 GeV electrons, the other for 3.1 GeV positrons. The energies of two beams are designed to produce the $\Upsilon(4S)$ resonance with a Lorentz boost $\beta\gamma$ of 0.56. The $\Upsilon(4S)$ resonance then decays instantly, with equal probabilities, to a B^+B^- or $B^0\overline{B}^0$ pair. While the two B mesons from one pair are almost at rest in the $\Upsilon(4S)$ center-of-mass (CM) frame, they are boosted with extra decay lengths significant enough in the lab frame to get separated.

The designed e^+e^- collision environment provides a very clean sample with high signal-to-background ratio. The rest production of the on-resonance collisions are lighter fermion pairs ($q\bar{q}$, $q = u,d,s,c$, $\tau^+\tau^-$, $\mu^+\mu^-$), which compose the continuum background for the full-reconstructed B decay signal. This background is studied by analyzing the *off-resonance* data, which are collected 40 MeV below the $\Upsilon(4S)$ resonance. This method is extremely useful for rare B decays with high continuum backgrounds.

After several years' of improvements, the PEP-II has scored a peak luminosity of over $12 \times 10^{33}\,\mathrm{cm^{-2}s^{-1}}$, which is four times of its initially designed luminosity goal. The high luminosity has provided abundant B mesons for accurate measurements.

2.2   The *BABAR* Detector

For the full reconstruction of the B meson decay chains, and unambiguous tagging on the B flavor, the detector was built to fulfill the following physical requirements [13]:

- High acceptance in the central-of-mass system. A large forward polar angle coverage is required along the boost direction.

- High tracking efficiencies for charged particles with transverse momentum p_t between ~ 60 MeV and ~ 4 GeV.

- Excellent momentum resolution for charged particles.

- Excellent energy and angular resolution for photons from radiative decays or π^0/η^0 decays.

- Highly efficient and accurate identification for charged particles (e, μ, π, K and p) and over a large kinematic range.
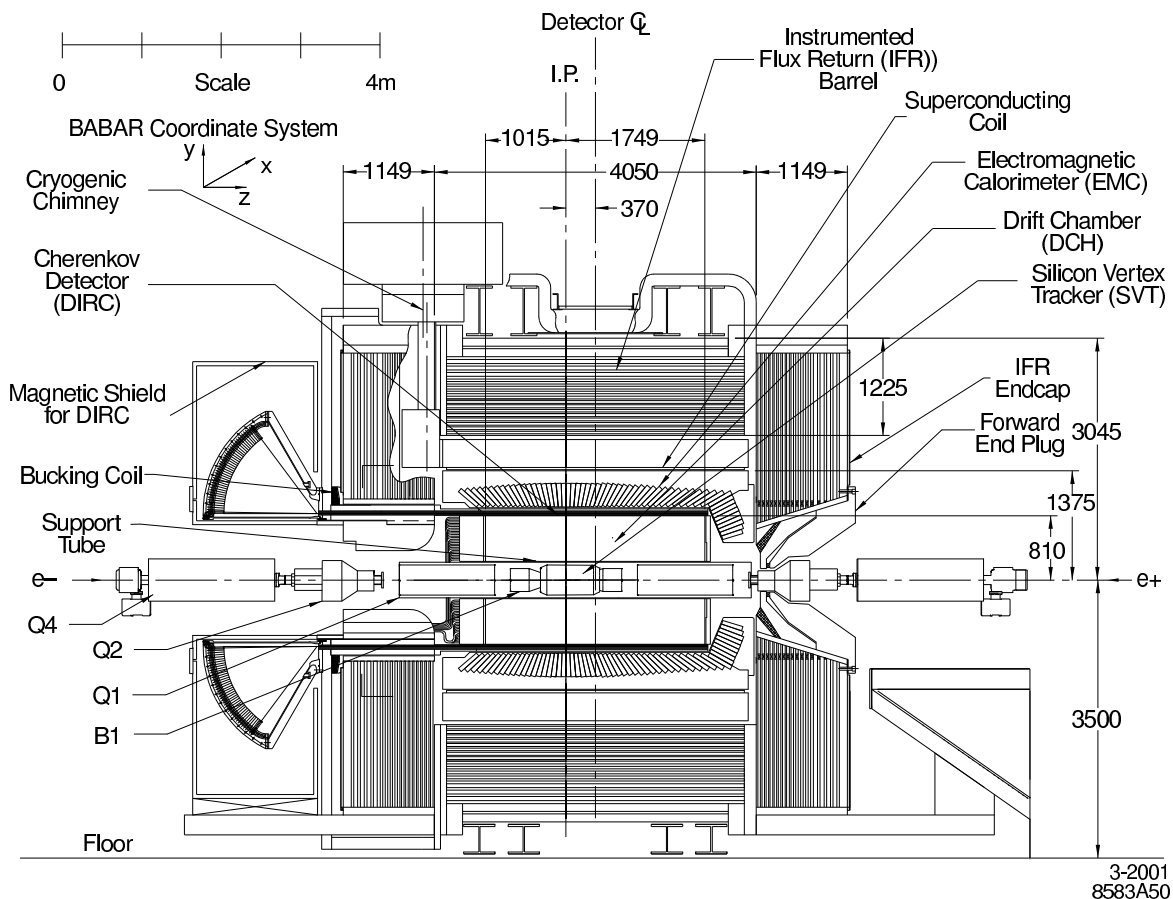
Figure 2.1: The longitudinal view of the *BABAR* detector [55]. $+z$ direction is always along the boost direction.

- Excellent transverse and beam-direction vertex resolution.

As shown in Figure 2.1, the *BABAR* detector consists of the following components:

- The Silicon Vertex Tracker (SVT). This provides precise position information of the charged tracks close to the interaction region.

- The Drift Chamber (DCH). This measures momenta of the charged tracks and helps in charged particle identification (PID) through energy loss measurements.

- The Detector of Internally Reflected Cherenkov light (DIRC). This provides main identification information for charged hadronic particles.

- The Electromagnetic Calorimeter (EMC). This measures photon energies and positions, and is used for electron identification and π^0 reconstruction.

- The Instrumented Flux Return (IFR). This provides muon and K_L^0 identifications.

Under a common electronic architecture, the data collected in different detector components as described above is transferred through the Front-End Electronics (FEE) mounted directly on the detector components, and forwarded to the trigger system. The trigger system then filters through the data to reduce the event rate low enough so that data can be kept in the storage for event reconstruction.

Besides these detector components which will be introduced in detail in the following subsections, there's also a superconducting coil placed between the EMC and IFR. The coil provides a 1.5 T solenoidal magnetic field to facilitate the momentum measurements for charged tracks.

2.2.1 The Silicon Vertex Tracker (SVT)

The main goal of the SVT is to measure B decay vertices separated from the primary vertex. The distance of these two vertices will be used to determine B and $\overline{B}$ decay time differences, and ultimately, for the measurement of time-dependent CP asymmetries in neutral B meson decays. The vertex reconstruction requires high z and $x - y$ plane position resolution to effectively reduce the background level. Furthermore, since charged particles with transverse momentum p_t lower than 100 MeV/c will not traverse the drift chamber, the SVT is the sole device we rely on to provide complete kinematic and position information for these tracks.

As shown in Figure 2.2, the SVT has five cylindrical layers, each layer consisting of azimuthally arranged modules. The number of modules is six for each of the inner three layers. The outer two layers have 16 and 18 modules, respectively. The inner layers are placed close enough to the interaction region for the optimization of the position resolution, while the outer layers are assembled in arch shapes to improve the solid angle coverage. The resulting polar angle coverage is from 20.1° to 150.2°.

Each module of the SVT layers is fully mounted with 4 – 8 double-sided silicon microstrip sensors, which sum up to a total number of 340 for the whole SVT. These

sensors are used to provide the position information of passing charged particles. Their inner sides, with strips placed parallel to the z-axis (ϕ strips) are used to measure the ϕ coordinate, while the outer sides with transversely oriented strips (z strips) are for the z coordinate measurement. There are around 150,000 readout channels for handling signals.

The silicon detector has an advantage of measuring positions with very high precision. As shown in Figure 2.3, the single-hit resolution varies from 20 to 40 μm for
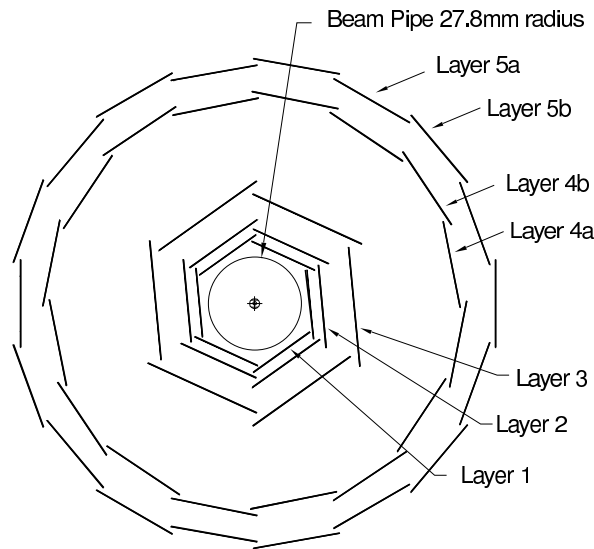
Figure 2.2: The cross-section layout of the *BABAR* SVT with five layers surrounding the beam pipe [55].
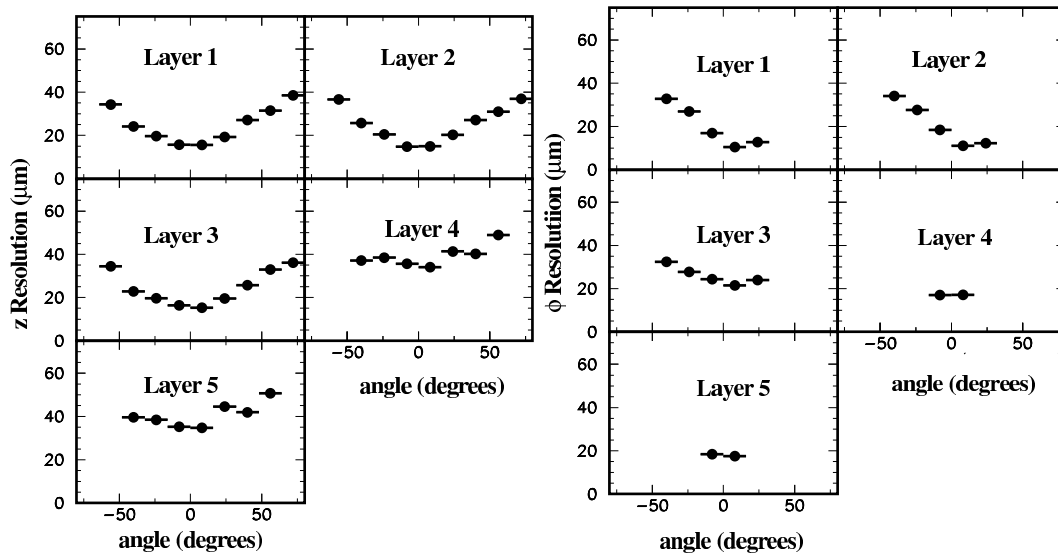
Figure 2.3: The hit resolutions of the *BABAR* SVT in the z (left) and ϕ (right) coordinates are plotted as a function of the track incident angle [55]. Each plot represents one SVT layer.

both z and ϕ directions, and also depends on the incident angle of charged tracks [55].

The reconstruction of the SVT hits is based on the clustering of the adjacent strips with hit signals, before discarding out-of-time signals relative to the DCH response. The position of a cluster is determined by the weighted average of the strip positions. The weight for each strip depends on its collected charge. The position information is further used for track finding. The reconstructed particle tracks are vital inputs for global and local alignment algorithms, which are performed as corrections for the tracking system involving the DCH as a whole.

2.2.2   The Drift Chamber (DCH)

Working together with the SVT, the drift chamber is used to provide precise spacial and kinematic measurements for charged particles with p_t above 100 MeV/c. The measurement of ionization-induced energy loss dE/dx plays an important role in the

Figure 2.4: Upper: Side view of the DCH [55]. Lower: Layout of the DCH layers [13].

Figure 2.5: The measured $\mathrm{d}E/\mathrm{d}x$ in the DCH as a function of momentum for various particle species [55]. The points are collected from data control samples, while the curves represent the predictions based on different particle hypotheses.

discrimination among different charged particles, particularly between K and π. The kinematic information for the detected track pairs in the DCH is also crucial for the reconstruction of a neutral K_s, whose decay vertex falls outside of the chamber.

Figure 2.4 shows the schematic side view of the DCH that consists of a 280 cm-long cylinder along the beam direction. Its inner and outer radii are 23.6 cm and 80.9 cm, respectively. Due to the asymmetric colliding beams, the chamber has an offset in the forward direction from the interaction point (IP). The forward endplate is made much thinner than the rear end-plate, so that the material in front of the EMC endcap can be minimized. The acceptance in polar angle ranges from 17.2° to 152.6°, which ascertains that incident particles with the polar angle within this range will at least pass through half of the total 40 layers in the chamber. Such a coverage is sufficient for a precise measurement.

The 40 layers in the chamber are grouped equally into 10 super-layers, as shown in Figure 2.4. These super-layers are arranged in the order "AUVAUVAUVA", in which "A" and "UV" represent axial (along the z axis) and stereo super-layers, respectively. For "U" super-layers, the stereo angles vary between 45 mrad and 69 mrad, while for "V" super-layers, the stereo angles are between -76 mrad and -52 mrad. The stereo angles are chosen so that the drilling patterns are identical for the two end-plates. The 7104 drift cells occupying these layers are hexagons of the size of approximately 1.2×1.8 cm^2. Each of these cells possesses a sense wire made of gold-plated tungsten-rhenium, and is surrounded by six gold-plated aluminum field wires. The chamber gas consists of a mixture of Helium-isobutane (80%:20%), that is light enough to minimize multiple scattering that effects the resolution of low momentum tracks.

When a track passes through the DCH, the ionized charge arriving at the sense wires and its arrival time are recorded. The DCH hits are reconstructed from the drift time and time-to-distance relationship determined from e^+e^- and $\mu^+\mu^-$ events. The ionization loss $\mathrm{d}E/\mathrm{d}x$ is measured by summing up all the collected charges, with a resolution of about 7% for low momentum tracks. This guarantees a $> 2\sigma$ K/π

separation up to $\sim 700\,\mathrm{MeV}/c$ [56], as shown in Figure 2.5.

To fully reconstruct an incident track, as discussed in the previous SVT part, hit information from both SVT and DCH is used. Five parameters are measured at the point of closest approach (POCA) to the z axis. They provide a full description of the reconstructed track, and are listed below, together with their resolutions measured from cosmic ray muons, e^+e^- and $\mu^+\mu^-$ events [55]:

d_0,z_0:   The distance to the z axis and z coordinate, $\sigma_{d_0} = 23\ \mu\mathrm{m}, \sigma_{z_0} = 29\ \mu\mathrm{m}$

ϕ_0:   The azimuthal angle, $\sigma_{\phi_0} = 0.43\ \mathrm{mrad}$

$\tan\lambda$:   The dip angle relative to the $x-y$ plane, $\sigma_{\tan\lambda} = 0.53 \times 10^{-3}$

$\omega\,(= 1/p_t)$: The curvature, $\sigma_{p_t}/p_t = (0.13 \pm 0.01)\% \cdot p_t + (0.45 \pm 0.03)\%$

Only d_0 and ω are assigned with a sign to indicate the charge of the track, and p_t is measured in unit of GeV/c.

2.2.3 The Cherenkov Detector (DIRC)

The DIRC is designed exclusively for the identification of charged particles. While working as a modified version of the Ring Imaging Cherenkov Counter (RICH), the DIRC provides excellent particle identification over a large momentum range, especially for high momentum hadrons. As indicated in the DCH section, the K/π distinguishing power using $\mathrm{d}E/\mathrm{d}x$ measurements will break down for track momenta above 0.7 GeV/c, the DIRC then works as an important complement at high momentum.
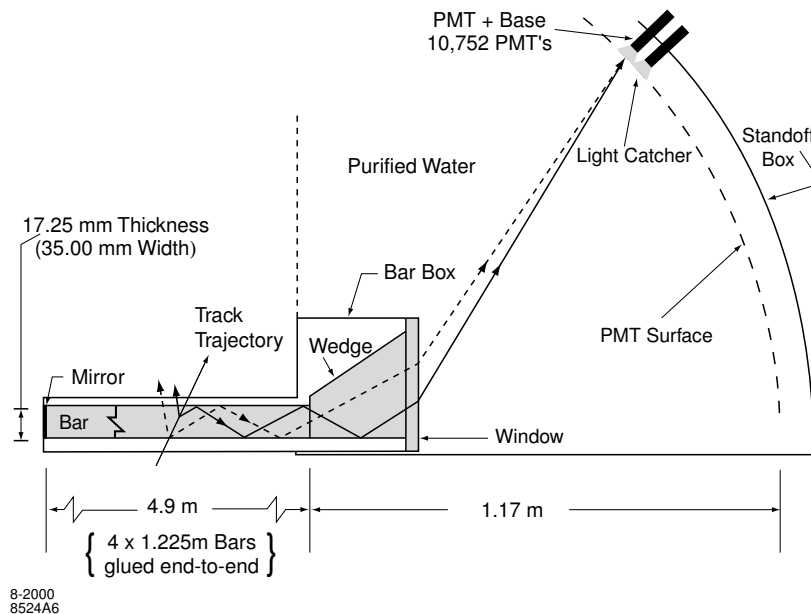
Figure 2.6: The layout of the DIRC radiator bar and imaging region [55]. The working principle of the DIRC is also illustrated.
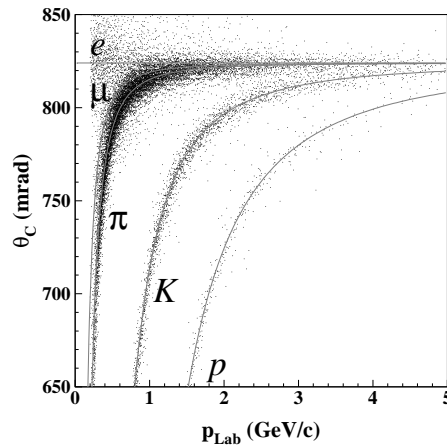
Figure 2.7: The fitted θ_c in the DIRC as a function of track momentum for various particle species [57]. The points are collected from data control samples, while the curves represent the predictions based on different particle hypotheses.

The DIRC also provides complementary PID information for low momentum muons, for which IFR will work satisfactorily.

The schematic of the DIRC is shown in Figure 2.6. Different from the traditional design of RICH, Cherenkov photons emitted by high-velocity incident particles are contained inside the detector due to total internal reflection on a flat surface. The Cherenkov photons are both produced and transported by the DIRC radiator, which is composed of 144 synthetic, fused quartz bars with a high refractive index of $n = 1.473$. The radiator bars are equally placed into 12 aluminum bar boxes and mounted in a barrel surrounding the DCH. The spatial coverage for the bars is about 94% of the azimuthal angle. A mirror is placed at the forward end of each bar to reflect back the emitted photons so that the photons will be guided towards the instrumented back end of the bar.

For the Cherenkov photons arriving at the bar back ends, most of them will enter a large water-filled expansion region called the Standoff Box. In the Standoff Box, the Cherenkov angles are projected onto a surface, so that they can be measured with high precision. The inside water of the Standoff Box is purified and has a refractive index of 1.346, which is very close to that of the quartz bars, and can thus minimize the reflection when photons pass through the quartz-water interface. A silica wedge prism is attached to each bar to preserve photons with large reflection angle. An array of 10,752 PMTs are mounted on the back surface of the Standoff Box and dipped inside the water to accept the Cherenkov photons in the visible and near-UV range.

The DIRC FEE provides arrival time measurements for each Cherenkov photon detected by the PMT array. The timing precision is constrained by the PMT intrinsic transit time spread (1.5 ns). The FEE is mounted right outside of the Standoff Box, and consists of 168 front-end boards, with each processing 64 PMT inputs. The PMT input signals are further amplified, digitized and transferred to the readout modules through optical fibers.

The space-time information of the PMT signals is transformed into the coordinates $(\theta_c, \phi_c, \delta t)$ in the Cherenkov cone system, with θ_c and ϕ_c as the polar and azimuthal angles relative to the cone direction, and δt as the time relative to the expected arrival. The Cherenkov cone associated with each passing charged track is thus reconstructed to provide discrimination among five stable particle types (e, μ, π, K, p) [55]. Figure 2.7 illustrates the Cherenkov angle θ_c as a powerful particle discriminator. The DIRC is capable of providing $\sim 4\sigma$ or better K/π separation for track momemtum p up to ~ 3 GeV/c, then the separation deteriorates gradually with p, being $\sim 2.5\sigma$ for $p = 4.1$ GeV/c [57].

2.2.4 The Electromagnetic Calorimeter (EMC)

The energy and position of electromagnetic showers are measured inside the thallium-doped cesium iodide (CsI(Tl)) crystals. The EMC detects photons and electrons with energies from 20 MeV to 9 GeV with nearly 100% efficiency. Energy and angular measurements of low energy photons are of crucial importance for the reconstruction of π^0s. Furthermore, the E/p ratio (energy measured in the EMC over momentum measured in the DCH) and the shower shape measured in the EMC play important roles in electron identification.

Figure 2.8 shows the EMC layout. The EMC is arranged into a cylindrical-shaped barrel and a conical-shaped forward endcap. The barrel covers a polar angle from 26.9° to 140.8°, and has a inner radius of 91 cm. 5760 CsI(Tl) crystals are groups into 48 polar angle (θ) rings, with each ring containing 120 identical crystal in azimuthal angle (ϕ). The barrel crystals are held in 280 modules mounted on the surface of a cylinder. Each module holds 21 crystals, 3 in ϕ and 7 in θ. The segmentations in θ
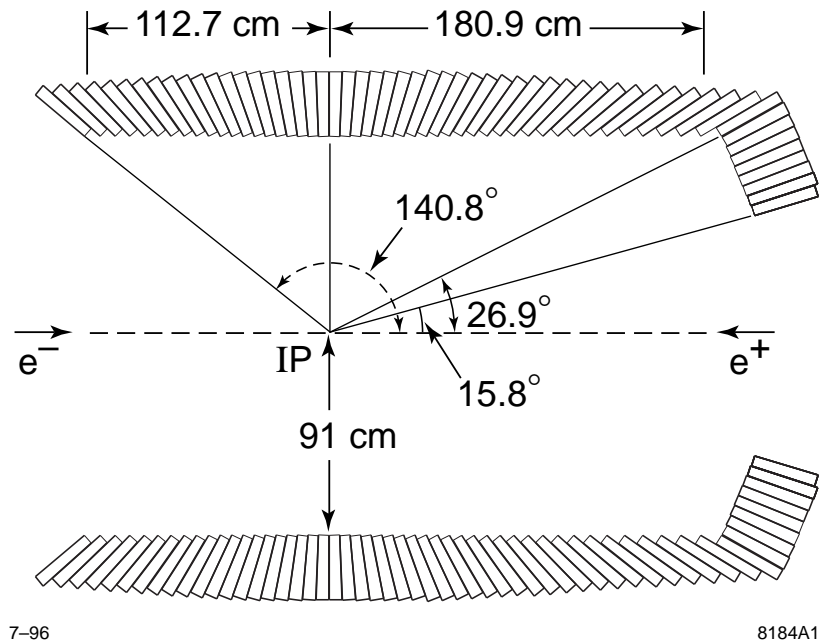
Figure 2.8: The layout of the EMC in side view [13].

and ϕ provide accurate angular measurements with a resolution of about a few mrad for high energy π^0 reconstruction. The endcap increase the polar-angle coverage down to 15.8°, and contains 820 crystals arranged in 8 θ rings. As in the barrel, the endcap crystals are also grouped into 20 modules, with each module containing 41 crystals around in ϕ. The full spatial coverage for the EMC is 90% in the CM frame. Except for the most forward ring, the crystals in the rest 55 rings increase from 29.6 cm to 32.4 cm along the boost direction, so that the effects of shower leakage can be minimized. The most forward ring has short crystals at the length of 30.5 cm due to overall spatial constraints. All the crystals are arranged in a quasi-projective geometry so that the core of a typical electromagnetic shower can be contained in one crystal.

The EMC crystals have a longitudinal cross-section of tapered trapezoidal shape. Their transverse cross-sections vary for different θ angles, with typical sizes for the front and back faces at 4.7×4.7 cm^2 and 6.1×6.0 cm^2, respectively. The crystals have a typical light yield of 50,000 photoelectrons (pe) per MeV. The scintillation light is transported via total reflection towards the rear surface of the crystals, where photodiodes and readout electronics are mounted. A small portion of the light escaping from the crystals is partly recovered through wrapping the crystals with two layers of white diffuse reflector. Before assembly, for each wrapped crystal, the signal from a highly collimated radioactive source placed at 20 points longitudinally along the crystal was recorded to measure the non-uniformity of light response. For each crystal, the non-uniformity is required to be within $\pm 2\%$ in its front half, then increase linearly to the maximum of $\pm 5\%$ at the back face. To fulfill this requirement, a series of adjustment techniques have been applied to the crystals. These techniques include wrapping the crystals in sheets with a mounted black-and-white pattern. However, the crystal non-uniformity may rise considerably after a few years' running, and the EMC energy resolution can be affected beyond a negligible level. This issue has been discussed in detail in Appendix I.

A typical electromagnetic shower spreads over a few crystals and forms a *cluster* of energy deposits in the EMC. To reconstruct the electromagnetic showers, clustering algorithms have been developed for efficient identification of the clusters. Each identified cluster is required to have at least one seed crystal with deposited energy above 10 MeV, and the crystals surrounding the seed crystals are absorbed into the cluster, if they have an energy above 1 MeV, or they are neighboring (including corners) to a crystal with energy above 3 MeV.

Since there exist possibilities that two electromagnetic showers may be close enough to be merged into a single cluster, the clustering algorithms are also responsible for splitting these clusters into *bumps* according to local energy maxima to identify single particle-induced showers. The energy of a bump as a fraction of the cluster energy is determined with a pattern-recognition algorithm. The position (centroid) of a bump is calculated using a center-of-gravity method [58]. The identified bumps are then used to match with charged tracks detected in the tracking system. The unmatched bumps are then considered as neutral particles.

Hadrons may interact hadronically and deposit a large amount of energy inside the EMC, which will make it difficult for electrons to get separated from hadrons using E/p information alone. However, since the length scale of the nuclear interaction is
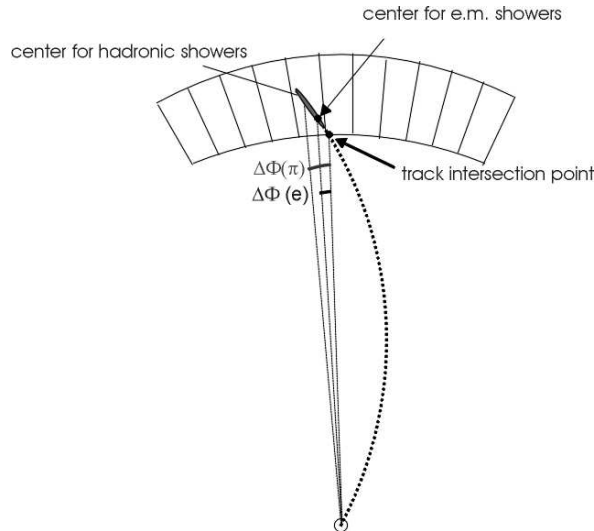
Figure 2.9: Definition of $\Delta\Phi$ for longitudinal shower shapes [60]. A hadron shower will typically reach its maximum farther from its intersection point on the surface of the EMC than an electromagnetic shower.

longer than the radiation length, the lateral and longitudinal energy distributions of a hadron shower and an electromagnetic shower will differ significantly. Therefore, for the improvement of electron/hadron separation, we measure two different variables for describing lateral and longitudinal shower shapes respectively. One is the lateral shower shape variable LAT defined as [59]:

$$
LAT = \frac{\sum_{i=3}^{N} E_i r_i^2}{\sum_{i=3}^{N} E_i r_i^2 + E_1 r_0^2 + E_2 r_0^2} \,,
\tag{2.1}
$$

where N is the number of crystals associated with a shower, E_i is the deposited energy in the i-th crystal, r_i is the lateral distance between the center of the shower and the i-th crystal, $r_0 \sim 5$ cm is the average distance between the center of two crystals. All the crystals associated with the shower are numbered in such a way that $E_1 > E_2 > \cdots > E_N$. Therefore the first and second crystals will have the highest deposited energies E_1 and E_2, while the sum $\sum_{i=3}^{N} E_i$ leaves out these two crystals. Since the Molière radius is 3.8 cm for CsI crystals, an electron will typically deposit most of its energy in 2 or 3 crystals near the shower center. According to Equation 2.1, The LAT for a typical electromagnetic shower is thus expected to be small, and its distribution peaks at ~ 0.3 [60]. The energy depositions for hadron showers, on the other hand, are less concentrated than electromagnetic showers. The resulting LAT distributions for hadron showers are broader than for electromagnetic showers, and peak in the range 0.4-1.0 [60].

The other shape variable is $\Delta\Phi$ for longitudinal shower shapes, which is described by the difference between the polar angles where a track intersect the EMC and the shower center, as illustrated in Figure 2.9. For a curved track in the $x - y$ plane, there is a displacement of $\Delta\Phi$ between the shower center and the intersection point on the
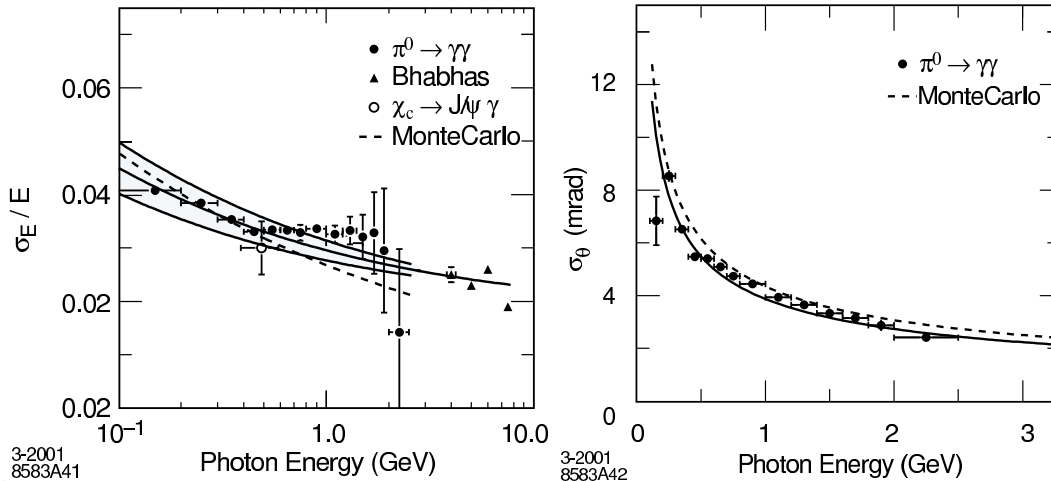
Figure 2.10: The energy (left) and angular (right) resolution for the *BABAR* EMC, measured from various processes [55]. The solid curves represent the fits to the points from the data control samples, while the shaded area in the left plot shows the uncertainties in the fit.

EMC surface. Figure 2.9 shows that typically hadron showers have larger $\Delta\Phi$ than electromagnetic showers. Similarly to LAT, the $\Delta\Phi$ distributions for charged hadrons are broader than for electrons [60].

As depicted in Figure 2.10, the calorimeter energy resolution is determined using various data samples in different energy ranges. These data samples include the radiative source, Bhabhas scattering, photons from $\chi_{c1} \to J/\psi\,\gamma$ events and π^0/η mesons decaying *symmetrically* into a pair of photons with approximately equal energies. A fit to the energy-dependent resolution yields the following function form:

$$\frac{\sigma_E}{E} = \frac{(2.32 \pm 0.30)\,\%}{\sqrt[4]{E\,(\mathrm{GeV})}} \oplus (1.85 \pm 0.12)\,\%. \tag{2.2}$$

Similarly, the angular resolution is also shown in Figure 2.10, which varies from $\sim$ 12 mrad to $\sim$ 3 mrad with the increase of photon energy. After fitting to the angular resolution as a function of energy, we have the following empirical function form:

$$\sigma_{\theta,\phi} = \left(\frac{3.87 \pm 0.07}{\sqrt{E\,(\mathrm{GeV})}} + 0.00 \pm 0.04\right)\mathrm{mrad}. \tag{2.3}$$

2.2.5 The Instrumented Flux Return (IFR)

As the outermost component of *BABAR* detector system, the IFR is primarily used for the muon detection at high efficiency and low mis-identification rate. As show in Figure 2.11 for the whole IFR assembly, the IFR consists of a barrel with 19 steel plates and two (backward and forward) endcaps, each with 18 steel plates. The steel plates also work as hadron absorbers, with a total iron thickness of 65 cm in the barrel, and
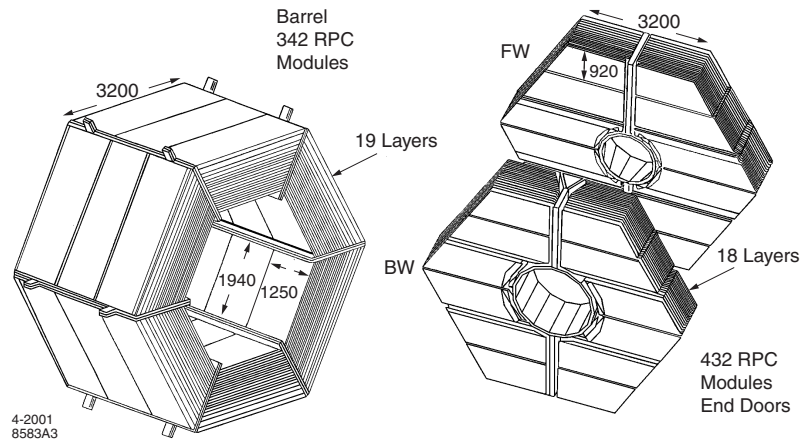
Figure 2.11: The layout of the IFR barrel (left) and endcap (right) sections [55].

60 cm in both forward and backward endcaps. Resistive plate chambers (RPCs) are installed within the gaps between steel plates for the detection of penetrating muons.

The cross section of a single RPC system is shown in Figure 2.12. Each RPC consists of a gas chamber filled with a mixture of Argon, Freon, and isobutane at high pressure. This gas layer is sandwiched by two layers of bakelite. The outer surfaces of these two bakelite layers are coated with graphite to provide an electric potential of ~ 8 kV. When charged particles pass through the gas layer, the discharge signal caused by ionization is read out by aluminum strips mounted outside of the graphite coatings. These strips are orthogonally oriented in different sides to provide two-dimensional coordinate information for track reconstruction. For RPCs in the barrel, the ϕ and z coordinate information is provided; while in the endcaps, the y and x coordinate information is provided.

A total number of nearly 53,000 strips are connected directly to 3300 front-end
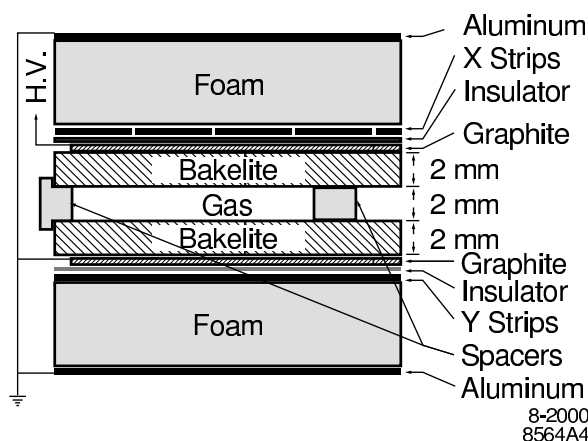
Figure 2.12: The cross-section of a RPC [55].
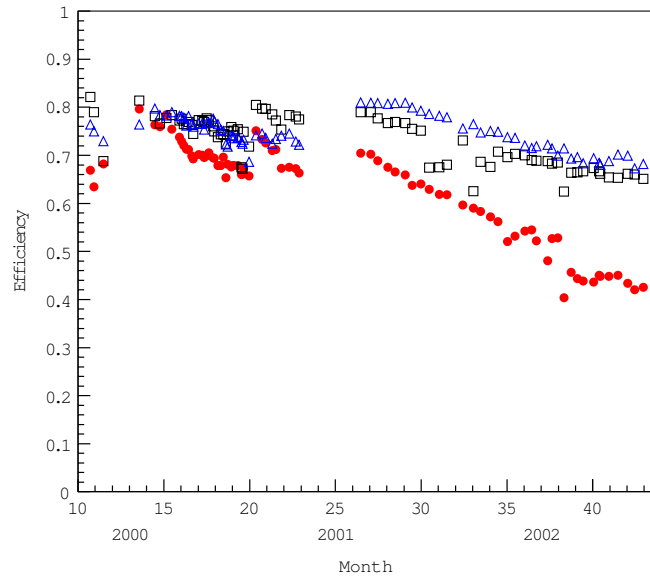
Figure 2.13: The averaged RPC efficiencies as a function of time until the summer of 2002 in three different IFR sections: the barrel (circles), forward endcap (triangles), and backward endcap (squares) [61].

cards, in which the input signal above a certain threshold is processed and transmitted to the trigger system. A clustering algorithm is adopted to join up the adjacent RPCs with hits into two-dimensional clusters, both in $r - \phi$ and z views. These clusters from different views are further combined into three-dimensional clusters. Another algorithm is then applied to associate the three-dimensional clusters with extrapolated tracks reconstructed in the DCH for a complete muon track reconstruction [55].

The RPCs in the IFR system suffered from a series of hardware failures [62], which resulted in continuous performance degradation for the IFR during the first few years' running. As depicted in Figure 2.13, the average RPC efficiencies had dropped significantly by the summer of 2002. In the barrel, the muon identification efficiency, determined using muons from $\mu^+\mu^-e^+e^-$ and $\mu^+\mu^-\gamma$ events, had fallen from 87% at the time of commissioning to 78% at a pion mis-identification rate of 4%. To stop the trend of degradation, a new generation of RPCs replaced the old ones and the absorber was increased in the forward endcap [61] prior to a new round of data-taking starting in November 2002. The new RPCs have shown satisfactory performance with high and stable efficiencies [63].

The performance of RPCs in the barrel continued to deteriorate until the summer of 2004, when they started to be replaced by the Limited Streamer Tubes (LSTs). Similar to RPCs, LSTs also rely on the ionized gas caused by the passing charged particles for providing position information. Each LST consists of 7 or 8 identical gas-filled cells. A gold-plated anode wire runs down the center of each cell, and a plane is placed below each tube. The ϕ and z coordinate information is provided through collecting the induced charge on the wire and the plane, respectively [64]. The first phase of LST installation ended in October 2004. During the period, the 18 inner RPC layers in the top and bottom sextants were replaced with 12 layers of

LSTs and 6 layers of brass, while the outermost layer is not accessible for operation. With the new LSTs, for high energy tracks with momentum between 2 and 4 GeV and in the IFR barrel, the muon efficiency is able to achieve $\sim 90\%$ at a pion misidentification rate of 4% [64]. This is significantly better than the initial performance of the IFR system with only RPCs. The second and last phase of LST installation on the remaining 4 sextants in the barrel was accomplished in the end of 2006, by that time the data-taking period for our analyses described in this thesis had already ended.

2.2.6   The Trigger System

For the design luminosity of 3×10^{33} cm^{-2}s^{-1} and at the $\Upsilon(4S)$ resonance, beam-related background events (e^+e^-) are produced at a typical rate of about 20 kHz, while $B\bar{B}$ and other events ($q\bar{q}$, $\mu^+\mu^-$, $\tau^+\tau^-$, etc.) which are of physics interest are produced at a much lower rate of a few Hz. This requires the trigger system to select events of interest at high efficiency and low deadtime while working under its manageable rate of about 120 Hz by rejecting e^+e^- backgrounds.

There are two hierarchically organized trigger levels in the _BABAR_ trigger system: Level 1 (L1) and Level 3 (L3). The L1 trigger system is implemented in hardware and configured to reduce the output rate to 1 kHz. The L1 trigger decision is based on primitives provided by the DCH trigger (DCT) and EMC trigger (EMT). These two triggers feed the information to the global trigger (GLT) for issuing the _L1 Accept_, which initializes the event readout. The IFR trigger is also linked to the GLT and mainly used for diagnostic purpose by triggering $\mu^+\mu^-$ and cosmic ray events. The L1 trigger efficiency for generic $B\bar{B}$ events is nearly 100%.

The L3 trigger software performs reconstruction and classification of events filtered by the L1 trigger, besides improving the beam background rejection, through running on the online computer farm. Two algorithms are employed: a tracking-based using DCH (L3Dch), and a clustering-based using EMC (L3Emc).

The L3Dch trigger is important for effectively suppressing beam-induced events produced near the IP, for which the L1 trigger lacks sufficient tracking resolution to recognize. To achieve this goal, a track look-up table based on the hit patterns from MC simulation is set up for pattern recognition of the track segments, which is provided by the DCT. The matched pattern is then passed over to an iterative track fitting algorithm for the identification of the tracks with p_t above 250 MeV/c.

The L3Emc trigger is responsible for identifying energy clusters in the EMC, which also works as a very important complement for suppressing Bhabha events. The noise-like crystal signals with energy below 20 MeV and outside of a 1.3 μs window of the event time is filtered out, before clusters are reconstructed using a fast look-up table. The energy, timing and shower shape information is calculated for clusters with a total energy above 100 MeV, the rest are abandoned.

The combined L1+L3 trigger efficiency for $B\bar{B}$ events remains high above 99.9%, while for continuum events the efficiency is at $\sim 97\%$. Both have met the original design goals [55].
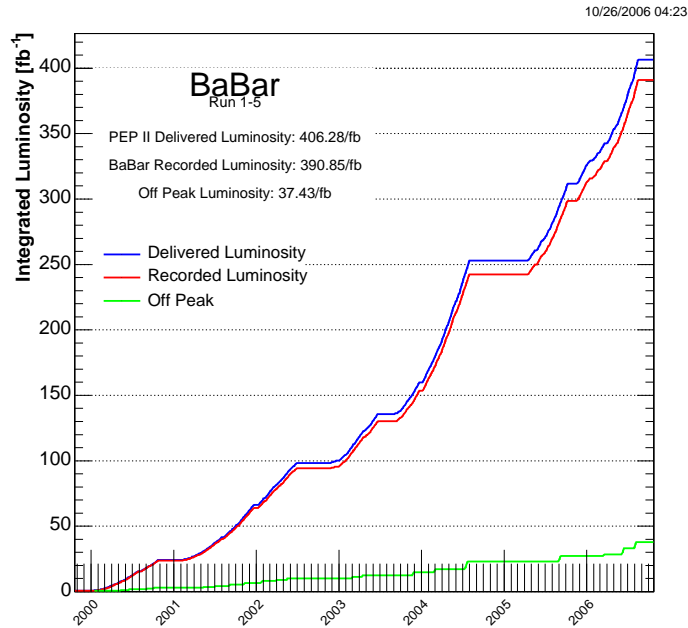
Figure 2.14: Integrated luminosity at PEP-II/*BABAR* as a function of time from 1999 to 2006.

2.3   Experimental Data

2.3.1   *BABAR* Data Sample

The data sample (Table 2.1) used in our analysis is collected from the Runs 1–5 datasets covering a run period of about 7 years since October 1999, which corresponds to a total integrated on-resonance luminosity of almost 350 fb^{-1}. The integrated luminosity as a function of time is shown in Figure 2.14. Under the assumption that $\Upsilon(4S)$ will 100% decay into $B\overline{B}$ pairs, counting $B\overline{B}$ pairs puts the number $n_{B\overline{B}}$ at about 384 million, with an uncertainty of 1.1%.

2.3.2   Simulated Data Samples

The MC simulated event samples (Tables 2.2-2.4) are first generated using two different event generators for different purposes: **EvtGen** [65] (for B decays to exclusive final states) and **Jetset** [66] (for generic continuum and inclusive B decay simulations). The CERN detector description and simulation tool **GEANT4** [67] is then applied to simulate the interaction between the generated particles and the detector components. The simulated detector response is used for the reconstruction of the MC events. The information both at the generator- and **GEANT4**- level (MC *truth*) is written into the event database, along with the reconstructed information, both of which are important for studies on detector resolution and efficiency.

Three distinct classes of MC simulated events are most relevant to our $B \rightarrow$

Run	Run Period	No. $B\overline{B}$	On-res $\int \mathcal{L}$ (fb^{-1})
1	Oct. 1999 - Nov. 2000	22.4	20.7
2	Feb. 2001 - Jun. 2002	67.3	60.9
3	Nov. 2002 - Jun. 2003	35.7	32.3
4	Sep. 2003 - Jul. 2004	110.7	101.1
5	Apr. 2005 - Aug. 2006	147.7	134.2
Total		383.8	349.2

Table 2.1: Number of $B\overline{B}$ decays and integrated luminosity in the data sample by run. Only good data are included in the sample.

$K^{(*)}\ell^+\ell^-$ analyses:

- $B \to K^{(*)}\ell^+\ell^-$ signal events (Table 2.2)[1], from which the signal reconstruction efficiencies are obtained. Yields are approximately scaled according to the measured branching ratios in the previous *BABAR* experiment [11]. The signal decay kinematics follows the form factor model of Ali *et al* [20]. All 12 decay modes introduced in Section 3.1 are simulated.

- $B \to K^{(*)}J/\psi$ ($\to \ell^+\ell^-$) and $B \to K^{(*)}\psi(2S)$ ($\to \ell^+\ell^-$) charmonium events (Table 2.3). Yields are scaled to the world average branching fractions [68]. These samples provide an estimate of the residual charmonium background escaping the charmonium veto and a cross-check on signal efficiency estimates, as well as other experimental techniques.

- Generic continuum and $B\overline{B}$ events (Table 2.4), which are used for event selection optimization to reduce purely combinatorial backgrounds. The samples of generic continuum events are scaled to appropriate expected cross-sections as listed in the table.

Besides these, we also have generated exclusive B decay samples such as $B^0 \to K^{(*)}\gamma(\to e^+e^-)$, which may fake as real signal events, for peaking background study, as described later in Section §4.6.

---

[1]Charge conjugation is assumed throughout this thesis unless specifically stated.

Mode	$\mathcal{B}(10^{-6})$ [11]	Events	Data/MC (10^{-3})
$K^+e^+e^-$	0.36	530000	0.26
$K^+\mu^+\mu^-$	0.36	530000	0.26
$K_s^0 e^+e^-$	$0.34 \cdot \frac{1}{2} \cdot \mathcal{B}(K_S^0 \to \pi^+\pi^-)$	530000	0.09
$K_s^0 \mu^+\mu^-$	$0.34 \cdot \frac{1}{2} \cdot \mathcal{B}(K_S^0 \to \pi^+\pi^-)$	530000	0.09
$K^+\pi^- e^+e^-$	$1.04 \cdot \frac{2}{3}$	530000	0.50
$K^+\pi^- \mu^+\mu^-$	$0.78 \cdot \frac{2}{3}$	530000	0.38
$K_s^0 \pi^+ e^+e^-$	$1.11 \cdot \frac{2}{3} \cdot \frac{1}{2} \cdot \mathcal{B}(K_S^0 \to \pi^+\pi^-)$	530000	0.19
$K_s^0 \pi^+ \mu^+\mu^-$	$0.84 \cdot \frac{2}{3} \cdot \frac{1}{2} \cdot \mathcal{B}(K_S^0 \to \pi^+\pi^-)$	530000	0.14
$K^+\pi^0 e^+e^-$	$1.11 \cdot \frac{1}{3}$	530000	0.27
$K^+\pi^0 \mu^+\mu^-$	$0.84 \cdot \frac{1}{3}$	530000	0.20
$K_s^0 \pi^0 e^+e^-$	$1.04 \cdot \frac{1}{3} \cdot \frac{1}{2} \cdot \mathcal{B}(K_S^0 \to \pi^+\pi^-)$	530000	0.03
$K_s^0 \pi^0 \mu^+\mu^-$	$0.78 \cdot \frac{1}{3} \cdot \frac{1}{2} \cdot \mathcal{B}(K_S^0 \to \pi^+\pi^-)$	1778000	0.07

Table 2.2: The number of MC simulated signal events and the ratio of the number of $B\overline{B}$ decays in the 349 fb^{-1} data to the number simulated for each decay mode. In each mode with multiple final state hadrons, the generated events decay through the $K^*(892)$ resonance. All simulated K_S^0s, which are only half of K^0s, are forced to decay into the $\pi^+\pi^-$ final state. The listed branching fractions include these effects.

Mode	$\mathcal{B}(10^{-3})$ [68]	Events	Data/MC (10^{-3})
$J/\psi K_S^0$	$0.87 \cdot \mathcal{B}(J/\psi \to \ell^+\ell^-) \cdot \frac{1}{2} \cdot \mathcal{B}(K_S^0 \to \pi^+\pi^-)$	10468000	1.31
$J/\psi K^+$	$1.01 \cdot \mathcal{B}(J/\psi \to \ell^+\ell^-)$	18504000	2.48
$J/\psi K^+\pi^-$	$1.33 \cdot \mathcal{B}(J/\psi \to \ell^+\ell^-) \cdot \frac{2}{3}$	8440000	4.78
$J/\psi K_S^0\pi^+$	$1.41 \cdot \mathcal{B}(J/\psi \to \ell^+\ell^-) \cdot \frac{2}{3} \cdot \frac{1}{2} \cdot \mathcal{B}(K_S^0 \to \pi^+\pi^-)$	8638000	1.54
$J/\psi K^+\pi^0$	$1.41 \cdot \mathcal{B}(J/\psi \to \ell^+\ell^-) \cdot \frac{1}{3}$	8638000	3.43
$J/\psi K_S^0\pi^0$	$1.33 \cdot \mathcal{B}(J/\psi \to \ell^+\ell^-) \cdot \frac{1}{3} \cdot \frac{1}{2} \cdot \mathcal{B}(K_S^0 \to \pi^+\pi^-)$	8482000	0.82
$\psi(2S)K_S^0$	$0.62 \cdot \mathcal{B}(\psi(2S) \to \ell^+\ell^-) \cdot \frac{1}{2} \cdot \mathcal{B}(K_S^0 \to \pi^+\pi^-)$	632400	1.93
$\psi(2S)K^+$	$0.65 \cdot \mathcal{B}(\psi(2S) \to \ell^+\ell^-)$	295500	12.48
$\psi(2S)K^+\pi^-$	$0.72 \cdot \mathcal{B}(\psi(2S) \to \ell^+\ell^-) \cdot \frac{2}{3}$	898000	3.04
$\psi(2S)K_S^0\pi^+$	$0.67 \cdot \mathcal{B}(\psi(2S) \to \ell^+\ell^-) \cdot \frac{2}{3} \cdot \frac{1}{2} \cdot \mathcal{B}(K_S^0 \to \pi^+\pi^-)$	862000	1.02
$\psi(2S)K^+\pi^0$	$0.67 \cdot \mathcal{B}(\psi(2S) \to \ell^+\ell^-) \cdot \frac{1}{3}$	862000	1.48
$\psi(2S)K_S^0\pi^0$	$0.72 \cdot \mathcal{B}(\psi(2S) \to \ell^+\ell^-) \cdot \frac{1}{3} \cdot \frac{1}{2} \cdot \mathcal{B}(K_S^0 \to \pi^+\pi^-)$	862000	0.49

Table 2.3: The number of MC simulated charmonium events and the ratio of the number of $B\overline{B}$ decays in data to the effective number simulated for each decay mode. The simulated J/ψ and $\psi(2S)$ events are forced to decay to di-lepton final states (with equal probabilities to di-electron or di-muon pairs), and in each mode with multiple final state hadrons, the generated events decay through the $K^*(892)$ resonance. All simulated K_S^0s (half of K^0s) are forced to decay into the $\pi^+\pi^-$ final state. The listed branching fractions and Data/MC ratios include these effects.

Mode	Nominal Cross-sec. (nb) [13]	Events	Data/MC
Generic B^+B^-	0.525	555572000	0.33
Generic $B^0\overline{B}^0$	0.525	552414000	0.33
Continuum $c\overline{c}$	1.30	591198000	0.77
Continuum uds	2.05	695820000	1.03

Table 2.4: The number of MC simulated generic events and the ratio of the number of $B\overline{B}$ decays (or, for continuum events, scaled cross-section) in the 349 fb^{-1} data to the number simulated for each mode.

Chapter 3

Basic Event Selection

This chapter introduces the event selection criteria that are essential for both the rate-based and the angular measurements of $B \to K^{(*)}\ell^+\ell^-$ decays.

3.1 Selection of Final State Particles

We have reconstructed 12 individual exclusive $B \to K^{(*)}\ell^+\ell^-$ final states:

- $B^\pm \to K^\pm \ell^+ \ell^-$

- $B^0 \to K_S^0 \ell^+ \ell^-$, with $K_S^0 \to \pi^+ \pi^-$

- $B^0 \to K^{*0} \ell^+ \ell^-$, where K^{*0} is reconstructed in the following two channels:
  $K^{*0} \to K^\pm \pi^\mp$;
  $K^{*0} \to K_S^0 \pi^0$, with $K_S^0 \to \pi^+ \pi^-$

- $B^\pm \to K^{*\pm} \ell^+ \ell^-$, where $K^{*\pm}$ is reconstructed in the following two channels:
  $K^{*\pm} \to K^\pm \pi^0$
  $K^{*\pm} \to K_S^0 \pi^\mp$, with $K_S^0 \to \pi^+ \pi^-$

In all the modes listed above, $\ell^+\ell^-$ is either $\mu^+\mu^-$ or e^+e^-.

For the full reconstruction of exclusive B decays, it is important to identify charged particles including electrons, muons, kaons and pions. In the particle identification (PID) processes, information from different detector components are combined to maximize the discrimination power, with the help of multivariate analysis tools, such as maximum likelihood method and neural networks (NN).

Look-up tables have been set up for different PID selectors, which store the information of efficiencies or mis-identification rates for different particles (e, μ, π, K, p) with different charges, in different ranges of momentum (p), polar angle (θ), azimuth angle (ϕ), and data-taking time. There are two sets of PID look-up tables available, one for MC simulation, the other for real data. Both sets of tables are determined from their corresponding control samples with high purity. The discrepancies of PID efficiencies between MC simulation and real data are used to correct PID selections in MC simulation, a procedure called *"PID tweaking"*.

With information from a pair of detected tracks with opposite charges assumed to be pions, we are able to reconstruct a K_S^0. Similarly, a π^0 is reconstructed from a pair of detected photons in the EMC.

3.1.1 Electron Identification and Bremsstrahlung Recovery

Electron identification utilizes the following information of three sub-systems: EMC, DCH and DIRC:

- The ratio of E/p, where E is the energy of an electromagnetic shower deposited in the EMC, and p is the momentum of the corresponding track measured in the DCH. The E/p distribution for electrons has a very sharp peak close to unity. This provides a distinctive signature for electrons. Since all other charged particles tend to lose energy in the EMC only via ionization, thus have a continuous distribution between 0 and 1.

- The lateral and longitudinal shower shapes (LAT and $\Delta\Phi$) in the EMC, as described in §2.2.4.

- The energy loss ($\mathrm{d}E/\mathrm{d}x$) in the DCH. The measured $\mathrm{d}E/\mathrm{d}x$ is compared to the expectation calculated based on the electron hypothesis.

- The Cherenkov angle θ_c measured in the DIRC. This is useful for identifying electrons with $p < 1.5\,\mathrm{GeV}/c$.

The discriminating variables mentioned above are first used for the pre-selection of candidate tracks by applying a series of loose criteria. They are later grouped into vectors x_{EMC}, x_{DCH} and x_{DIRC} according to which detector component they belong to. These vectors are combined into a global likelihood $\mathcal{L}(\xi)$ for each particle hypothesis $\xi \in \{e; \pi; K; p\}$:

$$\mathcal{L}(\xi) = \mathcal{L}(x_{EMC}; \xi) \cdot \mathcal{L}(x_{DCH}; \xi) \cdot \mathcal{L}(x_{DIRC}; \xi).$$

Each individual likelihood $\mathcal{L}(\xi)$ is weighted with an *a priori* probability p_ξ based on the relative fraction of charged particle species ξ produced in a typical B event. We select a track as electron if the likelihood ratio for the electron hypothesis lies above 0.98.

The electron identification efficiency and hadron mis-identification rate are both measured in different momentum p and polar angle θ ranges using different data samples with high purity. For electrons, the data samples of electrons from radiative Bhabha events are used. Figure 3.1 shows high identification efficiencies at $\sim 93\%$ for $e^\pm$ momenta above 0.7 GeV/c. The efficiency difference between e^+ and e^- is rather trivial. For pions, the probability of being mis-identified as an electron is determined using data samples of pions from τ and K_S^0 decays. As also shown in Figure 3.1, the pion mis-identification rate is at a negligible level of below 0.2% for the entire momentum range, and the rate for π^+ is slightly higher than that for π^-.

Decelerating charged particles will typically radiate photons and lose energy through bremsstrahlung process. As the lightest charged particles, the measured 4-momentum
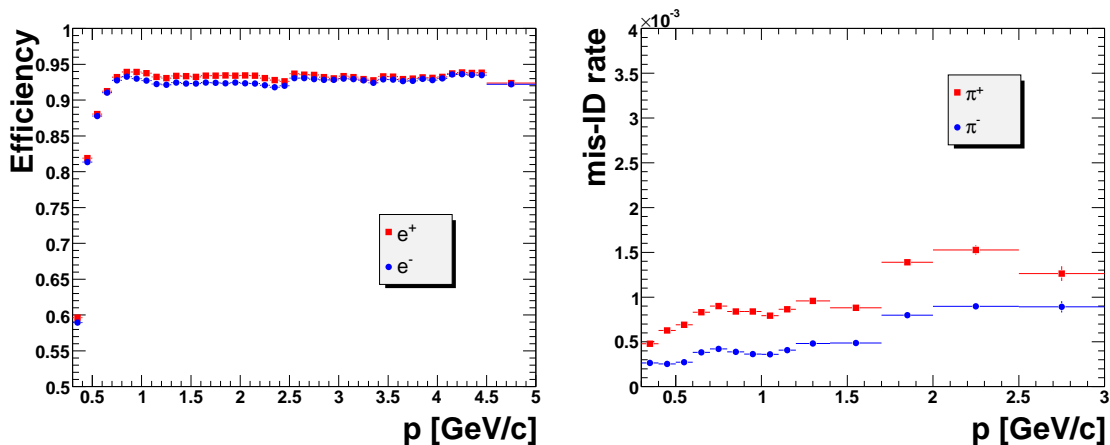
Figure 3.1: Electron identification efficiency (left) and pion mis-identification probability (right) as a function of momentum (p) in the electron selection.

of electrons will be considerably affected by the radiation. To improve the measurement, we try to include the radiated photons in the electron energy. The photons are required to have energy $E_\gamma > 30$ MeV and lie within a cone of 0.035 rad around the detected electron track. We use the bremsstrahlung recovery by including up to one nearby photon for each electron candidate.

3.1.2 Muon Identification

To identify a muon, the following information from the IFR and EMC is relevant:

- The energy deposited inside the EMC.

- The measured number of interaction lengths (λ_{meas}) traversed by the muon candidate in the *BABAR* detector.

- The difference of λ_{meas} and expected interaction lengths under a muon hypothesis.

- The continuity of the track from the DCH into the IFR.

- The average and standard deviation of the hit strip multiplicity per layer in the IFR.

- The goodness-of-fits (defined by $\chi^2/n.d.o.f.$) of the IFR hit strips with respect to a third-order polynomial fit and the track extrapolation in the three-dimensional IFR cluster.

The muon selector is based on the output of a neural network algorithm with the above information as inputs. The selector has several levels of selection criteria from loose to tight: "VeryLoose","Loose", "Tight", and "VeryTight". The muon efficiency
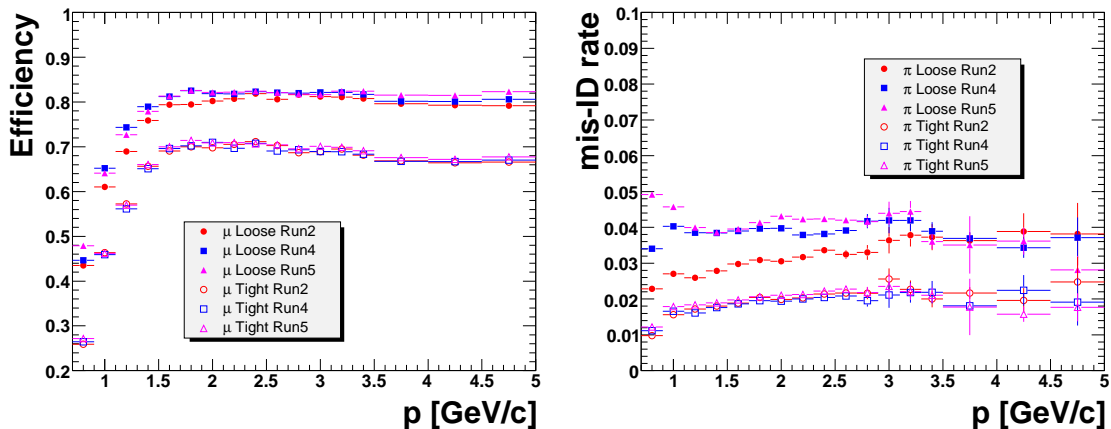
Figure 3.2: Muon identification efficiency (left) and pion mis-identification probability (right) as a function of momentum (p) in the muon selection with the "Loose" and "Tight" level criteria. The values from different data-taking periods defined in Table 2.1 are shown. More specifically, "Run2" corresponds to 61 fb^{-1} data collected before any IFR upgrades, "Run4" corresponds to 101 fb^{-1} data collected after new RPCs in the IFR forward encap, and "Run5" corresponds to 134 fb^{-1} data collected after the LST installation in the IFR barrel.

is determined using samples of muons produced in $e^+e^- \rightarrow \mu^+\mu^-\gamma$ events, while the pion mis-identification rate is determined with pions produced in $\tau^- \rightarrow \pi^-\pi^+\pi^-\nu_\tau$ events.

Since the IFR system experienced two major phases of upgrading (described in §2.2.5) before the completion of all five run periods listed in Table 2.1, the muon selection performance is expected to be time-dependent. In Figure 3.2, the muon selection performance is shown for three major run periods. Compared to Run 2, which is before any IFR upgrades, muon efficiencies in Run 4 and Run 5 are considerably improved for the entire momentum range. The pion mis-identification rates are kept at approximately the same level for all different runs, except for low momentum tracks with the "Loose" level muon selection criteria. Generally for all runs, after applying the "Loose" level criteria, the efficiency of selecting a muon is initially below 50% for its momentum p at ~ 0.7 GeV, and increases rapidly as p goes higher, then finally stays at $\sim 80\%$ for momentum above ~ 1.3 GeV/c. The pion mis-identification rate is generally insensitive to track momentum and keeps at $\sim 4\%$ for the entire momentum range shown in Figure 3.2. After applying the "Tight" level selection criteria, the pion mis-identification rate is effectively suppressed to $\sim 2\%$ level, however about 10% more real muons will be rejected as background.

3.1.3   Charged Kaon and Pion Identification

Identification of charged kaons and pions is based on the following information from the SVT, DCH and DIRC:
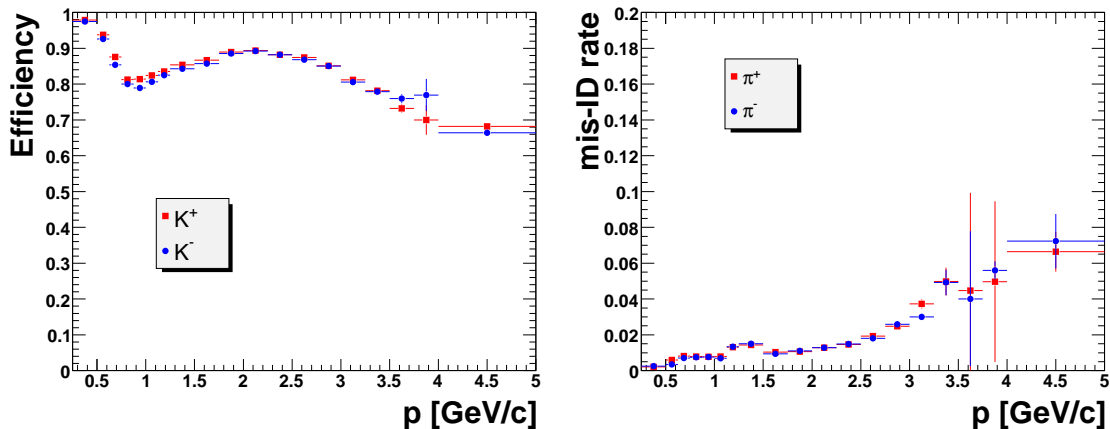
Figure 3.3: Kaon identification efficiency (left) and pion mis-identification probability (right) as a function of momentum (p) in the kaon selection.

- The energy loss ($\mathrm{d}E/\mathrm{d}x$) in the DCH and SVT.

- The Cherenkov angle (θ_C), number of observed photons, and track quality in the DIRC.

A global likelihood function for each particle hypothesis $\xi \in \{\pi, K, p\}$ is determined from three likelihood functions for the corresponding sub-detector systems mentioned above. The likelihood functions are calculated separately from the observations and likelihood functions evaluated for each particle hypothesis ξ:

$$\mathcal{L}_\xi = \mathcal{L}_\xi^{\mathrm{SVT}} \times \mathcal{L}_\xi^{\mathrm{DCH}} \times \mathcal{L}_\xi^{\mathrm{DIRC}} \, .$$

For the separation of two particle species, the relevant likelihood ratios are calculated. We require the K/π separation $\mathcal{L}_K/\mathcal{L}_\pi$ above 0.9 to accept a detected track as kaon, while those tracks failing this requirement will be considered as pions. Therefore, for a kaon, the probability of being identified in the kaon selection is the complement of the probability of being mis-identified as a pion in the pion selection, and likewise for a pion. Both pions and kaons in the data control samples are produced in $D^{*+} \rightarrow D^0 (\rightarrow K^- \pi^+) \pi^+ D^0$ processes and used to determine the identification efficiencies and mis-identification rates. The kaon PID selector performance for both kaons and pions are presented in Figure 3.3. For kaons with momenta $p < 1$ GeV/c, K/π separation power is predominantly provided by the $\mathrm{d}E/\mathrm{d}x$ information from the DCH, and the kaon efficiency drops rapidly with the increase of p from an initial value of nearly 100% down to $\sim 80\%$. For $p > 1$ GeV/c^2, we mainly rely on the Cherenkov angle measurements in the DIRC to discriminate kaons and pions. In this momentum range, the kaon efficiency is generally beyond 75%, and the mis-identification probability for pions is below 5%, except for tracks with very high momenta beyond ~ 4 GeV/c. Correspondingly, in the pion selection, for tracks with momenta p below ~ 4 GeV/c the pion efficiency is above 95%, and the kaon mis-identification rate is $\sim 20\%$.

3.1.4 π^0 and K_s^0 Reconstruction

A π^0 will predominantly decay into a pair of photons, which can be detected and measured in the EMC. The resolution of the invariant mass of the photon pair ($m_{\gamma\gamma}$) is ~ 6.5 MeV. We require that each photon reconstructing a π^0 has an energy $E_\gamma > 50$ MeV, and $LAT < 0.8$. The invariant mass of the gamma pair is require to be $115 < m_{\gamma\gamma} < 155\,\mathrm{MeV}/c^2$.

A K_s^0 is reconstructed in the decay $K_s^0 \to \pi^+\pi^-$. A pair of detected tracks with opposite charges are required to have an invariant mass within 9.3 MeV/c^2 of the nominal K_s^0 mass, which is about three times of the signal mass resolution. The track pair is fitted to determine the common vertex for pions as the K_s^0 decay vertex. Since K_s^0 has a relatively long life time τ with $c\tau = 2.68$ cm [68], K_s^0 will have a long flight length, and its decay vertex will be easily separated from the main B decay vertex. We require in addition for the reconstructed K_s^0 that the significance of K_s^0 flight length, defined as the measured flight length normalized by its uncertainty, must be greater than 3.

3.2 B Candidate Reconstruction

There are further requirements on the kinematic quantities of the particles before they are accepted to form a B candidate:

- Muon candidates must have momenta in the laboratory frame $p_{lab} > 0.7\,\mathrm{GeV}/c$.

- Electron candidates must have momenta in the laboratory frame $p_{lab} > 0.3\,\mathrm{GeV}/c$.

- Electron pairs are required to pass a gamma conversion filter which vetoes candidates with di-lepton invariant mass $m_{\ell\ell} < 0.03\,\mathrm{GeV}/c^2$ in $B \to Ke^+e^-$ modes; while in $B \to K^*e^+e^-$ modes, due to the enhancement of partial branching ratio at low di-lepton mass from the photon penguin contribution, the conversion veto is only applied when the radius at which the electron tracks intersect is less than 2 cm from the beam axis.

- The probability of the di-lepton vertex is required to be $> 10^{-10}$.

- The invariant mass of K and π candidates must have $0.7 < m_{K\pi} < 1.1\,\mathrm{GeV}/c^2$ for $K^*\ell^+\ell^-$ modes.

The reconstructed B candidates are discriminated from continuum events, and from random combinatorial backgrounds consisting of non-signal B decays, by using the following two kinematic quantities:

$$m_{\mathrm{ES}} = \sqrt{\frac{s}{2} + \frac{(p_0 \cdot p_B)^2}{E_0^2} - p_B^2}, \; \Delta E = E_B^* - \frac{\sqrt{s}}{2},$$

where p_B is the B momentum in the laboratory frame, E_B^* is the B energy in the CM frame, E_0 and p_0 are the energy and momentum of the $\Upsilon(4S)$ in the laboratory frame,

and $\sqrt{s}$ is the total CM energy. For the decay modes with a K^* in the final state, the reconstructed $K\pi$ invariant mass of K^* candidates, $m_{K\pi}$, is also useful. We define four regions in the space spanned by these quantities which are relevant here (Figure 3.4):

- **Fit Region**: The region which contains essentially all correctly reconstructed signal events, as well as sufficient background events to obtain well-characterized signal and combinatorial background normalizations, plus the combinatorial background shape, from the fits. A clear Gaussian-shape peak is visible in the right plot of Figure 3.4 for the projection of the simulated signal events in this region onto m_{ES}. The fit region is defined by:

  $m_{ES} > 5.2\,\text{GeV}/c^2$,

  $-0.08 < \Delta E < 0.05\,\text{GeV}$ or slightly narrower (see Table 3.1),

  $0.82 < m_{K\pi} < 0.97\,\text{GeV}/c^2$ for $K^* \ell^+\ell^-$ modes.

- **Signal Region**: A portion of the m_{ES} fit region containing nearly all signal candidates:

  $5.27 < m_{ES} < 5.29\,\text{GeV}/c^2$,

  ΔE and $m_{K\pi}$ selections as in the fit region.

- m_{ES} **Sideband Region**: The rest of the m_{ES} fit region excluding the signal region in the m_{ES}-ΔE plane is used to determine the combinatorial background PDFs. The $m_{K\pi}$ is the same as in the fit region for $K^*\ell^+\ell^-$ modes.

- **Grand Sideband (GSB) Region**: A broad sideband region dominated by combinatorial background surrounding the fit region in the m_{ES}-ΔE plane is defined by:

  $5.0 < m_{ES} < 5.2\,\text{GeV}/c^2$,

  $-0.5 < \Delta E < -0.5\,\text{GeV}$,

  $0.70 < m_{K\pi} < 0.82\,\text{GeV}/c^2$ or $0.97 < m_{K\pi} < 1.10\,\text{GeV}/c^2$ for $K^*\ell^+\ell^-$ modes.
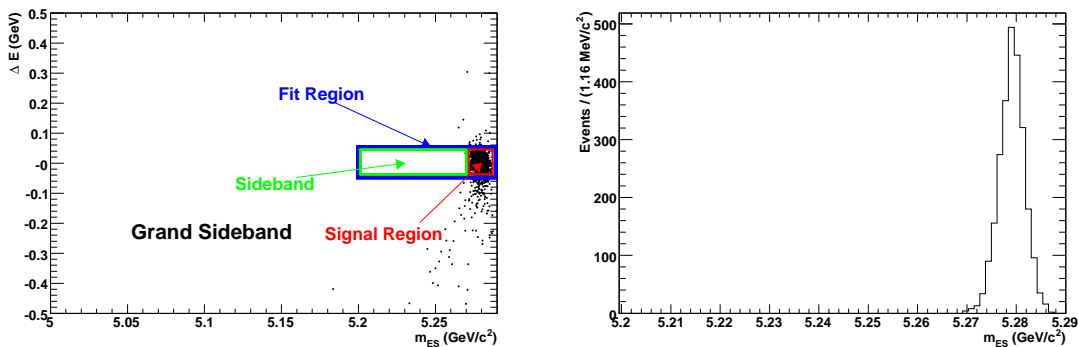
Figure 3.4: For the $B^+ \to K^+\mu^+\mu^-$ decays with di-lepton invariant mass above J/ψ resonance, the defined kinematic regions in the m_{ES}-ΔE plane are shown in the left plot, with the points representing the simulated $B^+ \to K^+\mu^+\mu^-$ signal events. The right plot shows the projection onto m_{ES} for the high density of points in the fit region.

Mode	Mass bin	low ΔE	high ΔE
$\mu^+\mu^-$	low	-0.04	0.04
e^+e^-	low	-0.07	0.04
$\mu^+\mu^-$	high	-0.05	0.05
e^+e^-	high	-0.08	0.05

Table 3.1: The ΔE selections for di-muon and di-electron modes in di-lepton mass regions below ("low ") and above ("high") the J/ψ resonance.

3.3   Vetoes Against Peaking Backgrounds

Peaking background events are decays that will peak in the m_{ES} distribution like true signals. The majority of two main sources of peaking background are vetoed using appropriate experimental techniques, as discussed in the following two sub-sections.

3.3.1   Charmonium vetoes

The largest peaking background source comes from decays $B \to (c\bar{c})K^{(*)}$, where $c\bar{c}$ is either a J/ψ or $\psi(2S)$ that decays into an $\ell^+\ell^-$ pair. The J/ψ and $\psi(2S)$ veto regions are defined respectively to remove the corresponding charmonium events.

For the electron modes, the J/ψ veto region is the union of the following three regions in the $\Delta E - m_{\ell\ell}$ plane:

- A di-lepton mass requirement $2.65 < m_{\ell\ell} < 3.20$ GeV/c^2

- For $m_{\ell\ell} > 3.20$ GeV/c^2, a band in the $\Delta E - m_{\ell\ell}$ plane, $(1.11 \times m_{\ell\ell} - 3.58) < \Delta E < (1.11 \times m_{\ell\ell} - 3.25)$ GeV

For the muon modes, the J/ψ veto region is the union of the following three regions in the $\Delta E - m_{\ell\ell}$ plane:

- A di-lepton mass requirement $2.65 < m_{\ell\ell} < 3.20$ GeV/c^2

- For $m_{\ell\ell} > 3.20$ GeV/c^2, a band in the $\Delta E - m_{\ell\ell}$ plane, $(1.11 \times m_{\ell\ell} - 3.53) < \Delta E < (1.11 \times m_{\ell\ell} - 3.31)$ GeV/c^2

For both the electron and muon modes, the $\psi(2S)$ veto region is the union of the following three regions in the $\Delta E - m_{\ell\ell}$ plane:

- A di-lepton mass requirement $3.60 < m_{\ell\ell} < 3.75$ GeV/c^2

- For $m_{\ell\ell} > 3.75$ GeV/c^2, a band in the $\Delta E - m_{\ell\ell}$ plane, $(1.11 \times m_{\ell\ell} - 4.14 < \Delta E < 1.11 \times m_{\ell\ell} - 3.97)$ GeV/c^2

- For $m_{\ell\ell} < 3.60$ GeV/c^2, a triangle in the $\Delta E - m_{\ell\ell}$ plane, $\Delta E < (1.11 \times m_{\ell\ell} - 3.97)$ GeV
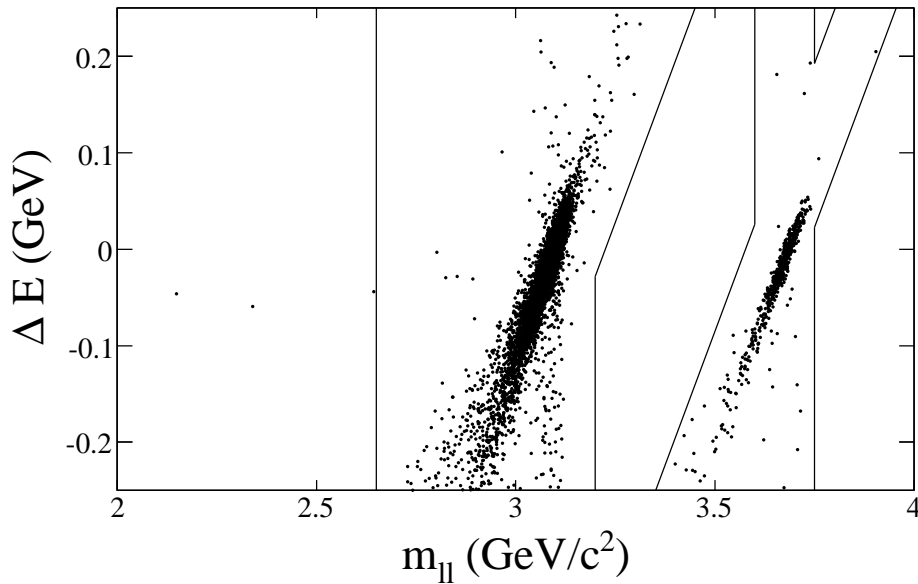
Figure 3.5: $B^+ \to K^+e^+e^-$ charmonium veto regions in the $m_{\ell\ell}$-ΔE plane. The points show the expected $B^+ \to K^+ J/\psi(\to e^+e^-)$ and $B^+ \to K^+\psi(2S)(\to e^+e^-)$ event distribution in 349 fb^{-1} data, from Monte Carlo simulation.

Figure 3.5 shows the vetoed region for the $B^+ \to K^+e^+e^-$ decay as an example.

Furthermore there is an additional charmonium veto imposed on the electron modes for those events that escape the vetoes described above. If a random photon is incorrectly associated with an electron, the event could escape the veto on the $m_{\ell\ell}$ mass. We reduce this possibility by requiring that the original di-electron mass, without bremsstrahlung recovery, does not lie in the regions $2.90 < m_{\ell\ell} < 3.20$ GeV/c^2 and $3.60 < m_{\ell\ell} < 3.75$ GeV/c^2.

3.3.2 Vetoes against $B \to D\pi$ backgrounds

Since hadrons are much more easily to be mis-identified as muons than as electrons, we only apply vetoes against $B \to D\pi$ backgrounds in the muon modes. For a total of 384 million $B\bar{B}$ events, we expect $\sim 100,000$ decays of the type $B \to D(\to K\pi)\pi$ before all signal selection requirements. If both pions are mis-identified as muons, decays of this type will satisfy our selection requirements and peak in the signal region for the $K\mu^+\mu^-$ modes. Similarly, a decay $B \to D(\to K^*\pi)\pi$ could peak in the signal region for the $K^*\mu^+\mu^-$ modes. For the $K^+\mu^+\mu^-$ mode, there may also be a background coming from events when a charged kaon and an opposite-sign pion are mis-identified as muons and the remaining pion is mis-identified as a kaon.

To veto these decays by construction, the $K^{\pm}$, K^{*0}, or $K^{*\pm}$ candidate 4-momentum is combined with a muon candidate 4-momentum whose charge is consistent with the appropriate D decay. The invariant mass of the $K^{(*)}\mu$ system is calculated assuming the muon is a pion, and the event is vetoed if the mass lies between 1.84 and 1.90 GeV/c^2. In the $K^+\mu^+\mu^-$ mode, the event is also vetoed if the invariant mass of the $\mu^+\mu^-$ pair, with one muon assumed to be a kaon and the other a pion, is consistent

with a D decay. This vetoes the background with all three decay products being mis-identified.

3.4   Continuum and $B\overline{B}$ Background Suppression

The random combinatorial background events are those which do not peak in the m_{ES} distribution. They originate either from continuum events, in which light u, d, s and c quark-antiquark pairs are produced, or from $B\overline{B}$ events. The background suppressions of $B\overline{B}$ and light quark events are treated separately using different neural networks, which are implemented in a Fortran package called JetNet 3.4 [69]. The neural networks are trained with MC simulated signal, and generic continuum and $B\overline{B}$ events, respectively. The events selected for the NN training and testing samples are required to pass the pre-selections described above. We separate the NN training and testing datasets into two bins of low and high di-lepton mass, which are divided by the J/ψ resonance. In the low-mass region below the J/ψ resonance, a further requirement of $m_{\ell\ell} > 2m_\mu$ suppresses large background contributing in the $K^* e^+ e^-$ modes near the photon pole region. However the signal events enhanced by the photon penguin contribution are also largely removed by this requirement. Therefore, in the low-mass region of each $K^* e^+ e^-$ mode, for the convenience of analyzing signal events in the pole region, another set of NNs is trained without the $m_{\ell\ell} > 2m_\mu$ requirement.

We now have at least four separate NNs trained for each of all twelve final states:

- continuum suppression in the low-mass region – for $B \to K^* e^+ e^-$, one NN includes pole region events, one NN does not;

- continuum suppression in the high-mass region;

- $B\overline{B}$ suppression in the low-mass region – for $B \to K^* e^+ e^-$, one NN includes pole region events, one NN does not;

- $B\overline{B}$ suppression in the high-mass region.

We select a set of 13 observables as signal/background discriminants for the NNs:

- The ratio of the second-to-zeroth Fox-Wolfram moments $\boldsymbol{R_2} = H_2/H_0$ [70], computed in the CM system using all charged tracks and neutral clusters in a event.

- The ratio of the second-to-zeroth Legendre moments $\boldsymbol{L_2/L_0}$, computed in the CM system using all charged tracks and neutral clusters.

- The m_{ES} of the rest of the event (ROE), $\boldsymbol{m_{ES}^{ROE}}$, computed in the laboratory frame by summing up all charged tracks and neutral clusters in each event which are not used to reconstruct the signal candidate.

- The ΔE of the rest of the event, $\boldsymbol{\Delta E^{ROE}}$, computed in the CM system from the same recoiling B candidate used in the calculation of m_{ES}^{ROE}.

- The magnitude of the total transverse vector momentum of an event $\boldsymbol{p_t}$, computed in the laboratory frame using all identified charged tracks and neutral clusters in an event.

- The Distance Of Closest Approach along the z-axis $\mathbf{DOCA(z)}$ to the primary interaction point by the di-lepton system.

- The Distance Of Closest Approach in the xy-plane $\mathbf{DOCA(xy)}$ to the primary interaction point by the di-lepton system.

- The following function of the vertex probability (vtxBprob) of the B candidate $\boldsymbol{vtx(B)}$:

$$vtx(B) = \frac{\text{acos}([\log_{10}(\text{vtxBprob}) + 10]/10)}{2\pi}$$

- The same functional form as directly above except substituting the vertex probability (vtxllprob) of the di-lepton system for $\boldsymbol{vtx(\ell\ell)}$:

$$vtx(\ell\ell) = \frac{\text{acos}([\log_{10}(\text{vtxllprob}) + 10]/10)}{2\pi}$$

- The value $\boldsymbol{\cos\theta_B}$, where θ_B is the angle between the B candidate's momentum and the z axis in the CM frame.

- The value $\boldsymbol{\cos\theta_{\text{thrust}}}$, where θ_{thrust} is the angle between the event's thrust axis [71, 72] and the z axis in the CM frame.

- The value $\boldsymbol{\cos\theta_{thr}^{ROE}}$, where $\theta_{\text{thrust}_{\text{ROE}}}$ is the angle between the ROE thrust axis (i.e., calculated with respect to all charge tracks and neutral clusters comprising the B candidate used for m_{ES}^{ROE} and ΔE^{ROE}) and the z axis in the CM frame.

- The value $\boldsymbol{\Delta\cos\theta_{\text{thrust}}}$, which is the cosine of the opening angle in the CM frame between the angles which are the arguments of $\cos\theta_{thr}^{ROE}$ and $\cos\theta_{\text{thrust}}$.

A slightly different selection of the above inputs is used for each of the four neural networks belonging to any particular final state. The assignment of input parameters to a particular NN is based on their discriminating power against background events. Table 3.2 shows the final choice of input parameters for the NNs. An example of the NN input parameters for MC simulated signal, $B\bar{B}$ and continuum events for the $B^+ \to K^+\mu^+\mu^-$ below-the-J/ψ NN training region is shown in Figure 3.6. Figure 3.7 shows the NN outputs using validation samples of MC simulated signal events and, respectively, the $B\bar{B}$ and continuum backgrounds. The normalizations of the NN output distributions are indicative of the relative numbers of signal and background events available for training each of the NNs, and do not indicate their relative signal-to-background fractions expected in the real data.
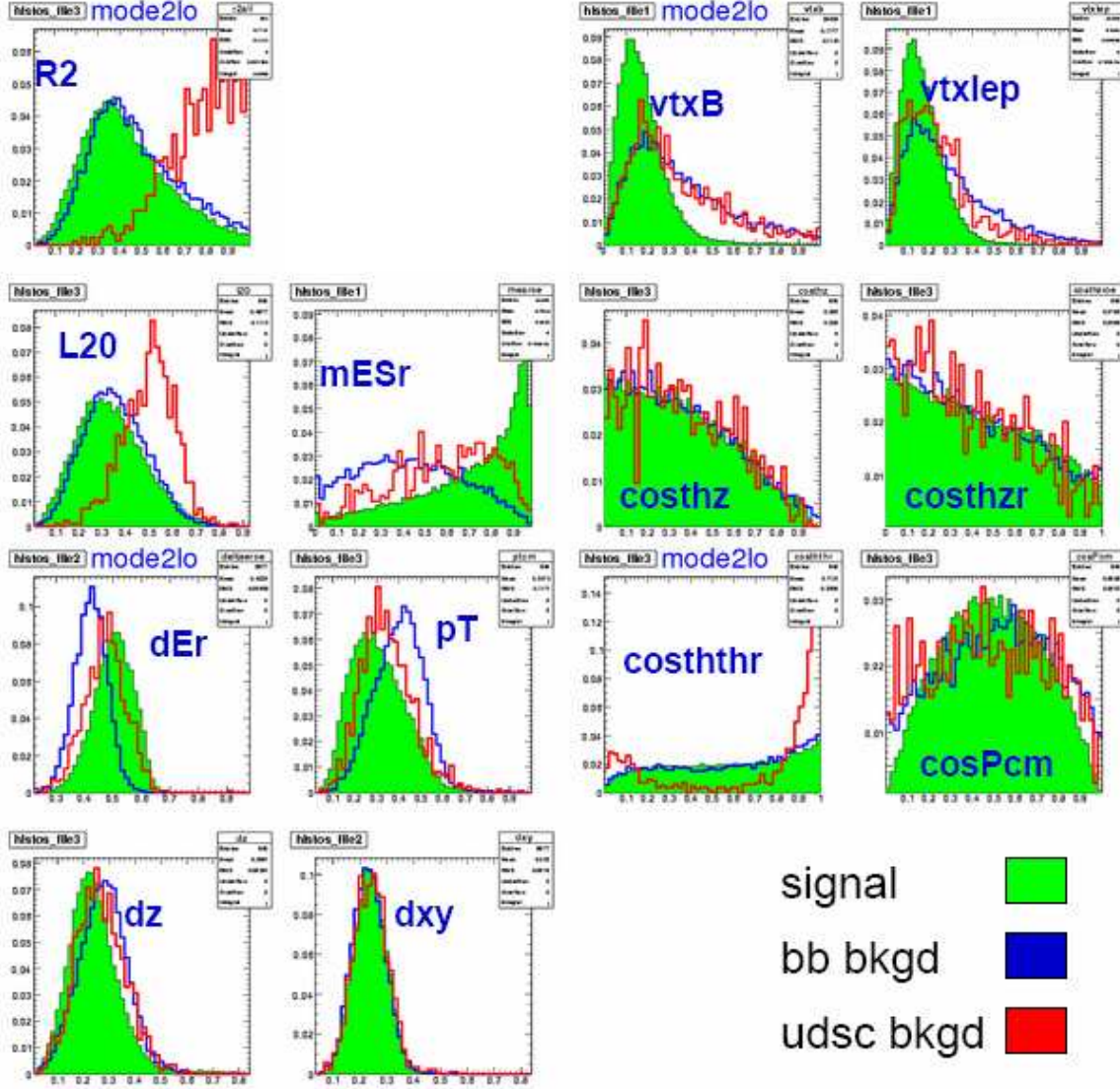
Figure 3.6: The truth-matched signal (green), generic $B\overline{B}$ (blue) and continuum (red) event distributions from MC simulation in $B^+ \to K^+\mu^+\mu^-$ low q^2 below J/ψ region are each normalized to unit area. The plot labels correspond to the following scaled NN inputs described in §3.4: R2=R_2; L20=L_2/L_0; mESr=m_{ES}^{ROE}; dEr=ΔE^{ROE}; pT=p_t; dz=DOCA(z); dxy=DOCA(xy); vtxB=$vtx(B)$; vtxlep=$vtx(\ell\ell)$; cosPcm=$\cos\theta_B$; costhz=$\cos\theta_{\mathrm{thrust}}$; costhzr=$\cos\theta_{thr}^{ROE}$; cosththr=$\Delta\cos\theta_{\mathrm{thrust}}$. The NN input normalizations are also to unit area.

Input	$B\bar{B}$ $\mu^+\mu^-$ low	high	$q\bar{q}$ $\mu^+\mu^-$ low	high	$B\bar{B}$ e^+e^- low	high	$q\bar{q}$ e^+e^- low	high
R_2			*	*			*	*
L_2/L_0			*	*			*	*
m_{ES}^{ROE}	*	*		*	*	*		*
ΔE^{ROE}	*	*		*	*	*		*
p_t	*	*		*	*	*		
DOCA(z)	*	*	*	*		*	*	*
DOCA(xy)							*	
$vtx(B)$	*	*	*	*	*	*	*	*
$vtx(\ell\ell)$	*	*	*	*	*	*	*	*
$\cos\theta_B$	*	*	*	*	*	*	*	*
$\cos\theta_{\mathrm{thrust}}$	*	*					*	*
$\cos\theta_{thr}^{ROE}$	*	*			*	*		
$\Delta\cos\theta_{\mathrm{thrust}}$		*	*	*		*	*	*
total inputs	9	10	7	10	7	9	9	10

Table 3.2: NN inputs in the order they are listed in the text. The $*$ show their assignment to particular NN classes. Abbreviations "$q\bar{q}$" for continuum, "low" for low di-lepton mass below the J/ψ resonance, "high" for high di-lepton mass above the J/ψ resonance. "e^+e^-" for electron modes, "$\mu^+\mu^-$" for muon modes.
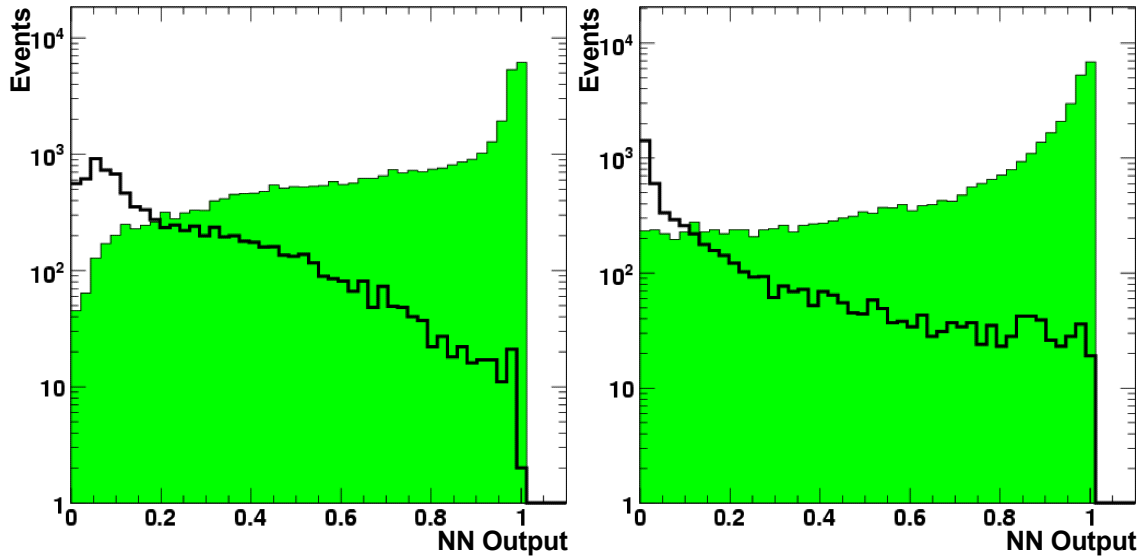
Figure 3.7: Distribution of $B\bar{B}$ (left) and continuum (right) NN outputs in $B^+ \rightarrow K^+\mu^+\mu^-$ low q^2. The black curves are for the background, and the shaded areas are for the signal.

3.5 Multiple Candidate Selection

After all selection criteria mentioned above have been applied, some events will contain more than one reconstructed B candidate in a particular mode. Typically such events will have two or three different candidates, where it is usually one (or more) of the hadrons that differs among them. The multiplicity of candidates in the K^* modes is somewhat higher than that in the K modes, reaching $\sim 20\%$ for the final states containing a π^0. We select a single candidate for each event in a particular mode (and reject all others), according to the following rules:

- For $B^+ \to K^+\ell^+\ell^-$ events, we choose the candidate with the largest number of DCH hits on the $K^\pm$ track.

- For $B^0 \to K^{*0}\ell^+\ell^-$ and $B^+ \to K^{*+}\ell^+\ell^-$ events with a K^0_S, we choose the candidate with the largest number of SVT hits on the $\pi^\pm$ track.

- For $B^+ \to K^{*+}\ell^+\ell^-$ events with a π^0, we choose the candidate with the π^0 mass closest to the nominal π^0 mass [68].

- In the very small number of cases in which application of the above rules still results in more than one candidate, or for $B^0 \to K^0_S\ell^+\ell^-$ events, we choose the first one in the candidate list for that event.

Chapter 4

The Rate and Asymmetry Measurements in $B \rightarrow K^{(*)}\ell^+\ell^-$ Decays

4.1 Measurement Goals

In this chapter the following measurements will be presented using the q^2 regions defined in Table 4.1.

- The total branching fractions (BFs) for $B \rightarrow K\ell^+\ell^-$ and $B \rightarrow K^*\ell^+\ell^-$, integrated over all q^2. To understand the role of the photon pole in $B \rightarrow K^*e^+e^-$, the latter measurement will be done with and without the photon pole included[1]. Similarly, we will measure the branching fractions in individual decay modes, as well as combined branching fractions for $B \rightarrow Ke^+e^-$, $B \rightarrow K\mu^+\mu^-$, $B \rightarrow K^*e^+e^-$, and $B \rightarrow K^*\mu^+\mu^-$.

- The partial branching fractions as a function of q^2 in different $B \rightarrow K^{(*)}\ell^+\ell^-$ modes in different q^2 regions.

- The direct CP asymmetry $\mathcal{A}_{CP}$ for the self-tagging modes $B^\pm \rightarrow K^\pm\ell^+\ell^-$ and $B \rightarrow K^*\ell^+\ell^-$, integrated over all q^2 and in q^2 regions.

- The ratios R_K and R_{K^*}. R_{K^*} determined both with and without inclusion of the pole region. R_K and R_{K^*} will be measured in q^2 regions.

- The isospin asymmetry $\mathcal{A}_I$ for $B \rightarrow K\ell^+\ell^-$ and $B \rightarrow K^*\ell^+\ell^-$ integrated over all q^2 and in q^2 regions.

4.2 Fit Model

We perform unbinned extended maximum likelihood m_{ES} fits to determine signal yields. The likelihood function for a dataset of n events is as follows:

---

[1] The all q^2 will not include the pole region, if not explicitly noted.

Region	q^2 min (GeV^2/c^4)	q^2 max (GeV^2/c^4)
Pole	**0.00**	**0.10**
Low-	**0.10**	**4.20**
Low+	**4.20**	**7.02**
J/ψ	7.02	10.24
High-	**10.24**	**12.96**
$\psi(2S)$	12.96	14.06
High+	**14.06**	$(\mathbf{m_B} - \mathbf{m_{K^{(*)}}})^2$

Table 4.1: q^2 regions (in bold) to be measured for $B \to K^{(*)}\ell^+\ell^-$ decays. The vetoed charmonium regions are listed for reference.

$$\mathcal{L} = \frac{\exp\left(-\sum_Q N^Q\right)}{n!} \prod_{i=1}^{n} \left(\sum_Q N^Q \mathcal{P}_i^Q\right) \tag{4.1}$$

where $\mathcal{P}_i^Q$ is the probability evaluated for event i with the expected yield N^Q, based on a PDF with notation Q. Q represents a certain PDF which could belong to either signal or a certain background category. These PDFs are introduced in the following sections.

4.2.1   Signal PDF

The signal m_{ES} distributions are modeled using a Gaussian PDF whose mean and width for each mode are determined from the relatively high-statistics J/ψ control samples (described in §4.5).

4.2.2   Feed-across Between Different Modes

The tight ΔE selections defined in Table 3.1 suppress the feed-up and feed-down backgrounds between $K\ell^+\ell^-$ and $K^*\ell^+\ell^-$ final states to a negligible level. There are also very small feed-across contributions between the $K^+\ell^+\ell^-$ and $K_s^0\ell^+\ell^-$ final states. However, there exist considerable feed-across backgrounds between the different $K^*\ell^+\ell^-$ final states, where typically a π^0 and π^+ are swapped in the event reconstruction. These backgrounds may be as large as $\sim 15\%$ of the correctly reconstructed signal events, with the largest effect in the high+ q^2 region. The swapped-in pion has a momentum inconsistent with that of the correctly reconstructed B decay products, thus smearing the m_{ES} distribution and producing a broad peak in the signal region. The shapes and normalizations for the feed-across PDFs are determined from signal MC simulation. The normalizations are relative to the expected signal yields,

and not absolute numbers directly taken from simulation. The functional form for these PDFs is a Crystal Ball function [73], which is based on the Gaussian PDF with a radiative tail on its low side:

$$f(x) \propto \begin{cases} \exp(-\frac{(x-\bar{x})^2}{2\sigma^2}), & \text{for } \frac{x-\bar{x}}{\sigma} > -\alpha \\ A \cdot (B - \frac{x-\bar{x}}{\sigma})^{-n}, & \text{for } \frac{x-\bar{x}}{\sigma} \leq -\alpha \end{cases} \tag{4.2}$$

where $A = \left(\frac{n}{\alpha}\right)^n \cdot \exp(-\frac{\alpha^2}{2})$, and $B = \frac{n}{\alpha} - \alpha$, $\alpha > 0$. The variables $\bar{x}$ and σ are the Gaussian mean and width, which are to be determined from fits to the simulated signal samples, along with other variables α and n.

4.2.3 Self-Crossfeed

There is also a significant component of self-crossfeed, in which a $K^*\ell^+\ell^-$ signal event gets reconstructed in the correct final state but with an incorrect final state particle. This effect is largest for the final state with $K^{*+} \to K^+\pi^0$, where the π^0 is often mis-reconstructed. As for the feed-across backgrounds, the PDFs for self-crossfeed events are also based on the Crystal Ball function and parametrized through fits to those mis-reconstructed simulated signal events.

4.2.4 Combinatorial Background PDF

An ARGUS function [74] is used to characterize the m_{ES} distribution of the random combinatorial background:

$$f(x) = N_B \cdot x\sqrt{1 - x^2}e^{-\xi(1-x^2)}, \tag{4.3}$$

where N_B is a normalization factor, $x \equiv m_{\text{ES}}/E_{\text{b}}$, E_{b} is the energy at the endpoint of the combinatorial background, ξ is the ARGUS shape parameter.

4.2.5 Fitting Strategy

The fixed and floating parameters in a one-dimensional m_{ES} fit are:

- **Fitted parameters:**

  N_S, signal yield

  N_B, combinatorial background yield

  ξ, combinatorial background ARGUS shape parameter

- **Fixed parameters:**

  Endpoint of the combinatorial background at $E_{\text{b}} = 5.29\,\text{GeV}/c^2$

  Shape of the signal Gaussian PDF from charmonium fits

  Shape of the crossfeed contributions from signal MC simulation

  Ratio of the crossfeed to signal yield from signal MC simulation

  Shape and normalization of the hadronic background (muon modes only, introduced in §4.6.1)

The results of the fits to J/ψ control samples given in §4.5.1 are used to fix the signal PDF shape parameters and to validate our method of modeling crossfeed contributions.

The package MINUIT [75] developed by CERN is used by us to perform all the fits, in which the negative logarithm likelihood (NLL) $(-\log\mathcal{L})$ is minimized. This is equivalent to the method of looking for the maximum likelihood directly.

4.3   Optimization of the Final Selections

For the events passing all the pre-selections as described in Chapter 3, we optimize the rest of event selections based on the statistical significance of the number of fitted signal events, which are obtained from ensembles of toy datasets generated and fit using the PDFs and fit methodology described in §4.2, including crossfeed contributions. We assume $B \to K\ell^+\ell^-$ and $B \to K^*\ell^+\ell^-$ branching fractions of approximately twice those found in the previous *BABAR* measurements [11], but consistent with the CDF and Belle results shown in Table 1.1 and Figure 1.3.

With the defined ΔE and hadronic mass selection in the fit region, we simultaneously optimize the $B\overline{B}$ and continuum NN event selectors in each mode and q^2 region. For $B \to K^*e^+e^-$, we separately optimize the lowest di-lepton mass range including and not including the pole region. The selections on NN outputs, which have a range from 0.0 to 1.0, are individually varied in steps of 0.1 from 0.0 to 0.6, and we generate and fit 1000 test datasets for each pair of NN selections. We do not perform our optimization with NN outputs beyond 0.6, as both the expected signal and background event numbers will be too low, and the fits to these test datasets will be subject to relatively large Poisson fluctuations. The expected statistical significance of the signal is then taken as the mean of the significance for each fit in the ensemble of 1000 datasets generated at one pair of NN selection values.

Figure 4.1 shows the variation of the expected statistical significance across the NN selection plane for $B^+ \to K^+\mu^+\mu^-$ high+ q^2 region. In that case, as the largest significance number is found at the selections of continuum NN output above 0.4, and $B\overline{B}$ NN output above 0.0, we will take this pair of NN selections as our optimal choice. The full set of optimized NN output selections are listed in Tables 4.2, 4.3 and 4.4 for different q^2 ranges in different modes.

Table 4.3 gives the expected signal significance in the data for each mode and q^2 region under the optimized NN selections. Based on the relatively low signal sensitivities in all different q^2 regions for $B^0 \to K_s^0\pi^0\mu^+\mu^-$ and $B^0 \to K_s^0\pi^0e^+e^-$, we exclude these signal modes from all subsequent analyses.

Besides optimizing NN selections, we also have considered the choice of muon selectors of different levels. Previous $B \to K^{(*)}\ell^+\ell^-$ analyses have typically adopted "Tight" or "VeryTight" muon PID selectors, with muon efficiencies $\sim 60-70\%$ and pion mis-identification rates $\sim 2-4\%$, respectively. We have re-examined this assumption by performing the event selection optimization described above on identically selected sets of simulated signal and background events, except for the muon PID list used, in $B^0 \to K_s^0\mu^+\mu^-$, $B^+ \to K^+\mu^+\mu^-$ and $B^0 \to K^+\pi^-\mu^+\mu^-$ in all different q^2 regions. Table 4.6 compares the statistical sensitivities for two muon PID selection levels, "Loose" and "Tight", and shows statistically significant gains in signal

Mode	low- $B\bar{B}$	low- $q\bar{q}$	low+ $B\bar{B}$	low+ $q\bar{q}$	high- $B\bar{B}$	high- $q\bar{q}$	high+ $B\bar{B}$	high+ $q\bar{q}$
$B^0 \to K_s^0 \mu^+ \mu^-$	0.2	0.3	0.0	0.2	0.0	0.5	0.2	0.4
$B^+ \to K^+ \mu^+ \mu^-$	0.0	0.5	0.0	0.3	0.1	0.6	0.0	0.4
$B^0 \to K_s^0 e^+ e^-$	0.2	0.4	0.1	0.5	0.0	0.6	0.1	0.4
$B^+ \to K^+ e^+ e^-$	0.0	0.2	0.1	0.6	0.0	0.2	0.0	0.4
$B^0 \to K_s^0 \pi^0 \mu^+ \mu^-$	0.2	0.1	0.0	0.5	0.6	0.1	0.4	0.4
$B^+ \to K^+ \pi^0 \mu^+ \mu^-$	0.1	0.2	0.0	0.4	0.6	0.6	0.3	0.0
$B^+ \to K_s^0 \pi^+ \mu^+ \mu^-$	0.1	0.4	0.0	0.0	0.1	0.6	0.2	0.0
$B^0 \to K^+ \pi^- \mu^+ \mu^-$	0.2	0.6	0.3	0.2	0.2	0.3	0.0	0.6
$B^0 \to K_s^0 \pi^0 e^+ e^-$	0.5	0.2	0.4	0.1	0.3	0.1	0.0	0.6
$B^+ \to K^+ \pi^0 e^+ e^-$	0.1	0.1	0.4	0.1	0.3	0.6	0.0	0.5
$B^+ \to K_s^0 \pi^+ e^+ e^-$	0.6	0.1	0.3	0.0	0.5	0.3	0.5	0.3
$B^0 \to K^+ \pi^- e^+ e^-$	0.2	0.2	0.1	0.5	0.4	0.3	0.5	0.0

Table 4.2: Optimized $B\bar{B}$ and continuum ($q\bar{q}$) NN output selections for low-, low+, high- and high+ q^2 in each mode. Events with NN outputs greater than the listed values are retained. The smallest value of NN output is 0.0 and a table entry of 0.0 indicates no NN output requirement is imposed.

Mode	pole + low- $B\bar{B}$	pole + low- $q\bar{q}$
$B^0 \to K_s^0 \pi^0 e^+ e^-$	0.2	0.4
$B^+ \to K^+ \pi^0 e^+ e^-$	0.5	0.5
$B^+ \to K_s^0 \pi^+ e^+ e^-$	0.5	0.6
$B^0 \to K^+ \pi^- e^+ e^-$	0.2	0.1

Table 4.3: Optimized $B\bar{B}$ and continuum ($q\bar{q}$) NN output selections for the concatenated pole + low- q^2 range in each mode. Events with NN outputs greater than the listed values are retained.

Mode	low $B\bar{B}$	low $q\bar{q}$	high $B\bar{B}$	high $q\bar{q}$
$B^0 \to K_s^0 \mu^+\mu^-$	0.1	0.5	0.2	0.4
$B^+ \to K^+ \mu^+\mu^-$	0.2	0.5	0.1	0.6
$B^0 \to K_s^0 e^+e^-$	0.2	0.4	0.3	0.5
$B^+ \to K^+ e^+e^-$	0.0	0.4	0.1	0.4
$B^0 \to K_s^0 \pi^0 \mu^+\mu^-$	0.1	0.4	0.4	0.5
$B^+ \to K^+ \pi^0 \mu^+\mu^-$	0.4	0.5	0.1	0.6
$B^+ \to K_s^0 \pi^+ \mu^+\mu^-$	0.4	0.2	0.1	0.3
$B^0 \to K^+ \pi^- \mu^+\mu^-$	0.0	0.5	0.3	0.5
$B^0 \to K_s^0 \pi^0 e^+e^-$	0.5	0.3	0.6	0.3
$B^+ \to K^+ \pi^0 e^+e^-$	0.6	0.3	0.4	0.6
$B^+ \to K_s^0 \pi^+ e^+e^-$	0.6	0.1	0.6	0.0
$B^0 \to K^+ \pi^- e^+e^-$	0.1	0.6	0.4	0.3

Table 4.4: Optimized selections on the $B\bar{B}$ and continuum ($q\bar{q}$) NN outputs in the low (concatenated low- and low+) q^2 and high (concatenated high- and high+) q^2 regions by mode integrated over all q^2 excluding pole region. Events with NN outputs greater than the listed values are retained. The smallest value of NN output is 0.0 and a table entry of 0.0 indicates no NN output requirement is imposed.

Mode	all q^2	low- q^2	low+ q^2	high- q^2	high+ q^2	low- q^2 w/ pole
$B^0 \to K_s^0 \mu^+\mu^-$	2.7	1.2	1.2	1.2	1.4	—
$B^+ \to K^+ \mu^+\mu^-$	4.1	1.7	1.8	2.0	2.2	—
$B^0 \to K_s^0 e^+e^-$	3.3	1.9	1.3	1.1	1.5	—
$B^+ \to K^+ e^+e^-$	5.3	3.0	2.1	2.1	2.8	—
$B^0 \to K_s^0 \pi^0 \mu^+\mu^-$	0.9	0.5	0.4	0.5	0.6	—
$B^+ \to K^+ \pi^0 \mu^+\mu^-$	1.6	0.7	0.6	0.8	0.9	—
$B^+ \to K_s^0 \pi^+ \mu^+\mu^-$	1.9	0.9	0.7	1.0	1.0	—
$B^0 \to K^+ \pi^- \mu^+\mu^-$	4.1	1.7	1.5	2.0	2.4	—
$B^0 \to K_s^0 \pi^0 e^+e^-$	1.3	0.8	0.5	0.6	0.7	1.1
$B^+ \to K^+ \pi^0 e^+e^-$	2.2	1.2	0.8	1.0	1.2	1.7
$B^+ \to K_s^0 \pi^+ e^+e^-$	2.5	1.5	0.8	0.9	1.3	2.1
$B^0 \to K^+ \pi^- e^+e^-$	4.8	2.7	1.7	2.2	2.4	3.9

Table 4.5: Expected signal significance (σ) by mode and q^2 region. The rightmost column in the table is for the pole included low- q^2 region.

sensitivity for almost all modes and q^2 regions from using "Loose" muon selector.

The obvious offset to the increase in statistical sensitivity is an increased systematic effect due to the peaking contribution from hadronic backgrounds associated with the increased pion mis-identification rate. Anticipating the results of §4.6.1, although the peaking contribution is indeed greater with the looser muon selection, the expected peaking contribution rates are still generally less than one event and much lower than the expected signal yields, which indicates that the overall systematic uncertainties will not be significantly enhanced.

4.4 Final Selection Efficiencies

Table 4.7 shows the reconstruction efficiency of signal events in each mode and q^2 region after all the event selections. As indicated in §2.3.2, simulated signal events are numerous. Thus, the statistical error of the signal efficiencies listed in the table is relatively small and not listed. All efficiency estimates are validated using charmonium control samples, as described in the next section.
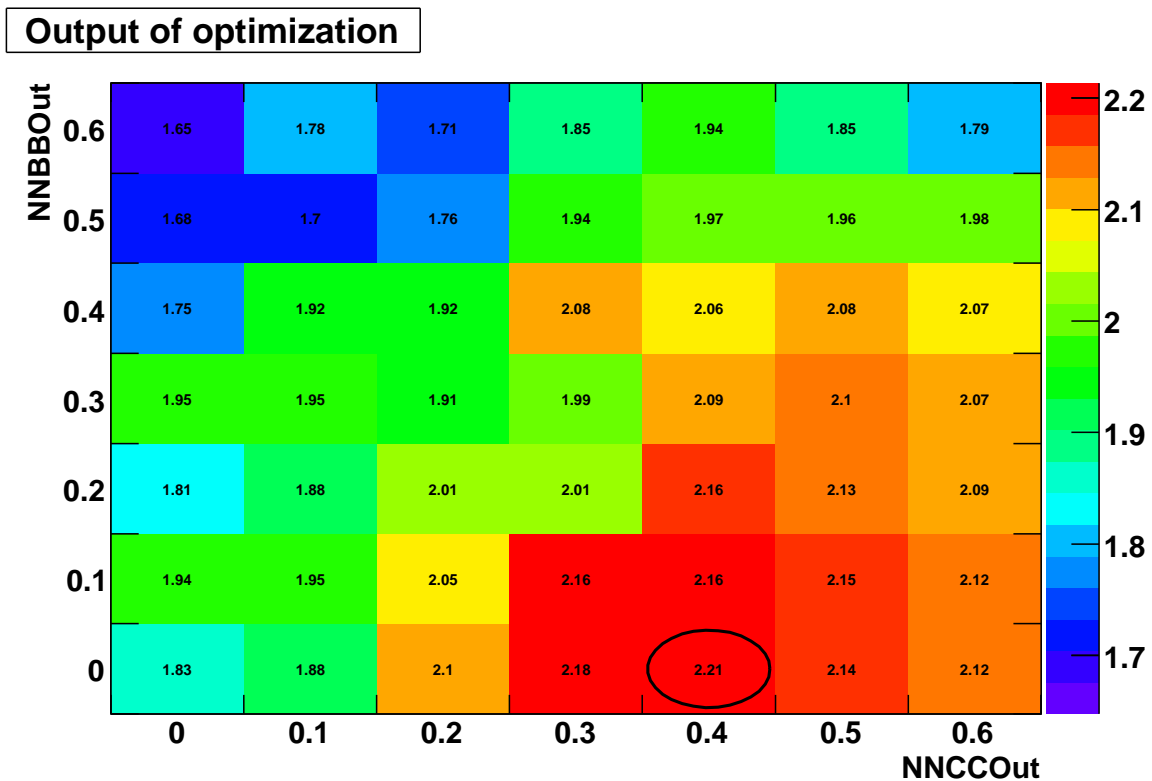
Figure 4.1: Expected statistical significance of the number of fit signal events as a function of the selections on the $B\overline{B}$ NN output NNBBOut and continuum NN output NNCCOut for $B^+ \to K^+ \mu^+ \mu^-$ high+ q^2 region.

Mode	q^2 region	"Loose" Significance	"Tight" Significance
$B^0 \to K_s^0 \mu^+\mu^-$	low-	1.2	1.0
	low+	1.2	0.9
	high-	1.2	1.1
	high+	1.4	1.3
$B^+ \to K^+\mu^+\mu^-$	low-	1.7	1.7
	low+	1.8	1.5
	high-	2.0	2.0
	high+	2.2	2.4
$B^0 \to K^+\pi^-\mu^+\mu^-$	low-	1.7	1.6
	low+	1.5	1.2
	high-	2.0	1.8
	high+	2.4	2.1

Table 4.6: Expected signal significance (σ) for "Loose" and "Tight" muon PID selectors in three muon modes.

Mode	Reconstruction Efficiency (%)			
	low-	low+	high-	high+
$B^0 \to K_s^0 \mu^+\mu^-$	13.4	20.2	19.9	17.3
$B^+ \to K^+\mu^+\mu^-$	11.1	18.8	20.0	21.1
$B^0 \to K_s^0 e^+e^-$	20.3	23.6	17.8	18.7
$B^+ \to K^+ e^+e^-$	22.3	21.1	21.1	22.6
$B^+ \to K^+\pi^0\mu^+\mu^-$	4.2	5.6	5.0	6.2
$B^+ \to K_s^0\pi^+\mu^+\mu^-$	6.0	9.1	8.0	8.6
$B^0 \to K^+\pi^-\mu^+\mu^-$	5.9	10.4	12.6	12.3
$B^+ \to K^+\pi^0 e^+e^-$	8.1	7.3	5.5	6.4
$B^+ \to K_s^0\pi^+ e^+e^-$	9.6	11.4	7.0	7.6
$B^0 \to K^+\pi^- e^+e^-$	13.4	13.8	10.8	12.9

Table 4.7: Final reconstruction efficiency for signal events by mode and q^2 region.

Mode	J/ψ BF (10^{-3})	Stat Err (10^{-3})	Discrepancy (σ)
$B^0 \to K^0_S \mu^+\mu^-$	0.886	0.026	0.3
$B^+ \to K^+ \mu^+\mu^-$	1.014	0.021	0.2
$B^0 \to K^0_S e^+e^-$	0.873	0.025	0.0
$B^+ \to K^+ e^+e^-$	1.017	0.020	0.2
$B^+ \to K^+\pi^0 \mu^+\mu^-$	1.401	0.054	-0.1
$B^+ \to K^0_S\pi^+ \mu^+\mu^-$	1.396	0.057	-0.1
$B^0 \to K^+\pi^- \mu^+\mu^-$	1.276	0.032	-0.8
$B^+ \to K^+\pi^0 e^+e^-$	1.494	0.056	0.9
$B^+ \to K^0_S\pi^+ e^+e^-$	1.432	0.055	0.2
$B^0 \to K^+\pi^- e^+e^-$	1.353	0.033	0.3

Table 4.8: J/ψ BF measured in different final states. The world average BF values for $B^+ \to K^0 J/\psi(\to \ell^+\ell^-)$, $B^+ \to K^+ J/\psi(\to \ell^+\ell^-)$, $B^0 \to K^{*0} J/\psi(\to \ell^+\ell^-)$ and $B^+ \to K^{*+} J/\psi(\to \ell^+\ell^-)$ are $(0.872 \pm 0.033, 1.008 \pm 0.035, 1.33 \pm 0.06, 1.41 \pm 0.08) \times 10^{-3}$, respectively [68]. The "Discrepancy" column shows in each mode the signed difference between our BF result and the world average value, normalized to the sum in quadrature of the statistical error from the fit and the error of the world average.

4.5 Charmonium Control Samples

4.5.1 J/ψ Control Sample Fits

We analyze the relatively large number of signal-like events in the data removed by the J/ψ vetoes in order to calibrate the signal m_{ES} PDFs and validate other aspects of the fit methodology. A J/ψ control sample for any particular mode is constructed by selecting events which are in the fit region and satisfy all other event selection criteria given in Chapter 3 except that they fail the J/ψ veto described in §3.3.1. The full fit model described in §4.2 is used to perform fits to this dataset: a Gaussian PDF for the J/ψ signal m_{ES} distribution, an ARGUS PDF for random combinatorial background, and PDFs modeling self-crossfeed and feed-across events between the different J/ψ modes. The crossfeed fit components are modeled using shapes and normalizations obtained from exclusive J/ψ MC simulated samples. The expected magnitudes of crossfeed backgrounds in most of the final state modes are negligible, while only in $B^+ \to K^+\pi^0 \mu^+\mu^-$ and $B^+ \to K^+\pi^0 e^+e^-$ modes, the crossfeed contribution can be higher than a few percent of correctly reconstructed signal events.

Table 4.8 gives the measured J/ψ BFs for different sets of NN selections used in high-q^2 region and for each mode, along with the statistical error and a numerical comparison with the world averages for these BF values [68]. We find good agreement within 1σ across all sets of selections and final states. Figure 4.2 shows m_{ES} fit with NN selections used in high-q^2 region for mode $B^+ \to K^+\pi^0 e^+e^-$, as the mode with the highest rate of crossfeed contribution.

Table 4.9 tabulates the fit shape parameters for the J/ψ signal m_{ES} PDFs by mode.
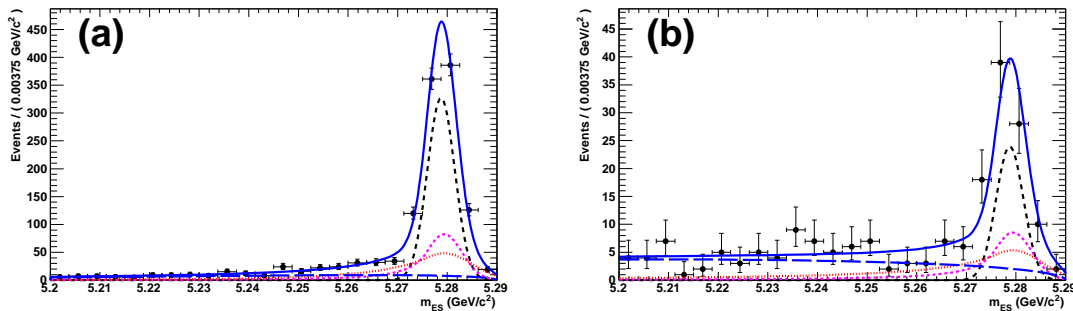
Figure 4.2: m_{ES} distributions in the (a) $B^+ \to J/\psi(\to e^+e^-)K^*(\to K^+\pi^0)$ data sample (after applying the NN selections in high- q^2 region) and (b) $B^+ \to \psi(2S)(\to e^+e^-)K^*(\to K^+\pi^0)$ data sample (after applying the NN selections in high+ q^2 region), with fits overlaid. The data points are shown along with total fit (solid), signal (medium dash), combinatorial (long dash), self-crossfeed (short dash) and feed-across (dots) background components superimposed.

There are small, but statistically significant, variations in the fit shape parameters of the signal m_{ES} PDF across modes, but there are no significant variations in the shape across the various sets of NN selections for any single mode. The table, therefore, gives the average values of the signal Gaussian mean and sigma for the J/ψ fits with different sets of NN selections from four regions of q^2 for each mode, along with the largest errors on the fit mean and sigma among these four individual fits entering into the average for any mode. These errors will be used as a source of systematic uncertainties for the signal PDFs.

4.5.2 $\psi(2S)$ Control Sample Fits

We select events and fit for the $\psi(2S)$ BF in a manner analogous to that for the J/ψ datasets above, except we use only the NN selections for the high+ q^2 region. An example fit plot for mode $B^+ \to K^+\pi^0 e^+e^-$ is given in Figure 4.2. Table 4.10 shows the BF results of these fits compared to the world averages [68]. Again we find good agreement for our measured $\psi(2S)$ BFs, with the largest discrepancy at 1.1σ.

4.5.3   Efficiency Corrections Using J/ψ Control Samples

In addition to providing validation of the event selection by reproducing well-characterized measurements and comparing our results to world averages, the large charmonium dataset is used to calibrate signal reconstruction efficiencies obtained from simulated events. For each final state, we fit vetoed J/ψ events in order to establish data-driven corrections to simulated efficiencies for each of the following: PID for leptons, K^+ and π^+; each pair ($B\bar{B}$ and continuum) of NN output selections; and the kinematic event selection parameters.

The general method is the same for all variations: a sample of data and MC simulated J/ψ events are selected using selection criteria relaxed in the relevant parameter, while all other event selection criteria are applied. Data and MC efficiencies are then

Mode	Gaussian Mean (GeV/c^2)	Gaussian Sigma (MeV/c^2)
$B^0 \to K_s^0 \mu^+ \mu^-$	5.27917 ± 0.00007	2.477 ± 0.047
$B^+ \to K^+ \mu^+ \mu^-$	5.27881 ± 0.00004	2.567 ± 0.028
$B^0 \to K_s^0 e^+ e^-$	5.27918 ± 0.00006	2.622 ± 0.048
$B^+ \to K^+ e^+ e^-$	5.27878 ± 0.00004	2.718 ± 0.027
$B^+ \to K^+ \pi^0 \mu^+ \mu^-$	5.27884 ± 0.00015	2.766 ± 0.122
$B^+ \to K_s^0 \pi^+ \mu^+ \mu^-$	5.27864 ± 0.00013	2.571 ± 0.108
$B^0 \to K^+ \pi^- \mu^+ \mu^-$	5.27918 ± 0.00005	2.504 ± 0.041
$B^+ \to K^+ \pi^0 e^+ e^-$	5.27875 ± 0.00015	2.763 ± 0.121
$B^+ \to K_s^0 \pi^+ e^+ e^-$	5.27883 ± 0.00012	2.586 ± 0.098
$B^0 \to K^+ \pi^- e^+ e^-$	5.27926 ± 0.00005	2.629 ± 0.042

Table 4.9: J/ψ m_{ES} Gaussian PDF shape parameters by mode.

Mode	$\psi(2S)$ BF (10^{-3})	Stat Err (10^{-3})	Discrepancy (σ)
$B^0 \to K_s^0 \mu^+ \mu^-$	0.600	0.085	-0.2
$B^+ \to K^+ \mu^+ \mu^-$	0.607	0.073	-0.5
$B^0 \to K_s^0 e^+ e^-$	0.593	0.057	-0.3
$B^+ \to K^+ e^+ e^-$	0.706	0.037	1.1
$B^+ \to K^+ \pi^0 \mu^+ \mu^-$	0.761	0.132	0.5
$B^+ \to K_s^0 \pi^+ \mu^+ \mu^-$	0.610	0.118	-0.3
$B^0 \to K^+ \pi^- \mu^+ \mu^-$	0.724	0.097	0.0
$B^+ \to K^+ \pi^0 e^+ e^-$	0.749	0.094	0.5
$B^+ \to K_s^0 \pi^+ e^+ e^-$	0.716	0.117	0.3
$B^0 \to K^+ \pi^- e^+ e^-$	0.708	0.058	-0.1

Table 4.10: $\psi(2S)$ BF by mode. The world averages for $B^+ \to K^0 \psi(2S)(\to \ell^+ \ell^-)$, $B^+ \to K^+ \psi(2S)(\to \ell^+ \ell^-)$, $B^0 \to K^{*0} \psi(2S)(\to \ell^+ \ell^-)$ and $B^+ \to K^{*+} \psi(2S)(\to \ell^+ \ell^-)$ are $(0.62 \pm 0.06, 0.648 \pm 0.035, 0.72 \pm 0.08, 0.67 \pm 0.14) \times 10^{-3}$, respectively [68]. The "Discrepancy" column shows in each mode the signed difference between our BF result and the world average value, normalized to the sum in quadrature of the statistical error from the fit and the error of the world average.

Mode	CP state	Data Eff.	MC Eff.	Corr. = (Data/MC) (%)
$B^+ \rightarrow K^+\mu^+\mu^-$	-,+	83.1 ± 0.5	82.8 ± 0.0	100.3 ± 0.6
	-	83.5 ± 0.7	82.8 ± 0.0	100.9 ± 0.8
	+	82.4 ± 0.7	82.8 ± 0.0	99.5 ± 0.8
$B^+ \rightarrow K^+e^+e^-$	-,+	83.1 ± 0.5	82.4 ± 0.0	100.8 ± 0.6
	-	82.9 ± 0.7	82.4 ± 0.0	100.6 ± 0.8
	+	83.2 ± 0.7	82.4 ± 0.0	101.0 ± 0.8

Table 4.11: Kaon PID efficiency corrections by lepton mode and CP state.

computed as the ratio of the yield of events (N^{pass}) passing the selection actually used in the analysis to the sum of N^{pass} and the yield of events (N^{fail}) failing the selection. The sum $N^{pass} + N^{fail}$ is equivalent to the total yield of events N^{total} before the selection. They are considered separately so as to avoid the correlation between the uncertainties of N^{pass} and N^{total} in the efficiency uncertainty calculation. The different event selections are described in detail below. The efficiency correction is taken as the ratio of data/MC efficiencies. The use of the results below in correcting efficiencies and in characterizing systematic effects is discussed in §4.8.

Hadron PID

The identification of $K^\pm$ is removed in both data and MC simulated $J/\psi K^\pm$ samples. Each sample is divided into two non-overlapping datasets, one where the $K^\pm$ candidate passes the kaon PID selection and another where it fails. The efficiency is then calculated as $\epsilon_{K^\pm} = N^{pass}_{K^\pm}/(N^{pass}_{K^\pm} + N^{fail}_{K^\pm})$. Signal MC efficiencies are calculated by directly counting the numbers of events, data efficiencies are computed with fits performed using the full methodology described earlier in this chapter. Efficiencies are computed separately for di-lepton and di-muon events. Table 4.11 shows the efficiencies in data and MC simulation, along with the data/MC ratios. This ratios will be used to correct the estimated signal efficiencies obtained using the simulated signal events. A systematic error will be assigned based on the error in the correction for each mode. We additionally divide $K^\pm$ candidates by charge and compute corrections using the same method. Where applicable, K^+ and K^- efficiencies will be separately corrected by the charge-specific ratios for different CP eigenstates and a systematic uncertainty is assigned using the errors on the ratios.

Charged pion efficiencies are corrected in a similar manner using the $J/\psi K^{*0}(\rightarrow K^+\pi^-)$ final state. Corrections and systematics will be applied for pions similarly to kaons. Only pions directly from K^* decays will be corrected. Pions from K^0_S are treated as part of the K^0_S systematics.

Mode	CP state	Data Eff.	MC Eff.	Corr. = (Data/MC) (%)
$B^0 \to K^+\pi^-\mu^+\mu^-$	-,+	99.3 ± 0.2	99.3 ± 0.0	99.9 ± 0.2
	-	99.1 ± 0.3	99.3 ± 0.0	99.7 ± 0.3
	+	99.6 ± 0.3	99.3 ± 0.0	100.3 ± 0.3
$B^0 \to K^+\pi^-e^+e^-$	-,+	99.5 ± 0.1	99.3 ± 0.0	100.1 ± 0.1
	-	99.5 ± 0.2	99.3 ± 0.0	100.1 ± 0.2
	+	99.5 ± 0.2	99.3 ± 0.0	100.2 ± 0.2

Table 4.12: Pion PID efficiency corrections by lepton mode and CP state.

Mode	Data Eff. (%)	MC Eff. (%)	Corr. = (Data/MC)² (%)
$B^+ \to K^+\mu^+\mu^-$	76.6 ± 0.4	77.9 ± 0.0	96.7 ± 1.0
$B^+ \to K^+e^+e^-$	92.0 ± 0.3	92.6 ± 0.0	98.7 ± 0.7

Table 4.13: Lepton efficiency corrections by lepton mode.

Lepton PID

These corrections are obtained in the same manner as for $K^\pm$, using $J/\psi K^\pm$ control samples in the data and comparing the result with the same measurement performed for exclusive charmonium samples in MC simulation. However, because the leptons in the di-lepton system are always treated together, there is a slightly different expression for the efficiency calculation. Separately for muons and electrons, we define three non-overlapping samples:

- LL: Both leptons pass lepton PID;

- TL: ℓ^- passes lepton PID, ℓ^+ fails;

- LT: ℓ^- fails lepton PID, ℓ^+ passes.

The lepton efficiency is calculated as

$$\epsilon = \frac{2 * N_{\text{LL}}}{2 * N_{\text{LL}} + N_{\text{TL}} + N_{\text{LT}}}, \tag{4.4}$$

where N_{LL}, N_{TL} and N_{LT} are the signal yields of the corresponding samples.

The efficiency ϵ is then for one lepton candidate, with the overall correction being the square of that for the di-lepton final states here. The simulated efficiency is corrected by the square of the data/MC ratio, with the systematic error taken as the error on the correction. The efficiency corrections and associated systematic errors are given in Table 4.13.

NN Event Selection

The correction on NN selection is obtained in a similar fashion as that for the PID corrections by measuring the efficiency of the NN selection in charmonium control samples and comparing the result with the same measurement performed for signal charmonium samples in the MC simulation. The relaxed event selection here is to remove all NN selections. Table 4.14 gives the correction with error for the individual NN selections used in each mode and q^2 region.

Kinematic Event Selection

Following the same procedures as above, a correction is obtained from measuring the efficiency of the selection on the kinematic quantities ΔE and $m_{K\pi}$ in charmonium control samples and comparing the result with the same measurement performed for the simulated signal charmonium samples. The relaxed event selection here selects events with $m_{\rm ES} > 5.2\,{\rm GeV}/c^2$, $|\Delta E| < 0.25\,{\rm GeV}$ and, for K^* final states, $0.7 < m_{K\pi} < 1.1\,{\rm GeV}/c^2$. By opening up the ΔE window, we also characterize the level at which crossfeed components in the data are mis-modeled in the simulation, and hence these corrections will account for that systematic effect in addition to purely kinematic event selection biases. Table 4.15 gives the corrections with error for the individual modes and q^2 regions. Only two (low and high) q^2 regions are used here for each mode, as the ΔE windows are only different for events with di-lepton mass below and above the J/ψ resonance (see Table 3.1).

4.6   Estimation of the Hadronic and Peaking Backgrounds

4.6.1   Hadronic Backgrounds

The hadronic background arises from hadronic B meson decays where both lepton candidates are actually hadrons. For example, the decay $B^\pm \to K^\pm \pi^+ \pi^-$ is a background to $B^+ \to K^+ \mu^+ \mu^-$ when both pions are mis-identified as muons. Only muon modes have a non-trivial background of this type, as electrons have a much lower hadron mis-identification rate compared to muon, which suppresses this background to a negligible level.

These backgrounds are estimated using a control sample of hadronic B decays collected in the 349 fb^{-1} BABAR data. A dedicated event selection is used, which is based on our baseline event selection except for the absence of muon PID. The final sample of these background events is selected by imposing requirements identical to that of signal candidates in each mode and q^2 region, except that the muon identification requirements have been removed from one of the lepton candidates. This results in a large sample of predominantly hadronic B decays. Each event is weighted by the product of the mis-identification rates for a hadron to produce each "muon" candidate, that is estimated using the PID look-up tables appropriate to the dataset here. A weighted distribution in $m_{\rm ES}$ is thus obtained. Separately parameterized for

Mode	NN selections	Data Eff. (%)	MC Eff. (%)	Corr. = (Data/MC) (%)
$B^0 \to K_s^0 \mu^+ \mu^-$	low-	88.5 ± 0.9	90.0 ± 0.0	98.3 ± 1.0
	low+	96.3 ± 0.6	96.9 ± 0.0	99.4 ± 0.6
	high-	89.7 ± 0.9	91.1 ± 0.0	98.4 ± 1.0
	high+	90.0 ± 0.9	90.3 ± 0.0	99.6 ± 1.0
$B^+ \to K^+ \mu^+ \mu^-$	low-	89.1 ± 0.5	90.1 ± 0.0	98.9 ± 0.5
	low+	93.9 ± 0.4	94.6 ± 0.0	99.2 ± 0.4
	high-	84.8 ± 0.6	86.0 ± 0.0	98.6 ± 0.7
	high+	91.9 ± 0.4	93.1 ± 0.0	98.7 ± 0.5
$B^0 \to K_s^0 e^+ e^-$	low-	91.0 ± 0.7	90.4 ± 0.0	100.6 ± 0.7
	low+	91.1 ± 0.7	91.0 ± 0.0	100.1 ± 0.7
	high-	88.6 ± 0.8	87.3 ± 0.0	101.4 ± 0.9
	high+	93.3 ± 0.6	92.3 ± 0.0	101.1 ± 0.6
$B^+ \to K^+ e^+ e^-$	low-	97.0 ± 0.2	97.2 ± 0.0	99.7 ± 0.2
	low+	84.7 ± 0.5	84.9 ± 0.0	99.7 ± 0.5
	high-	96.5 ± 0.2	96.8 ± 0.0	99.7 ± 0.2
	high+	92.0 ± 0.3	92.2 ± 0.0	99.9 ± 0.4
$B^+ \to K^+ \pi^0 \mu^+ \mu^-$	low-	92.9 ± 1.0	93.6 ± 0.1	99.3 ± 1.0
	low+	89.1 ± 1.2	90.0 ± 0.1	99.0 ± 1.3
	high-	67.9 ± 1.8	66.0 ± 0.1	102.9 ± 2.7
	high+	88.1 ± 1.3	85.5 ± 0.1	103.0 ± 1.5
$B^+ \to K_s^0 \pi^+ \mu^+ \mu^-$	low-	88.9 ± 1.3	89.9 ± 0.1	98.9 ± 1.4
	low+	100.0 ± 0.0	100.0 ± 0.0	100.0 ± 0.0
	high-	84.4 ± 1.5	86.0 ± 0.1	98.1 ± 1.7
	high+	91.9 ± 1.1	92.7 ± 0.0	99.1 ± 1.2
$B^0 \to K^+ \pi^- \mu^+ \mu^-$	low-	77.6 ± 0.9	79.9 ± 0.1	97.1 ± 1.2
	low+	82.8 ± 0.9	86.2 ± 0.1	96.1 ± 1.0
	high-	88.2 ± 0.7	88.7 ± 0.0	99.4 ± 0.8
	high+	86.2 ± 0.8	87.1 ± 0.1	99.0 ± 0.9
$B^+ \to K^+ \pi^0 e^+ e^-$	low-	96.5 ± 0.5	96.4 ± 0.0	100.2 ± 0.6
	low+	81.8 ± 1.1	82.4 ± 0.1	99.2 ± 1.3
	high-	64.6 ± 1.3	65.7 ± 0.1	98.3 ± 2.0
	high+	76.1 ± 1.2	76.2 ± 0.1	99.8 ± 1.5
$B^+ \to K_s^0 \pi^+ e^+ e^-$	low-	72.7 ± 1.5	74.0 ± 0.1	98.2 ± 2.0
	low+	87.6 ± 1.1	90.2 ± 0.0	97.2 ± 1.2
	high-	77.0 ± 1.4	76.9 ± 0.1	100.2 ± 1.8
	high+	77.0 ± 1.4	76.9 ± 0.1	100.2 ± 1.8
$B^0 \to K^+ \pi^- e^+ e^-$	low-	90.3 ± 0.5	91.7 ± 0.0	98.5 ± 0.6
	low+	87.8 ± 0.6	88.2 ± 0.0	99.5 ± 0.7
	high-	76.7 ± 0.7	76.0 ± 0.1	101.0 ± 1.0
	high+	81.1 ± 0.7	79.5 ± 0.0	102.1 ± 0.9

Table 4.14: Efficiency corrections for NN selections in different q^2 regions for different modes.

Mode	q^2 region	Data Eff. (%)	MC Eff. (%)	Corr. = (Data/MC) (%)
$B^0 \to K_s^0 \mu^+\mu^-$	low	92.2 ± 0.4	90.5 ± 0.0	101.9 ± 0.5
	high	95.0 ± 0.3	93.6 ± 0.0	101.5 ± 0.3
$B^+ \to K^+ \mu^+\mu^-$	low	89.7 ± 0.3	88.7 ± 0.0	101.1 ± 0.3
	high	93.0 ± 0.2	92.1 ± 0.0	101.0 ± 0.2
$B^0 \to K_s^0 e^+e^-$	low	83.8 ± 0.8	81.4 ± 0.0	102.9 ± 1.0
	high	87.3 ± 0.7	85.1 ± 0.0	102.5 ± 0.8
$B^+ \to K^+ e^+e^-$	low	82.5 ± 0.4	80.4 ± 0.0	102.6 ± 0.5
	high	86.4 ± 0.4	84.1 ± 0.0	102.8 ± 0.5
$B^+ \to K^+ \pi^0 \mu^+\mu^-$	low	67.0 ± 0.9	69.3 ± 0.1	96.8 ± 1.4
	high	73.2 ± 0.8	74.9 ± 0.1	97.7 ± 1.1
$B^+ \to K_s^0 \pi^+ \mu^+\mu^-$	low	77.9 ± 1.2	79.6 ± 0.1	97.9 ± 1.5
	high	80.9 ± 1.1	82.2 ± 0.1	98.4 ± 1.4
$B^0 \to K^+ \pi^- \mu^+\mu^-$	low	75.0 ± 0.8	78.9 ± 0.0	95.0 ± 1.0
	high	78.3 ± 0.7	81.6 ± 0.0	96.0 ± 0.9
$B^+ \to K^+ \pi^0 e^+e^-$	low	72.6 ± 0.7	73.2 ± 0.1	99.2 ± 1.0
	high	77.1 ± 0.7	77.7 ± 0.1	99.2 ± 0.9
$B^+ \to K_s^0 \pi^+ e^+e^-$	low	76.5 ± 1.1	77.7 ± 0.1	98.4 ± 1.5
	high	79.3 ± 1.0	81.0 ± 0.1	97.9 ± 1.3
$B^0 \to K^+ \pi^- e^+e^-$	low	74.8 ± 0.7	77.1 ± 0.0	97.0 ± 0.9
	high	77.7 ± 0.6	80.5 ± 0.0	96.6 ± 0.8

Table 4.15: Summary of the kinematic selection systematics. The definitions of "low" and "high" are the same as those in Table 3.1.

all muon modes in each q^2 region, these weighted distributions are used directly in the fits to data as histogram PDFs. For the $\mathcal{A}_{CP}$ measurements, the distributions are parameterized in the separate B and $\bar{B}$ samples.

In each mode, a sample of $K^{(*)}\mu^+h^-$ events is selected by requiring that the μ^+ candidate passes the "VeryLoose" muon PID selector, and that the μ^- candidate fails both the electron PID and "VeryLoose" muon PID selectors. The events are divided into four disjoint sub-samples:

- $K^{(*)}\pi^+\pi^-$ events, where both muon candidates fail the kaon PID;

- $K^{(*)}K^+\pi^-$ events, where the μ^+ candidate passes the kaon PID and the μ^- candidate fails the kaon PID;

- $K^{(*)}\pi^+K^-$ events, where the μ^+ candidate fails the kaon PID, and the μ^- candidate passes the kaon PID; and

- $K^{(*)}K^+K^-$ events, where both muon candidates pass the kaon PID.

For each event in each sub-sample, we define a weight

$$w(K^{(*)}\mu^+h^-) = \frac{1}{2} \times \frac{P(h^+ \to \mu^+_{NNL})}{P(h^+ \to \mu^+_{NNVL})\epsilon_{h^+}} \times \frac{P(h^- \to \mu^-_{NNL})}{\epsilon(h^-)}, \qquad (4.5)$$

where

- $P(h^\pm \to \mu^\pm_{NNL})$ is the probability for a charged hadron $h^\pm$ to be mis-identified by the "Loose" (NNL) muon PID selector;

- $P(h^+ \to \mu^+_{NNVL})$ is the probability for a positive charged hadron h^+ to be mis-identified by the "VeryLoose" ($NNVL$) muon PID selector;

- ϵ_{h^+} is the kaon PID efficiency $\epsilon_{K^+_{LH}}$ for kaons, or $1 - P(\pi^+ \to K^+_{LH})$ for pions, *i. e.*, the complement of the probability of a pion to be mis-identified by the kaon PID selector.

The efficiency $\epsilon(h^-)$ in Equation 4.5 is a product of three factors:

$$\epsilon(h^-) = (1 - P(h^- \to e^-_L)) \times (1 - P(h^- \to \mu^-_{NNL})) \times \epsilon_{h^-},$$

where

- $P(h^- \to e^-_L)$ is the probability for a negative charged hadron h^- to be mis-identified by the electron PID, and

- ϵ_{h^-} is defined as for ϵ_{h^+} except for opposite charges.

An analogous set of weights is determined for the $K^{(*)}h^+\mu^-$ sample. The factor of $\frac{1}{2}$ in the weights for both $K^{(*)}\mu^+h^-$ and $K^{(*)}h^+\mu^-$ samples is used to avoid double-counting in the background. The total hadronic background for each mode in each q^2 region is then obtained from the sum of the weighted distributions of the four disjoint $K^{(*)}\mu^+h^-$ and the four disjoint $K^{(*)}h^+\mu^-$ subsamples.
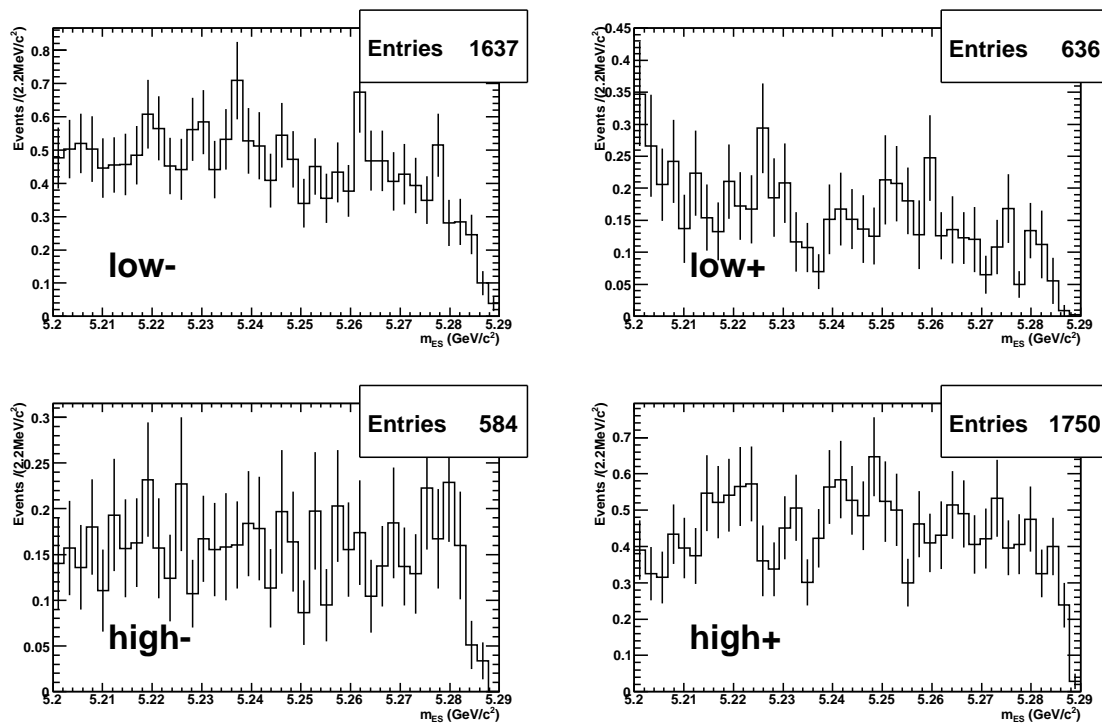
Figure 4.3: Hadronic background m_{ES} distributions in four q^2 regions of $B^0 \to K^0_S \mu^+\mu^-$ mode, expected in 349 fb^{-1} data.

In our fits, the hadronic background is modeled through binning these weighted m_{ES} distributions into histograms. Generally, a minimum of a few hundred weighted events contribute to each histogram. Figure 4.3 shows the weighted m_{ES} distributions projected into 40 bins for $B^0 \to K^0_S \mu^+\mu^-$ mode in four q^2 regions. Figure 4.4 shows the weighted m_{ES} distributions for the divided B and $\overline{B}$ datasets in the $B^+ \to K^+\mu^+\mu^-$ mode. In general, there are no substantial variations between the two CP-tagged datasets.

To estimate the number of expected peaking contribution from the hadronic background events for each mode in each q^2 region, a single Gaussian signal PDF and an ARGUS background shape are used in binned fits to the weighted m_{ES} distributions. Table 4.16 shows the averaged signal yield results from the fits to 20, 24, 28, 32, 36 and 40-bin histograms. The variation in the number of bins in the fit histograms is motivated by the not-purely-statistical nature of the weighted distributions due to the event-by-event use of the weights. These peaking contributions are only relevant for the estimation of the associated systematic effect on the final results.

4.6.2   Un-vetoed Charmonium Events

A main source of peaking backgrounds arises from charmonium events that are reconstructed outside the veto regions in the ΔE and $m_{\ell\ell}$ plane and below the lower limit on the low+ q^2 region. These contributions are determined using charmonium simulated samples. All final event selection requirements are applied to these samples and the
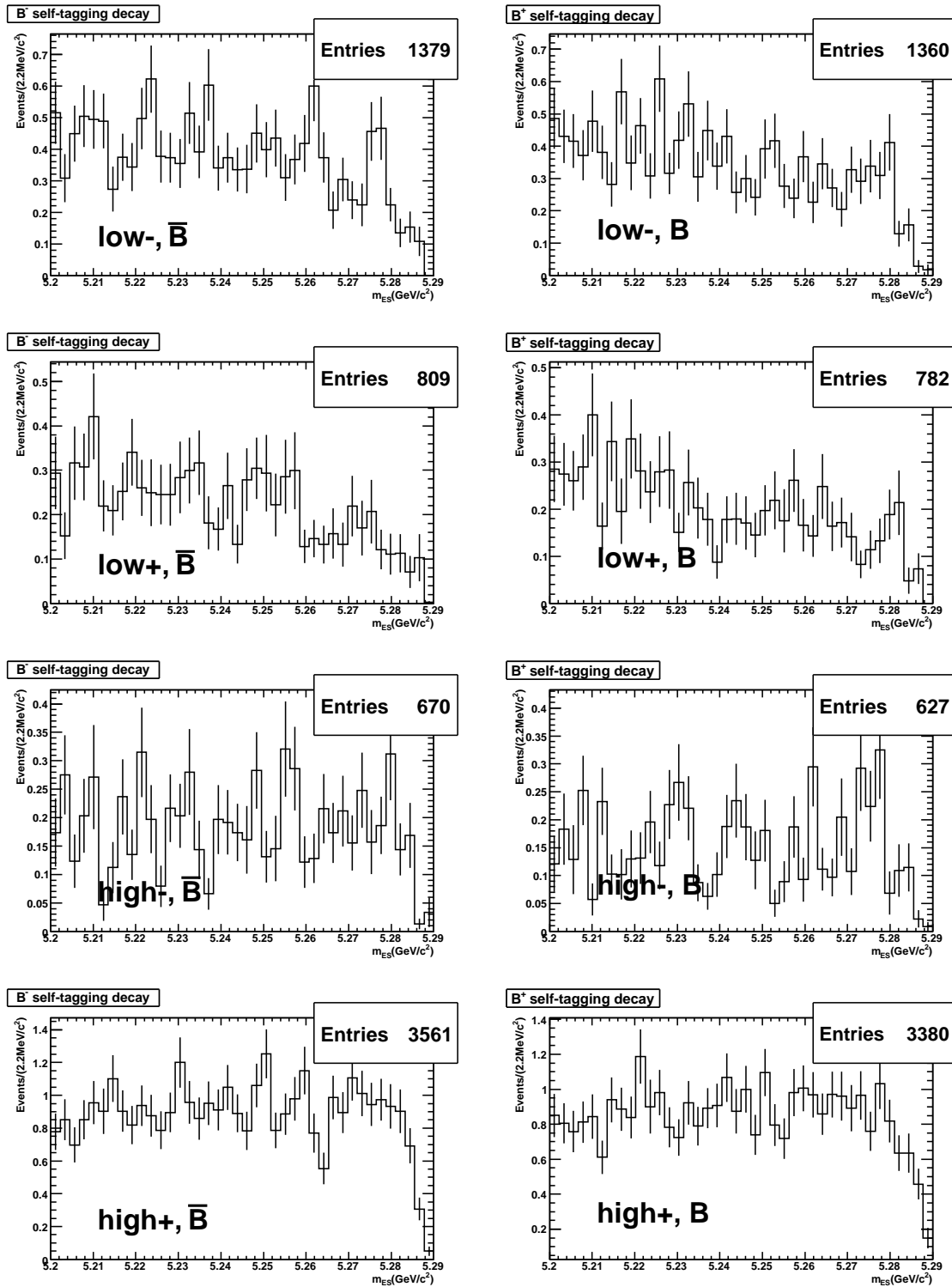
Figure 4.4: Hadronic background m_{ES} distributions for different B CP eigenstates, in four q^2 regions of $B^+ \to K^+ \mu^+ \mu^-$ mode, expected in 349 fb^{-1} data.

Mode	q^2 region	$N_{Peaking}$	(+) error	(-) error
$B^0 \rightarrow K_S^0 \mu^+\mu^-$	low-	0.42	+0.22	-0.20
	low+	0.24	+0.08	-0.08
	high-	0.32	+0.17	-0.13
	high+	0.64	+0.35	-0.37
$B^+ \rightarrow K^+ \mu^+\mu^-$	low-	0.80	+0.29	-0.25
	low+	0.42	+0.21	-0.18
	high-	0.81	+0.23	-0.22
	high+	3.14	+0.79	-0.80
$B^+ \rightarrow K^+\pi^0 \mu^+\mu^-$	low-	0.60	+0.48	-0.33
	low+	1.12	+0.36	-0.35
	high-	1.28	+0.44	-0.41
	high+	2.56	+0.94	-0.88
$B^+ \rightarrow K_S^0\pi^+ \mu^+\mu^-$	low-	1.08	+0.32	-0.32
	low+	0.39	+0.31	-0.28
	high-	0.33	+0.12	-0.14
	high+	0.34	+0.44	-0.16
$B^0 \rightarrow K^+\pi^- \mu^+\mu^-$	low-	0.46	+0.30	-0.25
	low+	0.71	+0.28	-0.28
	high-	1.75	+0.38	-0.37
	high+	1.47	+0.58	-0.61

Table 4.16: Estimated peaking contributions ($N_{Peaking}$) from the fits to the hadronic background by mode and q^2 region with "Loose" muon PID selector.

number of remaining charmonium events is determined using fits for signal-like events in the different q^2 regions. $B^+ \to K^+\mu^+\mu^-$ mode exhibits a larger background than $B^+ \to K^+e^+e^-$ mode, due to events where the kaon is mis-identified as a muon and vice versa; this is not a background for the $K^*\mu^+\mu^-$ modes, as in those cases a swap generally causes the event to fall outside the K^* mass window. The total expected contribution from this background source is less than one event in each final state and q^2 region.

4.6.3 Photon Conversions

The more copiously produced FCNC decay $B \to K^*\gamma$ will mimic $B \to K^*e^+e^-$ if the photon converts into an electron pair and subsequently escapes the conversion veto in our event selection. This rate is estimated from exclusive $B \to K^*\gamma$ simulated samples applying all final event selection requirements. The only non-trivial contributions from this background are in the pole region for $K^*e^+e^-$ modes, with the expected contribution in the 349 fb^{-1} data typically below 0.3 events. The $B^0 \to K^+\pi^-e^+e^-$ mode has the largest photon conversion contribution of ~ 1.1 events.

4.6.4 Dalitz Decays of Hadrons

There are small contributions from $B \to K^*\pi^0/\eta$, where the π^0 or η undergoes a Dalitz decay to a photon and an electron pair e^+e^-. The anticipated contribution of these backgrounds in each mode and q^2 region is well below one event.

4.6.5 Summary of Peaking Backgrounds

Table 4.17 summarizes the total contribution from all peaking background sources for each mode and q^2 region. The shapes and normalizations of these peaking backgrounds are determined from the simulated samples and fixed in fits to the 349 fb^{-1} data.

4.7 MC Experiments

In addition to validating the fit model with charmonium samples from data, in each MC experiment, we test the methodology by fitting to a simulated dataset where signal and background events are generated from appropriately normalized PDFs based on the expectations in the data sample (349 fb^{-1}). We also perform tests using an identical methodology in event generation except for signal events, which are embedded via randomly drawing events from MC simulated signal samples. For both test methods mentioned above, 1000 MC experiments are performed in each mode and q^2 region using the full fit model described in Section 4.2. The resulting distributions of the pulls of the signal yields, defined as the spread of the fitted value normalized by the fitted error, are compared to the standard normal distribution to test for fit bias. Figure 4.5 shows an example of a pull distribution of signal yields in mode $B^+ \to K_S^0\pi^+e^+e^-$ for the entire q^2 region.

Mode	pole	low-	low+	high-	high+
$B^0 \to K_S^0 \mu^+\mu^-$	—	—	—	0.13 ± 0.01	0.04 ± 0.01
$B^+ \to K^+ \mu^+\mu^-$	—	—	0.29 ± 0.03	1.02 ± 0.06	0.15 ± 0.04
$B^0 \to K_S^0 e^+e^-$	0.06 ± 0.01	0.02 ± 0.01	—	0.06 ± 0.01	0.03 ± 0.01
$B^+ \to K^+ e^+e^-$	0.21 ± 0.02	0.06 ± 0.01	—	0.56 ± 0.09	0.18 ± 0.05
$B^+ \to K^+ \pi^0 \mu^+\mu^-$	—	—	0.02 ± 0.01	0.10 ± 0.03	0.01 ± 0.01
$B^+ \to K_S^0 \pi^+ \mu^+\mu^-$	—	—	0.20 ± 0.02	0.13 ± 0.03	0.03 ± 0.01
$B^0 \to K^+ \pi^- \mu^+\mu^-$	—	—	0.43 ± 0.05	0.68 ± 0.07	0.06 ± 0.02
$B^+ \to K^+ \pi^0 e^+e^-$	0.24 ± 0.03	0.04 ± 0.01	0.02 ± 0.02	0.15 ± 0.04	0.04 ± 0.02
$B^+ \to K_S^0 \pi^+ e^+e^-$	0.27 ± 0.03	0.06 ± 0.01	—	0.05 ± 0.01	0.02 ± 0.01
$B^0 \to K^+ \pi^- e^+e^-$	1.27 ± 0.13	0.19 ± 0.03	0.01 ± 0.01	0.11 ± 0.04	0.09 ± 0.02

Table 4.17: Total peaking background contributions from all sources for each mode and q^2 region.

We have additionally examined what effect the binning in the hadronic background data distributions has on the fits. Thus, we have rerun the full set of MC experiments using a 28-bin histogram, rather than a 40-bin one, for the hadronic background PDFs. The pull distributions are compared for these two different binning choices in each muon mode, and no notable variation is observed.

Besides testing the robustness of the fit model for measuring signal decay rates, we also perform MC experiments in order to estimate the statistical sensitivity of various decay rate based observables and look for potential biases. The input values for these observables are based on the Standard Model expectations.
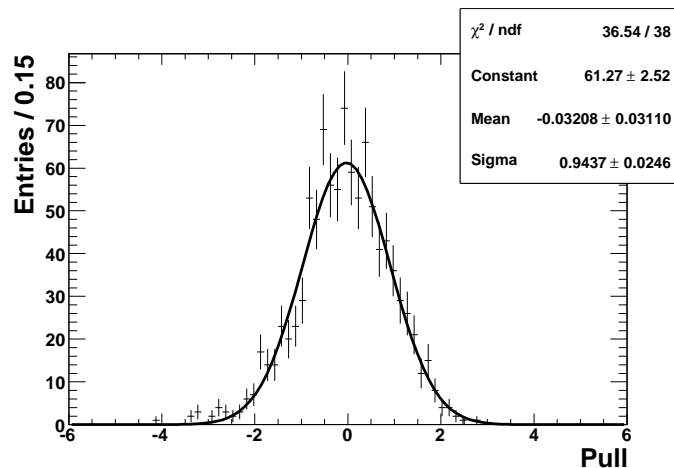
Figure 4.5: $B^+ \to K_S^0 \pi^+ e^+e^-$ signal yield pull distribution in the entire q^2 region with fit to a Gaussian function overlaid. The goodness-of-fit ($\chi^2/n.d.o.f$) and fit parameters and are shown in the text box.

For instance, the pull distributions for $\mathcal{A}_{CP}$ show significant bias in some of the modes and q^2 regions, due to limited statistics. For the $B^{\pm} \to K^{*\pm}\ell^+\ell^-$ mode shown in Figure 4.6, we observe a bias of $\sim 0.3\sigma$ in the low+ q^2 region. Therefore, we have performed another set of experiments in the concatenated low (low- & low+) and high (high- & high+) q^2 regions. Figure 4.7 indicates that the pull distributions in these two concatenated q^2 regions now behave pretty well with negligible biases.
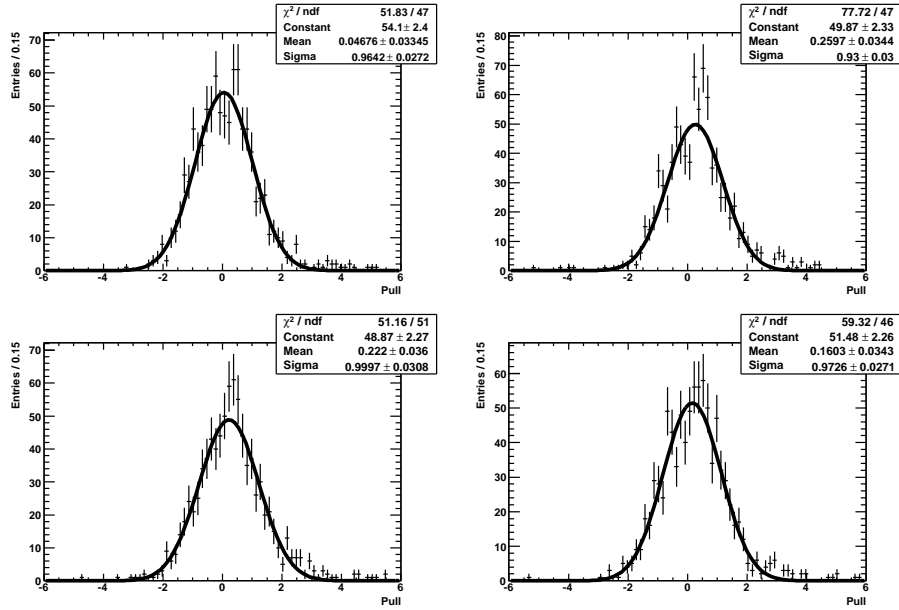
Figure 4.6: $B^{\pm} \to K^{*\pm}\ell^+\ell^-$ $\mathcal{A}_{CP}$ pull distributions in separate q^2 regions: low-, low+, high- and high+ (from top to bottom, from left to right), with fits to a Gaussian function overlaid. The goodness-of-fit ($\chi^2/n.d.o.f$) and fit parameters are shown in the text boxes. Large biases have been observed in the low+ and high- q^2 regions due to poor statistics.
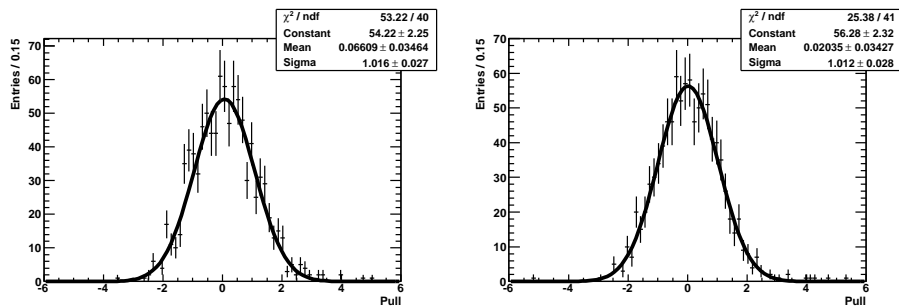
Figure 4.7: $B^{\pm} \to K^{*\pm}\ell^+\ell^-$ pull distributions in two concatenated q^2 regions: low-/low+ (left) and high-/high+ (right), with fits to a Gaussian function overlaid. The goodness-of-fit ($\chi^2/n.d.o.f$) and fit parameters are shown in the text boxes.

4.8 Systematic Errors

4.8.1 Systematic Errors for Rate Measurements

The branching fractions are calculated from the formula:

$$\mathcal{B} = \frac{N_S}{\epsilon \cdot N_{B\bar{B}}}, \tag{4.6}$$

where N_S is the signal yield obtained in a fit to data, ϵ is the signal efficiency determined from signal MC simulation, and $N_{B\bar{B}}$ is the total number of $B\bar{B}$ pairs, $(3.84 \pm 0.42) \times 10^8$.

Systematic uncertainties for the branching fractions are generally classified into multiplicative and additive uncertainties. Multiplicative uncertainties can affect how the observed signal yields are translated into rates, while additive uncertainties bias the actual measured signal yields. The total multiplicative systematic uncertainty is the sum in quadrature (except for the tracking efficiency uncertainties which are taken to be 100% correlated) of uncertainties from the following individual sources:

- Uncertainty in the tracking efficiency for leptons (**LepTrkCorr**), after applying the tracking efficiency corrections. This is a correlated uncertainty of $\pm 0.8\%$ per lepton track.

- Uncertainty in the tracking efficiency for hadron tracks (**HadTrkCorr**), including daughter pions from K_s^0's. This is a correlated uncertainty of $\pm 1.4\%$ per hadron track.

- Uncertainties in the efficiencies of the electron and muon PID (**ElecIDCorr, MuonIDCorr**). These are determined from the associated errors in the lepton PID efficiency corrections, as previously discussed in §4.5.3 and listed in Table 4.13.

- Uncertainty in the efficiencies of the kaon PID and the kaon PID veto for pions (**KaonIDCorr, PionIDCorr**). These are determined from the associated errors in the kaon and pion PID efficiency corrections, as previously discussed in §4.5.3 and listed in Tables 4.11 and 4.12.

- Uncertainty in the efficiency of K_s^0 identification as a function of flight distance (**KsDistCorr**). This is obtained from the maximum variation of mean efficiency by applying alternative parameterizations or selections for K_s^0 efficiency computation; the uncertainty is 0.9%.

- Uncertainty in the π^0 efficiency (**Pi0EffCorr**). This systematic is at 3% per π^0, which is determined through comparing the efficiencies between data and simulated π^0 samples. Because the hadronic final state with a π^0 is always used in conjunction with the other K^{*+} final state, the total contribution of this systematic uncertainty to the K^{*+} reconstruction efficiency error is $< 3\%$.

- Uncertainty in the $B\overline{B}$ counting (**BBCount**). This does not include uncertainties in the branching fraction of $\Upsilon(4S)$ to B^+B^- and $B^0\overline{B}^0$; the uncertainty is 1.1%.

- Uncertainty in the efficiency of the event selection NNs (**NNEffCorr**). This systematic effect is bounded by the measurements of the efficiency corrections, as described in §4.5.3. We will take the magnitude of the deviation from 100% for any particular mode and q^2 region given in Table 4.14 as the NN selection systematic uncertainty. If the correction is consistent with 100% within the given error, we will take the error as the systematic uncertainty.

- Uncertainty in the efficiency of the kinematic event selection (**KinemCorr**) using ΔE and, for the final states with K^*, the K^* mass window. Based on the corresponding efficiency correction as described in §4.5.3, The systematic uncertainty here is obtained using the same method as for NN selection systematics.

- Statistical uncertainties in the signal efficiencies from signal MC simulation (**MCStatEff**).

We consider additive systematic uncertainties in the fits for the signal yields arising from three sources:

- Uncertainties in the signal PDF shapes (**GaussMean, GaussWidth**) are characterized by varying the PDF Gaussian means and widths by the errors obtained in the fits to the J/ψ control samples (summarized in Table 4.9).

- Uncertainties in the contributions of hadronic backgrounds (**HadShape**) are characterized by varying the bin contents of the histogram PDFs modeling these backgrounds according to their associated error. We also perform fits with more than one choice of binning for these histogram PDFs as a qualitative cross-check, and no notable discrepancies from original results are observed.

- Uncertainties in the contributions of peaking backgrounds (**NonHadPeaks**) whose normalizations are taken from exclusive MC simulated samples are characterized by varying these normalizations by ±25%.

We also have considered the systematic effects in signal efficiencies resulting from using different theoretical models for the signal decays. These can be determined from comparing the signal efficiencies in MC simulated samples using different form factors. The previous *BABAR* measurement [11] found this type of systematic uncertainty to be negligible.

The total systematic uncertainty is then obtained by summing in quadrature the additive signal shape and peaking background uncertainties, along with the total multiplicative systematic.

Table 4.18 presents all sources of systematic uncertainties considered in the total branching fraction measurements for each individual mode.

Source	$K_s^0\mu^+\mu^-$	$K^\pm\mu^+\mu^-$	$K_s^0e^+e^-$	$K^\pm e^+e^-$	$K^{*\pm}\mu^+\mu^-$	$K^{*0}\mu^+\mu^-$	$K^{*\pm}e^+e^-$	$K^{*0}e^+e^-$
LepTrkCorr	±1.6	±1.6	±1.6	±1.6	±1.6	±1.6	±1.6	±1.6
HadTrkCorr	±2.8	±1.4	±2.8	±1.4	±3.4	±2.8	±3.0	±2.8
ElecIDCorr	—	—	±0.7	±0.7	—	—	±0.7	±0.7
MuonIDCorr	±1.0	±1.0	—	—	±1.0	±1.0	—	—
KaonIDCorr	—	±0.6	—	±0.6	±0.2	±0.6	±0.3	±0.6
PionIDCorr	—	—	—	—	±0.1	±0.2	±0.1	±0.1
KsDistCorr	±0.9	—	±0.9	—	±0.6	—	±0.5	—
Pi0EffCorr	—	—	—	—	±0.9	—	±1.3	—
BBCount	±1.1	±1.1	±1.1	±1.1	±1.1	±1.1	±1.1	±1.1
NNEffCorr	±0.0	±2.0	±1.6	±1.6	±2.0	±0.8	±2.0	±0.8
KinemCorr	±1.9	±1.1	±2.9	±2.8	±2.5	±5.0	±1.6	±3.4
MCStatEff	±0.4	±0.4	±0.4	±0.3	±0.6	±0.5	±0.7	±0.5
GaussMean	±0.6	±0.2	±9.8	±0.2	±1.5	±0.5	±0.6	±0.3
GaussWidth	±2.1	±0.6	±11.0	±0.2	±2.4	±0.2	±0.8	±0.3
HadShape	±4.2	±3.1	—	—	±4.5	±2.3	—	—
NonHadPeaks	±0.6	±2.3	±5.1	±0.8	±0.8	±0.9	±0.4	±0.4
Total Syst.	±7.0	±5.7	±16.6	±4.7	±8.2	±7.4	±5.8	±5.8

Table 4.18: Sources of systematic uncertainty (%) as percents of the measured total branching fractions in $K^{(*)}\ell^+\ell^-$ modes.

Source	$K^{\pm}\ell^+\ell^-$	$K^{*0}\ell^+\ell^-$	$K^{*\pm}\ell^+\ell^-$	$K^*\ell^+\ell^-$
KaonIDCorr	±0.008	±0.010	±0.006	±0.006
PionIDCorr	—	±0.003	±0.005	±0.003
GaussMean	±0.001	±0.002	±0.005	±0.001
GaussWidth	±0.001	±0.001	±0.012	±0.004
NonHadPeaks	±0.003	±0.001	±0.004	±0.001
HadShape	±0.008	±0.016	±0.012	±0.008
Total Syst.	±0.012	±0.019	±0.019	±0.011

Table 4.19: Sources of systematic uncertainty considered for $K^{(*)}\ell^+\ell^-$ $\mathcal{A}_{CP}$ measurements in the entire q^2 region.

4.8.2 $\mathcal{A}_{CP}$ Systematics

Most of the multiplicative systematic uncertainties in the rate measurements will be canceled out when $\mathcal{A}_{CP}$ is measured. The only notable efficiency related uncertainties are from the charge-specific corrections on $K^{\pm}$ and $\pi^{\pm}$ PID efficiencies, which have been discussed in §4.5.3. Their errors, as summarized in Table 4.11 and Table 4.12, will be used to bound the $\mathcal{A}_{CP}$ uncertainties on the efficiencies. The peaking backgrounds are major sources for the $\mathcal{A}_{CP}$ systematics in the fits. They are determined using the similar method as in the rate measurements. Table 4.19 summarizes all sources of systematic uncertainties considered in the $\mathcal{A}_{CP}$ measurements.

4.8.3 Systematics For Other Rate Asymmetries

The systematic errors in R_K and R_{K^*} are calculated by summing up in quadrature the systematic errors in muon and electron modes, while the common systematic effects canceled in the ratios, such as tracking, kaon PID, pion PID, K^0_S efficiency, and $B\overline{B}$ counting, are discarded.

For $\mathcal{A}_I$, the systematic errors are calculated by summing up in quadrature the systematic errors in B^0 and B^+ modes while excluding the common systematic effects (tracking and PID efficiencies for e and μ, $B\overline{B}$ counting).

Mode	all q^2	low q^2	high q^2	Figure
$B^0 \to K_s^0 \mu^+\mu^-$	$7.9^{+4.6}_{-4.0}$	$0.1^{+3.2}_{-2.6}$	$5.8^{+3.8}_{-3.2}$	4.8
$B^+ \to K^+ \mu^+\mu^-$	$18.8^{+7.3}_{-6.7}$	$6.5^{+4.3}_{-3.7}$	$8.9^{+6.1}_{-5.5}$	4.9
$B^0 \to K_s^0 e^+e^-$	$1.5^{+3.0}_{-2.4}$	$-1.4^{+1.7}_{-1.4}$	$4.2^{+2.8}_{-2.2}$	4.10
$B^+ \to K^+ e^+e^-$	$32.0^{+7.3}_{-6.7}$	$25.7^{+5.8}_{-5.2}$	$10.4^{+5.2}_{-4.6}$	4.11
$B^+ \to K^+ \pi^0 \mu^+\mu^-$	$6.4^{+3.4}_{-3.3}$	$4.3^{+2.9}_{-2.6}$	$5.5^{+3.1}_{-2.8}$	4.12
$B^+ \to K_s^0 \pi^+ \mu^+\mu^-$	$7.1^{+3.8}_{-3.7}$	$4.5^{+3.0}_{-2.7}$	$5.6^{+3.1}_{-2.8}$	4.12
$B^0 \to K^+ \pi^- \mu^+\mu^-$	$25.4^{+7.6}_{-7.0}$	$7.7^{+4.4}_{-3.8}$	$19.2^{+6.3}_{-5.7}$	4.13
$B^+ \to K^+ \pi^0 e^+e^-$	$7.4^{+2.5}_{-2.2}$	$10.5^{+3.1}_{-2.8}$	$1.5^{+1.7}_{-1.6}$	4.14
$B^+ \to K_s^0 \pi^+ e^+e^-$	$7.6^{+2.6}_{-2.3}$	$9.4^{+2.8}_{-2.5}$	$1.2^{+1.5}_{-1.3}$	4.14
$B^0 \to K^+ \pi^- e^+e^-$	$19.6^{+6.0}_{-5.3}$	$7.0^{+4.2}_{-3.6}$	$10.6^{+4.5}_{-4.0}$	4.15

Table 4.20: Signal yields by mode and q^2 region. The signal yields in all q^2 are not equal to the sums of the signal yields in low and high q^2 regions due to different sets of NN selections used.

4.9   Results

In the fits to data, we collect the fitted signal yields in separated q^2 regions as defined in Table 4.1 across all modes. The signal yields are generally lower than the assumed yields used in our MC experiments for testing fit biases. Thus, in the interest of preserving a high probability of performing unbiased fits, all results reported as a function of q^2 now include only the concatenated low- and low+ q^2 regions and the concatenated high- and high+ regions. Throughout the rest of this chapter, "low q^2" ($0.1 < q^2 < 7.02$ GeV$^2/c^4$) and "high q^2" ($10.24 < q^2 < 12.96$ GeV$^2/c^4$ and $q^2 > 14.06$ GeV$^2/c^4$) respectively refer to these concatenated q^2 regions below and above the J/ψ resonance.

4.9.1   Branching Fractions

Tables 4.20 and 4.21 respectively show the signal yields and branching fractions as functions of q^2 range in each mode. Figures 4.8-4.15 listed in the tables show the measured $m_{\rm ES}$ distributions with the one-dimensional fits overlaid. In these figures, the total fit curves in muon modes are not as smooth as those in electron modes, due to the presence of the hadronic background component in the fits. We do not find evidence for $B^0 \to K_s^0 \mu^+\mu^-$ and $B^0 \to K_s^0 e^+e^-$ signals in the low q^2 region, as indicated in Figures 4.9 and 4.11. The BF results obtained in the combined low q^2 and high q^2 regions are corrected for the vetoed charmonium regions to determine the total BFs integrated over all q^2, using signal MC simulation.

Mode	all q^2 (10^{-6})	low q^2 (10^{-6})	high q^2 (10^{-6})	Figure
$B^0 \to K^0 \mu^+ \mu^-$	$0.49^{+0.29}_{-0.25} \pm 0.03$ (2.2σ)	$0.01^{+0.15}_{-0.13} \pm 0.01$ (0.0σ)	$0.25^{+0.16}_{-0.14} \pm 0.02$ (1.9σ)	4.8
$B^+ \to K^+ \mu^+ \mu^-$	$0.41^{+0.16}_{-0.15} \pm 0.02$ (3.0σ)	$0.123^{+0.082}_{-0.071} \pm 0.007$ (1.8σ)	$0.116^{+0.079}_{-0.072} \pm 0.010$ (1.7σ)	4.9
$B^0 \to K^0 e^+ e^-$	$0.08^{+0.15}_{-0.12} \pm 0.01$ (0.6σ)	$-0.049^{+0.061}_{-0.049} \pm 0.004$ (—)	$0.177^{+0.118}_{-0.091} \pm 0.011$ (2.3σ)	4.10
$B^+ \to K^+ e^+ e^-$	$0.51^{+0.12}_{-0.11} \pm 0.02$ (5.8σ)	$0.308^{+0.070}_{-0.062} \pm 0.013$ (6.7σ)	$0.125^{+0.062}_{-0.055} \pm 0.006$ (2.5σ)	4.11
$B^+ \to K^{*+} \mu^+ \mu^-$	$1.46^{+0.79}_{-0.75} \pm 0.12$ (2.0σ)	$0.75^{+0.49}_{-0.45} \pm 0.07$ (1.7σ)	$0.78^{+0.43}_{-0.40} \pm 0.06$ (2.1σ)	4.12
$B^0 \to K^{*0} \mu^+ \mu^-$	$1.35^{+0.40}_{-0.37} \pm 0.10$ (4.1σ)	$0.41^{+0.24}_{-0.21} \pm 0.04$ (2.2σ)	$0.62^{+0.21}_{-0.19} \pm 0.05$ (3.8σ)	4.13
$B^+ \to K^{*+} e^+ e^-$	$1.38^{+0.47}_{-0.42} \pm 0.08$ (3.7σ)	$1.06^{+0.31}_{-0.28} \pm 0.07$ (4.7σ)	$0.19^{+0.23}_{-0.21} \pm 0.01$ (0.9σ)	4.14
$B^0 \to K^{*0} e^+ e^-$	$0.86^{+0.26}_{-0.24} \pm 0.05$ (4.2σ)	$0.20^{+0.12}_{-0.11} \pm 0.01$ (2.1σ)	$0.35^{+0.15}_{-0.13} \pm 0.02$ (3.0σ)	4.15

Table 4.21: Total and Partial Branching Fractions by mode and q^2 region. For each result, the first uncertainty is statistical, and the second is systematic. The statistical significance of each measurement is given in parenthesis.

Figure 4.8: m_{ES} distributions in $B^0 \to K_s^0\mu^+\mu^-$ all (left), low (mid), and high (right) q^2 regions, with fits overlaid. The data points are shown with total fit (solid), signal (medium dash), combinatorial (long dash), hadronic (short dash), and the sum of all peaking and crossfeed (dots) background components superimposed.

Figure 4.9: m_{ES} distributions in $B^+ \to K^+\mu^+\mu^-$ all (left), low (mid), and high (right) q^2 regions, with fits overlaid. The plotting convention follows that in Figure 4.8.
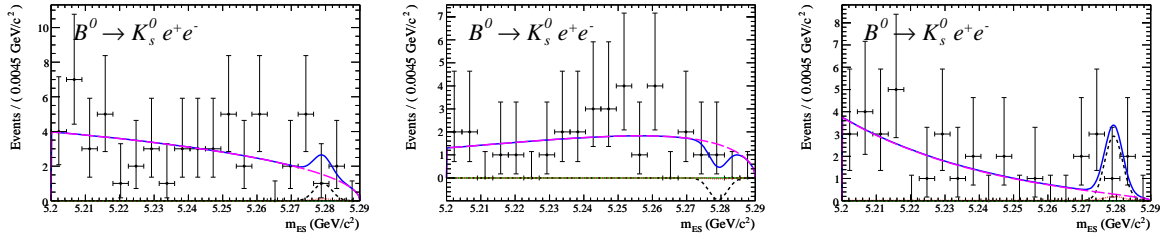
Figure 4.10: m_{ES} distributions in $B^0 \to K_s^0 e^+e^-$ all (left), low (mid), and high (right) q^2 regions, with fits overlaid. The plotting convention follows that in Figure 4.8.
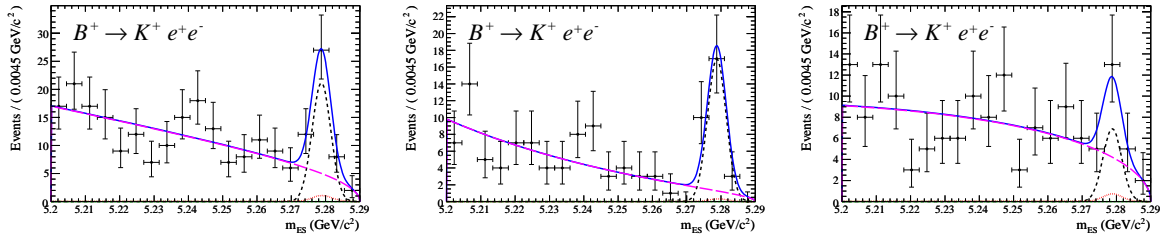
Figure 4.11: m_{ES} distributions in $B^+ \to K^+e^+e^-$ all (left), low (mid), and high (right) q^2 regions, with fits overlaid. The plotting convention follows that in Figure 4.8.
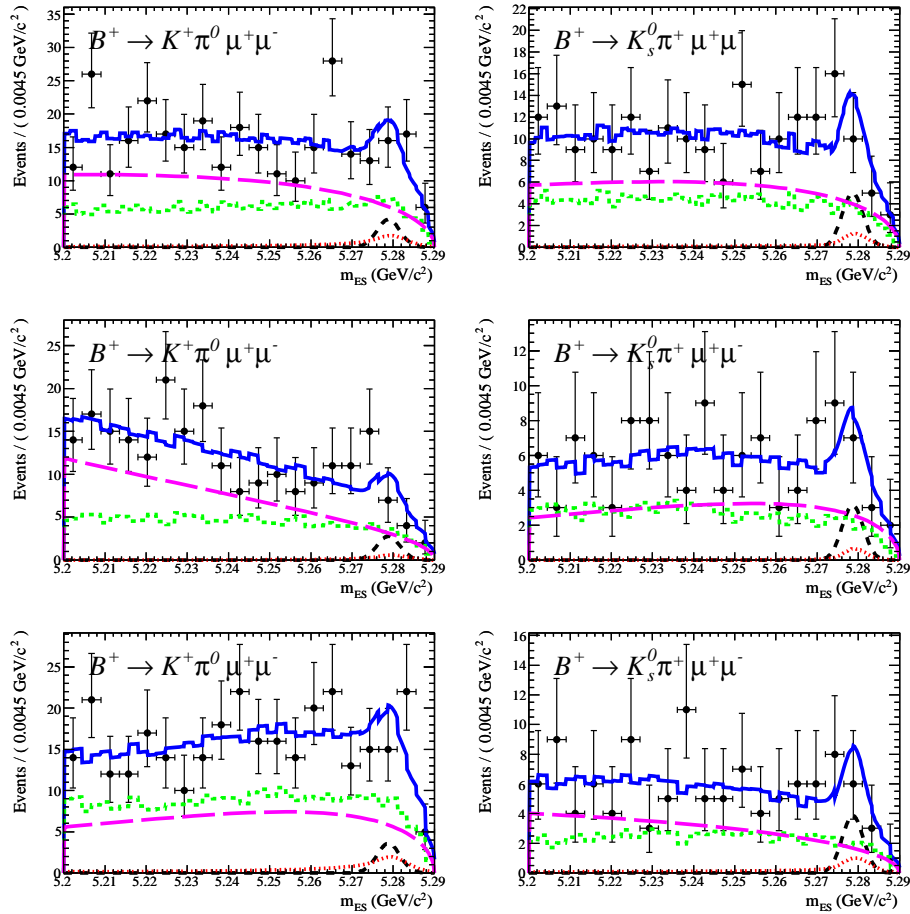
Figure 4.12: m_{ES} distributions in $B^+ \to K^{*+}\mu^+\mu^-$ all (top), low (mid), and high (bottom) q^2 regions, with fits overlaid. The plotting convention follows that in Figure 4.8.
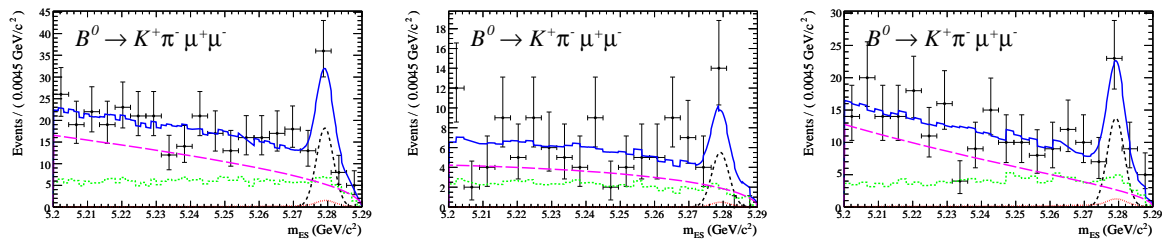
Figure 4.13: m_{ES} distributions in $B^0 \to K^+\pi^-\mu^+\mu^-$ all (left), low (mid), and high (right) q^2 regions, with fits overlaid. The plotting convention follows that in Figure 4.8.

Figure 4.14: m_{ES} distributions in $B^+ \to K^{*+}e^+e^-$ all (top), low (mid), and high (bottom) q^2 regions, with fits overlaid. The plotting convention follows that in Figure 4.8.
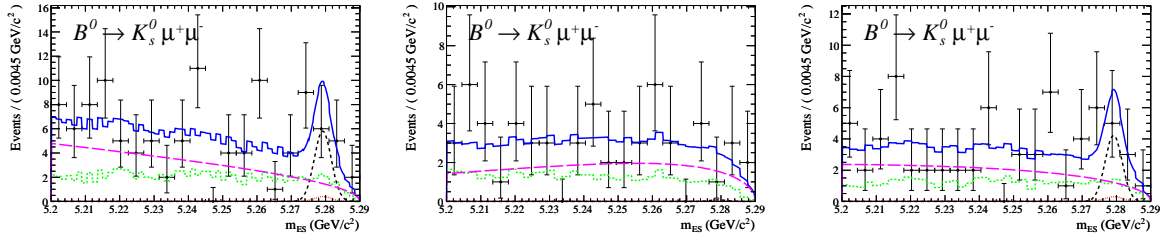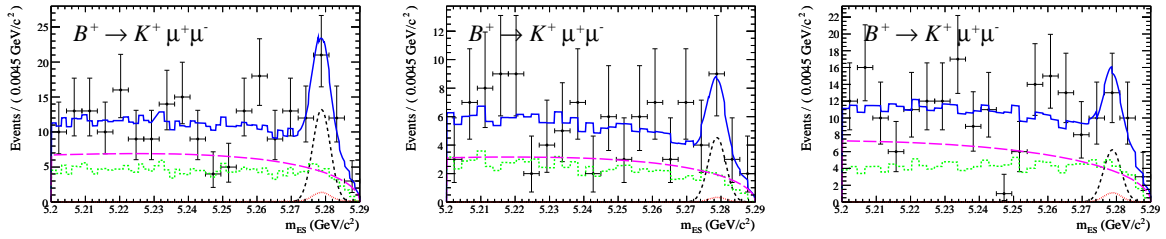

Figure 4.15: m_{ES} distributions in $B^0 \to K^+\pi^-e^+e^-$ all (left), low (mid), and high (right) q^2 regions, with fits overlaid. The plotting convention follows that in Figure 4.8.
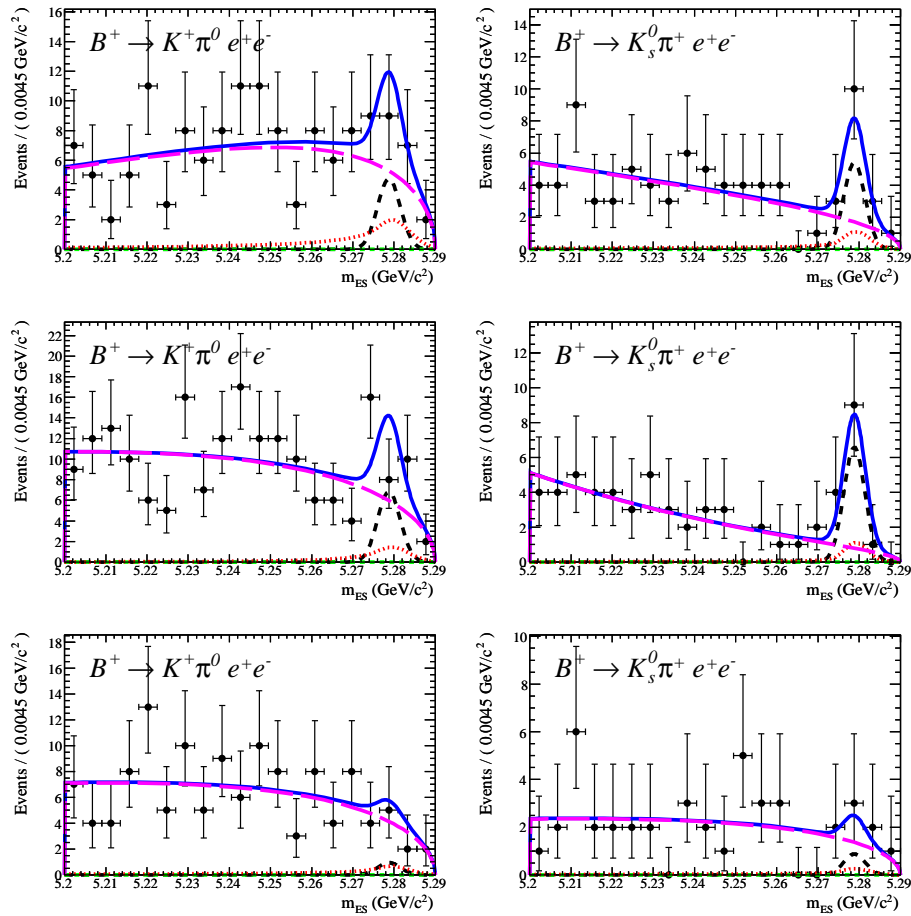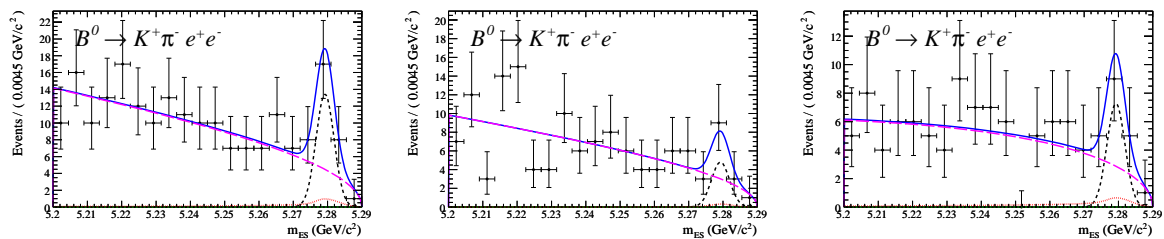
Mode	all q^2		low q^2		high q^2	
	Actual	Expected	Actual	Expected	Actual	Expected
$B^0 \to K_s^0 \mu^+ \mu^-$	7.9	11.3	0.1	5.7	5.8	6.1
$B^+ \to K^+ \mu^+ \mu^-$	18.8	30.0	6.5	13.3	8.9	18.7
$B^0 \to K_s^0 e^+ e^-$	1.5	13.5	-1.4	8.0	4.2	5.8
$B^+ \to K^+ e^+ e^-$	32.0	39.2	25.7	21.4	10.4	18.7
$B^+ \to K^+ \pi^0 \mu^+ \mu^-$	6.4	6.9	4.3	3.4	5.5	4.2
$B^+ \to K_s^0 \pi^+ \mu^+ \mu^-$	7.1	7.7	4.5	3.6	5.6	4.3
$B^0 \to K^+ \pi^- \mu^+ \mu^-$	25.4	29.5	7.7	11.0	19.2	18.3
$B^+ \to K^+ \pi^0 e^+ e^-$	7.4	7.9	10.5	6.6	1.5	4.1
$B^+ \to K_s^0 \pi^+ e^+ e^-$	7.6	8.2	9.4	5.3	1.2	3.5
$B^0 \to K^+ \pi^- e^+ e^-$	19.6	33.8	7.0	20.2	10.6	16.2

Table 4.22: Expected and actual signal yields by mode and q^2 region.

Table 4.22 compares the expected signal yields with the actual data yields. In particular, modes with a neutral strange meson in the low q^2 region are significantly suppressed compared to *a priori* expectations.

Along with the measured BF, the statistical significance of each measurement is given in Table 4.21, which is calculated from the change in $\sqrt{2\Delta \log \mathcal{L}}$ between our result and a null hypothesis. For measurements with a statistical significance less than 4.0σ (indicated by texts in bold type), we generate and fit ~ 8000 test datasets derived from our observations in the data and, after applying a Bayesian prior expectation of a physical signal yield, we compute the upper limits at the 90% and 95% confidence levels using the frequentist method. The upper limits are given in Table 4.23.

In addition to the above results, we perform fits that include the pole q^2 region for $K^* e^+ e^-$ final states where, as previously discussed in §1.3.4, a significant rate enhancement is expected. Tables 4.24 and 4.25 respectively show the signal yields and total and partial branching fractions in these modes for all q^2 and low q^2 regions with pole included.

We also perform fits by combining various hadronic and di-lepton final states which are then averaged assuming, as appropriate, isospin and lepton-flavor symmetry. For combined B^+ and B^0 modes, the branching fractions are expressed in terms of the B^0 total width by constraining the total width ratio $\Gamma(B^+)/\Gamma(B^0)$ to the lifetime ratio $r \equiv \tau_{B^0}/\tau_{B^+} = 1/(1.071 \pm 0.009)$ [68]. Table 4.26 shows total and partial branching fractions for the combined modes. For modes with less than 4.0σ significance, Table 4.27 gives 90% and 95% CL upper limits using the frequentist technique as previously described.

Mode	all q^2 (10^{-6})		low q^2 (10^{-6})		high q^2 (10^{-6})	
	90% CL	95% CL	90% CL	95% CL	90% CL	95% CL
$B^0 \to K^0 \mu^+\mu^-$	0.99	1.14	0.31	0.39	0.53	0.61
$B^+ \to K^+ \mu^+\mu^-$	0.62	0.70	0.25	0.29	0.24	0.27
$B^0 \to K^0 e^+e^-$	0.36	0.44	0.10	0.12	0.38	0.44
$B^+ \to K^+ e^+e^-$	—	—	—	—	0.21	0.24
$B^+ \to K^{*+} \mu^+\mu^-$	2.55	2.90	1.48	1.70	1.36	1.54
$B^0 \to K^{*0} \mu^+\mu^-$	—	—	0.83	0.94	0.97	1.08
$B^+ \to K^{*+} e^+e^-$	1.97	2.19	—	—	0.53	0.63
$B^0 \to K^{*0} e^+e^-$	—	—	0.42	0.48	0.60	0.67

Table 4.23: Upper limits for modes and q^2 regions with statistical significance $< 4.0\sigma$.

Mode	all q^2	low q^2
$B^+ \to K^+\pi^0 e^+e^-$	$10.2^{+3.2}_{-3.0}$	$7.5^{+2.3}_{-2.1}$
$B^+ \to K^0_S\pi^+ e^+e^-$	$10.5^{+3.3}_{-3.1}$	$9.6^{+3.0}_{-2.6}$
$B^0 \to K^+\pi^- e^+e^-$	$22.8^{+6.8}_{-6.2}$	$19.0^{+5.7}_{-5.0}$

Table 4.24: Signal yields in the q^2 regions including pole region.

Mode	all q^2 + pole (10^{-6})	low q^2 + pole (10^{-6})
$B^+ \to K^{*+} e^+e^-$	$1.90^{+0.59}_{-0.55} \pm 0.11$ (3.8σ)	$1.32^{+0.41}_{-0.36} \pm 0.09$ (4.8σ)
$B^0 \to K^{*0} e^+e^-$	$1.02^{+0.30}_{-0.28} \pm 0.06$ (4.2σ)	$0.73^{+0.22}_{-0.19} \pm 0.04$ (4.6σ)

Table 4.25: Branching fractions in the q^2 regions including pole region. For each result, the first uncertainty is statistical, the second is systematic, and the statistical significance is given in parenthesis.

Mode	all q^2 (10^{-6})	low q^2 (10^{-6})	high q^2 (10^{-6})
$B^0 \to K^0 \ell^+\ell^-$	$\mathbf{0.21^{+0.15}_{-0.13} \pm 0.02\ (1.7\sigma)}$	$\mathbf{-0.041^{+0.058}_{-0.047} \pm 0.004\ (\text{---})}$	$\mathbf{0.202^{+0.096}_{-0.081} \pm 0.013\ (3.0\sigma)}$
$B^+ \to K^+ \ell^+\ell^-$	$0.476^{+0.092}_{-0.086} \pm 0.022\ (6.5\sigma)$	$0.250^{+0.052}_{-0.047} \pm 0.010\ (6.7\sigma)$	$\mathbf{0.122^{+0.048}_{-0.044} \pm 0.006\ (3.0\sigma)}$
$B \to K\mu^+\mu^-$	$0.41^{+0.13}_{-0.12} \pm 0.02\ (4.7\sigma)$	$\mathbf{0.096^{+0.066}_{-0.059} \pm 0.006\ (2.1\sigma)}$	$\mathbf{0.139^{+0.067}_{-0.062} \pm 0.008\ (2.9\sigma)}$
$B \to Ke^+e^-$	$0.388^{+0.090}_{-0.083} \pm 0.020\ (5.6\sigma)$	$0.217^{+0.051}_{-0.046} \pm 0.010\ (5.9\sigma)$	$\mathbf{0.132^{+0.050}_{-0.045} \pm 0.007\ (3.5\sigma)}$
$B \to K\ell^+\ell^-$	$0.394^{+0.073}_{-0.069} \pm 0.020\ (7.3\sigma)$	$0.181^{+0.039}_{-0.036} \pm 0.008\ (6.1\sigma)$	$0.135^{+0.040}_{-0.037} \pm 0.007\ (4.5\sigma)$
$B^0 \to K^{*0} \ell^+\ell^-$	$1.03^{+0.22}_{-0.21} \pm 0.07\ (5.8\sigma)$	$\mathbf{0.257^{+0.110}_{-0.098} \pm 0.02\ (2.9\sigma)}$	$0.46^{+0.12}_{-0.11} \pm 0.03\ (4.7\sigma)$
$B^+ \to K^{*+} \ell^+\ell^-$	$1.40^{+0.40}_{-0.37} \pm 0.09\ (4.2\sigma)$	$0.98^{+0.26}_{-0.24} \pm 0.06\ (4.9\sigma)$	$\mathbf{0.34^{+0.21}_{-0.19} \pm 0.02\ (1.8\sigma)}$
$B \to K^*\mu^+\mu^-$	$1.35^{+0.35}_{-0.33} \pm 0.10\ (5.3\sigma)$	$\mathbf{0.47^{+0.21}_{-0.19} \pm 0.04\ (3.2\sigma)}$	$0.65^{+0.18}_{-0.17} \pm 0.05\ (4.7\sigma)$
$B \to K^*e^+e^-$	$0.99^{+0.23}_{-0.21} \pm 0.06\ (5.6\sigma)$	$0.42^{+0.13}_{-0.12} \pm 0.03\ (4.3\sigma)$	$\mathbf{0.30^{+0.12}_{-0.11} \pm 0.02\ (3.1\sigma)}$
$B \to K^*\ell^+\ell^-$	$1.11^{+0.19}_{-0.18} \pm 0.07\ (7.7\sigma)$	$0.43^{+0.11}_{-0.10} \pm 0.03\ (5.3\sigma)$	$0.42^{+0.10}_{-0.10} \pm 0.03\ (5.3\sigma)$

Table 4.26: Total and partial branching fractions in combined modes. For each result, the first uncertainty is statistical, the second is systematic, and the statistical significance is given in parenthesis.

Mode	all q^2 (10^{-6})		low q^2 (10^{-6})		high q^2 (10^{-6})	
	90% CL	95% CL	90% CL	95% CL	90% CL	95% CL
$B^0 \to K^0\ell^+\ell^-$	0.45	0.53	0.09	0.11	0.36	0.40
$B^+ \to K^+\ell^+\ell^-$	—	—	—	—	0.19	0.21
$B \to K\mu^+\mu^-$	—	—	0.21	0.25	0.25	0.29
$B \to Ke^+e^-$	—	—	—	—	0.21	0.24
$B^0 \to K^{*0}\ell^+\ell^-$	—	—	0.44	0.50	—	—
$B^+ \to K^{*+}\ell^+\ell^-$	—	—	—	—	0.63	0.72
$B \to K^*\mu^+\mu^-$	—	—	0.84	0.95	—	—
$B \to K^*e^+e^-$	—	—	—	—	0.49	0.55

Table 4.27: Upper limits for combined modes and q^2 regions with statistical significance $< 4.0\sigma$.
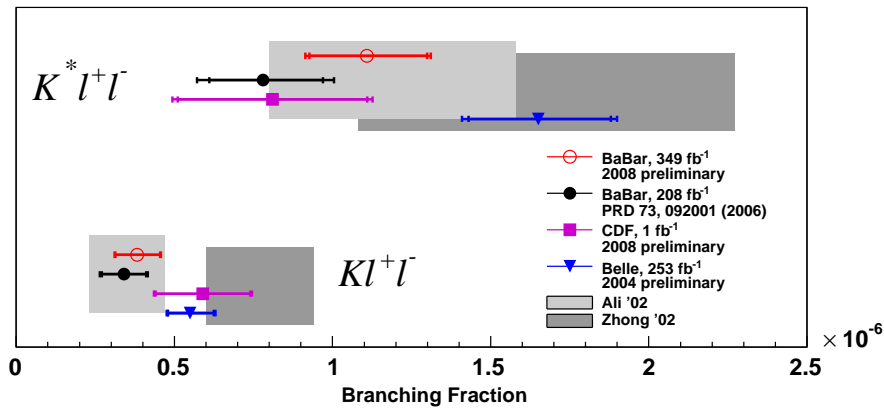

Figure 4.16: Predictions and measurements of the branching fractions of $B \to K^{(*)}\ell^+\ell^-$. Our results ("BaBar, 349 fb^{-1}") are compared to the recent results from Belle [41] and CDF [42], as well as the previous *BABAR* (208 fb^{-1}) measurements [11]. The theoretical predictions from "Ali '02" [20] and "Zhong '02" [36] are also shown as shaded areas.
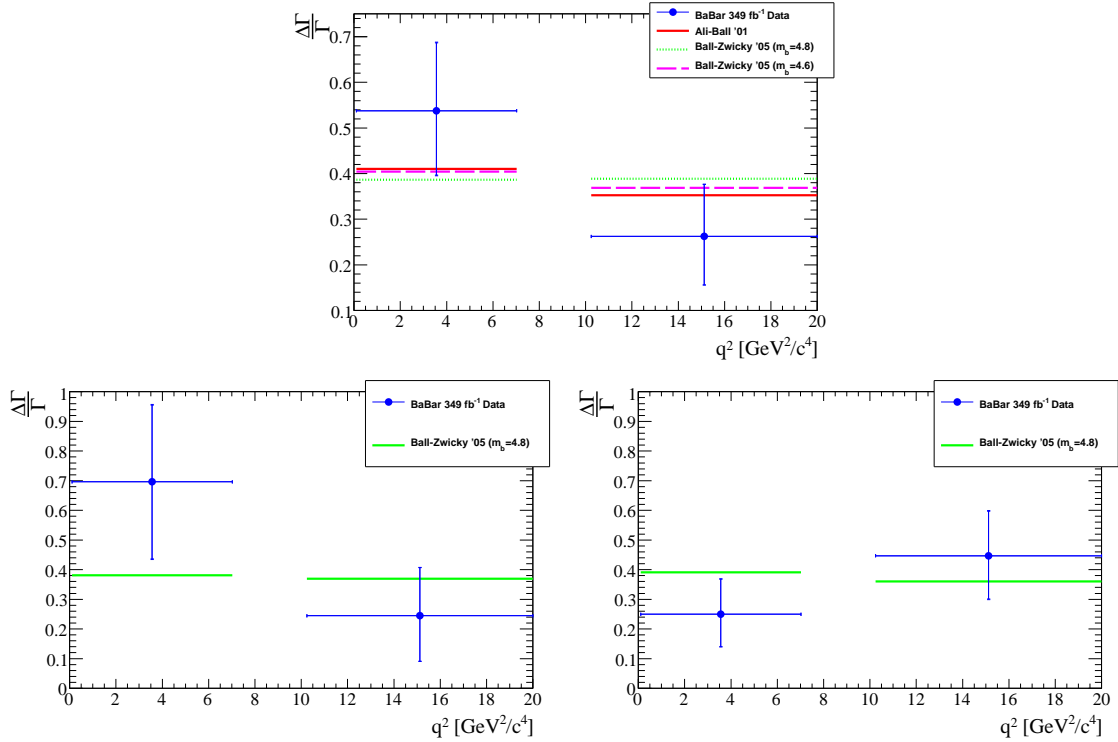
Figure 4.17: Partial branching fractions measured in data (points) compared to the central values of the predictions (lines) from different LCSR based form factor calculations for $B^+ \to K^+ \ell^+ \ell^-$ (top), $B^+ \to K^{*+} \ell^+ \ell^-$ (bottom left) and $B^0 \to K^{*0} \ell^+ \ell^-$ (bottom right). These form factor calculations include the "Ali-Ball '01" [20] and "Ball-Zwicky '05" for different b quark masses ($m_b = 4.8$ and 4.6 GeV) [76, 77]. In K^* modes, only the "Ball-Zwicky '05" calculation with $m_b = 4.8$ GeV is shown, as the one with $m_b = 4.6$ GeV is not available, and the predictions from the "Ali-Ball '01" calculation are almost identical to those from "Ball-Zwicky '05".

Our measured total branching fractions in combined $K\ell^+\ell^-$ and $K^*\ell^+\ell^-$ modes are compared to previous measurements and two theoretical predictions based on different form factor models, as summarized in Figure 4.16. Our $K\ell^+\ell^-$ and $K^*\ell^+\ell^-$ results show good agreement with the Standard Model predictions by Ali *et al.* [20] and the previous *BABAR* measurements with an integrated luminosity of 208 fb^{-1} [11]. The preliminary $K^{(*)}\ell^+\ell^-$ BF results reported by the Belle collaboration in 2004 [41] are both higher than ours at about one standard deviation level. The CDF measurement in 2008 [42] for $K^*\ell^+\ell^-$ agrees well with our result, while their $K\ell^+\ell^-$ result is higher, being more consistent with the Belle result and the corresponding prediction from Zhang *et al.* [20], than ours.

The resulting q^2 distributions in different modes are compared to the Standard Model predictions. In these predictions, different calculations of the $B \to K^{(*)}$ LCSR form factors are used. The results are shown in Figure 4.17, with the measured partial branching fractions normalized by the measured total branching fractions. In the high q^2 region, our measurements are in good agreement with the Standard Model predictions. For the low q^2 region, the measurements in both charged B modes tend

Source	q^2 range (GeV$^2/c^4$)	$\mathcal{B}$ (10^{-6})
BABAR 349 fb^{-1} data	$0.10 - 7.02$	$0.43^{+0.11}_{-0.10} \pm 0.03$
BABAR 208 fb^{-1} data [11]	$0.10 - 8.41$	$0.29^{+0.12}_{-0.10} \pm 0.05$
Belle 253 fb^{-1} data [41]	$0.00 - 8.00$	$0.96^{+0.25}_{-0.21} \pm 0.05 \pm 0.12$
Ali, *et* al. [35]	$1.00 - 7.00$	$0.27^{+0.05\,+0.03\,+0.02}_{-0.05\,-0.03\,-0.02}$
Beneke, *et* al. [29, 78]	$0.10 - 7.02$	$0.47^{+0.07}_{-0.05}$

Table 4.28: $K^*\ell^+\ell^-$ partial BFs in the low q^2 ranges from different experiments and the most recent predictions. The Belle result is a sum of separate measurements in two q^2 regions ($0 < q^2 < 4 \, \text{GeV}^2/c^4$ and $4 < q < 8 \, \text{GeV}^2/c^4$). For each of the experimental observations, the first error is statistical, and the second is systematic, while the third is due to model dependence for the Belle result. For the prediction from Ali, *et* al., the first and the second errors are from the form factors and the CKM matrix, respectively, while the third is due to the variation of other input parameters and the residual scale dependence. The prediction provided by Ali, *et* al. is based on SCET, while the other prediction from Beneke, *et* al. is based on QCD factorization.

to be higher than the predictions, while those in B^0 modes are lower ($B^0 \to K_s^0\ell^+\ell^-$ mode is not shown in Figure 4.17 due to null signal observation in the low q^2).

As discussed in §1.3.4, only the partial branching fraction predictions with q^2 below the J/ψ resonance are reliable. However it is hard to compare our partial BF measurements directly with the predictions and previous measurements due to different definitions of q^2 regions used. In the Table 4.28, the numerical results from different measurements and two of the most recent Standard Model based predictions are listed, along with different q^2 ranges used. Our observations show better agreement with both predictions than the results reported by Belle.

4.9.2   Rate Asymmetry Results

$\mathcal{A}_{CP}$ Results

Here we present the $\mathcal{A}_{CP}$ results from the fits in the combined modes, as shown in Table 4.29. For the different individual modes, we assume the lepton-flavor symmetry, while the isospin symmetry is only assumed in the high q^2 region. This is because we have observed large discrepancies between the partial BFs for $B^+ \to K^{*+}\ell^+\ell^-$ and $B^0 \to K^{*0}\ell^+\ell^-$ modes in the low q^2 region (see Table 4.26). We perform separate fits in the B and $\bar{B}$ datasets, sharing the same ARGUS shape parameter ξ. We also have

Figure 4.18: m_{ES} distributions in the $B^{\pm} \to K^{\pm}\ell^{+}\ell^{-}$ modes with different B CP eigenstates in all q^2 with fits for $\mathcal{A}_{CP}$ overlaid. The plotting convention follows that in Figure 4.8.

redone all the fits without sharing ξ between B and $\overline{B}$ datasets as a cross-check. We observe no notable deviation from original results.

Our measured direct CP asymmetries in all q^2 for $B^{\pm} \to K^{\pm}\ell^{+}\ell^{-}$ and $B \to K^{*}\ell^{+}\ell^{-}$ modes are both consistent with the Standard Model expectation of a negligible $\mathcal{A}_{CP}$.

Mode	all q^2	low q^2	high q^2
$B^{\pm} \to K^{\pm}\ell^{+}\ell^{-}$	$-0.18^{+0.18}_{-0.18} \pm 0.01$	$-0.18^{+0.19}_{-0.19} \pm 0.01$	$-0.08^{+0.36}_{-0.39} \pm 0.02$
$B^{\pm} \to K^{\pm}\ell^{+}\ell^{-}$	$0.02^{+0.20}_{-0.20} \pm 0.02$	$-0.24^{+0.38}_{-0.38} \pm 0.02$	$0.17^{+0.24}_{-0.24} \pm 0.02$
$B^{+} \to K^{*+}\ell^{+}\ell^{-}$	$0.01^{+0.26}_{-0.24} \pm 0.02$	$0.10^{+0.25}_{-0.24} \pm 0.02$	$-0.18^{+0.45}_{-0.55} \pm 0.04$
$B \to K^{*}\ell^{+}\ell^{-}$	$0.01^{+0.16}_{-0.15} \pm 0.01$	$0.01^{+0.21}_{-0.20} \pm 0.01$	$0.09^{+0.21}_{-0.21} \pm 0.02$

Table 4.29: Measured $\mathcal{A}_{CP}$ by mode and q^2 region. The statistical and systematic uncertainties for each measurement are given successively.
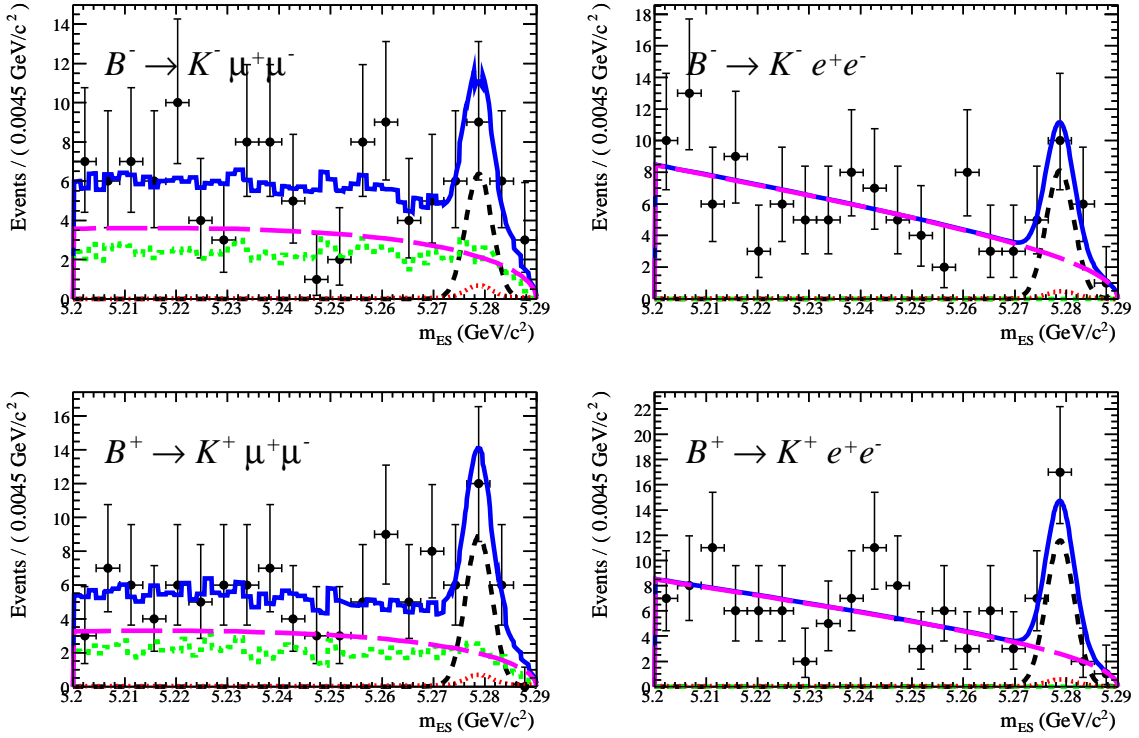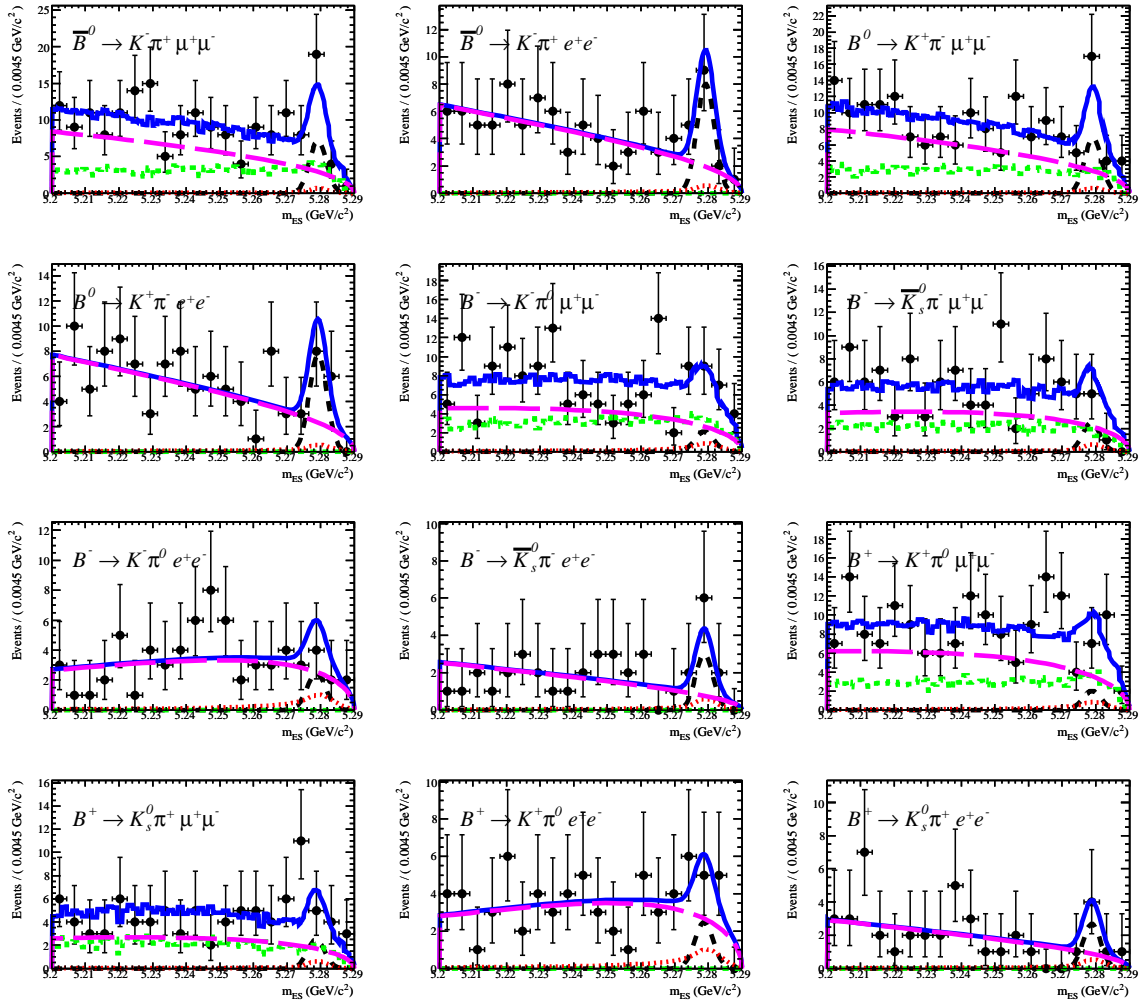
Figure 4.19: m_{ES} distributions in the $B \to K^*\ell^+\ell^-$ modes with different B CP eigenstates in all q^2 with fits for $\mathcal{A}_{CP}$ overlaid. The plotting convention follows that in Figure 4.8.

Mode	all q^2	low q^2	high q^2	all q^2 w/ pole	low q^2 w/ pole
R_K	$0.96^{+0.44}_{-0.34} \pm 0.05$	$0.40^{+0.30}_{-0.23} \pm 0.02$	$1.06^{+0.81}_{-0.51} \pm 0.06$	$0.95^{+0.45}_{-0.34} \pm 0.05$	$0.42^{+0.31}_{-0.24} \pm 0.02$
R_{K^*}	$1.37^{+0.53}_{-0.40} \pm 0.09$	$1.01^{+0.58}_{-0.44} \pm 0.08$	$2.15^{+1.42}_{-0.78} \pm 0.15$	$1.10^{+0.42}_{-0.32} \pm 0.07$	$0.56^{+0.29}_{-0.23} \pm 0.04$

Table 4.30: Measured lepton flavor asymmetries by mode and q^2 region. The statistical and systematic uncertainties for each measurement are given successively. The two rightmost columns in the table are for the pole included q^2 regions.

The fits for these modes are shown in Figures 4.18 and 4.19. The previous *BABAR* measurements obtained $\mathcal{A}_{CP}(B^\pm \to K^\pm \ell^+ \ell^-) = -0.07 \pm 0.22 \pm 0.02$ and $\mathcal{A}_{CP}(B \to K^* \ell^+ \ell^-) = +0.03 \pm 0.23 \pm 0.03$ [11] in the entire q^2 region, where the first error is statistical and the second is systematic. Our results are consistent with the previous results but possess much smaller errors.

R_K and R_{K^*} Results

Here the R_K and R_{K^*} results from fits across modes with different di-lepton flavors are summarized in Table 4.30. The table also shows R_{K^*} results in the q^2 regions with pole included. For K^* modes, due to increase in partial branching fractions for di-electron modes in the pole region, R_{K^*} values in these q^2 regions are expected to be well below unity. In the fits, isospin symmetry is also only assumed in the high q^2 region.

Figure 4.20 presents the R_K and R_{K^*} comparison between our observations and previous ones from the *BABAR* and Belle experiments, along with the Standard Model predictions. Our results are consistent with both the measurements and the Standard Model predictions.

$\mathcal{A}_I$ Results

As defined in Equation 1.16, the isospin asymmetries in the $B \to K\ell^+\ell^-$ and $B \to K^*\ell^+\ell^-$ decays are computed using the following form:

$$\mathcal{A}_I^{K^{(*)}} \equiv \frac{\mathcal{B}(B^0 \to K^{(*)0}\ell^+\ell^-) - r\mathcal{B}(B^\pm \to K^{(*)\pm}\ell^+\ell^-)}{\mathcal{B}(B^0 \to K^{(*)0}\ell^+\ell^-) + r\mathcal{B}(B^\pm \to K^{(*)\pm}\ell^+\ell^-)} \tag{4.7}$$

where the B^0/B^+ lifetime ratio r has been taken into account.

We directly perform simultaneous fits to data across the charged and neutral B modes for $\mathcal{A}_I^{K^{(*)}}$. In the fits for the combined $\ell^+\ell^-$ modes, the lepton flavor symmetry is assumed. The results for different modes in different q^2 regions are summarized in Table 4.31. We also have measured the isospin asymmetries in the pole-included low and all q^2 regions, as shown in Table 4.32.
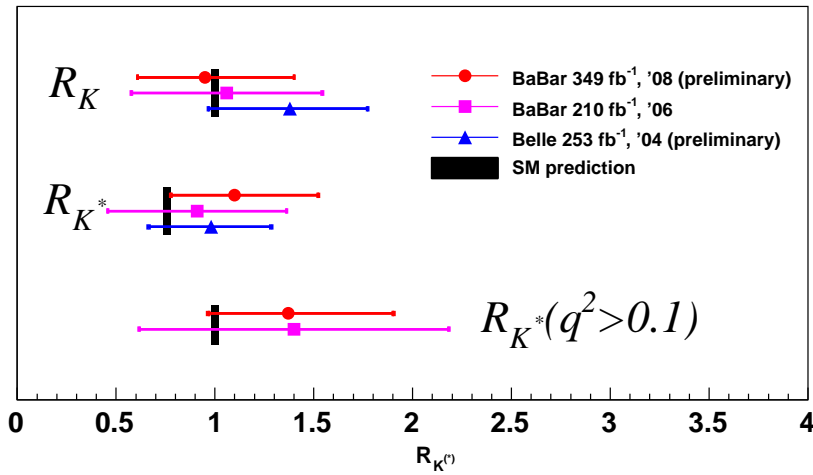
Figure 4.20: Recent predictions and measurements of $R_{K^{(*)}}$. Our results ("BaBar, 349 fb^{-1}") are compared to the recent results from Belle [41], and previous 208 fb^{-1} measurements [11]. The central values from the Standard Model predictions [46] are shown as vertical lines. The R_K and R_{K^*} here are for the entire q^2 region, including the pole, while the $R_{K^*}(q^2 > 0.1)$ here is for the pole excluded all q^2 region.
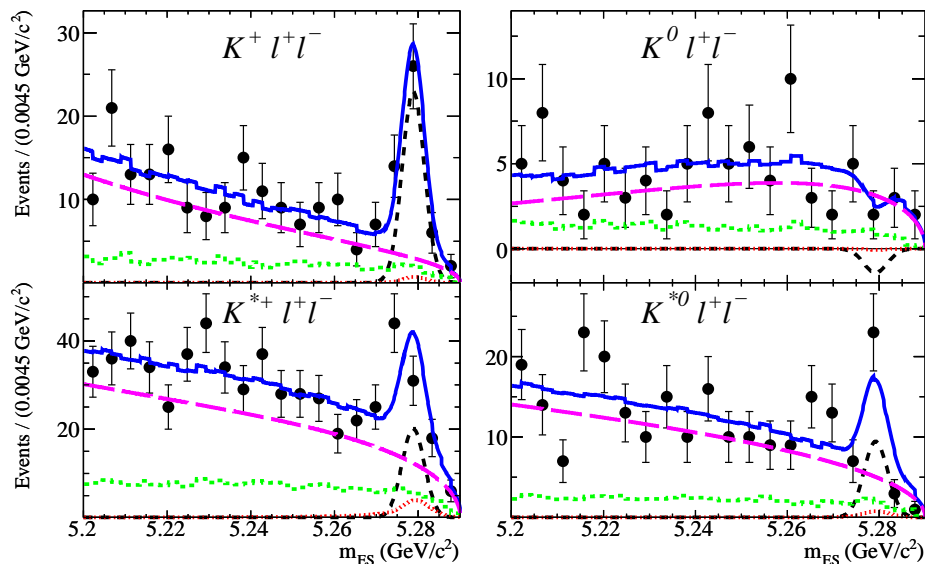
Figure 4.21: m_{ES} distributions for B^+ (left two) and B^0 (right two) modes low q^2 region, with fits for $\mathcal{A}_I^K$ (top two) and $\mathcal{A}_I^{K^*}$ (bottom two) overlaid. The fit conversion follows that in Figure 4.8.

Mode	all q^2	low q^2	high q^2
$B \to K\mu^+\mu^-$	$0.13^{+0.29}_{-0.37} \pm 0.04$	$-0.91^{+1.17}_{-\inf} \pm 0.18$	$0.39^{+0.35}_{-0.46} \pm 0.04$
$B \to Ke^+e^-$	$-0.73^{+0.39}_{-0.50} \pm 0.04$	$-1.41^{+0.49}_{-0.69} \pm 0.04$	$0.21^{+0.32}_{-0.41} \pm 0.03$
$B \to K\ell^+\ell^-$	$-0.37^{+0.27}_{-0.34} \pm 0.04$	$-1.43^{+0.56}_{-0.85} \pm 0.05$	$0.28^{+0.24}_{-0.30} \pm 0.03$
$B \to K^*\mu^+\mu^-$	$-0.00^{+0.36}_{-0.26} \pm 0.05$	$-0.26^{+0.50}_{-0.34} \pm 0.05$	$-0.08^{+0.37}_{-0.27} \pm 0.05$
$B \to K^*e^+e^-$	$-0.20^{+0.22}_{-0.20} \pm 0.03$	$-0.66^{+0.19}_{-0.17} \pm 0.02$	$0.32^{+0.75}_{-0.45} \pm 0.03$
$B \to K^*\ell^+\ell^-$	$-0.12^{+0.18}_{-0.16} \pm 0.04$	$-0.56^{+0.17}_{-0.15} \pm 0.03$	$0.18^{+0.36}_{-0.28} \pm 0.04$

Table 4.31: Measured $\mathcal{A}_I$ by mode and q^2 region. For each result, the first error is statistical, and the second is systematic.

Mode	all q^2 + pole	low q^2 + pole
$B \to K^*e^+e^-$	$-0.27^{+0.21}_{-0.18} \pm 0.03$	$-0.25^{+0.20}_{-0.18} \pm 0.03$

Table 4.32: Measured $\mathcal{A}_I$ by mode and q^2 region including the pole region. For each result, the first error is statistical, and the second is systematic.

We do not observe large isospin asymmetries significantly different from zero in the high q^2 and all q^2 regions for both $K\ell^+\ell^-$ and $K^*\ell^+\ell^-$ modes. Our observations in the pole-included q^2 regions for $K^*e^+e^-$ mode are also consistent with the Standard Model predictions of $\sim 10\%$ asymmetry, and with the measured isospin asymmetry $\mathcal{A}_I = 0.050 \pm 0.058$ for $B \to K^*\gamma$ decays based on $\sim 88 \times 10^6$ $B\bar{B}$ events [79]. However, we observe large negative isospin asymmetries in the low q^2 region. Figure 4.21 shows the $\mathcal{A}_I^{K^{(*)}}$ fits for this q^2 region. Due to null observation of signal events in the low q^2 for the $B^0 \to K_s^0\ell^+\ell^-$ modes, as indicated in §4.9.1 and Figure 4.21, the fitted $\mathcal{A}_I$ central values in these modes are well below the physical boundary -1.
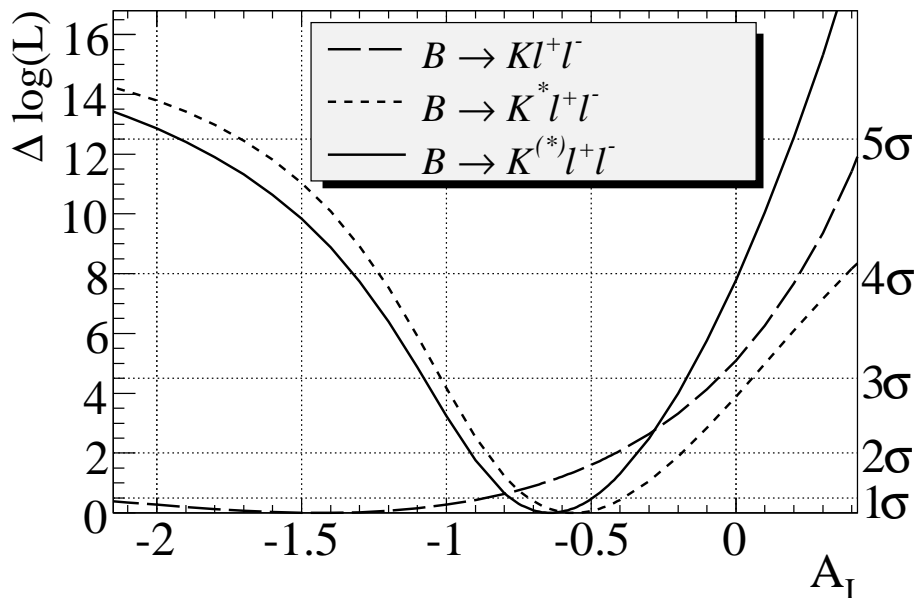

Figure 4.22: Likelihood curves for the $K^{(*)}\ell^+\ell^-$ $\mathcal{A}_I$ fits in the low q^2 region. The curves are statistical only. The right side of the y axis indicates the purely statistical significance levels based on $\sqrt{2\Delta \log \mathcal{L}}$.

We perform likelihood scans for $\mathcal{A}_I^K$ and $\mathcal{A}_I^{K^*}$ fits in the low q^2 region by refitting the data with $\mathcal{A}_I$ fixed to a series of values. The change in NLL $(-\log \mathcal{L})$ between this fit and the nominal fit is calculated for each $\mathcal{A}_I$ value. The $\mathcal{A}_I$ likelihood curves obtained from $K\ell^+\ell^-$ and $K^*\ell^+\ell^-$ fits are shown in Figure 4.22. Both curves show a parabolic shape for $\mathcal{A}_I > -1$, which indicates the Gaussian nature of our fit results in the $\mathcal{A}_I$ physical region. As the systematic errors associated with $\mathcal{A}_I^K$ and $\mathcal{A}_I^{K^*}$ are relatively small, they are treated as small perturbations on the statistical errors by summing both systematic and statistical errors in quadrature to make the total errors. The ratios of the total errors to the corresponding statistical ones are used as scaling factors on the changes in NLL. Therefore, by incorporating the systematic effects, we have the significance in the low q^2 region for $\mathcal{A}_I^K$ to be different from zero is 3.2σ. For $\mathcal{A}_I^{K^*}$ in the low q^2, the significance from zero is 2.7σ. These significance values with which a null hypothesis is rejected are verified by performing fits to ensembles of simulated datasets generated with $\mathcal{A}_I^K$ or $\mathcal{A}_I^{K^*}$ at zero. We find the frequentist coverage in both $K\ell^+\ell^-$ and $K^*\ell^+\ell^-$ modes consistent with the significance calculations.

As the isospin asymmetries in the low q^2 regions of both $K\ell^+\ell^-$ and $K^*\ell^+\ell^-$ modes are highly negative, this type of asymmetry may be insensitive to the hadronic final states. We thus sum up the $K\ell^+\ell^-$ and $K^*\ell^+\ell^-$ likelihood curves for the curve in the combined $K^{(*)}\ell^+\ell^-$ mode, as shown in Figure 4.22. The combined $K^{(*)}\ell^+\ell^-$ likelihood curve has been shifted back so that its minimum is still at zero. From this curve, we obtain the isospin asymmetry for the combined $K^{(*)}\ell^+\ell^-$ mode $\mathcal{A}_I^{K^{(*)}} = -0.64^{+0.15}_{-0.14} \pm 0.03$, while the first error is statistical, and the second is systematic. Including systematic uncertainties, the significance for the combined $\mathcal{A}_I^{K^{(*)}}$ from a null result is 3.9σ.

4.9.3 Cross-checks in $\mathcal{A}_I$ Measurements

Since the $\mathcal{A}_I$ results in the low q^2 region differ significantly from the Standard Model expectations, we have performed additional tests to probe for all potential biases in the measurements. The tests are listed as follows:

- There may exist a possibility of underestimating the charmonium leakage. More specifically, an unexpected amount of J/ψ events may leak into the low q^2 region for the $B^+ \to K^{*+}e^+e^-$ modes, which will increase $\mathcal{A}_I$ for $B \to K^*e^+e^-$. We have examined this possibility by varying the low q^2 upper bound from $m_{\ell\ell} < 2.65\,\mathrm{GeV}/c^2$ to $m_{\ell\ell} < 2.3\,\mathrm{GeV}/c^2$. If there exists any notable unexpected leakage, this bound shift will cause dramatic changes to $\mathcal{A}_I$ measurements in the low q^2. Table 4.33 gives the comparison between measured $\mathcal{A}_I$ with different low q^2 upper bounds.

- Since ARGUS shape parameters ξ are floating in the fits, the parameterization may be not optimal and thus produce a bias. In the test, we perform fits in which the ARGUS slopes are fixed to the predicted values from properly normalized generic MC simulated samples. The results are presented in Table 4.34.

- We have also studied the combinatorial background events in the ΔE sideband region which is defined as:

  $|\Delta E| < 0.25\,\mathrm{GeV}$ and outside of the signal region

  $m_{\mathrm{ES}} > 5.2\,\mathrm{GeV}/c^2$ and outside of the signal region

  $m_{K\pi}$ selection as in the signal region

  The ΔE sideband events from the data are compared with the events from the normalized generic MC samples after all the other event selection criteria used for the fit region are applied to both data/MC samples. The results are shown in Figure 4.23 for $B \to K^*e^+e^-$ modes in the low q^2 region. The expected number of events from the MC simulation and the number of events from data are consistent within 10%. This indicates an isospin asymmetry very close to zero for the combinatorial backgrounds.

- The NN selections may introduce a bias in $\mathcal{A}_I$. Thus we redo the partial BF measurements with all NN selections removed, using the $B \to K^*e^+e^-$ modes in the low q^2 region. The results are summarized in Table 4.35.

Mode	low q^2	
	$m_{\ell\ell} < 2.65\,\mathrm{GeV}/c^2$	$m_{\ell\ell} < 2.3\,\mathrm{GeV}/c^2$
$B \to K^*\mu^+\mu^-$	$-0.26^{+0.50}_{-0.34}$	$0.01^{+0.82}_{-0.44}$
$B \to K^*e^+e^-$	$-0.66^{+0.19}_{-0.17}$	$-0.56^{+0.25}_{-0.21}$
$B \to K^*\ell^+\ell^-$	$-0.56^{+0.17}_{-0.15}$	$-0.42^{+0.23}_{-0.20}$

Table 4.33: Measured $\mathcal{A}_I$ in different low q^2 upper bounds. The errors are statistical only.

Mode	all q^2		low q^2	
	fixed ξ	floating ξ	fixed ξ	floating ξ
$B \to K^*\mu^+\mu^-$	$-0.00^{+0.36}_{-0.26}$	$-0.04^{+0.31}_{-0.25}$	$-0.26^{+0.50}_{-0.34}$	$-0.30^{+0.36}_{-0.29}$
$B \to K^*e^+e^-$	$-0.20^{+0.22}_{-0.20}$	$-0.30^{+0.19}_{-0.18}$	$-0.66^{+0.19}_{-0.17}$	$-0.72^{+0.25}_{-0.16}$
$B \to K^*\ell^+\ell^-$	$-0.12^{+0.18}_{-0.16}$	$-0.20^{+0.15}_{-0.14}$	$-0.56^{+0.17}_{-0.15}$	$-0.60^{+0.16}_{-0.15}$

Table 4.34: Measured $\mathcal{A}_I$ with and without fixed ξ. The errors are statistical only.

- Instead of combining $K^+\pi^0$ and $K_S^0\pi^+$ modes in the K^{*+} fit, these two modes are measured individually for $K^{*+}\ell^+\ell^-$ partial BFs in the low q^2. Both results are consistent with the result obtained from the combined fit, as shown in Table 4.36.

All tests show good agreement with the original results, and prove the robustness of our $\mathcal{A}_I$ measurements. The measured isospin asymmetry in different q^2 regions could be of interest for theorists in examining $\mathcal{A}_I$ predictions as a function of q^2. Table 4.37 summarizes the $\mathcal{A}_I$ measurements we have performed in the different q^2 regions below the J/ψ resonance for combined $B \to K^*\ell^+\ell^-$ mode. The systematic uncertainties for these additional measurements have not been evaluated.
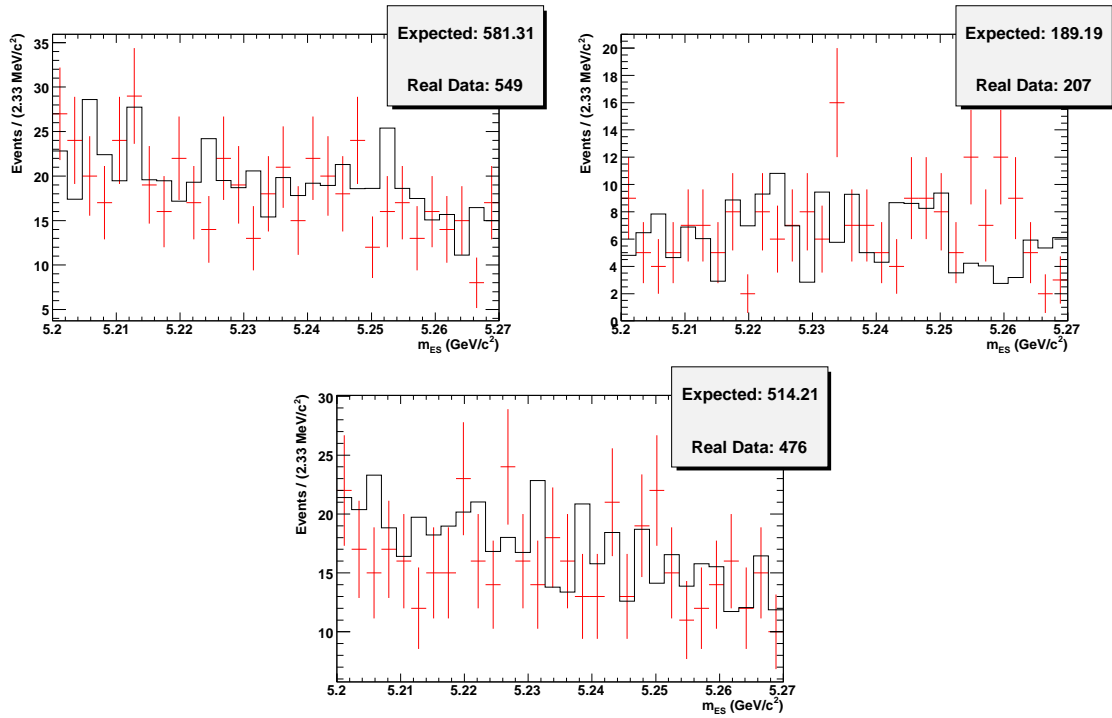
Figure 4.23: $B \to K^* e^+ e^-$ low q^2 m_{ES} distribution comparisons between data (points with error bars) and MC (solid lines) in the ΔE sideband. The corresponding modes are : $B^+ \to K^+ \pi^0 e^+ e^-$ (top left), $B^+ \to K^0_s \pi^+ e^+ e^-$ (top right), $B^0 \to K^+ \pi^- e^+ e^-$ (bottom). The actual numbers of events collected in the real data and the expected yields from MC simulation are listed in the text boxes for comparison.

| | low q^2 | |
Mode	with NN	without NN
$B^+ \to K^{*+} e^+ e^-$	$1.06^{+0.31}_{-0.28}$	$1.10^{+0.34}_{-0.31}$
$B^0 \to K^{*0} e^+ e^-$	$0.20^{+0.12}_{-0.11}$	$0.23^{+0.15}_{-0.13}$

Table 4.35: Partial branching fractions in the low q^2 region measured with and without NN selections. The errors are statistical only.

Modes	$B^+ \to K^+\pi^0 e^+e^-$	$B^+ \to K_s^0\pi^+e^+e^-$
Partial BF	$1.02^{+0.52}_{-0.49}$	$1.08^{+0.40}_{-0.34}$

Table 4.36: Measured partial BFs for individual $B^+ \to K^{*+}e^+e^-$ modes in the low q^2. The errors are statistical only.

q^2 region	$\mathcal{A}_I$	note
$0.10 < q^2 < 4.20$	$-0.38^{+0.28}_{-0.24}$	The low- q^2 as defined in Table 4.1.
$0.10 < q^2 < 5.29$	$-0.42^{+0.23}_{-0.20}$	
$0.10 < q^2 < 7.02$	$-0.56^{+0.18}_{-0.16}$	The low q^2
$0.10 < q^2 < 8.41$	$-0.55^{+0.17}_{-0.15}$	The low q^2 used in the previous measurements [11]
$1.00 < q^2 < 7.02$	$-0.49^{+0.22}_{-0.19}$	Useful for theorists

Table 4.37: Measured $\mathcal{A}_I$ in different q^2 regions below the J/ψ resonance for the combined $B \to K^*\ell^+\ell^-$ mode. The errors are statistical only.

Chapter 5

The Angular Asymmetry Measurements in $B \to K^* \ell^+ \ell^-$ Decays

5.1 Measurement Goals

This chapter will present the measurements of the integrated forward-backward asymmetry $\mathcal{A}_{FB}$ for the $B \to K^* \ell^+ \ell^-$ decays in the low q^2 and high q^2 regions separated by the J/ψ resonance. The longitudinal K polarization F_L is measured as an important input for the $\mathcal{A}_{FB}$ measurement. Furthermore, the forward-backward asymmetries in $B \to K \ell^+ \ell^-$ and $B \to J/\psi K^*$ decays are measured as cross-checks, for which null results are expected.

5.2 Optimization of the Final Selections

The definitions of low and high q^2 regions are almost the same as those in §4.9, except for a lower upper bound at $q^2 < 6.25 \, \mathrm{GeV}^2/c^4$ for the low q^2 region. This is due to a more conservative choice of the J/ψ veto region.

The event selections in the angular analysis use the same selection procedures as described in Chapter 3. For the muon PID, this analysis chooses the "Tight" selection instead of the "Loose" one used in the rate-based analysis. Thus the hadronic background is further suppressed at the cost of a reduced muon PID efficiency.

The optimization of the NN selections is based on the maximization of figure of merit $S/\sqrt{S+B}$, where S (B) is the expected yield of signal (combinatorial background) events after passing all event selection criteria in the signal region. The optimization is performed separately in each decay mode and each q^2 region.

We do not perform angular measurements in $B^0 \to K_S^0 \ell^+ \ell^-$ and $B^0 \to K_S^0 \pi^0 \ell^+ \ell^-$ modes since in these modes the flavor of b quark in a B meson cannot be tagged from its decay products. The efficiencies of final selection are similar to the numbers presented in Table 4.7 for electron modes, ranging from around 5% in the $B^+ \to K^+ \pi^0 e^+ e^-$ mode, to over 20% in the $B^+ \to K^+ e^+ e^-$ mode. The efficiencies in muon modes, however, are generally lower than those in Table 4.7 with the lowest value (1.5%)

in the $B^+ \to K^+ \pi^0 \mu^+ \mu^-$ mode low q^2 region and the highest value (9.5%) in the $B^0 \to K^+ \pi^- \mu^+ \mu^-$ mode high q^2 region.

5.3   Fit Model

The fit model is based on an unbinned maximum likelihood method for extracting F_L and $\mathcal{A}_{FB}$ in the $B \to K^* \ell^+ \ell^-$ decays. The fits are performed successively in a multi-level manner, in which the fitted values in a level are fixed and used as input for the fit in a higher level:

Fit 1   We sum all the $B \to K^* \ell^+ \ell^-$ candidate events into a combined m_{ES} distribution in the m_{ES} fit region ($m_{\mathrm{ES}} > 5.2 \, \mathrm{GeV}/c^2$) for each q^2 range. In this level, we perform a m_{ES} fit similar to that discussed in §4.2 to extract the signal and background yields.

Fit 2   In this level, we fit the $\cos\theta_K$ distribution in the signal region ($m_{\mathrm{ES}} > 5.27 \, \mathrm{GeV}/c^2$) for extracting F_L. The following parameters are fixed in the fit:

  – All fixed and floating parameters from Fit 1, as given in §4.2.5.

  – The $\cos\theta_K$ shape of the combinatorial background.

  – The $\cos\theta_K$ shape of the signal from theory and simulated efficiency corrections.

  – The $\cos\theta_K$ shape of the crossfeed contributions from simulated signal events.

Fit 3   In the highest level, we fit the $\cos\theta_\ell$ distribution also in the signal region ($m_{\mathrm{ES}} > 5.27 \, \mathrm{GeV}/c^2$) for extracting $\mathcal{A}_{FB}$. The following parameters are fixed in the fit:

  – All fixed and floating parameters from Fit 2.

  – The $\cos\theta_\ell$ shape of the combinatorial background.

  – The $\cos\theta_\ell$ shape of the signal from theory and simulated efficiency corrections.

  – The $\cos\theta_\ell$ shape of the crossfeed contributions from signal MC simulation.

It is technically possible to fit $\cos\theta_K$ and $\cos\theta_\ell$ simultaneously for improving the sensitivity of $\mathcal{A}_{FB}$ measurement. However, given the relatively small size of the fit dataset, a multi-dimensional fit will not have a high probability of converging and thus is not used.

We also perform successive fits to m_{ES} and $\cos\theta_\ell$ distributions in the combined $B^+ \to K^+ \ell^+ \ell^-$ mode. In this mode we expect a null result for $\mathcal{A}_{FB}$.

In the remainder of this section we describe the PDFs of the various signal and background components in the fits for the observables $\cos\theta_K$ and $\cos\theta_\ell$. The m_{ES} PDFs of all the components have been introduced in §4.2.

5.3.1 Signal PDFs

As already discussed in § 1.3.8, for the F_L fits in the $B \to K^*\ell^+\ell^-$ mode, the $\cos\theta_K$ signal distribution has the following theoretical form (see Equation 1.21):

$$\frac{1}{\Gamma}\frac{d\Gamma\,(B \to K^*\ell^+\ell^-)}{d\cos\theta_K} = \frac{3}{2}F_L\cos^2\theta_K + \frac{3}{4}\left(1 - F_L\right)\left(1 - \cos^2\theta_K\right). \qquad (5.1)$$

For the corresponding $\mathcal{A}_{FB}$ fits in the $B \to K^*\ell^+\ell^-$ mode, we have the following theoretical form for the $\cos\theta_\ell$ distribution (see Equation 1.25):

$$\frac{1}{\Gamma}\frac{d\Gamma\,(B \to K^*\ell^+\ell^-)}{d\cos\theta_\ell} = \frac{3}{4}F_L(1 - \cos^2\theta_\ell) + \frac{3}{8}(1 - F_L)(1 + \cos^2\theta_\ell) + A_{FB}\cos\theta_\ell. \qquad (5.2)$$

For the $\mathcal{A}_{FB}$ fits in the $B \to K\ell^+\ell^-$ decays we use (see Equation 1.26)

$$\frac{1}{\Gamma}\frac{d\Gamma\,(B \to K\ell^+\ell^-)}{d\cos\theta_\ell} = \frac{3}{4}(1 - F_S)(1 - \cos^2\theta_\ell) + \frac{1}{2}F_S + A_{FB}\cos\theta_\ell, \qquad (5.3)$$

where F_S will be fixed to zero in the fits.

In each mode and each q^2 region, the true angular distribution for $\cos\theta_\ell$ [$\cos\theta_K$] differ from its theoretical form shown above by folding with the corresponding efficiency function $\epsilon_\ell(\cos\theta_\ell)$ [$\epsilon_K(\cos\theta_K)$] in order to take into account the effect of detector acceptance:

$$P(\cos\theta_K) = \epsilon_K(\cos\theta_K) \times \frac{1}{\Gamma}\frac{d\Gamma}{d\cos\theta_K}, \qquad (5.4)$$

$$P(\cos\theta_\ell) = \epsilon_\ell(\cos\theta_\ell) \times \frac{1}{\Gamma}\frac{d\Gamma}{d\cos\theta_\ell}. \qquad (5.5)$$

The $\cos\theta_\ell$ [$\cos\theta_K$] efficiency function is parametrized as a ratio-of-histograms obtained separately for each mode and q^2 range using signal MC simulation. It is normalized by the correctly-reconstructed simulated signal events passing all event selections according to the underlying $\Gamma^{-1}d\Gamma/d\cos\theta_\ell$ [$\Gamma^{-1}d\Gamma/d\cos\theta_K$] distribution at the generator level. Figure 5.1 shows the signal efficiency functions $\epsilon_\ell(\cos\theta_\ell)$ and $\epsilon_K(\cos\theta_K)$ for $B^+ \to K^+\pi^0 e^+e^-$ in the high q^2 region as an example.

The fit methodology for extracting F_L and $\mathcal{A}_{FB}$ using Equations 5.1 and 5.2 is first tested on the simulated signal events at the generator level. These fits are performed in steps of q^2 for each $K^*\ell^+\ell^-$ sub-modes. Figure 5.2 shows the resulting values for F_L and $\mathcal{A}_{FB}$ for the $B^+ \to K^+\pi^0 e^+e^-$ mode. These fitted values are compared to the distributions predicted by the Standard Model shown in Figure 1.10. The distributions are mutually consistent.

The angular fit parameterization for $B \to K\ell^+\ell^-$ is tested at the generator level in the same way as for $B \to K^*\ell^+\ell^-$ discussed above. Again we find that $\mathcal{A}_{FB}$ is consistent with zero in the entire q^2 region.
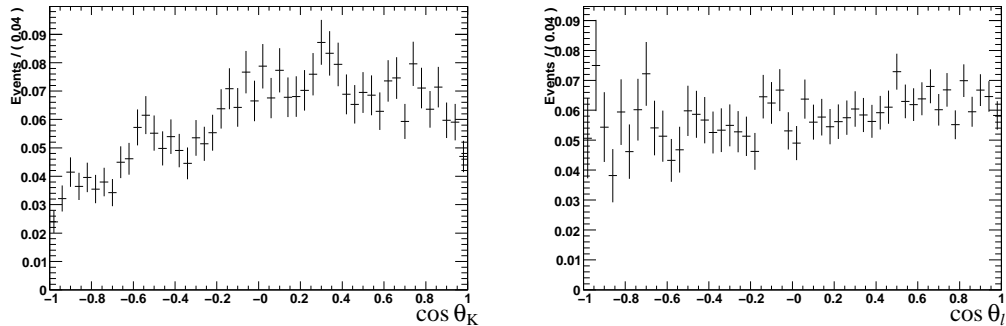
Figure 5.1: Signal efficiency as a function of $\cos\theta_K$ (left) and as a function of $\cos\theta_\ell$ (right) in the high q^2 region for $B^+ \to K^+\pi^0 e^+e^-$.
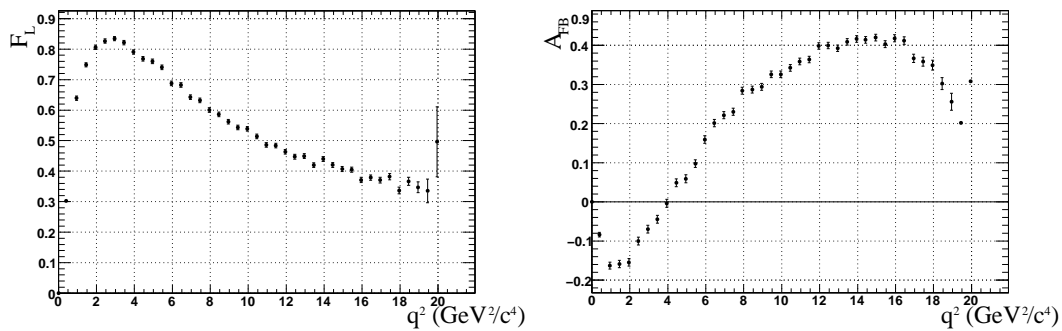

Figure 5.2: $B^+ \to K^+\pi^0 e^+e^-$ generator-level F_L (left) and $\mathcal{A}_{FB}$ (right) distribution versus q^2. Each point is the result of the fit of $\cos\theta_K$ ($\cos\theta_\ell$) distribution for F_L ($\mathcal{A}_{FB}$) in a narrow q^2 range surrounding each point. The q^2 value at which the result of each fit is reported is the center of the narrow q^2 region.
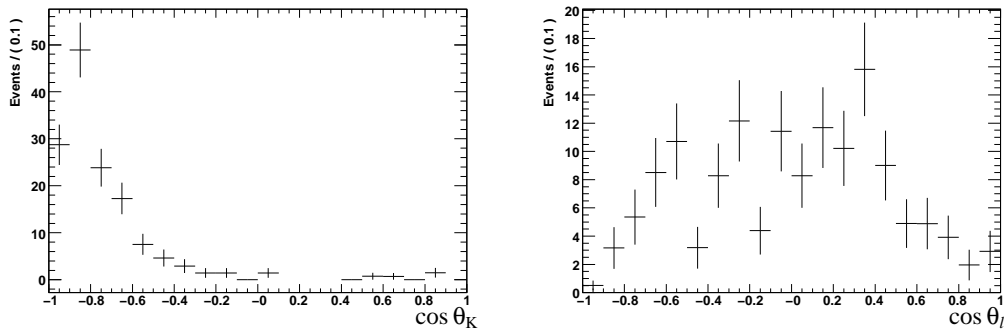
Figure 5.3: $B^0 \to K^+\pi^-e^+e^-$ feed-across as a function of $\cos\theta_K$ (left) and $\cos\theta_\ell$ (right) in the low q^2 region, both are directly taken from MC simulation, and not normalized.

Figure 5.4: $B^0 \to K^+\pi^-e^+e^-$ self-crossfeed as a function of $\cos\theta_K$ (left) and $\cos\theta_\ell$ (right) in the low q^2 region, both are directly taken from MC simulation, and not normalized.
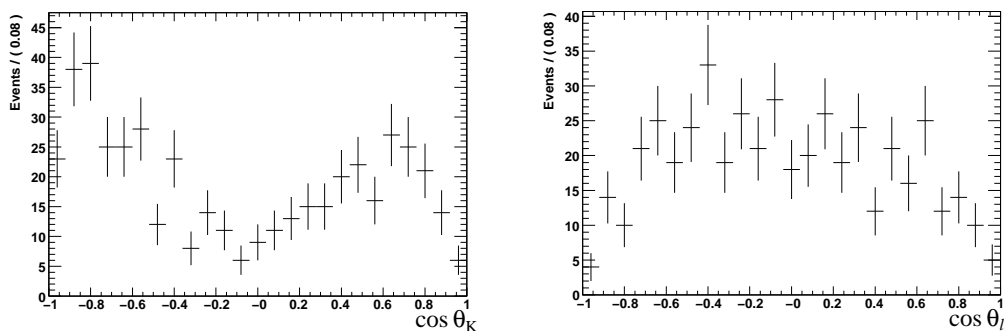
5.3.2 Feed-across between Different Modes

The $\cos\theta_K$ and $\cos\theta_\ell$ distributions for the feed-across contribution from other signal modes are modeled directly from properly normalized simulated signal events. Figure 5.3 shows the distributions of $\cos\theta_K$ and $\cos\theta_\ell$ from simulated feed-across background events for $B^0 \to K^+\pi^-e^+e^-$ in the low q^2 region.

5.3.3 Self-Crossfeed

The $\cos\theta_K$ and $\cos\theta_\ell$ distributions for the mis-reconstructed real signal events are modeled directly from corresponding simulated signal events. The normalization for this event class is taken as a fixed fraction of the fit signal yield. Figure 5.4 shows the distributions of $\cos\theta_K$ and $\cos\theta_\ell$ from simulated self-crossfeed events for $B^0 \to K^+\pi^-e^+e^-$ in the low q^2 region.

5.3.4 Combinatorial background PDFs

The $\cos\theta_\ell$ and $\cos\theta_K$ combinatorial background distributions for the angular fits are obtained from events in the m_{ES} sideband ($5.20 < m_{\mathrm{ES}} < 5.27\,\mathrm{GeV}/c^2$) of both lepton

flavor violating (LFV) $e^+ \mu^+$ and $\mu^+ e^-$ events and normal $e^+ e^-$ and $\mu^+ \mu^-$ events.

Lepton Flavor Violating (LFV) Samples

For the LFV samples we make an important distinction between μe and $e\mu$ events. In defining the lepton forward backward asymmetry for $e^+ e^-$ and $\mu^+ \mu^-$ events, the charge of the lepton which defines the angle is correlated with the flavor of the b quark (or equivalently with the presence of a K^* or $\overline{K}^*$ meson). To correctly model the $\mathcal{A}_{FB}$ distribution using the LFV events we need to make the same distinction. An event is $\mu^+ e^-$ or $e^+ \mu^-$ if it comes from a $\bar{b}$ decay and is associated with a K^{*+} or K^{*0} meson. By charge conjugation an event is $\mu^- e^+$ or $e^- \mu^+$ if it comes from a b decay, and is associated with a K^{*-} or $\overline{K}^{*0}$ meson. The μe sample is the combination of $\mu^+ e^-$ from $\bar{b}$ and $\mu^- e^+$ from b, and likewise for the $e\mu$ sample.

Angular PDFs

The combinatorial background events passing all the event selections mainly originate from two $B\overline{B}$ background sources. One source consists of $B\overline{B}$ events in which two uncorrelated leptons are produced in the semileptonical decays of both B mesons ("uncorrelated" background events). The other source is $B \to D^{(*)} \ell \nu$ events in which the D meson (or its long-lived charm daughter in the case of excited D states) subsequently decays semileptonically through $D \to \overline{K}^* \ell \nu$ ("cascade" background events). Since in each of these background sources, two leptons only have a charge correlation between each other to resemble a signal $K^* \ell^+ \ell^-$ event. Therefore, the samples of LFV decays from both real data and MC simulation can be used for modeling the combinatorial background.

In order to study the angular distributions for the combinatorial backgrounds, we have selected a large background data sample with relaxed requirements on the NN outputs. Figure 5.5 shows the $\cos \theta_\ell$ distribution for these events in the grand sideband region for each type of LFV and standard di-lepton events. Comparing these distributions with each other, we observe a very large discrepancy at $\cos \theta_\ell > 0.7$, where a prominent spike is present in the μe and $e^+ e^-$ events but substantially reduced in the $\mu^+ \mu^-$ and $e\mu$ events. These spikes are also not modeled in MC simulation. The differences are caused by different momentum requirements for the electron and muon candidates, $p_{lab} > 0.3 \, \text{GeV}/c$ and $p > 0.7 \, \text{GeV}/c$ respectively. In addition, for cascade background events, the momentum spectra of D decays are softer than those from B decays. Thus, compared to the $e\mu$ ($\mu^+ \mu^-$) samples, the μe ($e^+ e^-$) samples contain more cascade decays than the $e\mu$ ($\mu^+ \mu^-$) samples, which contribute to the spike at large $\cos \theta_\ell$.

Concerning the momentum acceptance effects shown above, the $\cos \theta_\ell$ distributions for the LFV and standard di-lepton events are reasonably well-correlated across the m_{ES}-ΔE plane. However, although there is no dramatic change in the distribution of $\cos \theta_\ell$ as a function of ΔE, there are variations with respect to m_{ES}. Figure 5.6 shows the concatenated data events in the GSB region with m_{ES} greater and less than $5.2 \, \text{GeV}/c^2$. The $\cos \theta_\ell$ distribution for events with $m_{\text{ES}} > 5.2 \, \text{GeV}/c^2$ is nearly monotonic with the greatest value at $\cos \theta_\ell \sim 1$.
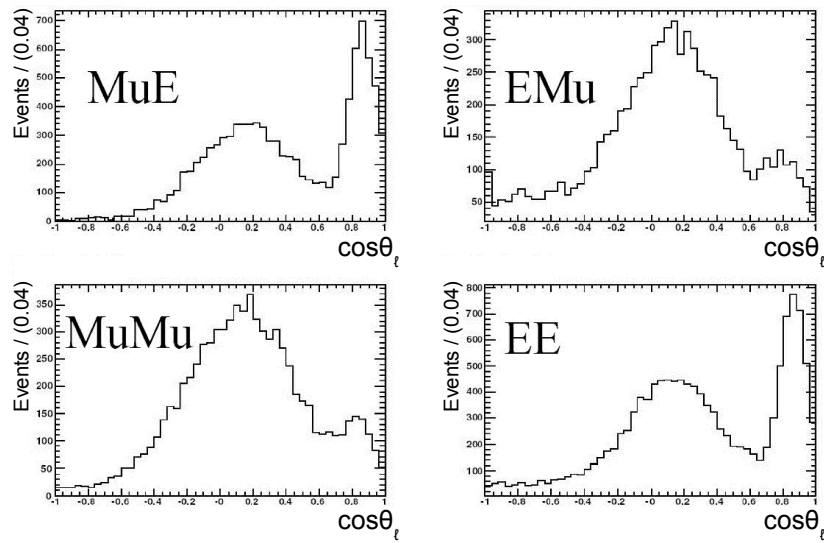
Figure 5.5: $\cos\theta_\ell$ distributions for standard and LFV data events in the GSB region with relaxed NN selections. "MuE" and "EMu" are for the μe and $e\mu$ LFV events, while "MuMu" and "EE" are for the standard e^+e^- and $\mu^+\mu^-$ events.
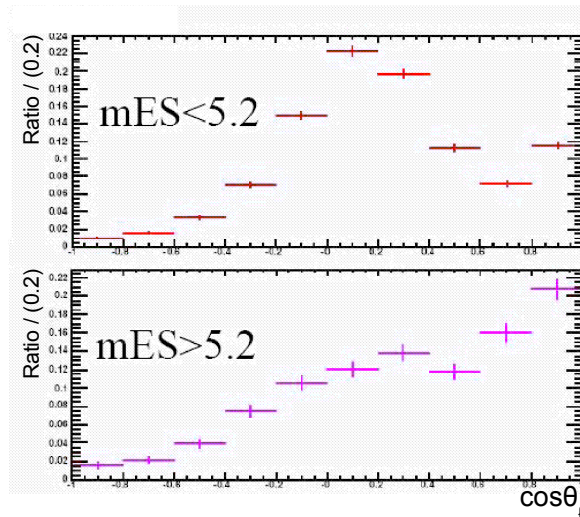

Figure 5.6: $\cos\theta_\ell$ distributions for the sum of the LFV and standard di-lepton data events in the GSB region with (top) $m_{\mathrm{ES}} < 5.2\,\mathrm{GeV}/c^2$ and (bottom) $m_{\mathrm{ES}} > 5.2\,\mathrm{GeV}/c^2$.
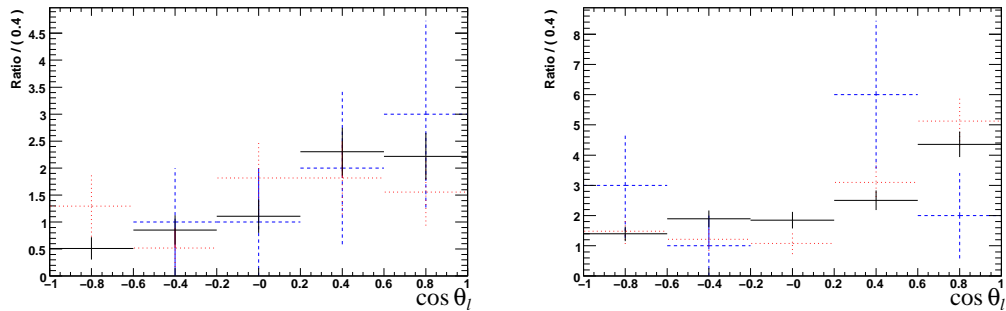
Figure 5.7: $\cos \theta_\ell$ distributions for different data events in the low q^2 (left) and high q^2 (right) regions: the LFV events in the signal region (dashed lines), the LFV events in the sideband region (dotted lines), the standard di-lepton events in the sideband region (solid lines). Each distribution is normalized to the number of LFV events in the signal region.

Figures 5.7 shows the $\cos \theta_\ell$ distributions of the LFV and standard data events in the m_{ES} sideband region, and the LFV data events in the signal region. For the $\cos \theta_\ell$ distributions in the sideband region, they are normalized to the distribution of the LFV events in the signal region. We have performed Kolmogorov tests [80] on the likelihoods between the $\cos \theta_\ell$ distributions from three classes of data samples mentioned above, which generally show large probabilities and tend to confirm the hypothesis that each distribution is equivalent to the others within the available statistical precision.

Modeling of Angular Distributions

We observe the following facts concerning the combinatorial background in the $\cos \theta_\ell$ distribution:

- It is poorly modeled in simulated events,

- It is affected by the lepton momentum acceptance,

- And it fluctuates as a function of m_{ES} and also has a weak dependence on ΔE.

Therefore, we conclude that a robust model for the combinatorial angular PDFs can only be obtained from data events that lie as close as possible to the signal region. We have shown that the LFV data events in the signal region is well-modeled by both the LFV and standard data events in the sideband region. Thus, we first perform the one-dimensional m_{ES} fit in order to obtain the signal and background yields and the ARGUS shape parameter. Now the angular fits will be limited to events in the signal region and the angular PDFs will be constructed as step functions. The shapes of the step functions are modeled using the LFV and standard data events in the m_{ES} sideband region. The normalization of the angular PDF in this region for the angular fits will be taken from a partial integration of the ARGUS PDF determined in the precedent m_{ES} fit over the m_{ES} signal region.

Additionally, although the $\cos \theta_K$ distributions show little of the correlations present in $\cos \theta_\ell$, we use exactly the same prescription given above to obtain the $\cos \theta_K$ combinatorial PDF and fit for F_L.
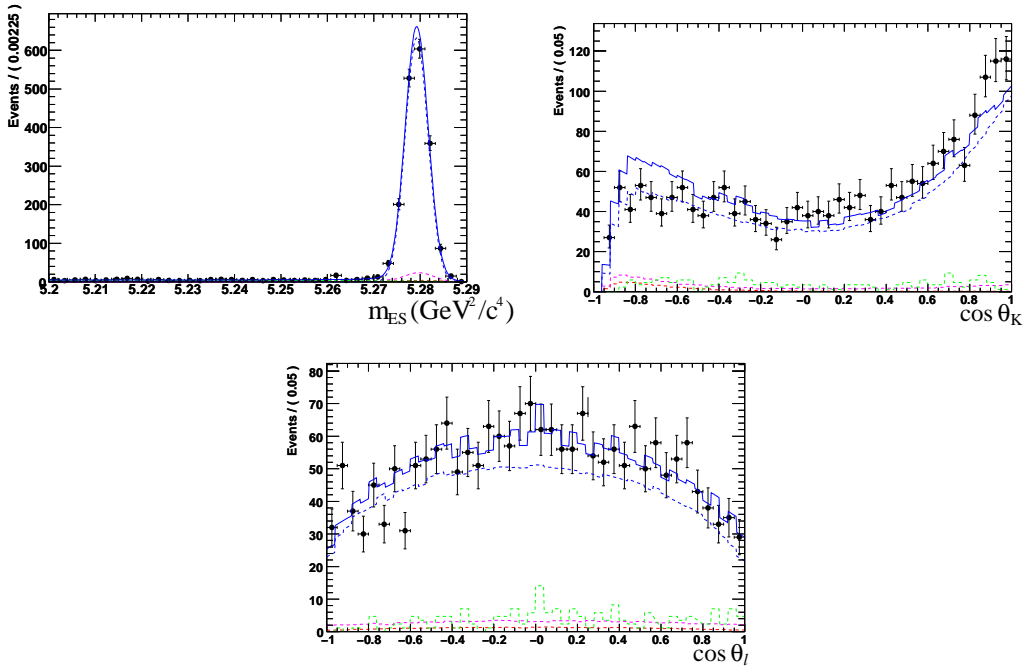
Figure 5.8: m_{ES}, $\cos\theta_K$ and $\cos\theta_\ell$ distributions (in clockwise direction) in the $B^0 \to J/\psi\,(\to \mu^+\mu^-)K^{*0}(\to K^+\pi^-)$ sample, with the successive fits for F_L and $\mathcal{A}_{FB}$ overlaid. In each plot, the data points are shown with total fit (solid), signal (dashed blue), combinatorial (dashed green), self-crossfeed (dashed magenta) and feed-across (dashed red) background components superimposed. All the background components are rather small compared to the signal.

5.4   Charmonium Control Samples

Similarly as for the rate-based analysis, we also examine the angular fits using large samples of vetoed charmonium events. In J/ψ samples, we account for all the signal and background PDF components described above and fit to all six K^* decay modes for extracting F_L and $\mathcal{A}_{FB}$.

Figure 5.8 shows the angular fits in the $B^0 \to J/\psi\,(\to \mu^+\mu^-)K^{*0}(\to K^+\pi^-)$ sample. The fits are performed in the same manner as discussed in §5.3. Table 5.1 shows the F_L and $\mathcal{A}_{FB}$ results for each $K^*\ell^+\ell^-$ mode using only the NN selections for the high q^2 range. The measured F_L values are compared to previously measured K^* polarization $F_L = 0.56 \pm 0.01$ in the $B \to J/\psi K^*$ decay [81]. The measured $\mathcal{A}_{FB}$ values are also compared to the null expectation of lepton asymmetry $\mathcal{A}_{FB} = 0$. The agreement is generally good to be within 2σ and indicate the robustness of our angluar fits.

Mode	$\mathcal{B}(10^{-3})$	F_L	$\mathcal{A}_{FB}$
$K^+\pi^0\mu^+\mu^-$	1.50 ± 0.09	0.54 ± 0.03	-0.04 ± 0.05
$K_S^0\pi^+\mu^+\mu^-$	1.43 ± 0.08	0.55 ± 0.02	$+0.00 \pm 0.05$
$K^+\pi^-\mu^+\mu^-$	1.30 ± 0.03	0.56 ± 0.02	-0.02 ± 0.02
$K^+\pi^0 e^+ e^-$	1.57 ± 0.06	0.54 ± 0.03	$+0.02 \pm 0.03$
$K_S^0\pi^+ e^+ e^-$	1.48 ± 0.06	0.55 ± 0.02	-0.02 ± 0.04
$K^+\pi^- e^+ e^-$	1.35 ± 0.03	0.56 ± 0.02	$+0.01 \pm 0.02$

Table 5.1: Measured $B \to J/\psi K^*$ branching fractions, F_L and $\mathcal{A}_{FB}$ in different final state modes. The NN selections for the high q^2 region are used. The world average values for $B^0 \to K^{*0} J/\psi(\to \ell^+\ell^-)$ and $B^+ \to K^{*+} J/\psi(\to \ell^+\ell^-)$ are $(1.33 \pm 0.06, 1.41 \pm 0.08) \times 10^{-3}$, respectively [68]. The previously measured K^* polarization is $F_L = 0.56 \pm 0.01$ [81], and the expected lepton asymmetry $\mathcal{A}_{FB} = 0$.

5.5   Estimation of the Hadronic and Peaking Backgrounds

5.5.1   Hadronic Backgrounds

The hadronic backgrounds are estimated using the procedure described in §4.6.1 with a slight modification. The weighting methodology for estimating the hadronic background contribution is about the same, except for using different muon PID selectors. The most prominent difference lies in the modeling of the hadronic PDFs. The rate-based analysis directly uses the weighted histograms, while in the angular analysis, these histograms are fitted with a Gaussian shape signal plus an ARGUS shape background for extracting peaking (signal-like) contributions only. The hadronic background m_{ES} distribution is now modeled by the fitted signal yield and Gaussian shape parameters, which is summarized for each mode in each q^2 region in Table 5.2. The ARGUS shape background is used to account for the combinatorial background contribution.

For the $\cos\theta_K$ and $\cos\theta_\ell$ distributions of the peaking contribution in the hadronic background, they are modeled from the weighted data control sample in the m_{ES} signal region, and with the combinatorial contribution subtracted. The normalization of the combinatorial contribution in the signal region is evaluated from the m_{ES} fits described above, while the angular distribution shapes of the combinatorial contribution are directly taken from events in the m_{ES} sideband.

5.5.2   Peaking backgrounds

Both the normalizations and the shapes of the peaking backgrounds from either charmonium leakage or dalitz decays (described in §4.6.2 and §4.6.4 respectively) are determined from the corresponding simulated events. The total expected contribution from these sources is trivial and less than one event in each final state and q^2 region.

Mode	q^2 region	N Peaking	(+) error	(-) error
$B^+ \to K^+ \mu^+ \mu^-$	low	0.259	+0.085	-0.090
" "	high	1.023	+0.349	-0.313
$B^+ \to K^+ \pi^0 \mu^+ \mu^-$	low	0.180	+0.082	-0.062
" "	high	0.450	+0.152	-0.162
$B^+ \to K_S^0 \pi^+ \mu^+ \mu^-$	low	0.171	+0.070	-0.060
" "	high	0.167	+0.188	-0.089
$B^0 \to K^+ \pi^- \mu^+ \mu^-$	low	0.368	+0.162	-0.130
" "	high	0.675	+0.234	-0.178

Table 5.2: Peaking contribution of the hadronic background by mode and q^2 range. "N Peaking" is the expected peaking contribution from the fitted signal yield. The fitted higher and lower errors are followed respectively.

5.6   MC Experiments

Based on the complete fit model described in §5.3, we perform MC experiments by fitting to 700 simulated datasets with embedded signal events drawn from signal MC samples in each q^2 region and for both $K\ell^+\ell^-$ and $K^*\ell^+\ell^-$ modes. The input Standard Model values of F_L and $\mathcal{A}_{FB}$ for the dataset generation are reproduced in the fits, with negligible biases, as the pull distributions shown in Figure 5.9. We also have performed the MC experiments with the embedded signal events generated based on various models beyond Standard Model, in which a wide range of values of Wilson coefficients C_7^{eff}, C_7^{eff} and C_9^{eff} are tested. Different inputs of F_L and $\mathcal{A}_{FB}$ predicted by these models are applied for generating test datasets, and again reproduced in the fits without significant biases.

5.7   Systematic Errors

We consider several sources of systematic uncertainty in the fit of F_L from the $\cos\theta_K$ distribution and $\mathcal{A}_{FB}$ from the $\cos\theta_\ell$ distribution:

- The error on the signal yield from the m_{ES} fit is propagated into the F_L and $\mathcal{A}_{FB}$ fits. To bound the systematic errors, we vary the fitted ARGUS shape parameter ξ by $\pm 1\sigma$ from its central value and repeat the m_{ES} fit with ξ fixed to extract new values for the signal and background yields. These new values are then used as inputs in the F_L and $\mathcal{A}_{FB}$ fits to determine the shift of the central values of F_L and $\mathcal{A}_{FB}$.

- The error on F_L from the fit to the $\cos\theta_K$ distribution is propagated into the $\mathcal{A}_{FB}$ fit. This systematic error of $\mathcal{A}_{FB}$ is determined through varying the value of F_L by $\pm 1\sigma$ from its fitted central value, and refitting the $\cos\theta_\ell$ distribution.

- The combinatorial background shape and normalization. We assign a systematic error from the background shape by dividing the sideband samples into two non-overlapping m_{ES} regions separated by $m_{\mathrm{ES}} = 5.23\,\mathrm{GeV}/c^2$. The average shifts of
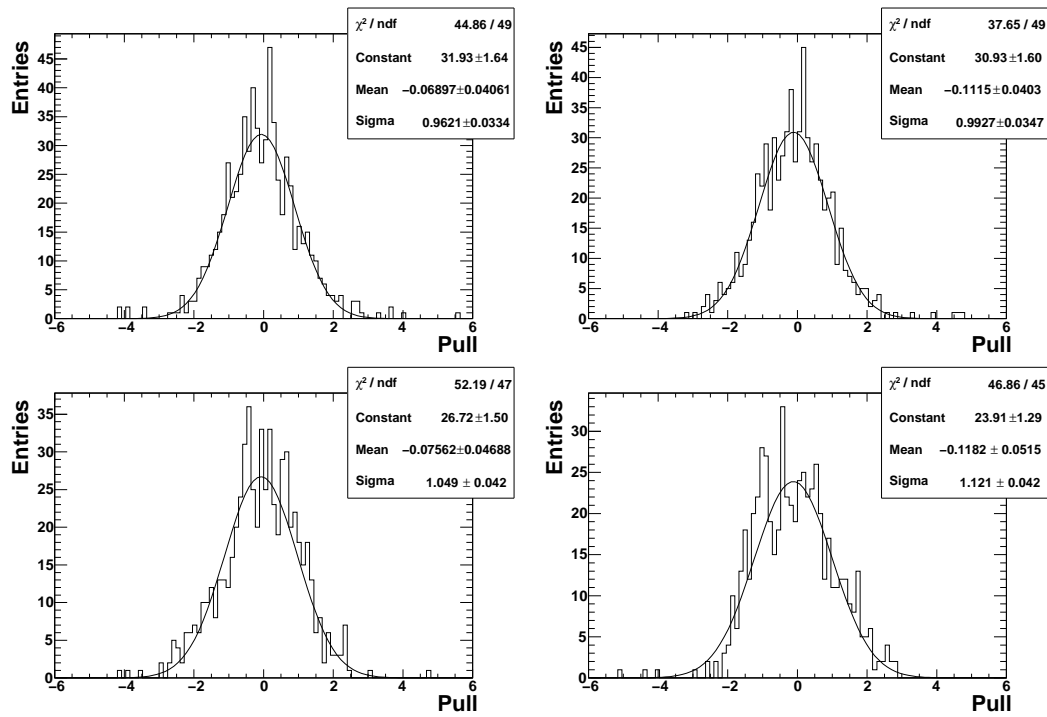
Figure 5.9: F_L (top two plots) and $\mathcal{A}_{FB}$ (bottom two) pull distributions for $K^* \ell^+ \ell^-$ decays in the low (left two) and high (right two) q^2 regions, with fits to a Gaussian distribution overlaid. The goodness-of-fits ($\chi^2/n.d.o.f$) and fit parameters are shown in the text boxes.

$\mathcal{A}_{FB}$ and F_L values between the default fits with the full sideband sample and the fits using the two sub-samples mentioned above are taken as the background shape systematics.

- Self-crossfeed within the signal mode and feed-across from other modes. The systematic error from these sources is bounded by floating their normalizations in the fits to the charmomium control samples.

- The Gaussian signal shape. This systematic error is bounded through varying the mean and the width of the Gaussian PDF within the ranges allowed by the m_{ES} fits to the charmomium control samples.

- The peaking backgrounds from hadronic decays and charmonium leakage. To determine the systematics for the charmonium leakage, we scale the background according to the $\sim 10\%$ uncertainty on the charmonium branching fraction. For the hadronic peaking backgrounds, we scale the background according to the fit errors from the hadronic control samples given in Table 5.2. Since these backgrounds are only at the level of ~ 0.1 events, the resulting systematic errors for F_L and $\mathcal{A}_{FB}$ are negligible.

- The signal efficiency as a function of variations in the Wilson coefficients C_7^{eff}, C_9^{eff} and C_{10}^{eff}. Samples of simulated signal events based on models with varied values of C_7^{eff}, C_9^{eff} and C_{10}^{eff} are used to analyze the shifts of the signal reconstruction efficiencies.

- The signal efficiency for different form factors. This systematics is also determined through generating signal events with different form factors [20, 77].

- The average bias on the central values of F_L and $\mathcal{A}_{FB}$ obtained from the MC experiments described in § 5.6

- The selection of the final ΔE fit window. This is treated only as a cross-check to ensure that there are no hidden systematics associated with our rather tight ΔE selection. We perform the complete analysis with different ΔE windows to collect the new values of F_L and $\mathcal{A}_{FB}$. No notable shift from the original results is observed.

For the sources of the systematics uncertainties listed above, with the exception of the last one, all these sources are treated as additive uncertainties on the central values of the asymmetries. They are regarded as independent and summed up in quadrature terms for the total systematics uncertainty. The systematic uncertainties are summarized in Table 5.3, where the modeling of the signal events is the largest uncertainty source.

| Source | F_L systematic | | $\mathcal{A}_{FB}$ systematic | |
of Error	low q^2	high q^2	low q^2	high q^2
m_{ES} fit yields	0.001	0.016	0.003	0.002
F_L fit error	—	—	0.025	0.022
Background shape	0.006	0.020	0.027	0.006
Signal model	0.036	0.034	0.030	0.038
Fit bias	0.012	0.020	0.023	0.052
Efficiency/crossfeed	0.010	0.010	0.020	0.020
Total	0.04	0.09	0.10	0.08

Table 5.3: Systematic errors on the measurements of F_L and $\mathcal{A}_{FB}$ for the $K^* \ell^+ \ell^-$ decays.

q^2 region	N_S	$\mathcal{A}_{FB}$
low	26.0 ± 5.7	$+0.04^{+0.16}_{-0.24}$
high	26.5 ± 6.7	$+0.20^{+0.14}_{-0.22}$

Table 5.4: Measured $\mathcal{A}_{FB}$ in $B^+ \to K^+ \ell^+ \ell^-$ decays. The included errors are only statistical. N_S is the signal yield obtained from the m_{ES} fit.

5.8   Final Results

5.8.1 $B^+ \to K^+ \ell^+ \ell^-$ Fits For $\mathcal{A}_{FB}$

Figure 5.10 shows the $B^+ \to K^+ \ell^+ \ell^-$ $\cos \theta_\ell$ fits for $\mathcal{A}_{FB}$ in the low q^2 and high q^2 regions. Table 5.4 lists the $\mathcal{A}_{FB}$ results from the successive m_{ES} and $\cos \theta_\ell$ fits to the data for the $B^+ \to K^+ \ell^+ \ell^-$ decays, along with the fitted signal yields. In both q^2 bins, the measured asymmetries are consistent with a null result, and again, prove the unbiased nature of our fit methodology.

5.8.2 $B \to K^* \ell^+ \ell^-$ Fits

Figure 5.13 shows the final fit results with the total fit, signal and random combinatorial PDF components overlaid on the data points. The measured F_L and $\mathcal{A}_{FB}$ results with systematic errors are presented in Table 5.5.

5.9   Comparison of the Results

We compare our F_L and $\mathcal{A}_{FB}$ results with the previous BABAR measurements based on $208 \, \text{fb}^{-1}$ data [11], which are summarized in Table 5.6. In the previous measurements, for $\mathcal{A}_{FB}$ in the low q^2 region only the lower limit at 95% confidence level was set due to an unconverged $\mathcal{A}_{FB}$ fit. Our new results for both F_L and $\mathcal{A}_{FB}$ are in good agreement with the previous observations. The largest deviation comes from the F_L measurement in the low q^2 region, which may due to a different low q^2 region and
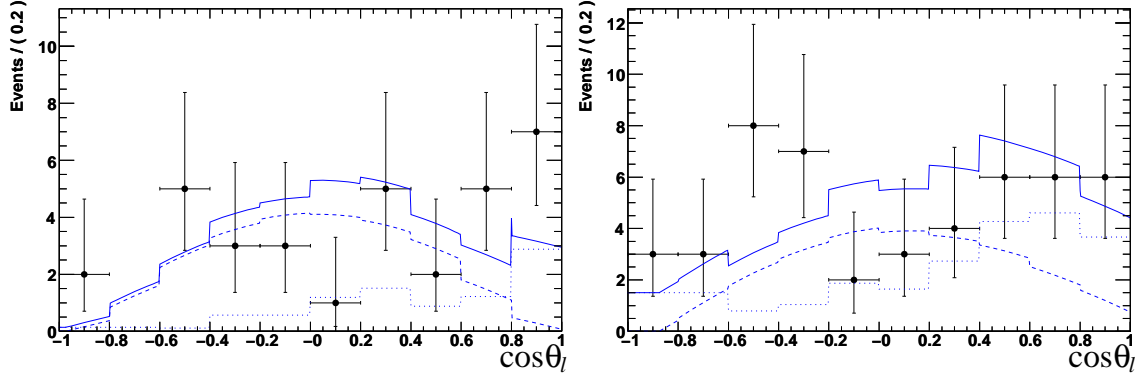
Figure 5.10: Distributions of $\cos\theta_\ell$ in the $B^+ \rightarrow K^+\ell^+\ell^-$ decays with fit curves overlaid for the low q^2 (left) and high q^2 (right) regions. In each plot, the data points are shown with the total fit (solid line), signal (dashed line), and random combinatorial background (dotted line) components superimposed.

q^2 region	N_S	F_L	$\mathcal{A}_{FB}$
low	27.2 ± 6.3	$0.35 \pm 0.16 \pm 0.04$	$+0.24^{+0.18}_{-0.23} \pm 0.05$
high	36.6 ± 9.6	$0.71^{+0.20}_{-0.22} \pm 0.04$	$+0.76^{+0.52}_{-0.32} \pm 0.07$

Table 5.5: Measured F_L and $\mathcal{A}_{FB}$ in the $B \rightarrow K^*\ell^+\ell^-$ decays. N_S is the signal yield obtained from the m_{ES} fit, for which only the statistical error is given. For F_L and $\mathcal{A}_{FB}$, both statistical and systematic errors are shown successively.
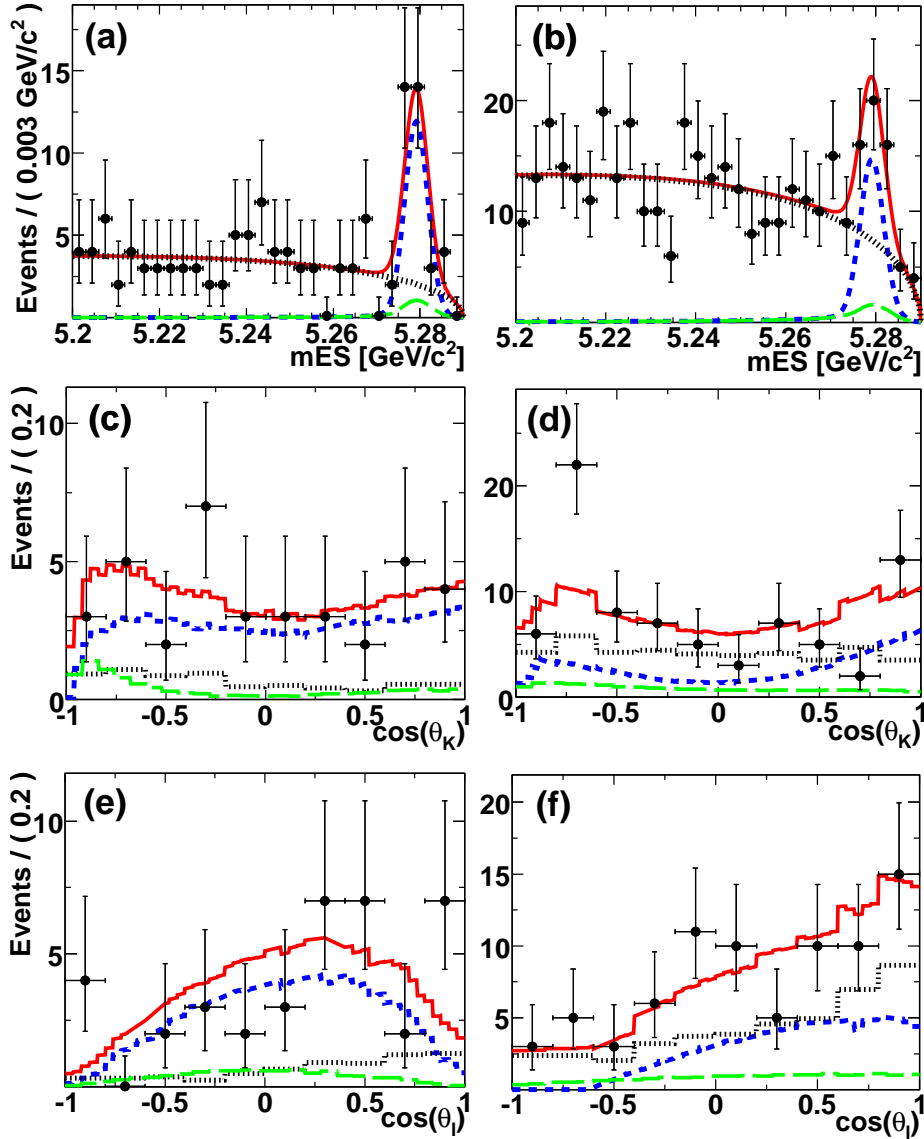
Figure 5.11: $K^*\ell^+\ell^-$ fits: (a) low q^2 m_{ES}, (b) high q^2 m_{ES}, (c) low q^2 $\cos\theta_K$, (d) high q^2 $\cos\theta_K$, (e) low q^2 $\cos\theta_\ell$, (f) high q^2 $\cos\theta_\ell$; with combinatorial (dots) and peaking (long dash) background, signal (short dash) and total (solid) fit distributions superimposed on the data points.

different combinatorial background suppression and modeling techniques used. We are more confident in our results since compared to previous measurements, (a) our fit techniques are simpler; (b) we use more sophisticated event selection techniques with NNs; (c) we have almost no dependence on simulated events. We also find good agreement through comparing our $\mathcal{A}_{FB}$ results with the latest Belle results based on 357 fb^{-1} data [82], as shown in Figure 5.12.

The comparison between our results and different theoretical predictions based on different C_7^{eff} and $C_9^{eff} C_{10}^{eff}$ signs is shown in Figure 5.13. In the low q^2 region,
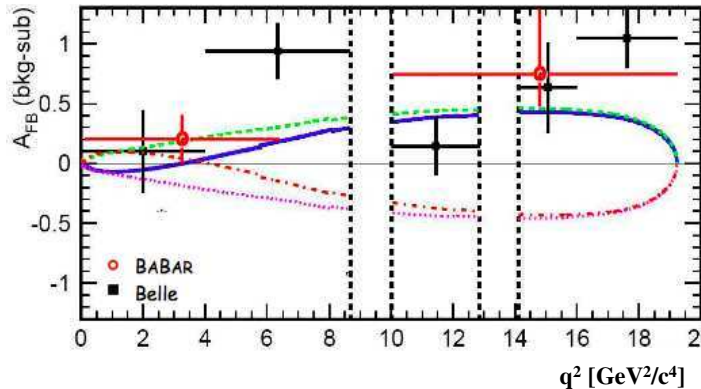
Figure 5.12: Comparison of the *BABAR* 349 fb^{-1} (open circles) and Belle 357 fb^{-1} (solid points) results for $\mathcal{A}_{FB}$ as a function of q^2 [83]. Different q^2 regions have been defined in different experiments.

Observable	q^2	208 fb^{-1} Result	349 fb^{-1} Result
F_L	low	$0.77^{+0.63}_{-0.30} \pm 0.07$	$0.35 \pm 0.16 \pm 0.04$
	high	$0.51^{+0.22}_{-0.25} \pm 0.08$	$+0.71^{+0.20}_{-0.22} \pm 0.04$
$\mathcal{A}_{FB}$	low	> 0.19 (95% CL)	$+0.24^{+0.18}_{-0.23} \pm 0.05$
	high	$+0.72^{+0.28}_{-0.26} \pm 0.08$	$+0.76^{+0.52}_{-0.32} \pm 0.07$

Table 5.6: Comparison of the previous ("208 fb^{-1}") [11] and our new ("349 fb^{-1}") F_L and $\mathcal{A}_{FB}$ results for $B \to K^*\ell^+\ell^-$ decays. Note that in the previous analysis, the upper bound for low q^2 is slightly higher at $q^2 < 8.41$ GeV/c^2. Both statistical and systematic errors are given successively for each result.

from the Standard Model predictions, we expect $\mathcal{A}_{FB} = -0.03 \pm 0.01$ [84] and $F_L = 0.63 \pm 0.03$ [51]. Our $\mathcal{A}_{FB}$ result, however, shows about one standard deviation from the Standard Model prediction and the flipped sign C_7^{eff} ($C_7^{eff} = -C_7^{SM}$) model is favored. While in the high q^2 region, the Standard Model expectation is $\mathcal{A}_{FB} = 0.26 \pm 0.01^{+0.00}_{-0.05}$ (where the first and second errors are due to uncertainties arising from perturbative and non-perturbative sources, respectively) [30, 85] and $F_L \sim 0.40$ [51]. In this q^2 region, our $\mathcal{A}_{FB}$ result excludes the flipped sign $C_9^{eff} C_{10}^{eff}$ models ($C_9^{eff} C_{10}^{eff} = -C_9^{SM} C_{10}^{SM}$) at more than 3σ significance level.
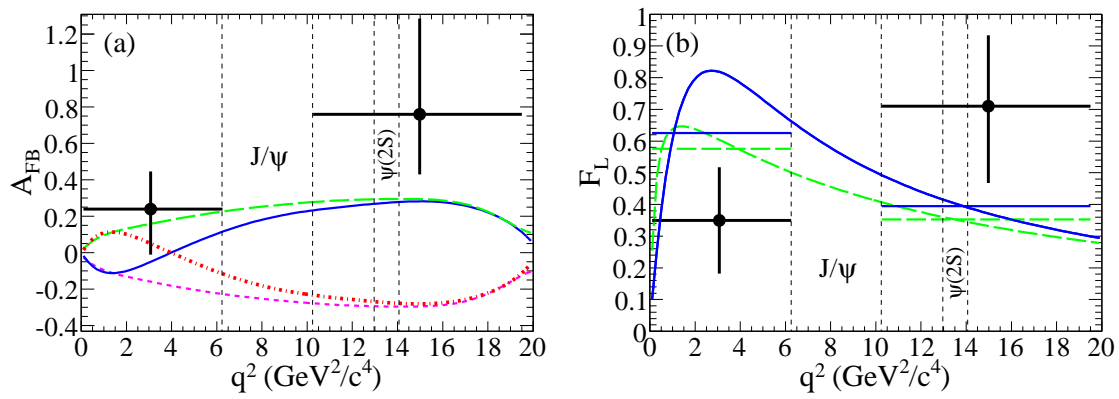
Figure 5.13: Our (a) $\mathcal{A}_{FB}$ and (b) F_L results (points with error bars) for the $B \to K^* \ell^+ \ell^-$ decays are compared to the predictions from the Standard Model (solid); $C_7^{eff} = -C_7^{SM}$ (long dash); $C_9^{eff} C_{10}^{eff} = -C_9^{SM} C_{10}^{SM}$ (short dash); $C_7^{eff} = -C_7^{SM}, C_9^{eff} C_{10}^{eff} = -C_9^{SM} C_{10}^{SM}$ (dash-dot). In our results, the statistical and systematic errors are added in quadrature terms. Expected F_L values from the integrations over both two q^2 regions are also shown as straight lines. The flipped-sign $C_9^{eff} C_{10}^{eff} = -C_9^{SM} C_{10}^{SM}$ will not bring notable changes to F_L values, and these F_L curves are thus not shown.

Chapter 6

Conclusion and Outlook

In summary, we have performed a series of measurements on the rare decays $B \rightarrow K\ell^+\ell^-$ and $B \rightarrow K^*\ell^+\ell^-$, based on a sample of 384 million $B\bar{B}$ events collected with the BABAR detector. Besides the total branching fractions, these measurements include the partial branching fractions, direct CP asymmetries, lepton flavor ratios, isospin asymmetries, longitudinal K^* polarization, and lepton forward-backward asymmetries for di-lepton invariant mass below and above the J/ψ resonance.

For the total branching fractions averaged between charged and neutral B mesons, we have measured:

$$\mathcal{B}(B_d \rightarrow K\ell^+\ell^-) = (0.394^{+0.073}_{-0.069} \pm 0.020) \times 10^{-6},$$
$$\mathcal{B}(B_d \rightarrow K^*\ell^+\ell^-) = (1.11^{+0.19}_{-0.18} \pm 0.07) \times 10^{-6}.$$

For each result, the first uncertainty is statistical, and the second is systematic. The observations are consistent with previous measurements, as well as the Standard Model predictions. Our partial BF measurements also agree well with the Standard Model predictions.

In the entire q^2 region, the measured direct CP asymmetries in the $B \rightarrow K^{(*)}\ell^+\ell^-$ decays are consistent with zero, and the measured $R_{K^{(*)}}$ ratios in different q^2 regions are consistent with lepton universality. We also find $\mathcal{A}_{CP}$ and $R_{K^{(*)}}$ consistent with the Standard Model predictions in separate q^2 regions.

Our $\mathcal{A}_I$ measurements for the $B \rightarrow K^{(*)}\ell^+\ell^-$ decays are the first of this type. We observe no statistically significant isospin asymmetries for either the entire q^2 region or the high q^2 region above the J/ψ resonance. However, in the low q^2 ($0.1 < q^2 < 7.02\,\text{GeV}^2/c^4$) region, we observe large isospin asymmetries for both $B \rightarrow K\ell^+\ell^-$ and $B \rightarrow K^*\ell^+\ell^-$ modes. Since we do not find any evidence for $B^0 \rightarrow K^0_S\ell^+\ell^-$ decays in the low q^2 region, the measurement in the $B \rightarrow K\ell^+\ell^-$ modes yields a result with an unphysical central value: $\mathcal{A}_I^K = -1.43^{+0.56}_{-0.85} \pm 0.05$. In the $B \rightarrow K^*\ell^+\ell^-$ modes, we observe $\mathcal{A}_I^{K^*} = -0.56^{+0.17}_{-0.15} \pm 0.03$, which is more consistent with the flipped-sign C_7^{eff} model than with the Standard Model. The significances for $\mathcal{A}_I^K$ and $\mathcal{A}_I^{K^*}$ to be different from a null hypothesis are 3.2σ and 2.7σ respectively, including systematic uncertainties. By combining the results from the $B \rightarrow K^{(*)}\ell^+\ell^-$ decays, we have $\mathcal{A}_I^{K^{(*)}} = -0.64^{+0.15}_{-0.14} \pm 0.03$, with a significance of 3.9σ from a null result including systematic uncertainties.

For the $B \to K^* \ell^+ \ell^-$ decays, we have measured $F_L = 0.35 \pm 0.16 \pm 0.04$, $\mathcal{A}_{FB} = 0.24^{+0.18}_{-0.23} \pm 0.05$ in the low q^2 $(0.1 < q^2 < 7.02 \,\text{GeV}^2/c^4$ region; and $F_L = 0.71^{+0.20}_{-0.22} \pm 0.04$, $\mathcal{A}_{FB} = 0.76^{+0.52}_{-0.32} \pm 0.07$ in the high q^2 $(q^2 > 10.24 \,\text{GeV}^2/c^4)$ region. All these results are consistent with previous *BABAR* and Belle measurements . The $\mathcal{A}_{FB}$ result in the low q^2 region also update the earlier *BABAR* measurement, in which only a lower limit was set. Though our results generally agree with the Standard Model predictions, they favor the flipped-sign C_7^{eff} model over the Standard Model. Furthermore, the flipped-sign $C_9^{eff} C_{10}^{eff}$ model is excluded at more than 3σ level.

The *BABAR* detector and PEP-II have ended operations since April 2008, and the full *BABAR* data sample comprises 465 million $B\overline{B}$ events, which is $\sim 20\%$ larger than that used in this thesis. We will update our current results by performing the same measurements on this data sample. With improved muon PID and event selection techniques, the improvements in measurement sensitivities are expected to be better than the purely statistical gain. We will also work on a sum of exclusive modes $B \to Kn\pi\ell^+\ell^-$ $(n \le 4$, with up to one $\pi^0)$ to approximate the inclusive $B \to X_s \ell^+ \ell^-$ decays using the full data sample. The measurements of the total and partial branching fractions, different rate-based asymmetries and $\mathcal{A}_{FB}$ in the inclusive $B \to X_s \ell^+ \ell^-$ decays are expected to place tight constraints on possible new physics, since these observables are better predicted than in the exclusive $B \to K^{(*)} \ell^+ \ell^-$ decays.

Since there is no more data from the *BABAR* experiment, we have to rely on future experiments to improve measurement precisions. The LHCb experiment located at CERN will start data-taking in 2008/2009. Based on one nominal year of data, a number of 3700 signal $B \to K^* \mu^+ \mu^-$ events in the q^2 range $4m_\mu^2 < q^2 < 9 \,\text{GeV}^2/c^4$ are expected, and the zero-crossing point for $\mathcal{A}_{FB}$ can be measured at a precision of $\sim 0.46 \,\text{GeV}^2/c^4$ [86]. The proposed SuperKEKB project as an upgrade to the current KEKB factory, has a design luminosity of 4×10^{35} cm^{-2}s^{-1} [87]. If realized, it will also accumulate sufficient data for precise measurements on the exclusive $B \to K^{(*)} \ell^+ \ell^-$ and inclusive $B \to X_s \ell^+ \ell^-$ decays. However, our ultimate hope for a statistically superior data sample lies in the proposed SuperB factory, which has a design luminosity of order 10^{36} cm^{-2}s^{-1} [88], and will produce more than 10 billion $B\overline{B}$ events in just one year's running.

Bibliography

[1] S. L. Glashow *Nucl. Phys.* **22** (1961) 579–588.

[2] S. Weinberg *Phys. Rev. Lett.* **19** (1967) 1264–1266.

[3] A. Salam. Originally printed in *Svartholm: Elementary Particle Theory, Proceedings Of The Nobel Symposium Held 1968 At Lerum, Sweden*, Stockholm 1968, 367-377.

[4] G. Buchalla, A. J. Buras, and M. E. Lautenbacher *Rev. Mod. Phys.* **68** (1996) 1125–1144, `arXiv:hep-ph/9512380`.

[5] F. Englert and R. Brout *Phys. Rev. Lett.* **13** (1964) 321–322.

[6] P. W. Higgs *Phys. Rev. Lett.* **13** (1964) 508–509.

[7] G. S. Guralnik, C. R. Hagen, and T. W. B. Kibble *Phys. Rev. Lett.* **13** (1964) 585–587.

[8] N. Cabibbo *Phys. Rev. Lett.* **10** (1963) 531–532.

[9] M. Kobayashi and T. Maskawa *Prog. Theor. Phys.* **49** (1973) 652–657.

[10] S. P. Martin `arXiv:hep-ph/9709356`.

[11] **BABAR** Collaboration, B. Aubert *et al. Phys. Rev.* **D73** (2006) 092001, `arXiv:hep-ex/0604007`.

[12] S. L. Glashow, J. Iliopoulos, and L. Maiani *Phys. Rev.* **D2** (1970) 1285–1292.

[13] **BABAR** Collaboration, e. Harrison, P. F. and e. Quinn, Helen R. Papers from Workshop on Physics at an Asymmetric B Factory (BaBar Collaboration Meeting), Rome, Italy, 11-14 Nov 1996, Princeton, NJ, 17-20 Mar 1997, Orsay, France, 16-19 Jun 1997 and Pasadena, CA, 22-24 Sep 1997.

[14] J. C. Collins, D. E. Soper, and G. Sterman *Adv. Ser. Direct. High Energy Phys.* **5** (1988) 1–91, `arXiv:hep-ph/0409313`.

[15] J. B. Kogut *Rev. Mod. Phys.* **55** (1983) 775.

[16] M. A. Shifman, A. I. Vainshtein, and V. I. Zakharov *Nucl. Phys.* **B147** (1979) 385–447.

[17] K. G. Wilson *Phys. Rev.* **179** (1969) 1499–1512.

[18] B. Grinstein, M. J. Savage, and M. B. Wise *Nucl. Phys.* **B319** (1989) 271–290.

[19] A. J. Buras and M. Munz *Phys. Rev.* **D52** (1995) 186–195, `arXiv:hep-ph/9501281`.

[20] C. G. A. Ali, E. Lunghi and G. Hiller *Phys. Rev.* **D66** (2002) 034002.

[21] A. Ali `arXiv:hep-ph/9606324`.

[22] C. Bobeth, M. Misiak, and J. Urban *Nucl. Phys.* **B574** (2000) 291–330, `arXiv:hep-ph/9910220`.

[23] H. H. Asatrian, H. M. Asatrian, C. Greub, and M. Walker *Phys. Lett.* **B507** (2001) 162–172, `arXiv:hep-ph/0103087`.

[24] H. H. Asatryan, H. M. Asatrian, C. Greub, and M. Walker *Phys. Rev.* **D65** (2002) 074004, `arXiv:hep-ph/0109140`.

[25] G. Burdman *Phys. Rev.* **D52** (1995) 6400–6410, `arXiv:hep-ph/9505352`.

[26] J. L. Hewett and J. D. Wells *Phys. Rev.* **D55** (1997) 5549–5560, `arXiv:hep-ph/9610323`.

[27] E. Lunghi, A. Masiero, I. Scimemi, and L. Silvestrini *Nucl. Phys.* **B568** (2000) 120–144, `arXiv:hep-ph/9906286`.

[28] T. Feldmann and J. Matias *JHEP* **01** (2003) 074, `arXiv:hep-ph/0212158`.

[29] M. Beneke, T. Feldmann, and D. Seidel *Eur. Phys. J.* **C41** (2005) 173–188, `arXiv:hep-ph/0412400`.

[30] A. Ali, P. Ball, L. T. Handoko, and G. Hiller *Phys. Rev.* **D61** (2000) 074024, `arXiv:hep-ph/9910221`.

[31] M. Beneke, G. Buchalla, M. Neubert, and C. T. Sachrajda *Nucl. Phys.* **B606** (2001) 245–321, `arXiv:hep-ph/0104110`.

[32] M. Beneke and T. Feldmann *Nucl. Phys.* **B592** (2001) 3–34, `arXiv:hep-ph/0008255`.

[33] M. Beneke, T. Feldmann, and D. Seidel *Nucl. Phys.* **B612** (2001) 25–58, `arXiv:hep-ph/0106067`.

[34] C. W. Bauer, D. Pirjol, I. Z. Rothstein, and I. W. Stewart *Phys. Rev.* **D70** (2004) 054015, `arXiv:hep-ph/0401188`.

[35] A. Ali, G. Kramer, and G.-h. Zhu *Eur. Phys. J.* **C47** (2006) 625–641, `arXiv:hep-ph/0601034`.

[36] M. Zhong, Y.-L. Wu, and W.-Y. Wang *Int. J. Mod. Phys.* **A18** (2003) 1959–1989, `arXiv:hep-ph/0206013`.

[37] A. Faessler, T. Gutsche, M. A. Ivanov, J. G. Korner, and V. E. Lyubovitskij *Eur. Phys. J. direct* **C4** (2002) 18, `arXiv:hep-ph/0205287`.

[38] D. Melikhov, N. Nikitin, and S. Simula *Phys. Rev.* **D57** (1998) 6814–6828, `arXiv:hep-ph/9711362`.

[39] C.-H. Chen and C. Q. Geng *Phys. Rev.* **D66** (2002) 094018, `arXiv:hep-ph/0209352`.

[40] **BABAR** Collaboration, B. Aubert *et al.* *Phys. Rev. Lett.* **91** (2003) 221802, `arXiv:hep-ex/0308042`.

[41] **Belle** Collaboration, K. Abe *et al.* `arXiv:hep-ex/0410006`.

[42] **CDF** Collaboration, T. Aaltonen *et al.* `arXiv:0804.3908 [hep-ex]`.

[43] F. Kruger, L. M. Sehgal, N. Sinha, and R. Sinha *Phys. Rev.* **D61** (2000) 114028, `arXiv:hep-ph/9907386`.

[44] F. Kruger and E. Lunghi *Phys. Rev.* **D63** (2001) 014013, `arXiv:hep-ph/0008210`.

[45] C. Bobeth, G. Hiller, and G. Piranishvili *JHEP* **07** (2008) 106, `arXiv:0805.2525 [hep-ph]`.

[46] G. Hiller and F. Kruger *Phys. Rev.* **D69** (2004) 074020, `arXiv:hep-ph/0310219`.

[47] M. Artuso *et al.* `arXiv:0801.1833 [hep-ph]`.

[48] Q.-S. Yan, C.-S. Huang, W. Liao, and S.-H. Zhu *Phys. Rev.* **D62** (2000) 094023, `arXiv:hep-ph/0004262`.

[49] G. Hiller *Phys. Rev.* **D70** (2004) 034018, `arXiv:hep-ph/0404220`.

[50] Y. Wang and D. Atwood *Phys. Rev.* **D68** (2003) 094016, `arXiv:hep-ph/0304248`.

[51] F. Kruger and J. Matias *Phys. Rev.* **D71** (2005) 094009, `arXiv:hep-ph/0502060`.

[52] A. Ali, T. Mannel, and T. Morozumi *Phys. Lett.* **B273** (1991) 505–512.

[53] C. Bobeth, T. Ewerth, F. Kruger, and J. Urban *Phys. Rev.* **D64** (2001) 074014, `arXiv:hep-ph/0104284`.

[54] D. A. Demir, K. A. Olive, and M. B. Voloshin *Phys. Rev.* **D66** (2002) 034015, `arXiv:hep-ph/0204119`.

[55] **BABAR** Collaboration, B. Aubert *et al. Nucl. Instrum. Meth.* **A479** (2002) 1–116, `arXiv:hep-ex/0105044`.

[56] **BABAR** Collaboration, M. H. Kelsey *Nucl. Instrum. Meth.* **A535** (2004) 206–211.

[57] **BABAR-DIRC** Collaboration, I. Adam *et al. Nucl. Instrum. Meth.* **A538** (2005) 281–357.

[58] B. B. Brabson *et al. Nucl. Instrum. Meth.* **A332** (1993) 419–443.

[59] A. Drescher *et al. Nucl. Instrum. Meth.* **A237** (1985) 464–474.

[60] T. Brandt, *Electron identification and measurement of the inclusive semileptonic branching fraction of B mesons at the BABAR experiment.* PhD thesis, Dresden, Tech. U., 2001.

[61] F. Anulli *et al. Nucl. Instrum. Meth.* **A539** (2005) 155–171.

[62] **BaBar** Collaboration, F. Anulli *et al. Nucl. Instrum. Meth.* **A494** (2002) 455–463.

[63] F. Anulli *et al. Nucl. Instrum. Meth.* **A552** (2005) 276–291.

[64] W. Menges *IEEE Nucl. Sci. Symp. Conf. Rec.* **5** (2006) 1470–1474, `arXiv:physics/0609039`.

[65] D. J. Lange *Nucl. Instrum. Meth.* **A462** (2001) 152–155.

[66] T. Sjostrand *Comput. Phys. Commun.* **82** (1994) 74–90.

[67] **GEANT4** Collaboration, S. Agostinelli *et al. Nucl. Instrum. Meth.* **A506** (2003) 250–303.

[68] **Particle Data Group** Collaboration, W. M. Yao *et al. J. Phys.* **G33** (2006) 1–1232.

[69] C. Peterson, T. Rognvaldsson, and L. Lonnblad *Comput. Phys. Commun.* **81** (1994) 185–220.

[70] G. C. Fox and S. Wolfram *Phys. Rev. Lett.* **41** (1978) 1581.

[71] S. Brandt, C. Peyrou, R. Sosnowski, and A. Wroblewski *Phys. Lett.* **12** (1964) 57–61.

[72] E. Farhi *Phys. Rev. Lett.* **39** (1977) 1587–1588.

[73] **BABAR** Collaboration, B. Aubert *et al. Phys. Rev. Lett.* **92** (2004) 111801, `arXiv:hep-ex/0306038`.

[74] **ARGUS** Collaboration, H. Albrecht *et al. Phys. Lett.* **B241** (1990) 278–282.

[75] F. James and M. Roos *Comput. Phys. Commun.* **10** (1975) 343–367.

[76] P. Ball and R. Zwicky *Phys. Rev.* **D71** (2005) 014015, `arXiv:hep-ph/0406232`.

[77] P. Ball and R. Zwicky *Phys. Rev.* **D71** (2005) 014029, `arXiv:hep-ph/0412079`.

[78] T. Feldmann *et al.* Private communication, Mar, 2008.

[79] **BABAR** Collaboration, B. Aubert *et al. Phys. Rev.* **D70** (2004) 112006, `arXiv:hep-ex/0407003`.

[80] NIST/SEMATECH, "e-handbook of statistical methods." `http://www.itl.nist.gov/div898/handbook/eda/section3/eda35g.htm`.

[81] **BABAR** Collaboration, B. Aubert *et al. Phys. Rev.* **D76** (2007) 031102, `arXiv:0704.0522 [hep-ex]`.

[82] A. Ishikawa *et al. Phys. Rev. Lett.* **96** (2006) 251801, `arXiv:hep-ex/0603018`.

[83] G. Eigen `arXiv:0807.4076 [hep-ex]`.

[84] T. Huber, T. Hurth, and E. Lunghi `arXiv:0712.3009 [hep-ph]`.

[85] A. Hovhannisyan, W.-S. Hou, and N. Mahajan *Phys. Rev.* **D77** (2008) 014016, `arXiv:hep-ph/0701046`.

[86] J. Dickens, V. Gibson, C. Lazzeroni, and M. Patel. CERN-LHCB-2007-039.

[87] T. Kageyama *AIP Conf. Proc.* **842** (2006) 1064–1066.

[88] M. Bona *et al.* `arXiv:0709.0451 [hep-ex]`.

Appendix I

Studying Nonlinear Non-uniformity in the BaBar EMC Crystals

Studying Nonlinear Non-uniformity in the BaBar EMC Crystals

G. Eigen, L. Sun

Sep 2007

Abstract

The light yield non-uniformity in the *BABAR* EMC crystals causes the disagreement between the measured neutral energy spectrum and the Monte Carlo simulation, since it has not been taken into account for in the current Monte Carlo simulation. In our study, Initial State Radiation (ISR) $\mu\mu\gamma$ samples are used to analyze the effect of different crystal non-uniformities on Monte Carlo energy line shape. Instead of modeling the end-to-end light yield variation of EMC crystals in a linear manner, we propose a new "V-shape" model, in which the light yield first decrease towards the center of the crystals and then increase again. The model proves to be successful in improving the agreement between the simulation and data.

1   Introduction

The light yield of the CsI crystals in the *BABAR* electromagnetic calorimeter (EMC) is not uniform along the crystal length. Since the crystals are projective, the light-yield is naturally non-uniform. The non-linear effects have been compensated by wrapping the crystals in sheets with a mounted black-and-white pattern[1].

Light yield tests on the bench have confirmed that the residual non-uniformities were a few percent showing a linear decrease in light yield from the tip of the crystal[2]. These test were performed before the crystals were mounted into the barrel and endcap modules.

After seven years of operation aging and radiation damage has caused modification in the surface of the crystals leading to an increase in light non-uniformities and a degradation of the energy resolution. Furthermore, the light yield modeling in the simulation becomes inaccurate. To account for this effect, in previous studies the crystals were divided into eight sections from front to rear. For each section a specific light correction factor was determined by assuming a linear light-yield variation with the crystal length. (eg. see J. L. Ritche *et al*[3]). In this study single-photon events were generated using the linear model of non-uniformities. An improvement was observed between data and simulation for low energy photons.

We start our study with a sample of simulated ISR $\mu\mu\gamma$ events, in which linearly-varying crystal non-uniformities are implemented. We vary the size of the non-uniformities between 0% and 50% and compare the simulated photon energies with measurements. A linearly-varying non-uniformity of about 30% can degrade the photon energy resolution sufficiently to obtain reasonable agreement with measurements. For low energies, however, the agreement of data and simulation is still poor. In this study, we propose a new non-uniformity model. The uniformity coefficients from front to rear first decrease linearly till a certain crystal section and then increase again linearly ("V-shape"). We divide the EMC into 7 sub-regions to obtain an improved agreement between data and Monte Carlo (MC) simulation. Measured energies of MC photons have been carefully scaled to align their peaks with data and only photons with an energy above 2 GeV are taken into consideration. The validation with symmetric π^0's from τ decays shows moderate improvements in agreement between simulation and data for low energy photons.

2 Method

For photons originating from ISR $\mu\mu\gamma$ decays, the energy measured in the EMC is correlated with the energy E_{fit} determined from a kinematic fit to $\mu\mu\gamma$ events. Since the latter is constrained by the tracking information of the 2 muons and the energy of the initial state, E_{fit} is determined with much higher precision than E_{reco} and may be regarded as the real photon energy E_{gen}. We evaluate the MC simulation by comparing the ratio E_{reco}/E_{fit} for data and MC samples.

The basic working environment in the study is based on the following requirements:

- Release 18.6.2a and a private test condition database (CDB) is set up with all the condition data imported and loaded

- Neutral correction is disabled

- ISR_mmg_emin_500MeV.tcl is used as a configuration file to generate ISR $\mu\mu\gamma$ decay events

- CONDALIAS is set to be "Sep2003" to compare with Run4 data

- Background Mixing is turned off by default

- NeutralMiniUser package (V00-00-07) is used to make n-tuples from generated collections with Tag-IncExclsr filter enabled to eliminate the high side tail in MC E_{reco}/E_{fit} histograms

The description of uniformity coefficients and the way to load them in the simulation can be found in the EmcSim package and Ref. [3].

2.1 Test with linearly-varying uniformity coefficients

Various crystal uniformity coefficients have been loaded into EMC condition database to test their effects on E_{reco}/E_{fit} histogram line shapes of generated $\mu\mu\gamma$ events. The non-uniformity of an EMC crystal is defined to be the difference between the uniformity coefficients in its first and last section. To avoid the artificial edge correction effect near 1 GeV in the EMC simulation, only ISR photons with an energy above 2 GeV are considered. Figure 1 shows a comparison of E_{reco}/E_{fit} distributions with different crystal non-uniformities simulated. The energy resolution improves with increasing non-uniformities, reaches at minimum at $\sim$10% non-uniformity and then deteriorates rapidly with increasing non-uniformities. For a non-uniformity of 30% the best MC-data agreement is achieved. Figure 2 shows the E_{reco}/E_{fit} distributions for different non-uniformities with fits to a Crystal Ball (CB) shape[4] overlaid.

Figure 3 shows the energy resolutions (FWHM/2.35 from the CB shape fit) for different non-uniformities. For Run4 data, the resolution (FWHM/2.35) is at around 0.02, which is close to what we obtain for a 30% non-uniformity.

Figures 4 and 5 show the E_{reco}/E_{fit} distributions for default MC and Run4 data. Figures 6 and 7 show the distributions for MC simulation with 30% non-uniformity and Run4 data. The simulated value of E_{reco} has been re-scaled to align the peaks of the distributions with those in the data. For high-energy (above 2 GeV) photons the best data/MC agreement is achieved in the linear model with a $\sim$30% non-uniformity. The two distributions still show substantial differences, especially near the peak. The data/MC agreement becomes worse for low energy photons.

2.2 Collecting EMC GHits information to test different parametrization

Since the linear model does not provide a satisfactory simulation of data, we have investigated other parameterizations of the uniformity coefficients.

To test different crystal uniformity coefficients, the conventional procedure is to write uniformity coefficients into a crystal profile, load that into a private condition database, then perform the MC simulations using Moose package.

In the EMC simulation process of a default Moose production, a EmcGHit list is scored on a single EMC crystal and digitized into a EmcDigi. EmcGHit::exs1()..exs8() are 8 GHit energies deposited on the 8 longitudinal slices of each crystal. They are multiplied by eight coefficients $\{c_1, c_2, \cdots, c_8\}$ assigned to this crystal and summed up yielding the energy of EmcDigi. All EmcDigi energies associated with a neutral candidate are further summed up in the event reconstruction stage and calibrated to make the E_{reco}.
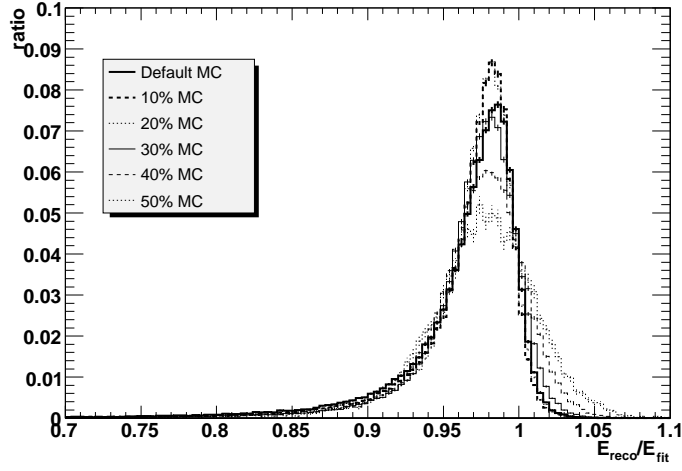
Figure 1: Normalized E_{reco}/E_{fit} histograms for perfect uniformity (default MC), 10%, 20%, 30% and 50% non-uniformities, the E_{reco} distributions with non-uniformity effects are scaled that their peaks are aligned with the peaks of distribution of the default MC.
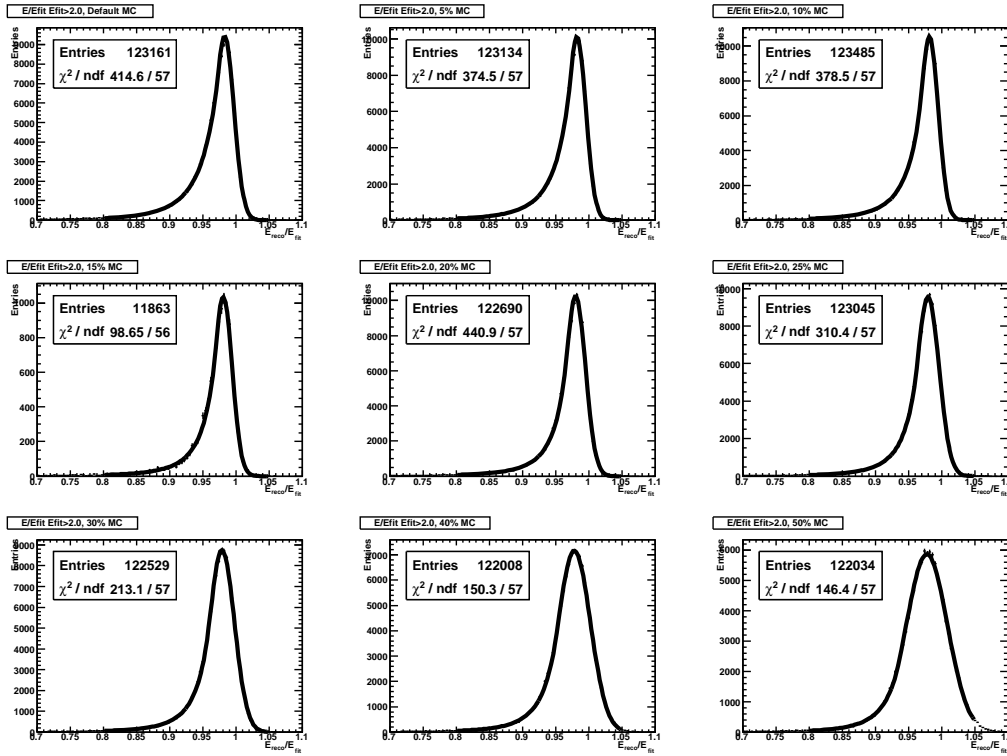

Figure 2: E_{reco}/E_{fit} histograms (points) for simulations with perfect uniformity and different non-uniformities from 5% to 50%, are fitted with a Crystal Ball distribution (solid curves).
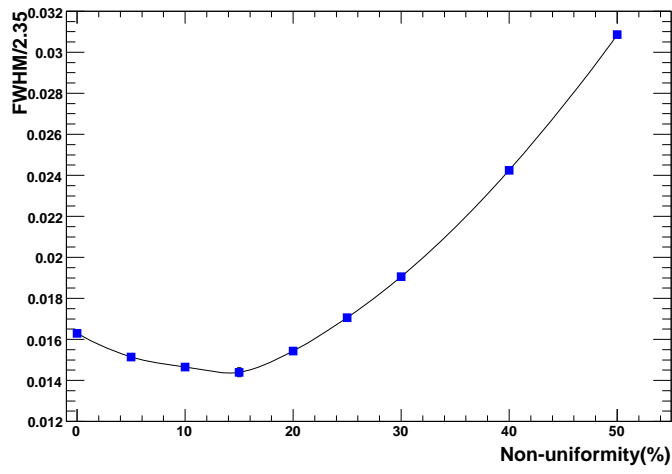
3

Figure 3: Energy resolution versus crystal non-uniformity.
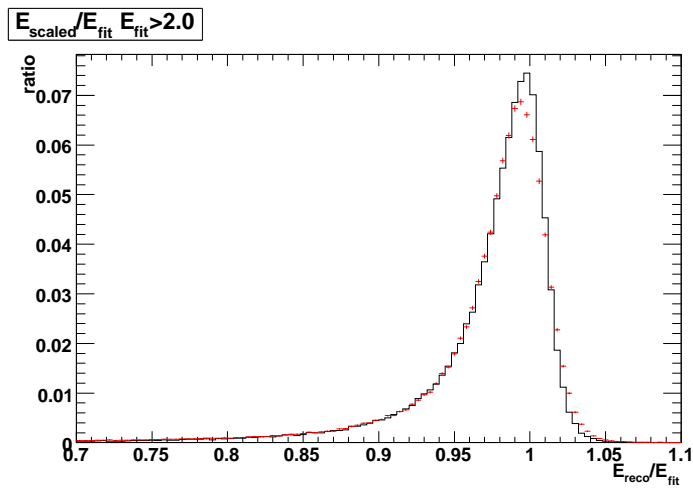
Figure 4: Default MC (solid line) and Run4 data (points with error bars) with photon energies above 2 GeV, E_{reco} in MC has been scaled according to data.
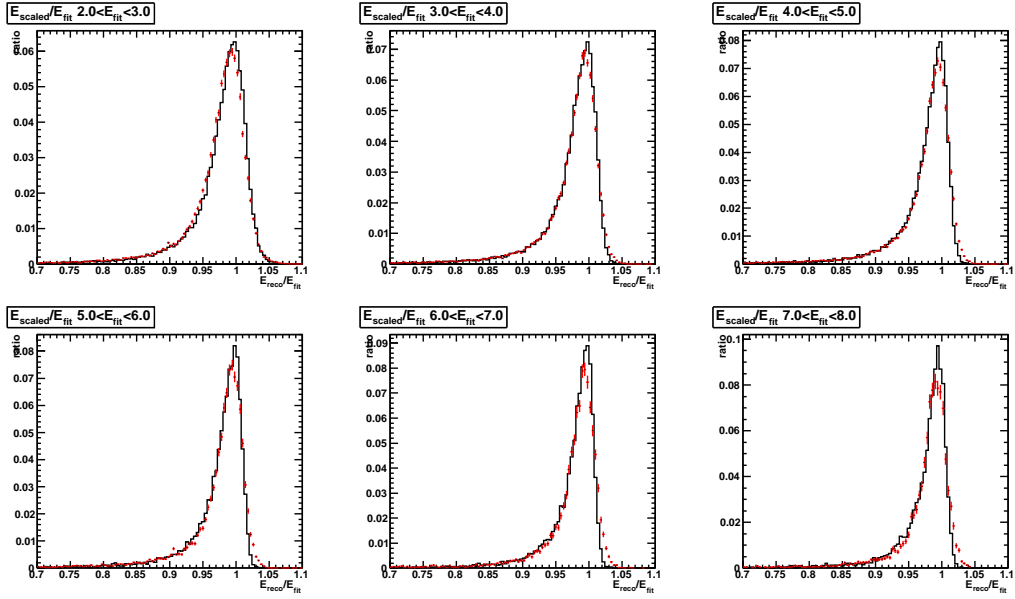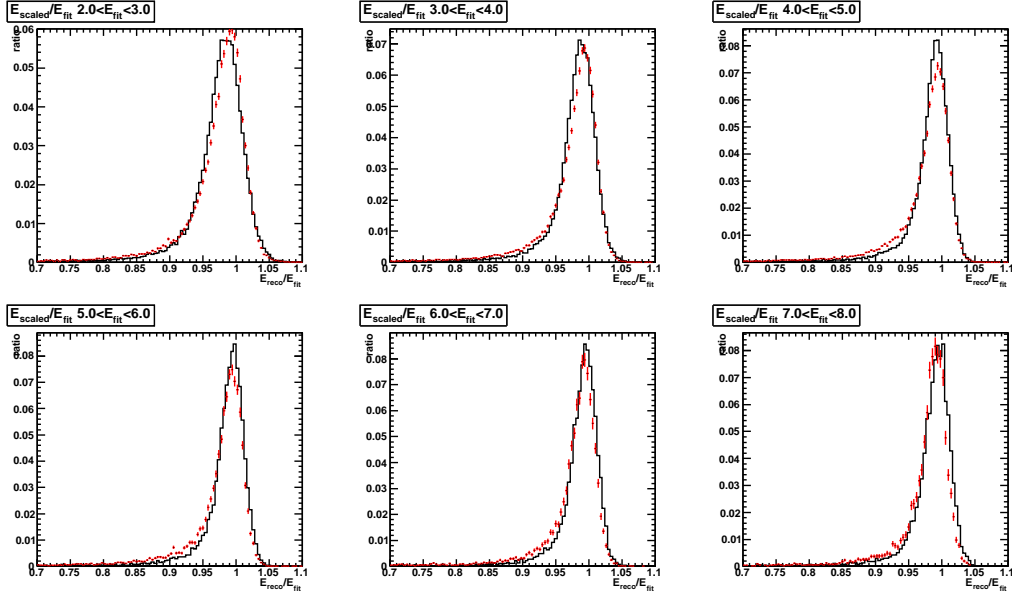
Figure 5: Comparison between default MC (solid line, after scaling of E_{reco}) and Run4 data (points with error bars) in 6 E_{fit} bins between 2 and 8 GeV.
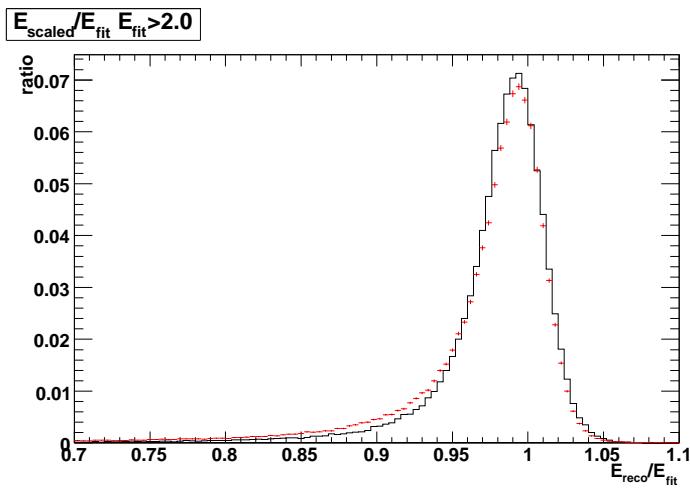
Figure 6: Comparison between MC with 30% non-uniformity (solid line, after scaling of E_{reco}) and Run4 data (points with error bars) with photon energies above 2 GeV.

Figure 7: Comparison between 30% non-uniformity MC (solid line, after scaling of E_{reco}) and Run4 data (points with error bars) in 6 E_{fit} bins between 2 and 8 GeV.

In the end of Moose production, generated MC events are saved into output data collections after digitization and reconstruction, with EMC GHits information discarded. The Beta analysis packages such as NeutralMiniUser are used to manipulate BtaCandidates stored in these collections and write out useful event and candidate variables for n-tuple stage analysis.

The whole optimization procedure using different parameterization of the uniformity coefficients becomes rather cumbersome. To simplify this, we perform the parameterization of the uniformity coefficients exclusively in the n-tuple stage. Therefore we need to track down necessary GHits information associated with each neutral candidate, then write it into the n-tuples as additional candidate variables for EMC energy reconstruction. Obviously this cannot be done in the Beta stage alone due the unavailability of EMC GHits information. We need to integrate Beta jobs into the Moose production by appending $\mu\mu\gamma$ Beta modules taken from the NeutralMiniUser package after normal Moose sequences. During the execution of these $\mu\mu\gamma$ modules, for each neutral candidate in a event, eight GHit energies associated with each member of the candidate's EmcDigi list are summed up separately yielding eight energy fractions of the candidate raw energy. These eight energies $\{E_i\}$ are then calibrated in the same manner as the raw energy of the candidate and written into final n-tuples together with other variables of the candidate.

A tester for different uniformity coefficients $\{c_i\}$ can thus be established. In the n-tuple stage, neutral energies can be reconstructed using the following formula:

$$E_{reco} = \sum c_i E_i, \quad \sum c_i = 8. \tag{1}$$

An example of eight E_i/E_{fit} distributions is shown in Figure 8.

2.3 The partition of EMC crystals in the barrel region

Since the radiation dose depends on the crystal position in the EMC, we study six regions in the barrel and the endcap separately. The individual regions are shown in Figure 9 and are specified in Table 1. Since the crystals in each region are assumed to be homogeneous, all crystals in each detector region are assigned with a unique set of uniformity coefficients $\{c_i\}$.
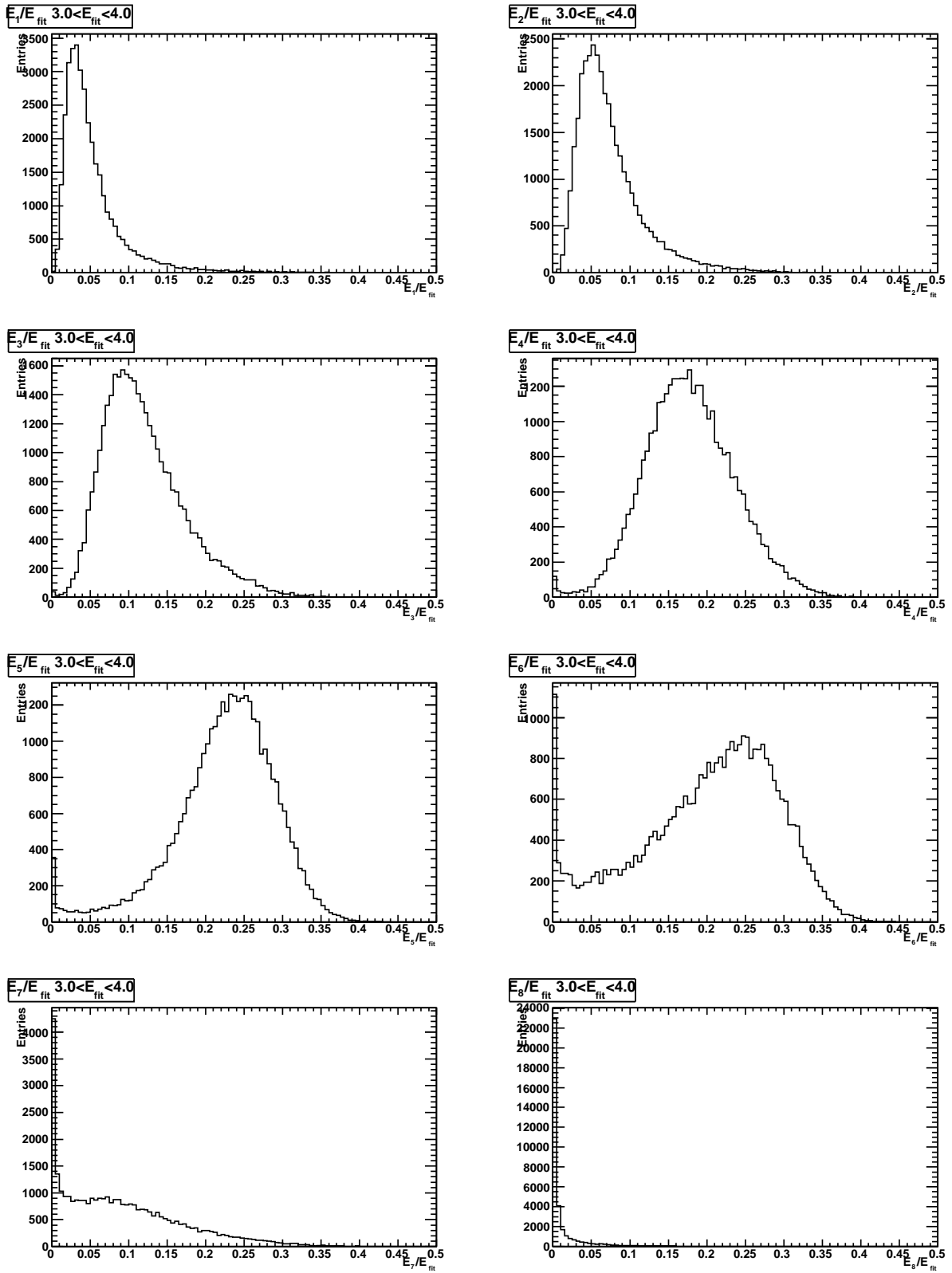
Figure 8: E_i/E_{fit} distributions in the 8 crystal regions for photon energies between 3 and 4 GeV.

Region No.	1	2	3	4	5	6
Theta Index	9 - 15	16 - 22	23 - 29	30 - 36	37 - 45	46 - 56
Theta Interval (radians)	0.473 - 0.654	0.655 - 0.901	0.902 - 1.213	1.214 - 1.571	1.571 - 1.978	1.978 - 2.456
Crystal Length (X_0)	17.5	17.0	16.5	16.0	16.0	16.0

Table 1: Partition of EMC barrel region
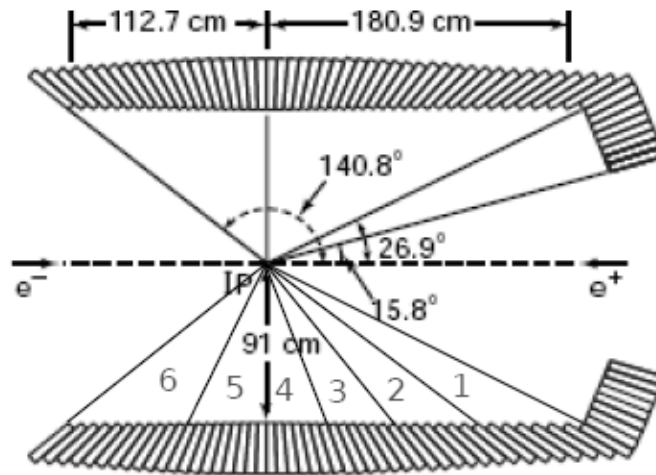
Figure 9: Side view of the *BABAR* EMC[1]. The partition of six regions in the barrel is shown, EMC endcap region is numbered as Region 0 for completion.

c1=1.071	c2=1.030	c3=0.990	c4=0.950	c5=0.910	c6=0.963	c7=1.017	c8=1.071

Figure 10: An example of the uniformity coefficients $\{c_i\}$ in EMC barrel region 1, the length of each section is shown proportional to its actual size, the line is the variation curve of the coefficients.

2.4   Definition and minimization of χ^2

For a given set of uniformity coefficients $\{c_i\}$, E_{reco} is reconstructed via Eq. 1 for each neutral candidate. The resulting distribution is multiplied with a calibration factor to align the peak of E_{reco}/E_{fit} distribution with that in the data. To evaluate the discrepancy of E_{reco}/E_{fit} distributions between MC and data, we calculate the χ^2 on a bin-by-bin basis by

$$\chi^2 = \sum \frac{\left(x_i^{MC} - x_i^{Data}\right)^2}{\left(\sigma_i^{MC}\right)^2 + \left(\sigma_i^{Data}\right)^2}, \tag{2}$$

where x_i^{MC} and x_i^{Data} are the contents of bin number i of scaled MC histogram and data histogram, σ_i^{MC} and σ_i^{Data} are their statistical errors.

For sufficiently high statistics, in principle we can use MINUIT in order to determine the coefficients $\{c_i\}$. Due to statistical fluctuations, it is practically not possible to find the best set. We, therefore, try a simple model in which we tune a few parameters and minimize the χ^2.

2.5   A new model for the light yield variation along the crystals

In the seven different detector regions, a "V-shape" model is proposed in this note to determine the coefficients $\{c_i\}$ region by region. In this model, we first decrease the non-uniformities from the rear (8th section) towards the center of the crystal and then increase them again towards the front of the crystal. The coefficients c_1 and c_8 are chosen to be equal. This model is completely determined by two parameters, the value k of the minimum and the overall non-uniformity. The minimal non-uniformity is in section k (typically between 3 and 5). The 8 coefficients are further normalized to fix their sum at 8, according to Eq. 1. The non-uniformity of a crystal is now defined to be the difference between the maximal coefficient c_1 and minimal coefficient c_k before the normalization. By setting $k = 1$ we retain the linear model. An example coefficients $\{c_i\}$ is shown in Figure 10, with a non-uniformity of 16.3% and $k = 5$. This is the optimal set of coefficients for EMC barrel region 1.

To find the optimal non-uniformity and k values in a certain EMC region, we fix k at a integral value between 1 and 8, scan non-uniformity values in different energy regions and select a non-uniformity value by eye where the χ^2 values from these energy regions are all at their minima. An example is shown in Figure 11.
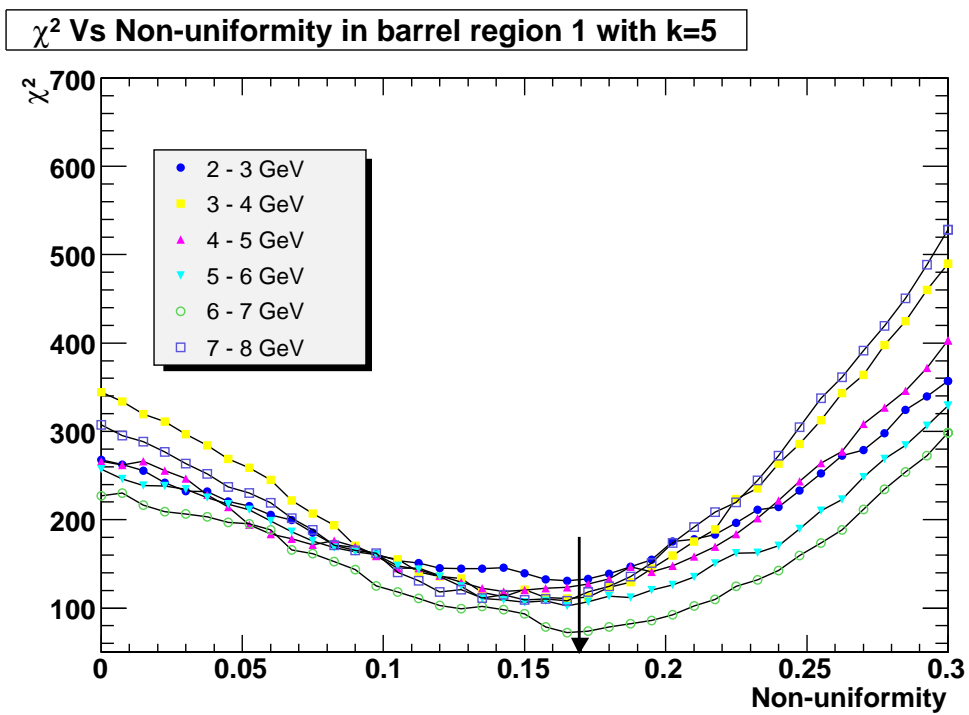
Figure 11: The χ^2 versus the non-uniformity in barrel region 1, k is fixed at 5. The arrow indicates the common optimal non-uniformity value for all six energy regions.
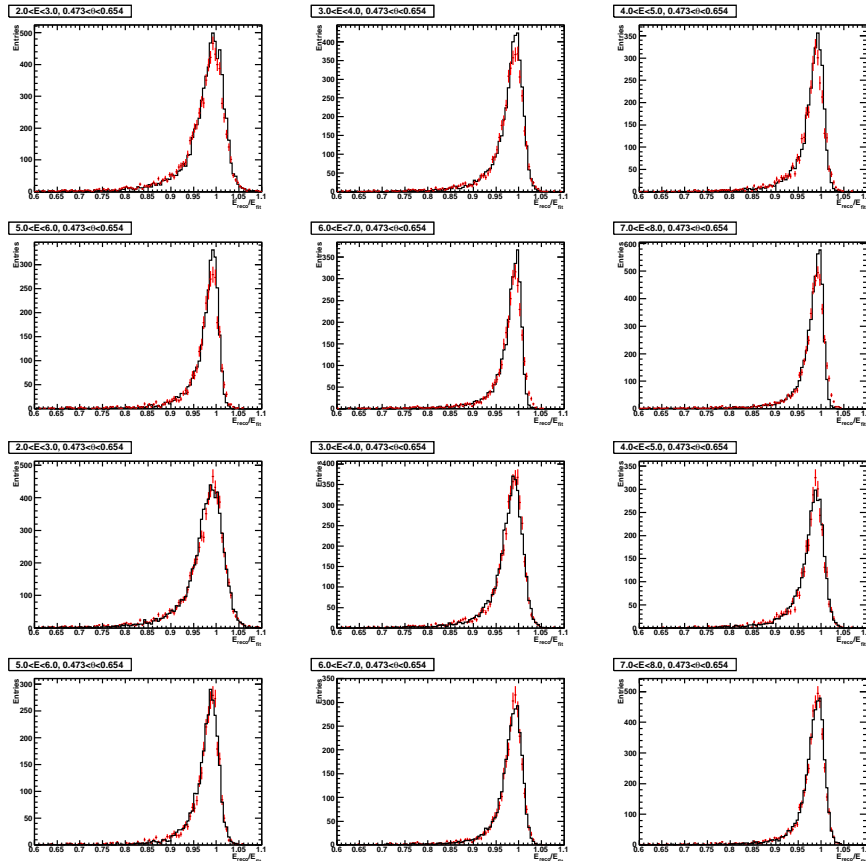
Figure 12: The E_{reco}/E_{fit} distribution in barrel region 1 for the 6 energy bins between 2 and 8 GeV for data and simulation. The top 6 plots are for uniform crystal response; the bottom 6 plots are for our "V-shape" model shown in Table 2. (Data are shown by points with error bars and MC by solid lines.)

3   Results and rescaling

We have performed the optimization in 6 energy bins (2 - 3 GeV, 3 - 4 GeV, 4 - 5 GeV, 5 - 6 GeV, 6 - 7 GeV, 7 - 8 GeV) for 7 detector regions. Figures 12-18 show the E_{reco}/E_{fit} distributions in the 7 detector regions for the "V-shape" model as well as for a uniform response in comparison to Run4 data. In some EMC barrel regions, we were not able to determine the non-uniformity parameters for high photon energies due to low statistics. A summary of our optimal results is presented in Table 2.

For our optimal choices of uniformity coefficients in the V-shape model, we observe a significant improvement in the data/MC comparison. The simulation yields an energy resolution compatible with that observed in the data. In addition, the tail of the energy distribution is well described. In this approach, however, the reconstructed energy depends on uniformity coefficients defined in Eq. 1. After our non-uniformity correction, the peaks in the simulated E_{reco}/E_{fit} distributions will be shifted with respect to those in default MC simulation and thus require rescaling. The rescaling factor is energy dependent and varies for the different detector regions. The individual results are depicted in Figure 19. The variations for photon energy between 2 GeV and 8 GeV are less than 0.3%. In order to include our parametrization in the MC production, we select the factors of the 3 - 4 GeV energy regions in different detector regions to scale the obtained optimal uniformity coefficients assigned to the corresponding regions. These scaled uniformity coefficients are further written into a crystal profile and loaded into our conditions database. For photon energies above 2 GeV, the shifts of the E_{reco}/E_{fit} peaks resulting from the non-uniformity correction are properly removed.
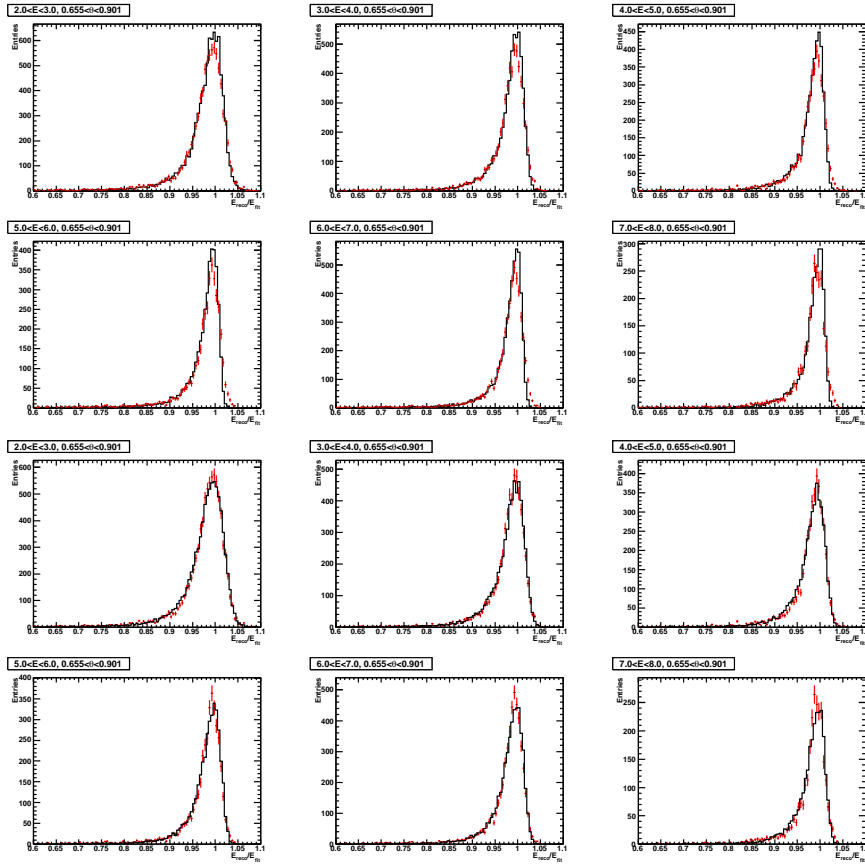
11

Figure 13: The E_{reco}/E_{fit} distribution in barrel region 2 for the 6 energy bins between 2 and 8 GeV for data and simulation. The top 6 plots are for uniform crystal response; the bottom 6 plots are for our "V-shape" model shown in Table 2. (Data are shown by points with error bars and MC by solid lines.)
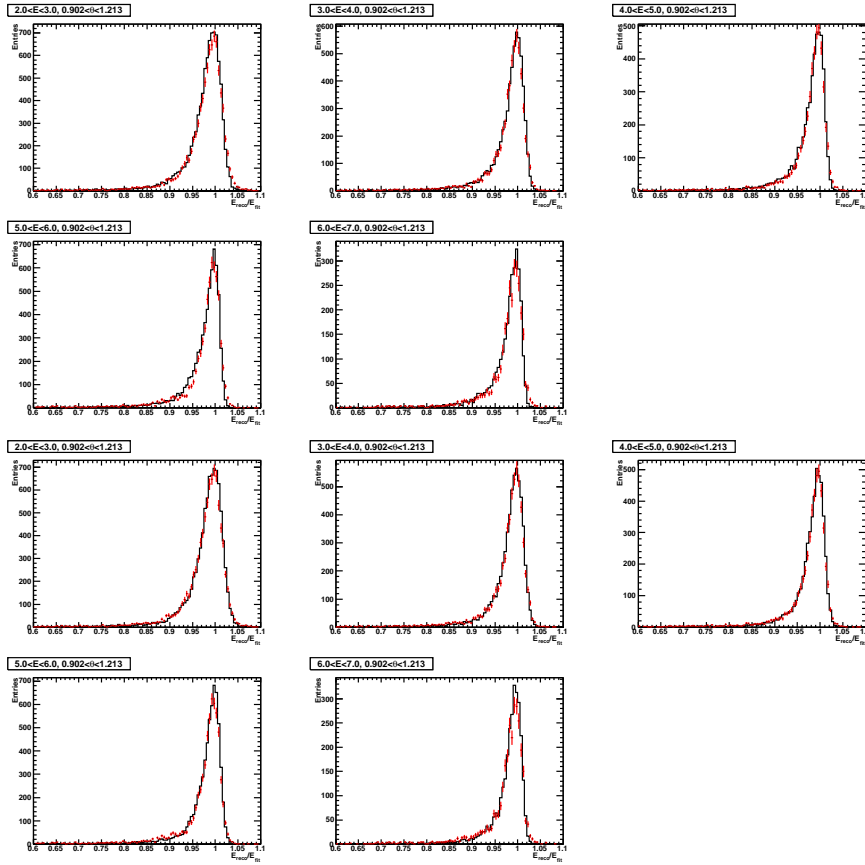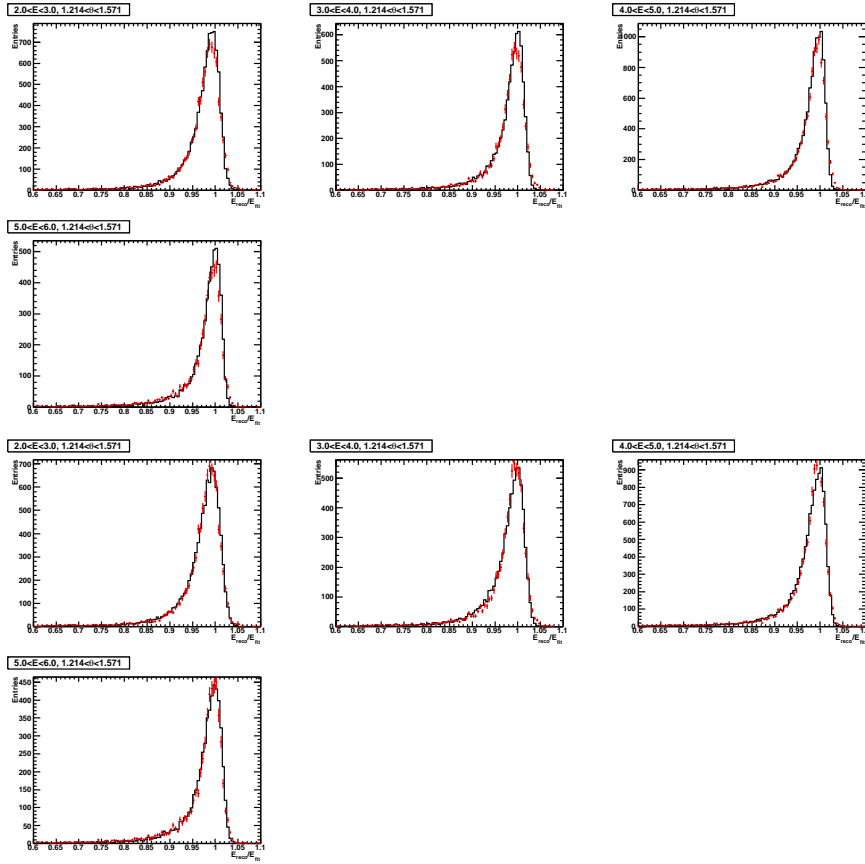
Figure 14: The E_{reco}/E_{fit} distribution in barrel region 3 for the 5 energy bins between 2 and 7 GeV for data and simulation. The top 5 plots are for uniform crystal response; the bottom 5 plots are for our "V-shape" model shown in Table 2. (Data are shown by points with error bars and MC by solid lines.)
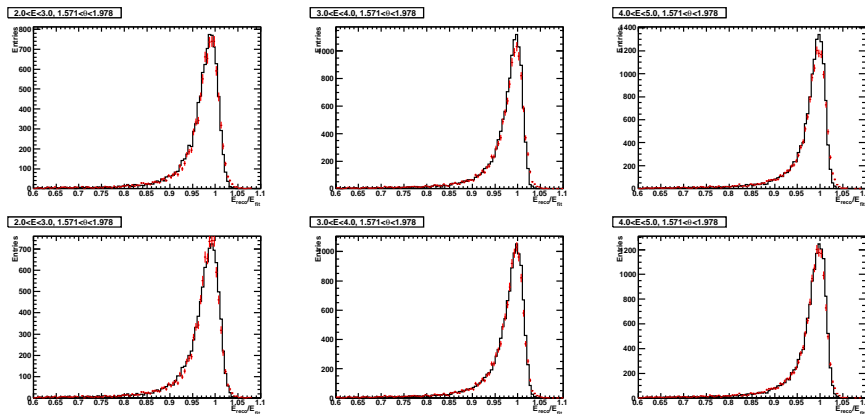
Figure 15: The E_{reco}/E_{fit} distribution in barrel region 4 for the 4 energy bins between 2 and 6 GeV for data and simulation. The top 4 plots are for uniform crystal response; the bottom 4 plots are for our "V-shape" model shown in Table 2. (Data are shown by points with error bars and MC by solid lines.)
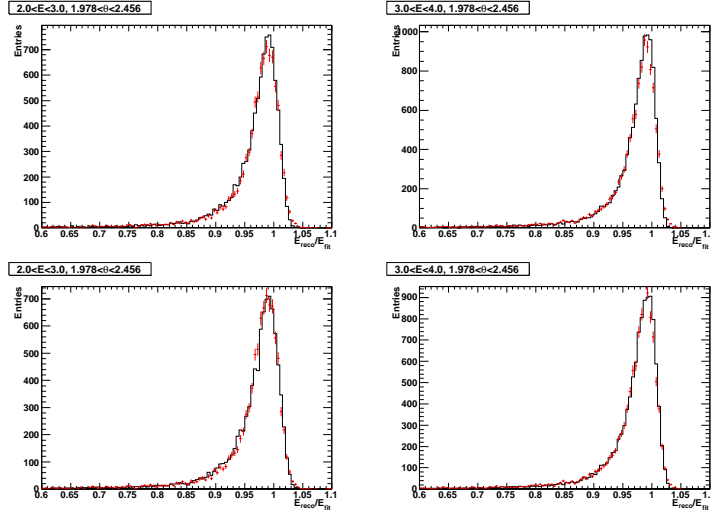

Figure 16: The E_{reco}/E_{fit} distribution in barrel region 5 for the 3 energy bins between 2 and 6 GeV for data and simulation. The top 3 plots are for uniform crystal response; the bottom 3 plots are for our "V-shape" model shown in Table 2. (Data are shown by points with error bars and MC by solid lines.)
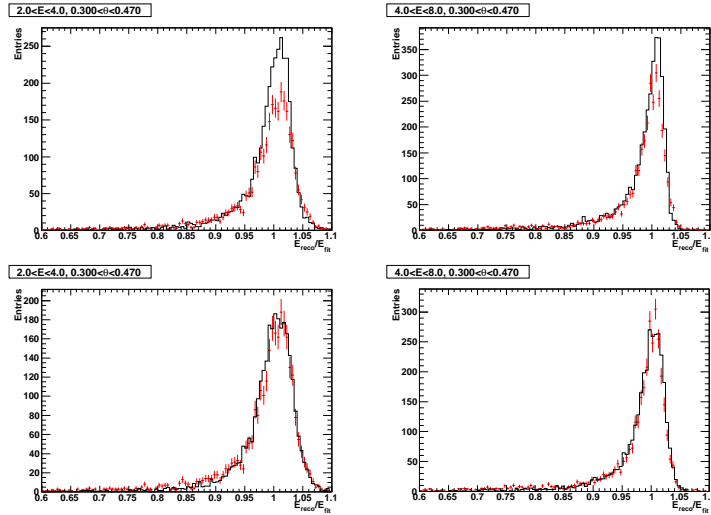
14

Figure 17: The E_{reco}/E_{fit} distribution in barrel region 6 for the 2 energy bins between 2 and 4 GeV for data and simulation. The top 2 plots are for uniform crystal response; the bottom 2 plots are for our "V-shape" model shown in Table 2. (Data are shown by points with error bars and MC by solid lines.)

Figure 18: The E_{reco}/E_{fit} distribution in endcap region for the 2 energy bins between 2 and 8 GeV for data and simulation. The top 2 plots are for uniform crystal response; the bottom 2 plots are for our "V-shape" model shown in Table 2. (Data are shown by points with error bars and MC by solid lines.)
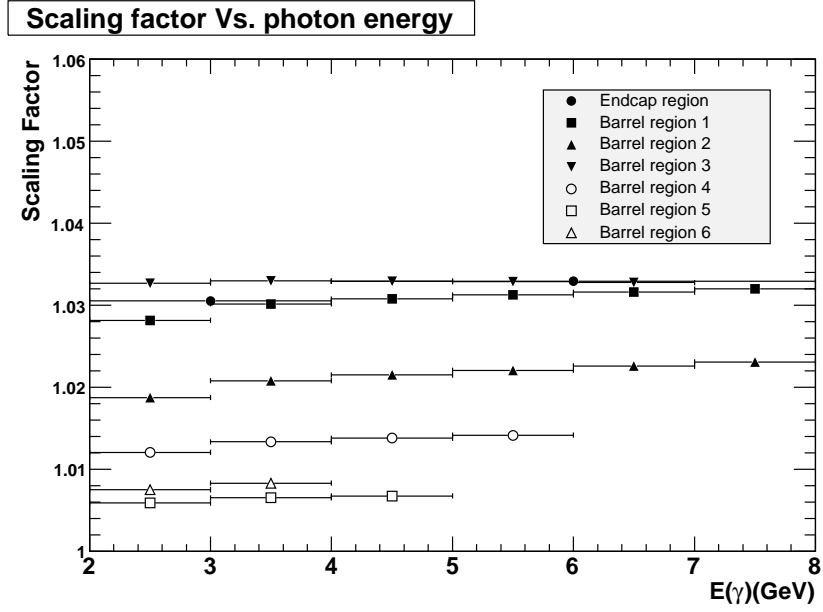
Figure 19: Scaling factors for different photon energies and in different EMC regions are applied to correct extra energy peak shifts brought in by our "V-shape" model.

Region No.	0	1	2	3	4	5	6
Theta Interval (radians)	0.277 - 0.470	0.473 - 0.654	0.655 - 0.901	0.902 - 1.213	1.214 - 1.571	1.571 - 1.978	1.978 - 2.456
Non-uniformity (%)	16.94	16.29	13.65	14.54	9.15	4.50	5.71
k	5	5	4	5	3	3	3

Table 2: A summary of the optimized tuning parameters, Region 0 is the endcap region.

4 Validation with symmetric π^0

So far, our analysis was focused on photons from $\mu\mu\gamma$ decays with photon energies above 2 GeV. In order to validate our "V-shape" model, for low-energy photons, we select π^0 mesons from generic τ decays. Previous studies of the π^0 mass and width are presented in Ref. [5, 6]. In our validation, only symmetric π^0 mesons are selected by restricting both of their daughter EMC photons to have a energy fraction $E_\gamma/E_{\pi^0} \in [0.35, 0.65]$ in the lab frame.

After loading our scaled optimal uniformity coefficients into the conditions database for generating generic SP tau events (SP-3429), π^0 mesons are reconstructed from two neutral candidates with energies reconstructed using Eq. 1. For photon energies E_{reco} lower than 2 GeV, the scaling factors previously implemented in the uniformity coefficients are not sufficient to compensate the shifts of the energy peaks resulting from the non-uniformity corrections. These energies are further multiplied by a common scaling factor. Figure 23 shows the distribution after the additional rescaling. The NeutralMiniUser package is used to generate Tau n-tuples for the "V-shape" model. The Tau n-tuples for the data and the MC simulation with uniform crystal response are taken from the directories indicated in the webpage[7]. Only Run4 September data is used for the validation.

π^0 mass spectra are fit with the Novosibirsk function[8] plus a linear background, in different photon energy regions, as shown in Figures 20, 21, 22 for different samples, respectively.

The reconstructed π^0 mass widths are shown in Figure 24. Due to low statistics, the error bars in the last photon energy bin are rather large. The plot shows that the data and the MC simulation still differ in particular at low photon energies. The "V-shape" model, however, provides an improvement over the MC simulation with uniform crystal response in describing the observed widths of the π^0 mass distributions.
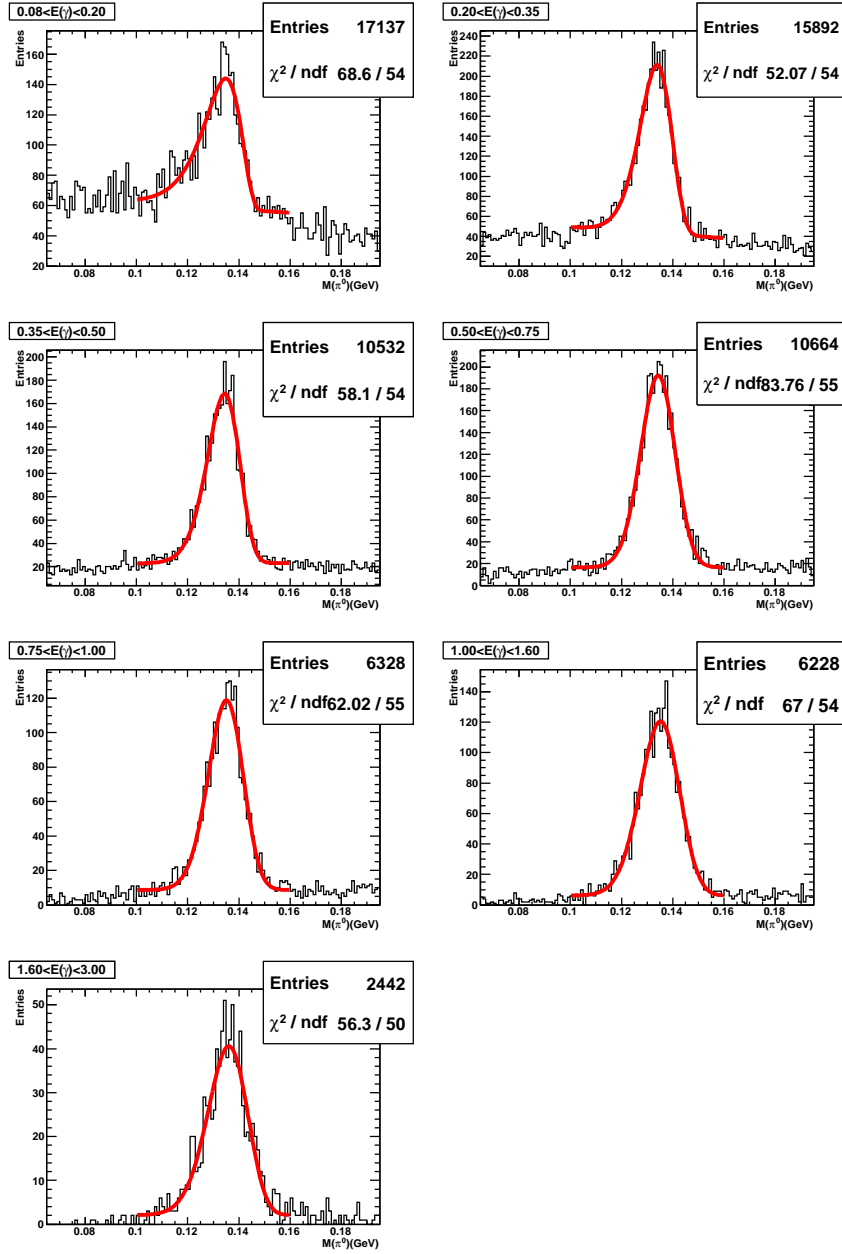
Figure 20: The π^0 mass spectra reconstructed from $\gamma\gamma$ decays in seven photon energy bins between 0.08 and 3.0 GeV for a Run4 data sub-sample. The curves show fits to the Novosibirsk function plus a linear function.
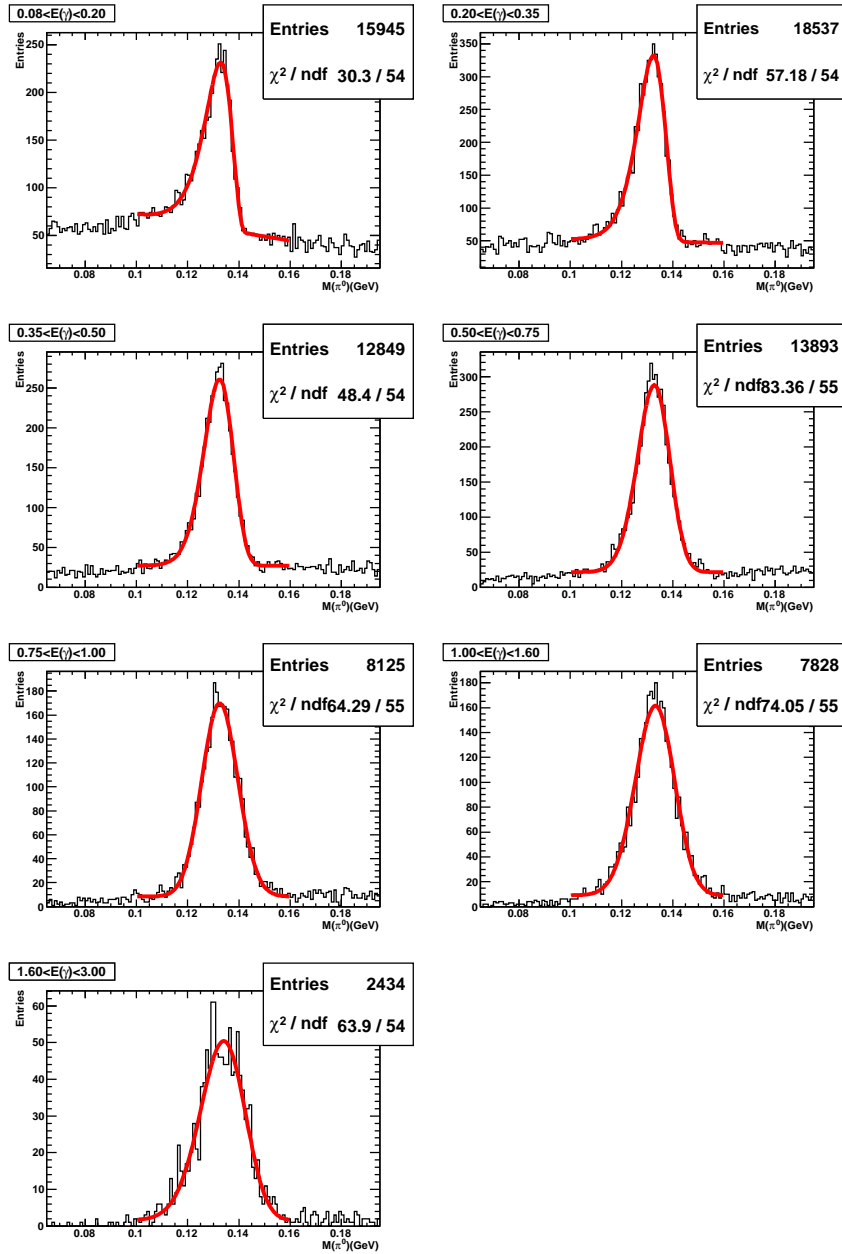
Figure 21: The π^0 mass spectra reconstructed from $\gamma\gamma$ decays in seven photon energy bins 0.08 to 3.0 GeV for the MC sample with complete uniform EMC crystals. The curves show fits to the Novosibirsk function plus a linear function.
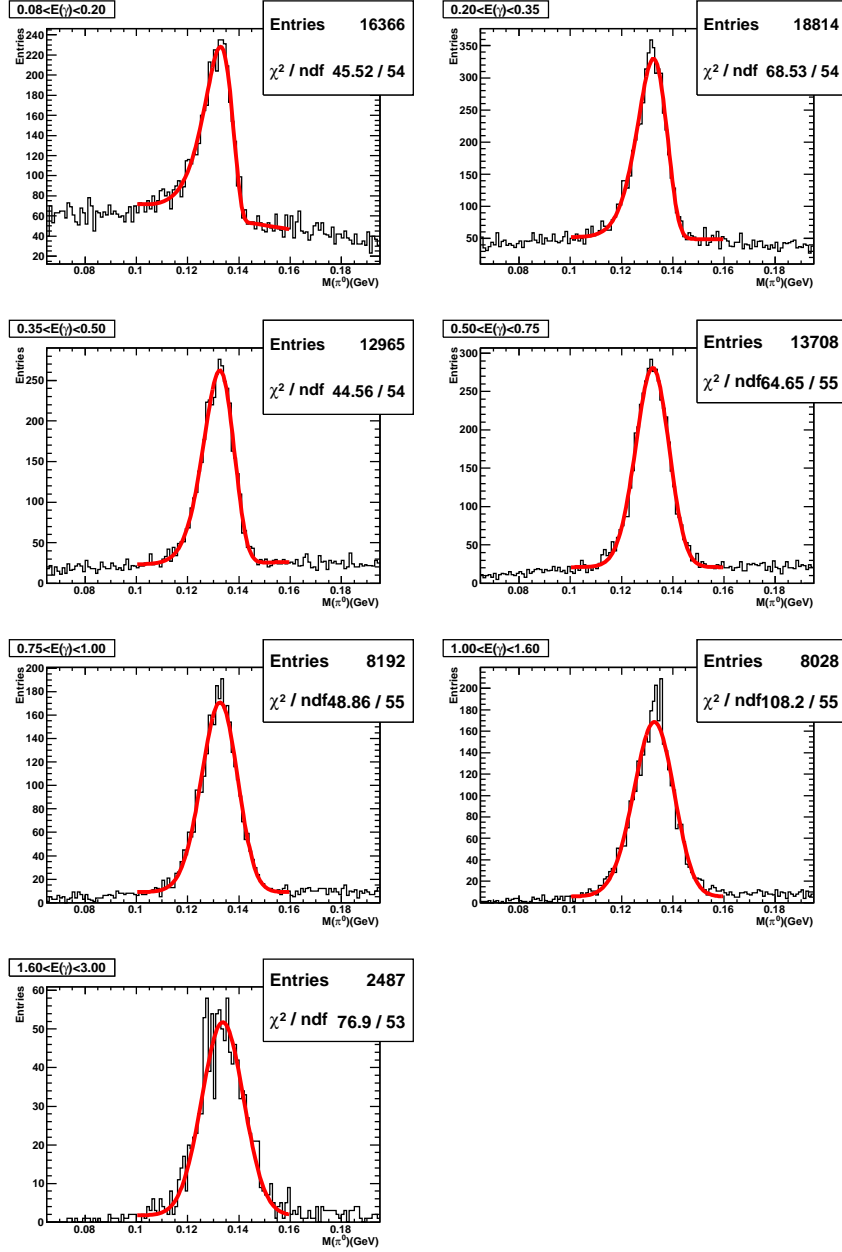
Figure 22: The π^0 mass spectra reconstructed from $\gamma\gamma$ decays in seven photon energy bins between 0.08 and 3.0 GeV for the MC sample with the obtained optimal crystal uniformity coefficients loaded. The curves show fits to the Novosibirsk function plus a linear function.
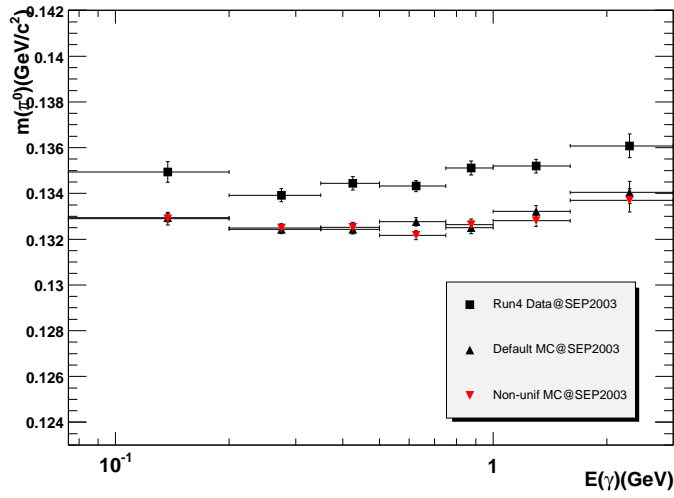
Figure 23: The position of the π^0 mass peak for different photon energies for data, simulation with uniform crystal response and for our "V-shape" model.
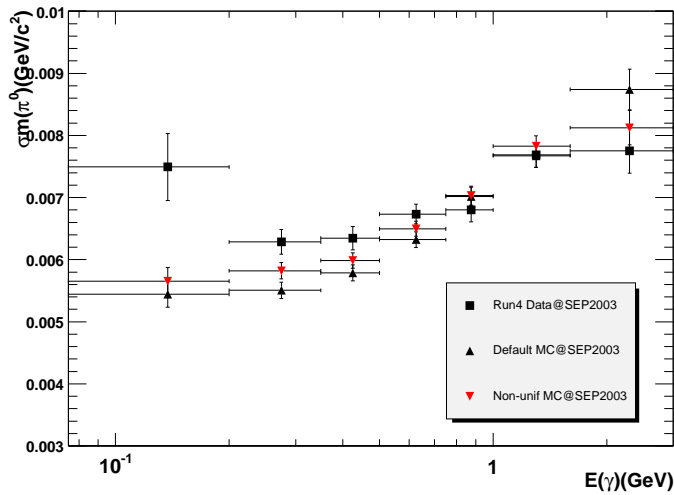

Figure 24: The widths of π^0 mass spectra for different photon energies for data, simulation with uniform crystal response and for our "V-shape" model.

5　Summary

We have performed a study of the non-uniformities in the *BABAR* CsI crystals using ISR $\mu\mu\gamma$ events. We show that linear model is not satisfactory. Instead we have introduced the "V-shape" model that is specified by two parameters, the overall non-uniformity and the position of the minimum k. We have optimized the non-uniformity parameters in photon energy bins between 2 and 8 GeV for seven different EMC regions. We have shown that the "V-shape" model provides a reasonably good parametrization of the CsI crystal non-uniformities. The simulation provides an excellent description of the data. We have further extended the analysis to photon energies below 2 GeV using low-energy photons from π^0 decays produced in generic τ decays. Our results show that the "V-shape" model also improves the data/MC agreement for photon energies below 2 GeV.

References

[1] BaBar Collaboration, *The BABAR Physics Book* (1998)

[2] Tetiana Hryn'ova, *et al.*, *A Study of the Impact of Radiation Exposure on Uniformity of Large CsI(Tl) Crystals for the BaBar Detector*, slac-pub-10352

[3] Jack L. Ritchie and Chris J Schilling, *EMC Crystal Nonuniformity in the BaBar Monte Carlo*

[4] The Crystal Ball (CB) distribution is a modified version of Gaussian probability density function with a smooth transition to a tail function on the low side: $f_{CB}(x,\mu,\sigma,n,\alpha) = \exp\left(-t^2/2\right)$ for $t > -\alpha$ and $\frac{(n/\alpha)^n \exp\left(-\alpha^2/2\right)}{(-t+n/\alpha-\alpha)^n}$ for $t \leq -\alpha$, where $t = \frac{x-\mu}{\sigma}$ and $\alpha > 0$.

[5] Louise Aspinwall, *et al.*, BAD#20*: Reconstruction of pi0 in BaBar*

[6] Jim Olsen, *et al.*, BAD#62: *Study of high energy pi0s in tau 1-on-1 decays*

[7] http://www.slac.stanford.edu/BFROOT/www/Physics/Analysis/AWG/Neutrals/ntuples.html

[8] The Novosibirsk function is defined as: $f(x) = A\exp(-0.5\ln^2[1+\Lambda\tau(x-x_0)]/\tau^2 + \tau^2)$, where $\Lambda = \sinh(\tau\sqrt{\ln 4})/(\sigma\tau\ln 4)$, x_0 is the peak position, σ is the width of the distribution, τ is the asymmetry parameter.